

**IMPERIAL COLLEGE OF SCIENCE TECHNOLOGY AND MEDICINE**

University of London

**THE USE OF DIFFUSE FIELD MEASUREMENTS FOR ACOUSTIC EMISSION**

by

**Mark J. Evans**

A thesis submitted to the University of London

for the degree of Doctor of Philosophy

Department of Mechanical Engineering

Imperial College of Science, Technology and Medicine

London SW7 2BX

September 1997

## Abstract

An understanding of the behaviour of diffuse fields in solid structures would greatly enhance the accuracy and applicability of Acoustic Emission (AE) measurements. The diffuse field approximation is a method whereby a complex wave field can be represented statistically in a very simple manner. However, there are certain conditions which must be satisfied before these approximations are valid. The aims of this thesis are to determine whether the necessary conditions are met by the wave fields generated by acoustic emission sources in real structures, to develop signal processing techniques to take advantage of diffuse field approximations, and to demonstrate the benefits which can be gained by treating AE signals in this manner. In practical applications the ultrasonic source would be an AE event, such as an extending crack, but for the purposes of this project a simulated source was used instead to generate a pseudo-AE signal which was both repeatable and controllable. A measurement system consisting of conical piezoelectric transducers has been developed and calibrated.

Variable transducer coupling has been highlighted as a major shortcoming of standard contact transduction methods. The unpredictable nature of the effect of coupling on the transducer response causes uncertainties as to the amplitude and frequency content of the incident signal. A novel method has been developed to measure the transducer coupling independently which shows great promise for improving the repeatability of AE measurements using contact transducers.

Experiments were carried out using this equipment on aluminium plate structures to determine whether the field generated was diffuse. The size, geometry and damping were systematically varied, thus demonstrating required conditions for a diffuse field to be sustained. Results have shown that diffuse fields are readily sustained in aluminium plate structures in the absence of additional damping; however, bolted and adhesively bonded structures are unlikely to behave diffusely due to the damping introduced by the joint. A Statistical Energy Analysis (SEA) model has been used to predict the time for a diffuse field to be generated in the plate structures and these results were compared with experimental data. The results for these experiments are presented with conclusions regarding the applicability of diffuse field measurements.

## Acknowledgements

I would like to thank Prof. Peter Cawley for his supervision and encouragement during the course of this project. Additionally I must thank Dr. John Webster of Rolls Royce for the initial impetus for the work and for advice during the last 3 years.

The members of the NDT lab have provided me with invaluable discussion and ideas and have also provided much-needed distractions. I have thoroughly enjoyed my time working with you all.

Finally thanks to EPSRC and Rolls Royce for their financial support.

# Contents

Abstract .....	2
Acknowledgements .....	3
Contents .....	4
List of tables .....	7
List of figures .....	8
Nomenclature .....	14
<b>1. BACKGROUND .....</b>	<b>15</b>
1.1 AN INTRODUCTION TO ACOUSTIC EMISSION .....	15
<i>1.1.1 Definition .....</i>	<i>15</i>
<i>1.1.2 Measurement techniques.....</i>	<i>16</i>
<i>1.1.3 Signal processing .....</i>	<i>18</i>
<i>1.1.4 Acoustic emission applications .....</i>	<i>19</i>
<i>1.1.5 Limitations of current techniques .....</i>	<i>21</i>
1.2 AN INTRODUCTION TO DIFFUSE FIELDS.....	22
<i>1.2.1 Definition .....</i>	<i>22</i>
<i>1.2.2 Literature review.....</i>	<i>24</i>
1.3 OUTLINE OF THESIS .....	27
<b>2. TRANSDUCER SELECTION AND DEVELOPMENT.....</b>	<b>31</b>
2.1 INTRODUCTION .....	31
<i>2.1.1 Overview of chapter.....</i>	<i>31</i>
<i>2.1.2 Review and comparison of transducers .....</i>	<i>31</i>
2.2 DESIGN CRITERIA FOR CONICAL PIEZOELECTRIC TRANSDUCERS.....	35
<i>2.2.1 Geometrical considerations .....</i>	<i>35</i>
<i>2.2.2 Transducer backing .....</i>	<i>36</i>
<i>2.2.3 The effect of transducer aperture.....</i>	<i>37</i>
2.3 TRANSDUCER DESIGN, MANUFACTURE AND TESTING .....	38
<i>2.3.1 Overview of the testing procedure .....</i>	<i>38</i>
<i>2.3.2 Brass backed transducers .....</i>	<i>39</i>
<i>2.3.3 Tungsten/epoxy backed transducers .....</i>	<i>40</i>
<i>2.3.4 Transducer assembly .....</i>	<i>43</i>
<i>2.3.5 Comparison of brass and tungsten/epoxy backed transducers.....</i>	<i>43</i>
2.4 ELECTRICAL IMPEDANCE MEASUREMENTS .....	44
<i>2.4.1 Background .....</i>	<i>44</i>
<i>2.4.2 Unbacked transducer response.....</i>	<i>45</i>
<i>2.4.3 Backed transducer response .....</i>	<i>46</i>
2.5 CONCLUSIONS .....	47
<b>3. SIMULATED ACOUSTIC EMISSION SOURCES .....</b>	<b>68</b>
3.1 INTRODUCTION .....	68
<i>3.1.1 Overview of chapter.....</i>	<i>68</i>
<i>3.1.2 Experimental set-up .....</i>	<i>68</i>
3.2 FRACTURE SOURCES.....	69
<i>3.2.1 Pencil break source.....</i>	<i>69</i>
<i>3.2.2 Glass capillary fracture source .....</i>	<i>70</i>
3.3 IMPACT SOURCES .....	70

3.3.1 Theory .....	70
3.3.2 Ball impact source .....	72
3.3.3 Micro-hammer source.....	73
3.4 PIEZOELECTRIC SOURCES .....	75
3.5 CONCLUSIONS .....	76
<b>4. CALIBRATION AND MODELLING OF CONICAL TRANSDUCERS.....</b>	<b>94</b>
4.1 INTRODUCTION .....	94
4.1.1 <i>Overview of chapter</i> .....	94
4.2 TRANSDUCER CALIBRATION.....	94
4.2.1 <i>Literature review</i> .....	94
4.2.2 <i>Calibration set-up and specimen preparation</i> .....	99
4.2.3 <i>Michelson interferometer as a primary standard</i> .....	100
4.2.4 <i>Laser source</i> .....	102
4.2.5 <i>Signal processing</i> .....	103
4.2.6 <i>Results</i> .....	105
4.3 MODELLING OF CONICAL PIEZOELECTRIC TRANSDUCERS.....	107
4.3.1 <i>Introduction</i> .....	107
4.3.2 <i>The Greenspan model for conical transducers</i> .....	108
4.3.3 <i>Results and comparisons with calibration curves</i> .....	109
4.3.4 <i>The effect of fronting material properties</i> .....	110
4.4 AUTO-NORMALISING ULTRASONIC TRANSDUCER .....	112
4.4.1 <i>Introduction</i> .....	112
4.4.2 <i>Design and manufacture</i> .....	112
4.4.3 <i>Methodology and testing</i> .....	113
4.4.4 <i>Results</i> .....	115
4.5 CONCLUSIONS .....	117
<b>5. PREDICTION OF DIFFUSE BEHAVIOUR IN COUPLED PLATES .....</b>	<b>144</b>
5.1 OVERVIEW OF CHAPTER .....	144
5.2 STATISTICAL ENERGY ANALYSIS (SEA) .....	144
5.2.1 <i>Introduction</i> .....	144
5.2.2 <i>Discussion of assumptions</i> .....	146
5.3 CALCULATION OF LAMB WAVE REFLECTION COEFFICIENTS.....	147
5.3.1 <i>Introduction</i> .....	147
5.3.2 <i>Lamb wave propagation</i> .....	148
5.3.3 <i>The Finite Element models</i> .....	150
5.3.4 <i>Method of calculation of strain energy</i> .....	151
5.3.5 <i>Results</i> .....	153
5.4 PREDICTION OF ENERGY FLOW BETWEEN COUPLED SYSTEMS USING SEA .....	153
5.4.1 <i>Introduction</i> .....	153
5.4.2 <i>Exact and iterative SEA models of two-field systems</i> .....	153
5.4.3 <i>Coupling strength</i> .....	156
5.4.4 <i>Multiple fields</i> .....	157
5.5 CONCLUSIONS .....	158
<b>6. MEASUREMENT OF DIFFUSE FIELDS IN STRUCTURES .....</b>	<b>174</b>
6.1 INTRODUCTION .....	174
6.1.1 <i>Overview of chapter</i> .....	174
6.2 MEASUREMENT EQUIPMENT.....	175

6.2.1 Introduction.....	175
6.2.2 Excitation .....	175
6.2.3 Reception, amplification and sampling .....	176
6.2.4 Signal processing.....	177
6.2.5 Measurement of energy density .....	178
<b>6.3 EXPERIMENTAL CONFIRMATION OF DIFFUSE FIELD GENERATION IN PLANE PLATES</b>	
.....	180
6.3.1 Introduction.....	180
6.3.2 Measurement of experimental errors.....	181
6.3.3 Diffuse field verification .....	183
6.3.4 Near-field effects.....	186
6.3.5 The effect of mode conversion on the decay rate.....	187
6.3.6 Discussion .....	190
<b>6.4 EXPERIMENTAL MEASUREMENTS OF ENERGY SHARING IN COUPLED STRUCTURES</b>	190
6.4.1 Simple coupled plates .....	190
6.4.2 Plates with bolted junctions .....	192
6.4.3 Plates with adhesively bonded joints .....	195
6.4.4 Plates with step changes of thickness .....	197
6.4.5 Discussion .....	200
<b>6.5 GENERAL CONCLUSIONS</b> .....	201
<b>7. CONCLUSIONS .....</b>	<b>226</b>
7.1 REVIEW OF THESIS .....	226
7.2 SUMMARY OF FINDINGS .....	227
References.....	232
Appendix A: Predicted Lamb wave reflection coefficients.....	238

## List of tables

Table 2.1 Conical element geometries.....	39
Table 4.1 Conical element dimensions used by Greenspan (1987).....	110
Table 5.1 Calculated energy density ratios for $S_0$ and $A_0$ ( $\times 10^{11}$ J/m <sup>4</sup> ) where $U_1$ is in-plane displacement and $U_2$ is out-of-plane displacement. ....	152
Table 6.1 Experimental errors expressed as the ratio of the standard deviation to the mean value for each parameter(%). .....	182
Table 6.2 Material properties for aluminium based on Kaye and Laby (1995) and Selfridge (1985).....	183
Table 6.3 Calculated parameters for plate structures with plan areas, 1) 0.2m×0.3m and 2) 1m×1m.....	184
Table 6.4 Standard deviations of parameters measured on plane plates expressed as a percentage of the mean value. Values in brackets show the expected standard deviations due to experimental errors. ....	185
Table 6.5 Standard deviations of the envelope area measurements, expressed as a percentage of the mean value, variation with delay.....	185
Table 6.6 Variation of decay rate, the standard deviation of envelope area (EA) measurements and the envelope area difference between the near and far sides with the overlap area of a bolted joint. ....	193
Table 6.7 The equivalent attenuation per wave transit caused by increasing joint overlap area.....	194
Table 6.8 Variation of decay rate, the standard deviation of envelope area (EA) measurements and the envelope area difference between the near and far sides of the joint with the overlap area of an adhesively bonded joint.....	195
Table 6.9 The equivalent attenuation per wave transit caused by increasing joint overlap area for an adhesive joint.....	196
Table 6.10 Variation of $A_0$ and $S_0$ group velocities with thickness at 150kHz for an aluminium plate in vacuum. ....	197
Table 6.11 Envelope energy in (mVs) <sup>2</sup> measured on sections of the stepped plates. ....	199
Table 6.12 Corrected envelope energy(arbitrary units) measured on sections of the stepped plates and the ratio of energies in each case. ....	199

# List of figures

Figure 1.1 a) Idealised representation of a discrete AE event, b) Indication of the simple waveform parameters used to characterise AE signals. ....	29
Figure 1.2 a) The reflected field from a diffusely reflecting surface obeying Lambert's law, b) The reflected field from a specularly reflecting surface obeying Snell's law.....	30
Figure 2.1 Schematic diagram of a capacitive transducer. ....	49
Figure 2.2 Comparison between a) A standard AE transducer b) A conical transducer. ....	50
Figure 2.3 Transducer with a circular aperture receiving surface waves parallel to its face. ....	51
Figure 2.4 The relative sensitivity of a 10mm diameter transducer on aluminium caused by the aperture effect.....	52
Figure 2.5 Experimental equipment used to evaluate the conical transducer response.....	53
Figure 2.6 Original design of brass backed transducers. ....	54
Figure 2.7 Comparison of the responses of three brass backed transducers to the same pencil break source. ....	55
Figure 2.8 The vacuum impregnation process.....	56
Figure 2.9 Measured impedance of the tungsten/epoxy material with respect to pressure plotted against values obtained from Silk (1984). ....	57
Figure 2.10 Measured attenuation of tungsten/epoxy material with respect to pressure. ....	58
Figure 2.11 Design of new tungsten/epoxy backed transducers.....	59
Figure 2.12 a) Comparison of time domain responses of a brass backed transducer and a tungsten/epoxy backed transducer to the same pencil source, b) Frequency content of signals shown in a). ....	61
Figure 2.13 a). Comparison of the time domain responses of a brass backed transducer and a tungsten/epoxy backed transducer to the 0.5MHz input signal, b) Frequency content of signals shown in a).....	63
Figure 2.14 Measured electrical impedance of an unbacked 10mm diameter 3mm thick PZT disk.....	64
Figure 2.15 Measured electrical impedance of a 3mm thick unbacked PZT cone. ....	65
Figure 2.16 Measured electrical impedance of a 3mm thick PZT cone with brass backing. ....	66
Figure 2.17 Measured electrical impedance of a 3mm thick PZT cone with tungsten/epoxy backing, comparison of three transducers. ....	67

Figure 3.1 Experimental set-up used for the source comparisons. ....	78
Figure 3.2 a) Time domain first arrival signal measured from a pencil break source, b) Frequency content of signal shown in a).....	80
Figure 3.3 Theoretical frequency content of an impact source showing characteristic lobed shape. ....	81
Figure 3.4 a) Time domain first arrival signal measured from the impact of a 30mg, 2mm diameter steel ball, b) Frequency content of signal shown in a) together with theoretical prediction using Equation (3.4). ....	83
Figure 3.5 a) Schematic diagram of the micro-hammer, b) Detailed view of hammer and spring assembly.....	84
Figure 3.6 a) Time domain first arrival signal measured from the 0.85mm micro-hammer, b) Frequency content of signal shown in a). ....	86
Figure 3.7 a) Time domain first arrival signal measured from the 0.39mm micro-hammer, b). Frequency content of signal shown in a). ....	88
Figure 3.8 Time domain signal measured from three successive impacts of the 0.85mm micro-hammer showing the first arrival and the first edge reflection. ....	89
Figure 3.9 a) Time domain signal measured from three successive couplings of the piezoelectric source, b) Frequency content of signal shown in a) with spectrum of input signal sent to source transducer. ....	91
Figure 3.10 Response of the source transducer to a 5 cycle 150kHz Hanning windowed tone burst signal showing the frequency content of the input signal sent to source transducer. ....	92
Figure 4.1 Calibration set-up showing measurement equipment including source and receiver locations for, a) The through transmission configuration and, b) The surface configuration.....	119
Figure 4.2 A schematic diagram of the path-stabilised Michelson interferometer used in the calibration experiments.....	121
Figure 4.3 Comparison of time domain signals measured simultaneously by the interferometer and the conical transducer in the through transmission configuration showing the first arrival of the longitudinal (L) and shear (S) waves. ....	122
Figure 4.4 Effect of time domain windowing of the shear wave arrival shown in the previous figure. ....	123
Figure 4.5 Comparison of the calibration curve generated from windowed and unwindowed signals.....	124
Figure 4.6 Comparison of the time domain signals measured simultaneously by the interferometer and the conical transducer in the surface configuration showing the first arrival of the longitudinal (L) and Rayleigh (R) wave. ....	125

Figure 4.7 Effect of time domain windowing of the Rayleigh wave arrival shown in Figure 4.6.....	126
Figure 4.8 Three successive calibration curves measured for transducer WE1 after recoupling showing the change in transducer response with coupling. The thicker line is the average of the three recouplings. ....	127
Figure 4.9 Comparison of the calibration curves generated for transducers WE1 to WE3 using the through transmission configuration. ....	128
Figure 4.10 Comparison of the calibration curve measured for transducer WE1 using both the through transmission and surface wave configurations.....	129
Figure 4.11 The calibration curves for all seven transducers measured using the surface wave configuration. ....	130
Figure 4.12 a) A schematic diagram of a piezoelectric shear element with electrodes, b) The equivalent three port network.....	131
Figure 4.13 Mason equivalent circuit for a thin disk transducer showing the mechanical and electrical ports. ....	132
Figure 4.14 Predicted response of a tungsten/epoxy backed conical transducer on aluminium with a front face diameter of 1mm, back face diameter of 10mm and length of 3mm plotted with the actual measured response of a transducer of this geometry. ....	133
Figure 4.15 Comparison of theoretical model with calibration results for brass backed conical transducers, after Greenspan (1987) where the light lines are measurement and the heavy lines are theory. Cone dimensions are given in Table 4.1. ....	134
Figure 4.16 Comparison of the predicted transducer response with a variety of front materials, the backing for these predictions was tungsten/epoxy. ....	135
Figure 4.17 Measured response of transducer WE7 on stainless steel, brass and aluminium half-spaces (compare with predictions shown in previous figure). ....	136
Figure 4.18 Schematic diagram of the auto-normalising transducer showing the conical element and pinducer mounted in the backing material. ....	137
Figure 4.19 A representative backing signal measured from the auto-normalising transducer coupled to an aluminium block. The excitation signal was a five cycle, Hanning windowed toneburst at 140kHz. ....	138
Figure 4.20 Experimental set-up used for testing the auto-normalising transducer. ....	139
Figure 4.21 Results obtained from the auto-normalising transducer at 140kHz on stainless steel, brass and aluminium half-spaces and a 5mm thick aluminium plate, the solid lines are least squares fits. ....	140

Figure 4.22 Results obtained from the auto-normalising transducer at 850kHz on the stainless steel half-space showing the opposite gradient.....	141
Figure 4.23 Schematic diagram of the effect of coupling on natural frequency and the corresponding change of transducer response above and below resonance.....	142
Figure 4.24 The Fourier transform of the backing signals obtained at 0%, 50% and 100% coupling to a stainless steel half-space. The excitation signal was a 1 cycle tone burst at 450kHz.....	143
Figure 5.1 a) A simple plate structure b) Symmetric boundaries do not allow mode conversion and two separate fields of $S_0$ and $A_0$ exist c) Asymmetric boundaries promote mode conversion which couples the $S_0$ and $A_0$ fields.....	159
Figure 5.2 Mode shapes for the fundamental Lamb modes $S_0$ and $A_0$ at 0.75MHz-mm.....	160
Figure 5.3 Group velocity dispersion curves for the first four Lamb modes on a 5mm thick aluminium plate in vacuum.....	161
Figure 5.4 Example of the finite element mesh used for reflection, transmission and mode conversion coefficient calculations.....	162
Figure 5.5 A finite element predicted time domain trace of the incident and reflected signals from an asymmetric notch.....	163
Figure 5.6 Two-dimensional Fourier transform (2-D FFT) of the incident signal at 150kHz showing a single peak corresponding to $A_0$ .....	164
Figure 5.7 Two-dimensional Fourier transform (2-D FFT) of reflected signal at 150kHz showing peaks corresponding to the reflected $A_0$ and mode converted $S_0$ .....	165
Figure 5.8 Reflection coefficients calculated for a symmetric notch at 150kHz.....	166
Figure 5.9 Reflection coefficients calculated for an asymmetric notch at 150kHz.....	167
Figure 5.10 The geometry and SEA model for a simple plate system without mode conversion.....	168
Figure 5.11 The predicted response of the SEA model shown in Figure 5.10 without damping, showing clearly the steady state partitioning of energy.....	169
Figure 5.12 A weakly coupled system showing the predicted value of $t^*$ .....	170
Figure 5.13 A strongly coupled system showing the predicted value of $t^*$ .....	171
Figure 5.14 Predicted response of a plate system coupled by an asymmetric notch with $A_0$ input in substructure 1.....	172
Figure 5.15 Response of the same plate system as used in the previous figure with $S_0$ input in substructure 1 demonstrating the same $t^*$ and final energy ratios.....	173

Figure 6.1. Schematic diagram of the experimental set-up showing conical piezoelectric source and receiver along with the associated signal generation, amplification, filtering and storage equipment .....	203
Figure 6.2 a) Five cycle tone burst signal at 150kHz, b) Corresponding frequency content.....	205
Figure 6.3 Example of raw signal before and after demodulation.....	206
Figure 6.4 Signal processing techniques applied to the demodulated signal envelopes.....	207
Figure 6.5 Envelope energy plotted against input energy showing a linear relationship, solid line is least squares fit .....	208
Figure 6.6 Envelope energy plotted against plan area for constant source amplitude, error bars represent 1 standard deviation.....	209
Figure 6.7 Predicted source energy plotted against plan area of structure, solid line is the mean value and error bars indicate one standard deviation ..	210
Figure 6.8 Schematic diagram of plane plate tests showing measurement grid and structural supports .....	211
Figure 6.9 Near-field effects measured on a 5mm thick plate.....	212
Figure 6.10 Signal envelopes measured at radial increments of 5mm from the source location .....	213
Figure 6.11 Signal envelopes measured from plane plates with symmetric and asymmetric edges showing the effect of mode conversion on the decay rate.....	214
Figure 6.12 Attenuation of the fundamental Lamb modes in aluminium due to material absorption.....	215
Figure 6.13 Attenuation of the fundamental Lamb modes in aluminium due to leakage into air.....	216
Figure 6.14 A notched plate.....	217
Figure 6.15 Averaged signal envelopes from notched plate substructures showing equipartition occurring .....	218
Figure 6.16 Prediction of the response of the system measured in Figure 6.15 .....	219
Figure 6.17 Geometry of the bolted plates used showing two possible configurations with differing overlap area.....	220
Figure 6.18 Decay rate versus joint overlap area for a bolted plate, error bars indicate 1 standard deviation and solid line is a least squares fit .....	221
Figure 6.19 Decay rate versus joint overlap area for a adhesively bonded plate, error bars indicate 1 standard deviation and solid line is a least squares fit .....	222
Figure 6.20 Geometry of the stepped plates used showing the cross section of the stepped region .....	223

Figure 6.21 SEA prediction for the energy sharing between the  $S_0$  and  $A_0$  modes  
in the 5mm and 2.5mm thick plate regions ..... 224

Figure 6.22 SEA prediction for the energy sharing between the  $S_0$  and  $A_0$  modes  
in the 5mm and 1.25mm thick plate regions ..... 225

# Nomenclature

$N$	Ring-down count
$\delta$	Signal duration
$T$	Period
$I$	Wave intensity
$\theta_0$	Angle of incidence
$r$	Radius
$dS$	Increment of surface area
$\bar{l}$	Mean free path length
$\alpha$	Material absorption
$c$	Wave velocity
$D_f$	Modal density
$\Delta f$	Frequency band
$A_p$	Plan area
$h$	Plate thickness
$C$	Capacitance
$\varepsilon$	Permittivity
$x$	Electrode spacing
$\eta$	Amplifier gain
$Q$	Charge
$t$	Time
$t^*$	Time for diffuse field to develop
$z$	Acoustic impedance
$T_{12}$	Transmission coefficient of boundary between material 1 and 2
$R_{12}$	Reflection coefficient of boundary between material 1 and 2
$\omega$	Circular frequency
$k$	Wavenumber
$\lambda$	Wavelength
$z_0$	Impact duration
$V$	Impact velocity
$E^*$	Averaged Young's modulus for impact model
$\nu$	Poisson's ratio
$\bar{V}$	DC bias voltage applied to a capacitive transducer
$V_0$	Fringe amplitude of a laser interferometer
$C_0$	Clamped capacitance of a piezoelectric element
$h_{x5}$	Piezoelectric coefficient
$\bar{c}_{44}$	Stiffened Young's modulus of a piezoelectric element
$c_{ph}$	Phase velocity
$c_{gr}$	Group velocity
$\bar{n}$	Mean reflection frequency
$\eta_{12}$	Coupling loss factor between fields 1 and 2
$\eta_1$	Damping loss factor from field 1
$\Delta$	Time increment

# 1. Background

---

In order to fully explore the application of diffuse field approximations to practical acoustic emission (AE) testing it is first necessary to review the current state of the art concerning AE and diffuse fields. This chapter is divided into three sections; the first section introduces the subject of acoustic emission, its history, methodology and applications. The second section discusses the diffuse field approximation and its application to AE testing, giving a review of the work carried out to date in this area. The third section outlines the benefits which may be gained by using diffuse field methods and presents the project aims.

The introduction to acoustic emission has been completed with reference to several general texts, (Miller (1987) and Williams (1980)); where appropriate, additional references are given in the text to highlight specific areas of interest.

## 1.1 An introduction to acoustic emission

### 1.1.1 *Definition*

Formally defined, "AE is the class of phenomena whereby transient elastic waves are generated by the rapid release of energy from localised sources within a material, or the transient elastic waves so generated" ASTM (1982). Clearly, from this description, there are two distinct phenomena, namely, the generation of stress waves within the material and the propagation of these waves from the source location throughout the structure. The work reported in this thesis is primarily concerned with the wave propagation phenomenon and the interaction of these waves with the structure, however, a summary of the AE generation mechanisms is given below to demonstrate the versatility and applicability of the technique.

As indicated, AE differs from standard ultrasonic methods in that the ultrasonic waves are generated within the material due to some natural process, rather than an ultrasonic transducer. The most common sources of acoustic emission are caused by mechanical processes such as fracture, rubbing and impact which all generate broadband signals; audible examples of such sources are, the noise generated by a crack growing in a piece of glass, squeaking of door hinges caused by rubbing of the hinge surfaces and the impact noise of a golf ball being struck. There are other

mechanisms which are encompassed by AE and can be detected using the same equipment; for example, plastic deformation, leaks in piping, cavitation in flowing liquids, liquefaction/solidification of materials and chemical phase transformations in solids. These mechanisms are referred to as secondary sources to distinguish them from the standard mechanical deformation sources. All AE generation mechanisms are active, in other words they require an external influence in order for the source to generate stress waves. For example, crack growth will only occur if the structure is sufficiently loaded.

Acoustic emission is generally termed a non-destructive testing (NDT) technique although in most cases AE does rely on some damage occurring in the material, albeit on a microscopic level. Acoustic emission is a useful tool in the NDT of structures in service using either continuous monitoring or during routine in-service inspection. The main advantage over conventional ultrasonic or radiographic testing is that large areas or volumes can be tested at once with a small number of transducers.

The signals generated by an AE source can be broadly divided into two categories, discrete or continuous. Crack growth is an excellent example of a discrete AE generation mechanism, being characterised by individual events or bursts of energy separated by periods of apparent inactivity; these events have been shown to be related to minute increments of crack growth (Hanto (1975)). Continuous AE signals are generated by such sources as fluid leaks, cavitation in flowing liquids and the plastic deformation of solids. The AE sources of interest for the current work are predominantly associated with fracture and so only discrete signals are considered.

### **1.1.2 Measurement techniques**

Acoustic emission sources generally produce very weak signals, orders of magnitude lower in amplitude than those generated by standard ultrasonic methods. The amplitude and frequency content of the AE signature is governed by the generation mechanism, the material properties and the loading conditions; for example, brittle fracture in a high strength material will generate higher AE signal amplitudes with higher frequency components than plastic deformation. The required sensitivity and bandwidth of the measurement system is governed by the specific nature of the source in each application which may not be known *a priori*.

An additional complicating factor is the existence of background mechanical noise such as traffic rumble and vibrations generated by other machines in the vicinity; these unwanted sources of ultrasound can mask the signals of interest. If the background noise cannot be removed by insulation or shutting down all unnecessary facilities, the frequency range over which measurements are taken must be carefully chosen to optimise the signal to noise ratio and enhance the AE signals. The most useful range of frequencies for AE measurements has been found to be between 100kHz and 1MHz (depending on the application); below 100kHz mechanical noise tends to dominate over the AE signals. Most transducers used for standard AE measurements have a resonant frequency of between 150 and 300kHz. Although most AE measurements are taken at frequencies below 1MHz there is evidence that in some cases AE activity is present up to 50MHz (Hanto (1975)).

The most common solution to the problem of sensitivity and background noise is to use highly resonant transducers, typically surface mounted piezoelectric contact transducers (a thorough description is given in Chapter 2). These transducers perform two functions:

- Resonant transducers are extremely sensitive giving excellent signal to noise ratios but over an extremely narrow bandwidth, the high sensitivity is of paramount importance when the acoustic emission signals are extremely weak.
- Due to their limited bandwidth the transducers operate as a band-pass filter and, with careful selection of the transducer operating frequency, can be tuned to a specific application.

Practical AE measurements are aided by the sensitivity and filtering characteristics of such transducers, however, some care should be taken in choosing the operating frequency when using this equipment for a new application.

Acoustic emission measurement systems vary in complexity from portable, single-channel systems to large multi-channel testing rigs. All systems consist of transducers, amplifiers and signal processing/storage devices. Amplification is almost always necessary with real AE signals even when the most sensitive resonant transducers are being used. Preamplifiers are used either in or close to the transducer itself to minimise electromagnetic noise; preamplifier gains of 40 to 60dB are most

common with optional high and low-pass filtering. Secondary amplifiers are often used to further boost the signal and set the overall system sensitivity; overall system gains of up to 120dB are commonly used.

Typically AE tests run over long time scales, continuously monitoring the structure using many transducers. Storage of the entire time domain signal from all transducers is not generally feasible and online signal processing methods are applied to isolate the important information for storage.

### ***1.1.3 Signal processing***

Discrete acoustic emission sources are individual bursts of energy with amplitudes well above the noise floor and well separated in time. The individual events are complex, usually rising in amplitude rapidly until a maximum is reached and decaying exponentially to the background noise level. When using a highly resonant transducer the resulting signal can be approximated to a damped sinusoidal function, see Figure 1.1a). In order to identify events, a threshold level is set; this level must be higher than the background noise level but lower than the event amplitudes, see Figure 1.1b). The waveform parameters most commonly measured are as follows:

***Ring-down count:*** The severity of an AE event may be estimated by counting the number of cycles in each event which pass above the threshold level; thus complicated AE events may be represented by a single number, or count (for example, the count for the signal shown in Figure 1.1 would be 4). A rapid increase in the cumulative number of counts per minute signifies an increase of AE activity which may indicate imminent failure of the structure. The count is very dependent on the threshold level and consequently this counting method is very biased towards larger amplitude signals. This is a rather simple method but is still used in many practical applications.

***Signal Duration:*** The signal duration is given by the time between the first and last level crossings for an individual event, see Figure 1.1b). The duration of a harmonic signal, such as would be measured by a highly resonant transducer, is linearly related to the ring-down count and is given by,

$$\delta = NT \quad (1.1)$$

where  $\delta$  is the signal duration,  $N$  is the number of counts and  $T$  is the period of each cycle. The signal duration is also affected by the threshold level as well as the overall damping in the structure.

**Time of Arrival:** The time of arrival of an AE event is the time at which the first level crossing is measured for that event.

**Signal Amplitude:** The peak signal amplitude is another parameter which is commonly used to assess the severity of an AE source. Unlike the ring-down count and signal duration, the signal amplitude is unaffected by the threshold level. The relative positions of the source and receiver, however, will alter the amplitude strongly; a direct path from source to receiver will result in much higher peak amplitude than an indirect path, for the same source strength.

**Energy analysis:** Since AE activity is caused by rapid release of energy within the structure it would seem reasonable to try to relate the energy content of the measured signal to that which was released. Energy analysis procedures involve squaring and integrating the time signal, the signal energy being proportional to the area under the curve. By looking at the area beneath the curves this technique is not biased towards larger amplitude events and a more general picture may be obtained. The transducers used during energy analysis tests are broader band than typical AE transducers allowing several generation mechanisms of differing frequency contents to be monitored simultaneously. The signal energy has been shown in Section 6.2.5 to be directly proportional to the source energy for certain structures.

**Pattern Recognition:** As well as the standard techniques of ring down counting and energy analysis, more advanced techniques are also becoming more common; one example of such a technique is pattern recognition. Pattern recognition methods have been used in order to characterise AE sources which involves classifying each signal as it arrives at the sensor. These systems use adaptive learning and therefore must be trained on the signals from known sources, see for example Prine and Hopwood (1985).

#### **1.1.4 Acoustic emission applications**

Acoustic emission techniques were first used commercially in the late 1960's for the testing of pressurised systems for the chemical and aerospace industries and have

since become widely used. Applications for which AE is routinely used include quality assurance of new vessels (Cross (1982)), regular short term field evaluations to assess vessel degradation and continuous long term monitoring (Tscheliesnig and Theiretzbacher (1985)). Hydrostatic proof tests are normally carried out on new pressure vessels to 150% of the working pressure to ensure system integrity and relieve high residual stresses at joints introduced during fabrication. During these tests acoustic emission measurements can also be carried out which can be compared with subsequent tests on the same vessel to examine changes over its working life.

The acoustic emission systems used for pressure vessel testing are complex multi-channel devices using many transducers simultaneously. The transducers are placed at predetermined, regular intervals over the entire vessel surface such that the emissions from all parts of the vessel can be measured. With knowledge of the transducer positions and arrival times of specific events the source (defect) location can be estimated using triangulation. Once the approximate location of a defect has been found, other NDT techniques can be used to accurately characterise the defect.

Acoustic emission has also been successfully used for the non-destructive testing of steel and pre-stressed concrete structures such as bridges, dams and skyscrapers (Dunne (1985), Lovass (1985)). Transducers are often mounted permanently to important points on the structure such as around joints and can be continuously monitored. The number and placement of transducers depends on the specific structure but single transducers can be used if one particular joint in a structure is under examination.

Some other applications where acoustic emission techniques have successfully been used are,

- Online assessment of welding processes (Jolly (1970)).
- Testing the integrity of electrical components and the presence of loose particles within assembled electronic equipment (McCullough (1976), Harman (1979)).
- Detecting and locating leaks in pressurised vessels and pipelines (Tscheliesnig and Theiretzbacher (1985)).

- Assessment of artificial joint replacements for biomedical engineering (Wright and Carr (1981)) where high energy AE events indicate loosening of the prosthetic component within the bone.

### ***1.1.5 Limitations of current techniques***

AE measurements suffer from several major drawbacks, for example:

- The measured waveform parameters depend on the test equipment used, for example the precise frequency of operation, sensitivity of the transducer and amplifier gains. If repeat measurements on the same structure are to be compared quantitatively, all experiments must be carried out using identical equipment. This usually means permanently bonding transducers to the structure as repeatable transducer response and coupling between tests cannot be guaranteed.
- The effect of the geometry and material properties of the structure under test is not fully understood. The complex signals measured from AE events generally contain multiple reverberations of the initial source waveform within the structure and consequently are affected by the precise properties of the structure such as damping and wave speed. Therefore, it is not possible to directly compare the AE signals measured from structures of different geometry with any degree of certainty.
- The experimental layout can affect some or all of the measured waveform parameters in an unpredictable fashion; for example, the relative locations of the source (defect) and receiver can alter the maximum amplitude of the resulting waveform. Consequently, measurements taken on identical structures may not be directly comparable if the source location is different in each case.

Clearly, current methods only give a qualitative indication of the change of state of the component rather than a quantitative indication of the absolute level of damage. What is required is a method by which the source severity (energy released) can be measured at a location on the material surface regardless of the source location. For this to be possible the initial source energy must be evenly spread throughout the structure; in other words the wave field within the structure must become diffuse.

## 1.2 An introduction to diffuse fields

### 1.2.1 Definition

A diffuse wave field is an enclosed area in which the wave energy is evenly distributed, that is to say that the amplitude and directional distribution of the waves throughout the enclosure is random and the waves are uncorrelated with respect to phase (i.e. no standing waves exist). If these requirements are fulfilled a greatly simplified description of the wave field can be used. The concept of a wave becomes of minor importance and the wave field can be treated as a whole in a stochastic manner. A diffuse field is guaranteed to occur if all boundaries within the enclosure are diffuse reflectors; totally diffuse reflectors obey Lambert's cosine law whereby the distribution of the reflected wave field is independent of the original angle of the incident wave. Consider a small area  $dS$  which is illuminated by a bundle of parallel rays at an angle of  $\theta_0$  to the wall normal, with an intensity  $I_0$ . The intensity of the incident waves normal to the wall is given by,

$$I_n = I_0 \cos \theta_0 \quad (1.2)$$

and Lambert's law states that the intensity of scattered rays at a radius  $r$  and angle  $\theta$  is given by (Kuttruff (1973)),

$$I(r, \theta) = I_n dS \frac{\cos \theta}{\pi r^2} \quad (1.3)$$

see Figure 1.2a). In practice no boundary exhibits perfect diffuse reflection but rough and irregular surfaces may be a reasonable approximation if the wavelength is of similar dimensions to the surface features.

A diffuse field cannot strictly be generated in an enclosure if all the boundaries are specular reflectors (obeying Snell's law, see Figure 1.2b)); but in certain cases the fields generated are approximately diffuse. If the source is non-directional (small with respect to the wavelength) and excites waves over a finite bandwidth (rather than a single frequency), all normal modes (or structural modes) of the enclosure which have natural frequencies within the excitation bandwidth will be excited simultaneously. Each normal mode, if excited individually, is clearly not diffuse; the amplitude distribution is not random throughout the enclosure due to the nodes and anti-nodes of the mode. However, in the case where many modes are excited over a

finite frequency band, the motion at any point within the enclosure is a superposition of all the modes present; thus, as the number of modes increases, the overall motion pattern becomes more uniform and the diffuse field approximation becomes valid. Diffuse field approximations have been used for many years for room acoustics and geometrical optics (Kuttruff (1973)).

It is important at this stage to clarify the terms ‘propagating mode’ and ‘structural mode’ (often referred to as normal modes in room acoustics). Propagating modes, as their name suggests, move through the material transporting energy and the direction in which the energy is travelling is termed the direction of propagation. Propagating modes can exist in many forms depending on the geometry and material properties of the media through which they are propagating; for example, bulk longitudinal and shear waves can exist in any bounded or unbounded media (shear waves can only exist in materials which can sustain a shear stress) and Rayleigh waves can exist along the boundary between solid and fluid media. If the medium is homogeneous and unbounded these waves will propagate in a straight line for an infinite distance (or until material losses completely attenuate the signal). If the medium is bounded on all sides an enclosure is formed; the propagating modes interact with the boundaries of the enclosure causing reflection and refraction. Some of the incident energy will be reflected back into the enclosure and some will be transmitted into the surrounding medium (if there is one). The reflected waves are re-reflected when they encounter another boundary and this process repeats until all of the wave energy is lost either across the boundary or due to material losses. Structural modes arise due to the interference between all the reflected and re-reflected waves within the enclosure. This interference causes standing waves which are responsible for the mode shape of the structural mode; areas of constructive interference exhibit large motions (referred to as nodes) and areas of destructive interference exhibit little or no motion (referred to as anti-nodes).

When considering stress waves in a solid, such as those generated by acoustic emission sources, the enclosure is the structure itself. The wave field is more complex than that commonly found in room acoustics due the presence of more than one mode of propagation. In room acoustics the propagating medium is a fluid (air) in which only bulk longitudinal waves can exist. In a solid structure several

additional propagating modes can exist. These include, bulk shear waves, surface waves (Rayleigh (1885)), interfacial waves (Stonely (1924)) and plate waves (Lamb (1917)). The exact combination of propagating modes which are present will depend on the geometry of the structure and the frequency range of the excitation signal.

### **1.2.2 Literature review**

Research has previously been carried out into the use of diffuse field approximations for acoustic emission. The first recorded work in this area was by Egle (1979) whose aim was to calculate the initial power, spectral content and decay rate of an AE event from ring-down counting data. To do this he assumed that the signal was a product of a slowly decaying function and a stationary Gaussian random process (this requires the field to be diffuse). He found that it is possible to extract the mean square stationary component which represents the initial power and the zero-crossing rate which gives some idea of the frequency content of the signal. He then extended the diffuse field theory of room acoustics to solid structures having two propagating modes to calculate the proportion of energy in these modes (Egle (1981)). He assumed that the field generated in a solid is an isotropic random superposition of plane waves and only longitudinal and transverse waves exist (ignoring Rayleigh and Lamb waves). He numerically predicted the flow of energy between the transverse and longitudinal modes caused by mode conversion at the boundaries and predicted that after a calculable time,  $t^*$ , the energy present in these modes reaches an equilibrium state. He also predicted that, at equilibrium, the energy present in the transverse mode in an aluminium structure accounts for 97% of the total energy in the system regardless of the initial conditions, the ratio of energies between the longitudinal and transverse modes being dependent only on the Poisson's ratio of the material.

Weaver (1982) analytically reinterpreted and extended the theories of Egle. He assumed that if a structure is excited over a finite frequency band, all structural modes (with natural frequencies within the excitation band) are excited with equal energy. He termed this ‘The equipartition assumption’ which has strong parallels with the Statistical Energy Analysis assumptions (see Section 5.2). Weaver then subdivided the structural modes into two categories, one for modes which consist of predominantly transverse particle displacements and the other for longitudinal particle

displacements. Thus the ratio of energy densities between the transverse and longitudinal motion present is equal to the ratio of number of transverse to longitudinal modes within the frequency band of interest. He concluded, as Egle, that the equilibrium state is predominately transverse for a steady state diffuse field in a solid. He also predicted, however, that the surface wave field will be detected more strongly by transducers mounted on the surface of the material than either the bulk transverse or bulk longitudinal fields. This is extremely important since virtually all AE transducers measure the surface response.

The relationship between this measurable ‘surface energy density’ and the total energy density was explored (Weaver (1984)) for finite plates. The main assumptions made were that the time domain was long compared to the acoustic transit time across the structure (this allows many randomising reflections), that the normal modes of the plate can be approximated by standing waves of Rayleigh, Shear-Horizontal and Lamb types (referred to by Weaver as ‘Pseudo Modes’) and that the frequency range is large compared to the modal density of the plate. He concluded that a diffuse field in a finite plate will partition its time averaged energy amongst the several propagating branches with a weighting independent of source nature and the total spectral energy density can be deduced from a measure of the surface energy density. This theory was later expanded to a half-space (Weaver (1985)) where the participation of the surface in the general disturbance was predicted. A term  $\bar{G}$  was introduced describing the linear proportionality between the total energy in the body and the mean square displacement at position  $x_0$  on the surface. This value was, however, very difficult to calculate for all but the simplest geometries.

An experimental study (Weaver (1986)) was carried out to verify the existence of a diffuse field in a aluminium plate. This plate had many randomly oriented saw cuts at the edges which were intended to aid the generation of a diffuse field. A contact piezoelectric transducer was used to sample the field generated by a pencil break source in the range 50kHz to 500kHz. Results from fifteen source and receiver positions were averaged over a 16ms sample period. A delay of 1.6ms was inserted to ensure that the field had time to randomise before full waveform sampling. The signal decay was assumed to be exponential, caused by internal losses, and the time zero amplitudes were calculated by back fitting the decaying signal over a range of

frequencies. Weaver concluded that a diffuse field can be generated quickly long before any appreciable absorption occurs in the system used and the results agreed well with predictions from Weaver (1984).

In (Weaver (1988)) an overview of the diffuse field method is given with a description of the necessary conditions concerning bandwidth and modal density for a diffuse field to be sustained, namely,

$$\bar{l} \alpha / c \ll 1 \quad (1.4)$$

$$D_f \Delta f \gg 1 \quad (1.5)$$

where  $\bar{l}$  is the mean free path length (m),  $\alpha$  is the material absorption (Nepers/s),  $c$  is the acoustic wave speed of interest (m/s),  $\Delta f$  is the frequency bandwidth (Hz) and  $D_f$  is the modal density. For plate structures this is given by,

$$D_f \approx A_p / hc \quad (1.6)$$

where  $A_p$  is the plan area ( $m^2$ ) and  $h$  is the thickness (m), (Lyon (1976)). These guidelines can be used to assess whether a given structure is likely to behave in a diffuse manner.

A comparison of the diffuse field and Green's function approaches to source characterisation are given by Clough (1987) and Clough (1992). He argues that a diffuse field should be produced after only three reflections, although no proof is given. A demonstration of why low-pass filtering is required to remove the dominating effect of the lower order structural modes is also furnished. A laser source of known energy was used to calibrate various plate structures of differing dimensions and volumes which showed that measured energy is proportional to source energy and independent of source position.

In summary it has been demonstrated that diffuse fields exist in a randomised ideal structure under laboratory conditions. It has been predicted that in a well developed steady state diffuse field, energy partitioning between modes is controlled by the material properties rather than the specific geometry of the structure (given sufficient structural asymmetry).

A structure capable of sustaining a diffuse field must be lightly damped, allowing many reflections of the initial wave energy. The number of reflections required will depend on the geometry of the structure and the directivity of the initial source of energy. Previous authors have assumed a value of 20 reflections to be sufficient (Egle (1981)), but others have suggested that as few as 3 reflections are necessary (Clough (1992)).

The number of resonant modes (modal density) within the excitation bandwidth is extremely important for diffuse field approximations to be valid. Small structures will have a low modal density, increasing the likelihood of individual modes dominating the structural response. This problem can be reduced if the bandwidth of the signal is broad and the initial source is non-directional. Large structures will have high modal density but the initial energy will undergo fewer reflections before being damped away; thus the field may not have a chance to become diffuse.

It is not clear from the literature, however, whether a diffuse field can be sustained in a real structure, for example, a structure consisting of several acoustically connected substructures (as will be the case in the vast majority of applications in the field). The experimental work which has previously been carried out has required enormous amounts of data and signal processing and is, therefore, unlikely to be of any practical use outside the laboratory.

### 1.3 Outline of thesis

The two major aims of the thesis are,

- To experimentally determine the conditions under which diffuse fields exist in structures such as coupled and stepped plates, specifically with reference to Equations (1.4) and (1.5) regarding internal damping and excitation bandwidth. Equipment must be designed, manufactured and calibrated to facilitate these measurements.
- Secondly, if validated, signal processing will be necessary to take full advantage of the diffuse field assumptions. Measurement and calibration methods must be proposed and validated to improve source strength determination and characterisation on a variety of structures.

The selection, manufacture and testing of suitable transducers and simulated sources are presented in Chapters 2 and 3 respectively. A conical piezoelectric transducer design has been selected as the most versatile solution for both transmission and reception.

The calibration and modelling required to measure and predict the response of the transducers on a variety of materials is presented in Chapter 4. Additionally a novel technique for the measurement of transducer coupling has been devised and a suitable device designed and manufactured; results presented at the end of the chapter indicate the ability of the device to measure transducer coupling independently on a variety of materials.

Chapter 5 presents the Statistical Energy Analysis (SEA) method; a model is developed which predicts the energy partitioning between Lamb modes in a plane aluminium plate. The model is then used to predict the energy sharing between connected regions of assembled and stepped plate structures.

In Chapter 6 experimental verification of the existence of diffuse fields is furnished. The proportionality between signal energy and source energy is confirmed and this measurement is shown to be indicative of the energy density in the structure at the measurement location. Coupled plate structures have then been studied and the results show good agreement to the SEA predictions of energy sharing and the time taken for a diffuse field to be generated. The effect of bolted and adhesive joints has been examined showing that the damping caused by such joints detrimentally affects the diffuse field properties of the structure. Additionally, stepped plate structures have been analysed and the results have been found to be consistent with the SEA predictions.

The conclusions and recommendations are presented in Chapter 7 with suggestions for future work in this area.

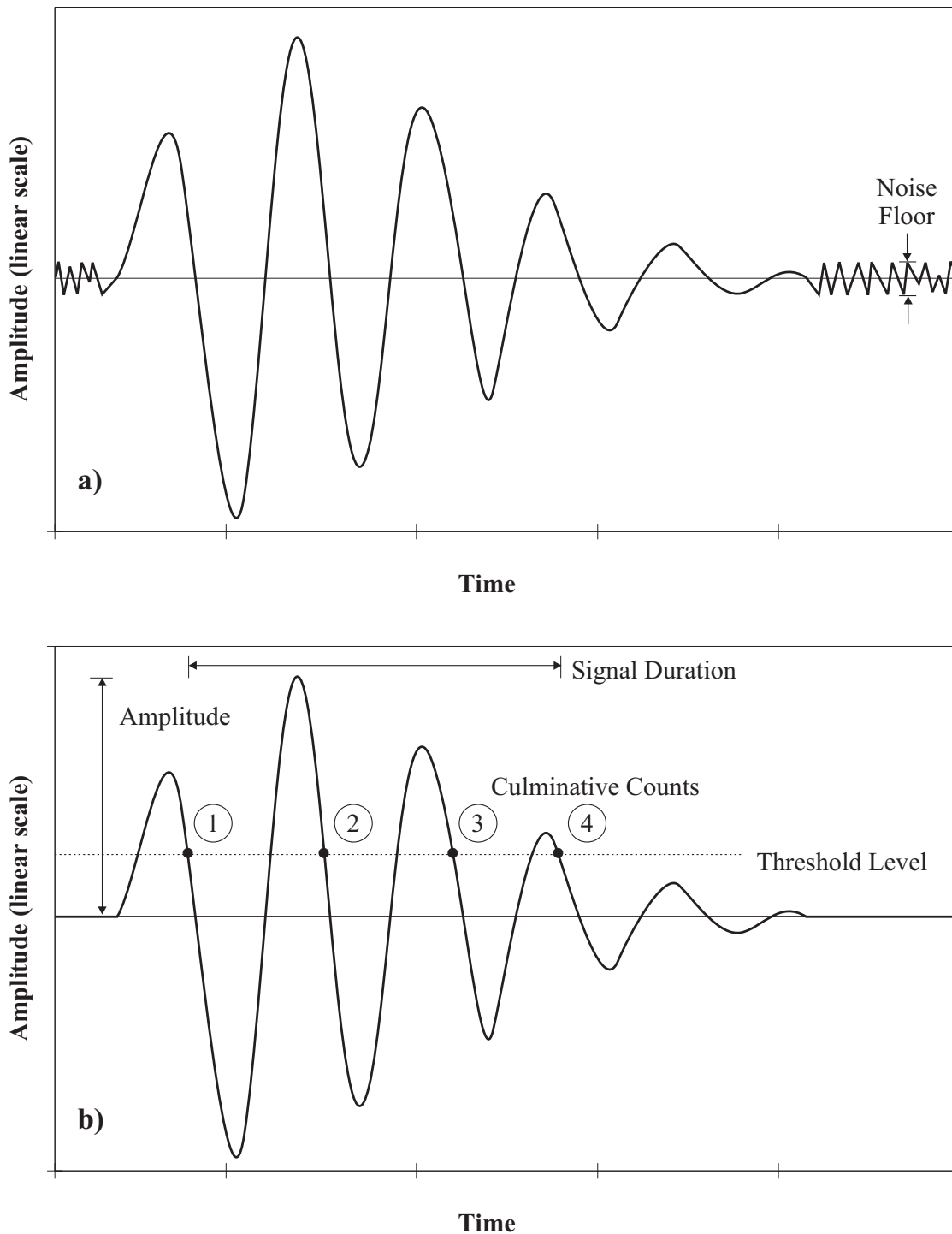


Figure 1.1 a) Idealised representation of a discrete AE event, b) Indication of the simple waveform parameters used to characterise AE signals.

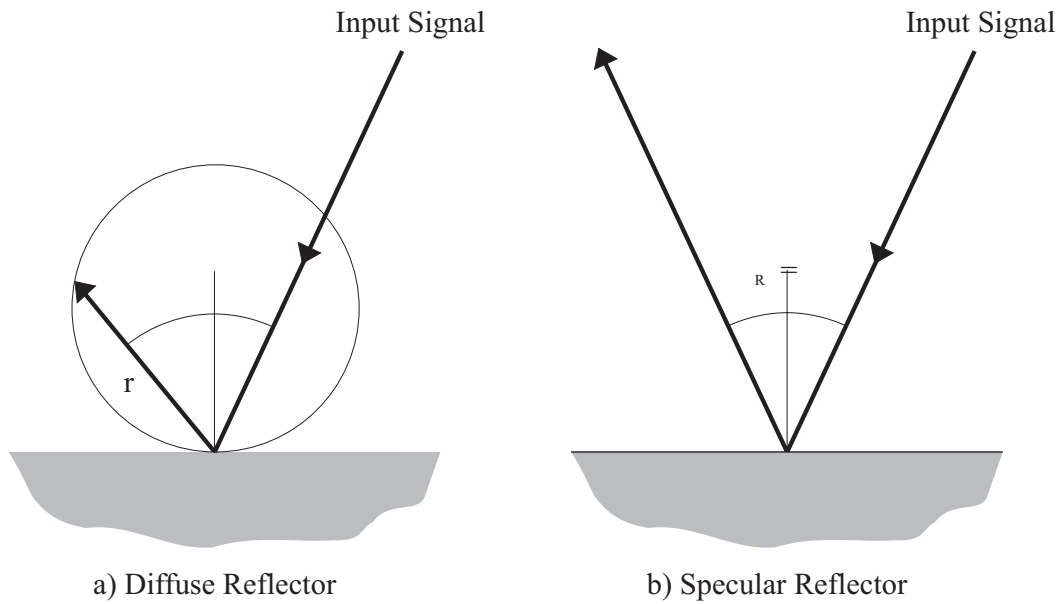


Figure 1.2 a) The reflected field from a diffusely reflecting surface obeying Lambert's law, b) The reflected field from a specularly reflecting surface obeying Snell's law.

## 2. Transducer selection and development

---

### 2.1 Introduction

#### 2.1.1 Overview of chapter

The first stage in the work is to select and assemble appropriate experimental equipment to carry out the proposed study of the diffuse field phenomenon in structures. This chapter sets out the transducer characteristics required to measure diffuse fields in structures and reviews four transducer types for their suitability. The transducer types reviewed are, standard piezoelectric AE transducers, conical piezoelectric transducers, capacitive transducers and laser interferometers. The transducer characteristics which have been chosen as most important for the diffuse field experiments are, repeatability, high sensitivity, low damping, broad bandwidth and small measurement area.

A review of possible transducer types has resulted in a conical, contacting piezoelectric transducer design being selected. Improvements to this design have been made by manufacturing an alternative backing material with increased damping to make the transducer more suitable for the long time-scale measurements required for the experiments and new electrodes for use on non-conducting materials. The response of the improved transducer has been measured and compared with the original design showing significant improvement. Electrical impedance measurements have also been carried out to quantify this improvement.

Results are presented at the end of the chapter to demonstrate the effectiveness of this new transducer and conclusions are made as to the suitability of the transducer and possibilities of future improvements.

#### 2.1.2 Review and comparison of transducers

This review has been carried out with specific reference to the suitability of the transducer for the diffuse field measurements, and is not intended as a statement regarding the most suitable transducer for general AE measurements. Before comparing the characteristics of each transducer it is important to clarify the criteria by which they are being judged and explain why these criteria are important in this context.

**Repeatability:** refers to the consistency of the transducer response between measurements taken at different times, different locations and on different structures. The diffuse field experiments will use measurements taken at many locations on a structure to demonstrate its diffuse field behaviour. Any variation of the transducer response between measurements could invalidate the measurements; in the case of contact transducers a major source of variation is in the acoustic coupling of the transducer to the material surface.

**High sensitivity:** is required to give a good signal to noise ratio. The ultrasonic sources used during the experimental work generate relatively weak signals making the sensitivity of the transducer important.

**Low damping:** refers to the amount of damping added to the structure due to the presence of the transducer. The subtle changes in the decay rate of wave fields have been found to give important information regarding the structure and material properties in addition to demonstrating if the field is truly diffuse. Changes of the structural damping caused by the transducer can mask these effects and consequently low damping is essential.

**Broad bandwidth:** For the purposes of this project a broad band receiving transducer is required, the bandwidth of interest being 100KHz to 1MHz. This bandwidth is required to allow flexibility in the frequency range over which the experiments will be carried out which will help to ascertain the frequency range, if any, over which the diffuse field approximation is valid. Additionally, as discussed in the previous chapter, for the diffuse field approximation to be valid for a structure the bandwidth must be broad enough to include many structural modes.

**Measurement area:** is defined as the area over which the motion is being measured by the transducer. Small measurement areas are favoured for several reasons; firstly, the aperture effect is reduced if the measurement area is reduced (a thorough description of the aperture effect is given in Section 2.2.3); and secondly a small measurement area has also been found to improve the repeatability of coupling and reduce the damping of contact transducers.

A literature review was carried out of the transducer types available in order to determine the most suitable for the project; additional review papers are (Dewhurst, et

al. (1987), Grabec and Platte (1984) and Boltz, et al. (1995)). The findings may be summarised as follows:-

**Standard AE transducers:** Standard piezoelectric AE transducers have been found to be poorly suited to the diffuse field investigations (Weaver (1986)) due to their narrow bandwidth, aperture effects and the additional damping which they add to the structure under test (Dempsey and Egle (1985)). Additionally the acoustic coupling of the transducer to the surface causes large variations in the sensitivity of standard transducers. Standard AE transducers will undoubtedly be useful in the application of diffuse field methods to genuine acoustic emission problems, however, they do not possess the necessary characteristics for this experimental investigation.

The problems of damping and coupling variation can be alleviated by using non-contacting transducers such as capacitive and optical methods.

**Capacitive transducers:** Capacitive transducers are non-contacting transducers which directly measure the surface displacement of the material; a stationary electrode is suspended above the material surface and a bias voltage ( $V_s$ ) is applied to it, see Figure 2.1, (the material surface must be an electrical conductor and electrically earthed). The capacitance of the transducer can be related to the electrode gap using the following equation,

$$C = \frac{\epsilon A}{x} \quad (2.1)$$

where  $C$  is the capacitance,  $A$  is the area of the electrode,  $x$  is the electrode gap and  $\epsilon$  is the permittivity of the dielectric medium. The voltage output from the charge amplifier is then,

$$V(t) = \eta Q(t) = \eta V_s C(t) = \eta V_s \frac{\epsilon A}{x(t)} \quad (2.2)$$

where  $\eta$  is the amplifier gain and  $Q$  is the charge on the electrode.

The electrode gap is typically  $10\mu\text{m}$  with electrode areas of  $1\text{cm}^2$  being commonplace; in order to maintain such a small gap accurately both the stationary electrode and the material surface must be polished optically flat and be free from contaminants. Equation (2.2) clearly demonstrates that the sensitivity of the transducer is directly proportional to the bias voltage, the electrode area and the

permittivity; the dielectric material is usually air which fixes the permittivity. Therefore, for maximum sensitivity the area and bias voltage must be as high as possible. The area is constrained by both the physical size of the transducer and the aperture effects (see Section 2.2.3) and the bias voltage is limited by the electrical breakdown of the dielectric, which for air has been measured to be  $35\text{V}/\mu\text{m}$  (Scruby and Wadley (1978)). Typically bias voltages of around 50 to 100V have been used in the literature.

A number of capacitive transducer designs have been investigated; Breckenridge and Greenspan (1981) used a cylindrical transducer with minimum electrode gap of  $4\mu\text{m}$  and a bias voltage of 100V giving an overall sensitivity of  $12\text{V}/\mu\text{m}$  over a 5MHz bandwidth; a point-like transducer was used by Boler and Spetzler (1984) with an electrode area of  $0.01\text{mm}^2$  and an electrode gap of  $0.1\mu\text{m}$  giving a resolution of  $7\text{V}/\mu\text{m}$  over a 6MHz bandwidth; more standard, parallel plate designs were used by (Kim and Sachse (1986), Kim, et al. (1989) and Scruby and Wadley (1978)) giving similar sensitivities. The flat frequency response of capacitive transducers makes them very easy to calibrate; a DC calibration is valid over the entire working frequency range.

Capacitive transducers have some favourable characteristics for diffuse field measurements; the damping added to the structure by the transducer is negligible and the bandwidth of operation is ample for the purposes of this project. However, some major shortcomings exist which preclude the use of capacitive transducers for the diffuse field measurements. The transducer sensitivity is low, as much as 1000 times less than a piezoelectric transducer in some cases (Boltz, et al. (1995)); the measurement area is generally large which causes aperture effects (Breckenridge, et al. (1984)); and, in order to maintain the narrow electrodes spacing, both the electrode and the material surface must be polished optically flat.

**Laser interferometers:** Laser interferometry is an alternative non-contact method for ultrasonic reception; a comprehensive description of interferometers is given in Section 4.2.3 in the context of transducer calibration. Interferometers directly measure the surface motion (displacement or velocity, depending on the interferometer layout) and have flat frequency response over bandwidths of 20MHz or more. The incident laser beam can be focused onto the material surface making the

measurement area small, thus reducing aperture effects and, being non-contacting, no damping is added to the structure by the interferometer and the coupling repeatability is excellent.

Laser interferometers generally have similar sensitivities to capacitive transducers making them relatively insensitive (as compared to piezoelectric devices) and, like capacitive transducers, require extremely careful surface preparation. Laser systems are also delicate and expensive making them poorly suited to the diffuse field measurements.

***Conical piezoelectric transducers:*** The conical piezoelectric transducer (Proctor (1982) and Greenspan (1987)) has been found to be a reasonable compromise for the purposes of this project (a detailed description of the transducer design is give in Section 2.2). This is a contacting piezoelectric transducer with a conical element with a very small measurement area which exhibits many of the required transducer characteristics. The small transducer area has been found to reduce the damping introduced by the transducer to the structure and increase the coupling repeatability whilst also reducing the aperture effects. Greenspan (1987) has also shown that the conical shape of the element increases the bandwidth of the device as compared to the response of a standard disk element.

In conclusion, the conical transducer design has been selected as the best compromise for the diffuse field measurements and the following section discusses the design in more detail.

## 2.2 Design criteria for conical piezoelectric transducers

### 2.2.1 Geometrical considerations

Conical piezoelectric transducers were first developed at the National Bureau of Standards (now the National Institute for Standards and Technology) as an improved acoustic emission transducer (Proctor (1982)); a comparison between the design of a standard PZT transducers and the conical transducer is given in Figure 2.2. The basic design is very simple consisting of a conical Lead Zirconate Titanate (PZT) element attached to a large brass backing; the backing acts as one electrode as well as damping for the element. The front face electrode is pressed directly onto the material surface which acts as the earth electrode.

The conical shape of the element has several advantages over standard AE transducers,

- The contact area of the transducer is very small (around  $1\text{mm}^2$ ) which reduces aperture effects, coupling variability and the damping effect.
- The conical element has more mechanical resonances than a disk element but these resonances are less dominant giving the transducer better broadband response.

The conical element shape reduces the effect of the through-thickness and radial modes by smoothing out the resonant response of the element over a wide bandwidth. This occurs due to the inherently non-resonant behaviour of cones due to their lack of parallel, plane boundaries. The effectiveness of the conical element at suppressing resonant behaviour is demonstrated by the electrical impedance measurements presented in Section 2.4.

### **2.2.2 Transducer backing**

The primary purposes of transducer backing are to provide damping and loading to piezoelectric element. Transducers are damped to minimise the effect of mechanical resonances present in the piezoelectric element thus broadening the overall bandwidth of the transducer. An effective backing material must extract and absorb ultrasonic energy from the piezoelectric element; this is inevitably linked with some loss of sensitivity at the resonant frequencies. The transducer backing, being large in comparison with the piezoelectric element, also provides convenient attachment for wires and guides for the transducer.

The acoustic impedance ( $Z$ ) of the backing material must be similar to that of the piezoelectric element for it to be effective in removing energy. If the materials are poorly matched (dissimilar  $Z$ ) very little ultrasonic energy crosses the boundary into the backing and the energy is trapped in the piezoelectric element. The transmission coefficient across a boundary (say from material 1 to material 2) can be defined as the proportion of the intensity (energy) of the incident ultrasonic signal which is transmitted through the interface. This can be written in terms of the acoustic impedances of the materials as follows (Szilard (1980)),

$$T_{12} = \frac{4m}{(m+1)^2} \quad (2.3)$$

where  $m$  is the ratio of the acoustic impedances and is given by  $m=Z_2/Z_1$  and  $T_{12}$  is the transmission coefficient from material 1 to 2. Also the acoustic impedance is given by,

$$Z = \rho c \quad (2.4)$$

where  $\rho$  is the material density and  $c$  is the bulk longitudinal velocity.

Complete transmission occurs when the materials are matched i.e. when  $Z_1=Z_2$ ; therefore an ideal backing material matches the piezoelectric element. Brass was used as a backing for the original conical transducer design because it is well acoustically matched to the PZT element, ( $Z_{\text{BRASS}}=37\text{MRayls}$  and  $Z_{\text{PZT}}=32\text{MRayls}$ , material properties obtained from Kaye and Laby (1995)). Thus, according to Equation (2.3), the transmission coefficient for a PZT/Brass interface is 0.995 (99.5% transmission). Brass, however, is not a highly attenuative material making the damping characteristics poor and for this reason the backing used was large.

### 2.2.3 The effect of transducer aperture

Acoustic emission transducers generally measure out-of-plane surface motion over a circular contact area. They are, however, predominantly used to receive surface waves (Miller (1987)) which are travelling along the surface of the material (i.e. parallel to the transducer face), see Figure 2.3. Assuming the transducer output is proportional to the average displacement over the transducer face with uniform sensitivity across that face, the transducer response can be written as,

$$U(t) = \frac{1}{A} \iint_S u(x,y,t) \cdot dy dx \quad (2.5)$$

where the  $x$ - $y$  plane is the material surface,  $S$  is the surface of the transducer face,  $A$  is the area and  $u(x,y,t)$  is the out-of-plane surface displacement.

Assuming that the incoming waves have a plane wavefront, travelling in the  $x$  direction, incident on a circular transducer having radius  $a$  and with a wave of the form,

$$u(x,t) = B \cos(kx - \omega t) \quad (2.6)$$

where  $k$  is the wave number and is given by  $k=2\pi/\lambda$ , where  $\lambda$  is the wavelength. If the wave amplitude ( $B$ ) is assumed to be unity, the transducer sensitivity may be written as (Breckenridge, et al. (1984)),

$$U(t) = \left[ \frac{2J_1(ka)}{ka} \right] \cdot \cos(\omega t) \quad (2.7)$$

where  $J_1$  is the Bessel function of the first type. The amplitude of Equation (2.7) is plotted in Figure 2.4 against  $2a/\lambda$ , ( $2a$  being the transducer diameter). The sensitivity drops rapidly as the wavelength decreases and the interference effects increase, the null points represent frequencies at which destructive interference causes the integral of the motion over the transducer area to be zero. The first null for a circular aperture with an incident wave with a plane wavefront is at approximately  $2a/\lambda=1.2$ ; subsequent nulls are spaced at integer intervals from this (for example the second null is at  $2a/\lambda =2.2$  etc.). To put this in perspective, consider a 10mm diameter transducers on an aluminium surface; according to Equation (2.7) the first null point for the reception of surface waves occurs at 365kHz (assuming a surface wave velocity of 3km/s). AE transducers with diameters of 20mm and more are commonplace giving the first null in response at 190kHz or less.

The aperture effect is therefore an extremely important consideration when designing a broad band transducer. Regardless of how well a transducer performs in terms of mechanical resonances and damping, if the transducer face is too large the bandwidth will be severely limited. Capacitive transducers are a good example of this. The frequency response of the transducers is excellent; however, large electrode diameters are normal in order to improve the sensitivity and this can lead to aperture problems.

## 2.3 Transducer design, manufacture and testing

### 2.3.1 Overview of the testing procedure

A conical transducer design has been selected as the most suitable for the current project, improvements have been made to this original design to make the transducers more suitable to the long time-scale measurements (up to 100ms duration) required for the diffuse field experiments.

A schematic diagram of the experimental equipment used to compare the transducer responses is shown in Figure 2.5. The transducers were mounted on a large cylindrical aluminium block with dimensions 300mm diameter by 300mm high; the corners of the block were machined to a 40mm radius to prevent edge reflections. A source was mounted in the middle of the top surface of the block and two transducers under test were mounted at equal distances from the source on the same surface. A pencil break source (Breckenridge, et al. (1984)) was used for most of the transducer comparisons, a detailed description of pencil break sources is given in Section 3.2.1. The signals from the transducers were amplified using a 40dB pre-amplifier and sampled using a digital oscilloscope.

### 2.3.2 Brass backed transducers

Initially, brass back transducers were designed and constructed similar to the NBS transducers. The brass backing was in the form of a round bar, see Figure 2.6, which was ground on one face for bonding of the PZT element. The PZT element was machined from a disk into a conical shape using a diamond wheel. During the machining process the temperature of the ceramic must remain well below the Curie temperature, which for PZT is quoted by the manufacturer to be  $365 \pm 5^\circ\text{C}$ , otherwise the piezoelectric properties are lost. Several dimensions of cones were compared, all having a tip diameter of 1mm.

Transducer	Height(mm)	Tip Diameter(mm)	Base Diameter(mm)
BR3	3	1	10
BR5	5	1	10
BR10	10	1	10

Table 2.1 Conical element geometries.

The conical PZT element was then attached to the backing using a silver loaded epoxy; this is an electrically conductive epoxy-based adhesive which connects the components mechanically and electrically. The bond line thickness was estimated by measuring a bond formed between two sheets of glass using the same adhesive; this measurement indicated a bond line thickness of  $40\mu\text{m}$  which is small with respect to the wavelength even at the highest frequencies of interest.

The three transducer geometries were compared by measuring their response to a pencil break source. Figure 2.7 shows a comparison of the responses recorded from the transducers shown in Table 2.1, where each result is an average of eight consecutive events. The longitudinal (L) and Rayleigh (R) wave arrivals are indicated in Figure 2.7, the results are to the same scale and the tests were carried out under identical conditions.

Transducer BR3 was found to exhibit the highest sensitivity and broadest bandwidth of the transducers. The only difference between the transducers was the thickness of the cone and so it was concluded that the 3mm thick cone exhibits the best qualities and this geometry was used for all subsequent transducers. The general trend demonstrated by Figure 2.7 is that as the cone becomes thinner both the amplitude and frequency response improve. Transducer elements thinner than 3mm may have even better response, however, due to the machining difficulties 3mm was the thinnest which could be satisfactorily manufactured. It must also be noted that transducer BR5 (5mm thick conical element) shows obvious signs of ringing after the Rayleigh wave arrival. The frequency of this ringing was measured to be 400kHz which coincides with the through thickness resonance of a 5mm thick disk. This suggests that the bonding of the piezoelectric element was poor allowing energy to remain in the cone rather than leaking into the backing.

These results show that the conical design produces only very slight resonant behaviour within the element. However, ringing in the backing can be seen to occur after 80 $\mu$ s which corresponds to one shear wave transit to the end of the brass backing and back to the piezoelectric element. Interestingly there is no sign of a longitudinal wave arrival, which would be expected at around 40 $\mu$ s; the reason for this is unknown. The intended use of the transducers will cover time-scales up to 100ms, it is important therefore to keep the backing reverberations to a minimum and for this reason it was decided to look for a more suitable material with higher acoustic attenuation.

### **2.3.3 Tungsten/epoxy backed transducers**

A common material to be used for transducer backing is tungsten loaded epoxy; this is a composite material made from fine tungsten powder suspended in an epoxy matrix. The acoustic impedance of the material can be altered by changing the percentage

content of tungsten in the mix, i.e. higher tungsten content means higher density and therefore higher impedance, see Equation (2.4). In order for the impedance of the tungsten/epoxy to match that of the PZT the percentage tungsten required is around 70% by volume (Silk (1984)). It is impossible to attain this ratio by simple mixing procedures and so more specialised techniques are required.

A technique known as vacuum impregnation was used to make the tungsten epoxy backing material for this project (Khuri-Yakub (1994)); Figure 2.8 shows the four main stages of the process:

- a) The tungsten powder was placed in a specially designed mould which has a removable base with an vacuum seal; the tungsten powder used for all of the backing samples had a grain size of  $8\mu\text{m}$ .
- a) The powder was then compressed using a Mayes material testing machine and the load was held for ten minutes to allow shakedown of the powder to occur. The loading used at this stage governed the final density of the material and so accurate and consistent loading was essential.
- a) Low viscosity epoxy (Ciba Geigy CY1301 with hardener HY1300) was then poured into the mould onto the powder slug. The whole mould was then placed in a vacuum chamber for ten minutes. During this time any air which was trapped between the tungsten powder grains expanded and bubbled through the epoxy.
- a) Finally the mould was removed from the vacuum chamber. Atmospheric pressure then forced the epoxy resin to impregnate the tungsten powder and occupy the evacuated spaces. The assembly was left for 12 hours at room temperature to allow the epoxy to cure before the slug of material was pushed out of the mould.

The acoustic impedance of the tungsten/epoxy samples versus pressure is shown in Figure 2.9. The impedance was calculated by measuring the density and longitudinal wave velocity and using Equation (2.4); the measured impedance agrees well with previous measurements made by (Silk (1984)). The longitudinal attenuation of the tungsten/epoxy samples was measured in through transmission configuration at 1MHz and the results are presented in Figure 2.10. The small dimensions of the

tungsten/epoxy specimens (20mm diameter and 14mm long) precluded the use of lower frequency measurements.

As expected the measurements show that the material impedance increases with pressure and the attenuation decreases. It was found that 14MPa was the maximum useable pressure, further compression caused incomplete impregnation by the epoxy. The use of a less viscous epoxy resin or thinning the existing resin could improve this situation, however, further compression would cause an unwanted reduction in the material attenuation. A compromise must be made between the transmission coefficient across the element/backing interface and the attenuation losses in the backing.

The maximum acoustic impedance attained was 16MRayls which, using Equation (2.3), gives a transmission coefficient of 0.89; therefore 89% of the energy incident on the interface will be transmitted into the backing and 11% will be reflected back into the element. The attenuation of this material was measured to be 45Nepers/m (at 1MHz); the maximum backing dimensions attainable were 14mm long which gives a total path length of 28mm. Therefore, the attenuation experienced by a wave travelling the full length of the backing would be 1.26Nepers (11dB) which gives an overall loss of 72% in the amplitude of the wave returning from the backing. By comparison the longitudinal attenuation of brass has been measured to be 2.5Nepers/m (at 1MHz); for a path length of 28mm this would give an attenuation of 0.07Nepers (0.61dB), therefore, the amplitude of the wave returning from the backing would have only been attenuated by 7%. It must be stressed that these predictions are only valid at a frequency of 1MHz, at lower frequency the attenuation values for tungsten/epoxy and brass are likely to be considerably lower. The measured attenuation values and predicted losses in the backing are meant for comparison purposes to demonstrate the relative improvement afforded by the tungsten/epoxy material. A comprehensive investigation of the variation of the attenuation of the tungsten/epoxy material with frequency is beyond the scope of the current work.

The calculations indicate that the tungsten/epoxy backing should considerably improve the transducer response. Further compression of the tungsten powder during manufacture was not deemed to be necessary.

### 2.3.4 Transducer assembly

Transducers were manufactured using the new tungsten epoxy backing material to the design shown in Figure 2.11. The important features marked are:-

**Tungsten Epoxy Backing:** The maximum thickness of tungsten powder which can be impregnated using the current method is 14mm, however, in order to make the backing larger and more easily handled the backing block was machined to a length of 28mm, see Figure 2.11. Thus, the backing block consists of 14mm of tungsten/epoxy and 14mm of pure epoxy.

**PZT Cone:** The conical element was machined from PZT material with a height of 3mm, base diameter 10mm and tip diameter 1mm. The element was then bonded to the backing using silver loaded epoxy.

**Electrodes:** A 50 $\mu\text{m}$  thick brass shim was bonded to the tip electrode with conductive epoxy to serve as a wear plate and electrical contact. The shim is sufficiently thin for it to have no effect on the frequency response of the transducer within its working range (the first through-thickness resonance of a 50 $\mu\text{m}$  brass shim being 47MHz). This electrode configuration also allows the transducer to be used on non-conducting materials.

**Shielding and Guides:** The backing assembly was mounted in an aluminium case which provides shielding for the electrical connections. PTFE guides were used to allow the backing to move freely in and out whilst keeping it oriented correctly with respect to the surface. The case was mounted on three aluminium feet which hold the case clear of the surface whilst maintaining the correct orientation.

**Spring:** During operation of the transducer the backing assembly was pressed onto the surface using a mechanical spring with a spring force of 10N. This allows the transducer to be used at any angle, even upside down, with repeatable coupling force.

### 2.3.5 Comparison of brass and tungsten/epoxy backed transducers

The new tungsten/epoxy backed transducers were compared with the original brass backed type to ascertain whether any measurable improvements in performance had been made. The time domain response of the transducers to the same pencil break source is shown in Figure 2.12a), where the plots are to the same scale and one is offset for clarity. Firstly it is important to note that the peak amplitudes measured by

both transducers are almost identical and the general shape of the signals are very similar. The ringing in the brass backed transducer can be clearly seen after 80 $\mu$ s as before, no corresponding ringing is seen in the signal measured by the tungsten epoxy backed transducer. The Fourier transforms of these signals are shown in Figure 2.12b). Both signals have broadly the same frequency content with energy up to 1MHz. The tungsten epoxy backed transducer shows a great deal less fine detail and has a smoother response over this frequency range.

A similar comparison is shown in Figure 2.13a) where the source was generated by an additional conical piezoelectric device driven using a high voltage signal; the generating waveform was a single cycle 0.5MHz sinusoidal wave with an amplitude of 200Vpkpk. The backing reverberations caused by wave reflections returning from the end of the backing can be clearly seen in the signal measured by the brass backed transducer, no such reflections are present in the signal measured by the tungsten/epoxy backed transducer. Additionally, severe ringing can be seen immediately following the first arrival signal measured by the brass backed transducer (bearing in mind that the received signal should be a single cycle). This manifests itself clearly in the frequency content of the signal, showing a regular series of minima spaced at 90kHz, see Figure 2.13b). The first radial mode of the 25mm diameter brass cylinder is at around 80kHz and this is believed to be responsible for this resonant behaviour of the brass backed transducer. Again, the signal measured by the tungsten/epoxy backed transducer shows improved response, there is some ringing directly following the first arrival but the frequency content of the signal shows a much smoother response.

## 2.4 Electrical impedance measurements

### 2.4.1 Background

It is clear from the transducer models discussed in Section 4.3 that there is a direct link between the mechanical and electrical properties of piezoelectric transducers; the electrical properties of a transducer can therefore give important information regarding its acoustic response. The electrical input impedance of a transducer can easily be measured as a function of frequency using commercially available impedance analysers making impedance measurements a straightforward method for indicating the potential response of a transducer. It is important to bear in mind

however that impedance analysers generally measure the variation of the impedance with frequency by using a harmonic sinusoidal input which is swept in frequency. The impulse response of a transducer has been found to differ from the continuous wave response significantly in some cases (Silk (1984)), suggesting some non-linearity in the system; therefore, if absolute measurements of the impulse response of a transducer are required the impedance must be measured using a pulsed technique. As the current measurements are intended to indicate the change in the acoustic response caused by differing element geometries and backing materials the continuous wave response is adequate.

A Schlumberger impedance analyser was used to measure the frequency dependence of the impedance of several disks, cones and backed cones to ascertain the relative effects of backing and changing the piezoelectric element geometry. The impedance analyser operates by applying a sinusoidal voltage across the terminals of the piezoelectric element at a single frequency. The amplitude and phase of the voltage and current are measured and the complex impedance calculated; once the measurement has been taken the frequency is changed and the new impedance measured and so on. Using this method the variation of impedance with frequency was measured between 10kHz and 1MHz.

The impedance versus frequency curves for a piezoelectric element have several key features:

- The piezoelectric element is fundamentally capacitive which has an impedance proportional to  $1/\omega$ ; therefore, as the frequency tends towards zero the impedance tends towards infinity.
- Mechanical resonances of the piezoelectric element are indicated by peaks in the impedance versus frequency plot, and minima in impedance occur at the electrical resonances of the system. The relative amplitude of the impedance between these two cases gives an indication of the strength of the resonant behaviour (Kino (1987)).

#### ***2.4.2 Unbacked transducer response***

The measured variation of the modulus of the input impedance for an unbacked PZT disk element of 10mm diameter and 3mm thickness is shown in Figure 2.14. As

expected, the impedance tends to infinity as the frequency tends to zero due to the inherent capacitive nature of the element. The first two resonant peaks ( $R_1$  and  $R_2$ ) have been identified as the first two radial modes of the disk; the electrical resonances for these modes can be seen as impedance minima just before the resonant peak in each case. The first thickness mode is expected to have a natural frequency of 780kHz which corresponds to the peak marked  $T_1$ . The peaks in between are likely to be higher order radial modes.

Figure 2.15 shows the corresponding impedance plot for a 3mm thick unbacked PZT cone, (note the change of scale). The response of the conical element is more complex than that of a disk element; more modes are present as expected, the frequencies at which these resonances occur are not the same as for the disk which demonstrates that different modes are present. The resonant peaks are less dominant than are present in the disk element which demonstrates that the conical element goes some way to improving the bandwidth of a transducer. At low frequencies the impedance of the element has increased as compared to the disk element, for example at 10kHz the disk element has an impedance of  $46\text{k}\Omega$  and the cone has an impedance of  $487\text{k}\Omega$ . This increase is due to a reduction in the capacitance of the element caused by the reduction in electrode area (this accounts for the change of scale between Figure 2.14 and Figure 2.15).

#### ***2.4.3 Backed transducer response***

As previously discussed in Section 2.2.2 it is common to back the piezoelectric element with a material which has similar acoustic impedance to the element itself. The backing improves the transducer response by absorbing energy from the element and constraining the radial and flexural motion of the element.

The effect of bonding the 3mm thick conical piezoelectric element to a cylindrical brass backing 25mm diameter and 70mm long is shown in Figure 2.16. The resonant behaviour has been greatly reduced, especially in the frequency range above 0.5MHz. At lower frequencies there are still some resonant peaks present, demonstrating that the attenuation afforded by the brass backing is insufficient to damp the transducer response fully.

The effect of bonding the conical element to a cylindrical tungsten/epoxy backing is shown in Figure 2.17, where the backing dimensions are identical to that shown in Figure 2.11; three such transducers have been made and their responses are shown for comparison purposes. Clearly there is virtually no resonant behaviour and the tungsten epoxy backing is performing well as a backing material. The impedance plots for the three transducers are very similar in shape; however, transducer WE3 shows consistently higher impedance across the entire frequency range. This is caused by an inaccuracy in the machining of the conical element which has a front face diameter of 0.8mm as compared to 1mm for transducers WE1 and WE2.

## 2.5 Conclusions

Standard piezoelectric AE transducers are unsuitable for the diffuse field experiments due to the difficulty in attaining repeatable transducer coupling between measurements. Additionally the damping added to the structure by these transducers is unacceptably high.

In terms of bandwidth, coupling repeatability and damping the non-contacting methods discussed are well suited to the project needs, however, they are relatively insensitive and require extremely careful surface preparation making these methods impractical for the current application.

A conical piezoelectric transducer has been selected as the most suitable transducer for the diffuse field measurements. The conical element shape improves the bandwidth of the transducer (as compared to standard disk elements) whilst also reducing the front face diameter. This reduction of the transducer contact area reduces the aperture effects, improves the coupling repeatability and reduces the damping effect caused by the transducer.

Aperture effects have been found to be extremely important in determining the maximum transducer size which is useable. For maximum bandwidth the transducer face should be as small as possible; at frequencies where the wavelength is smaller than or equal to the transducer diameter the sensitivity of the transducer is reduced by at least 85%.

A transducer has been manufactured with a 3mm thick conical PZT element, the front face diameter being 1mm. A tungsten/epoxy backing has been used which prevents

backing reflections and smoothes the transducer response. The response of this transducer design has been found to be adequate for the diffuse field measurements.

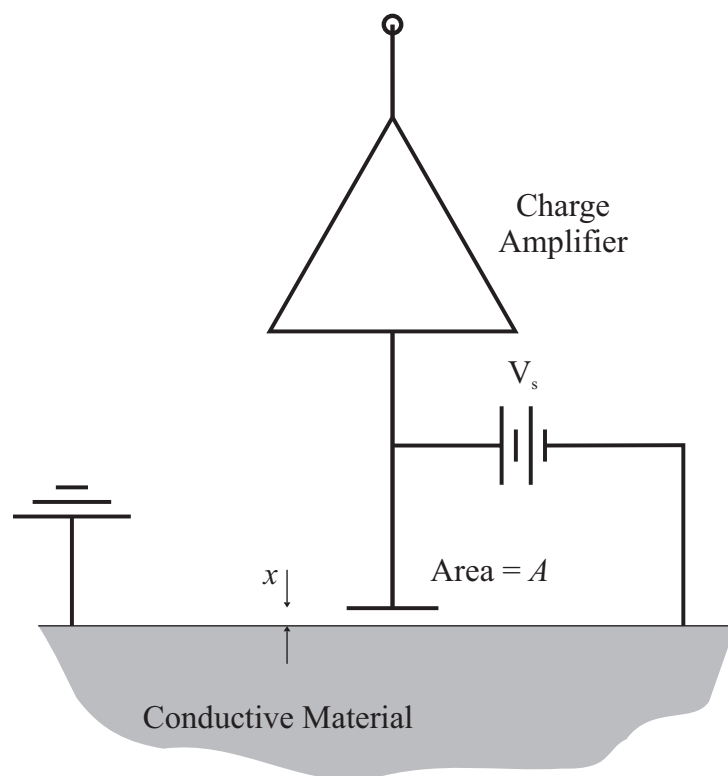


Figure 2.1 Schematic diagram of a capacitive transducer.

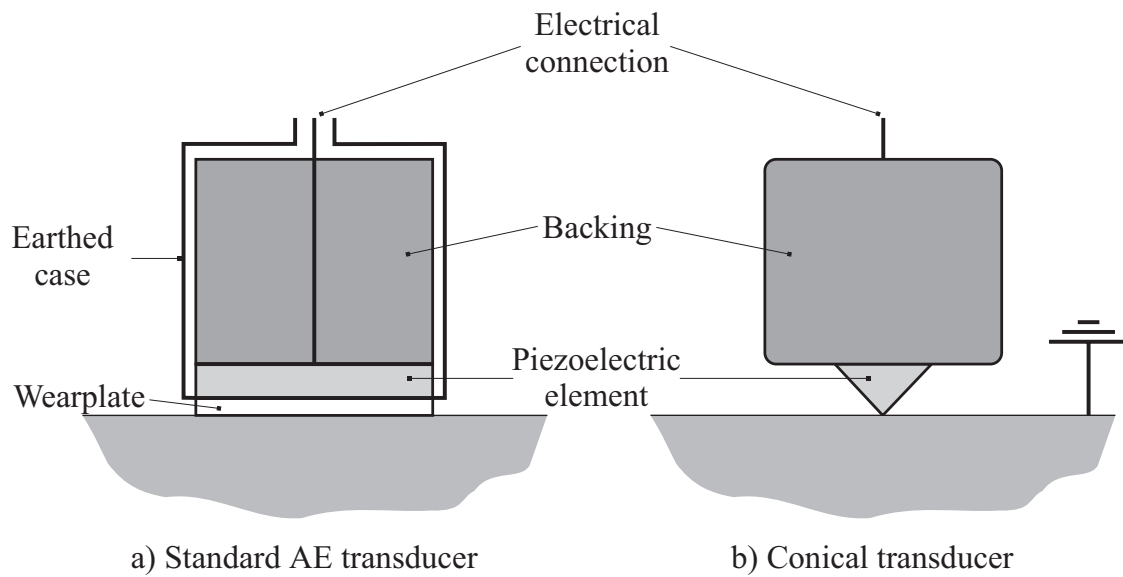


Figure 2.2 Comparison between a) A standard AE transducer b) A conical transducer.

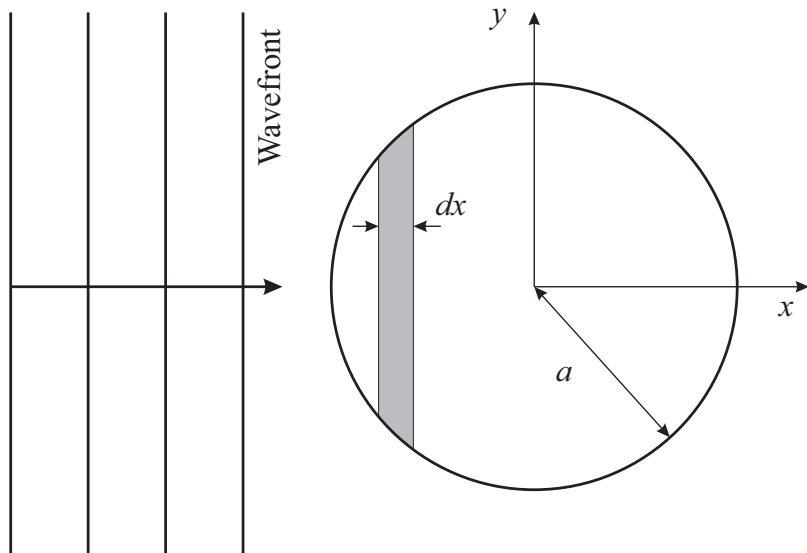


Figure 2.3 Transducer with a circular aperture receiving surface waves parallel to its face.

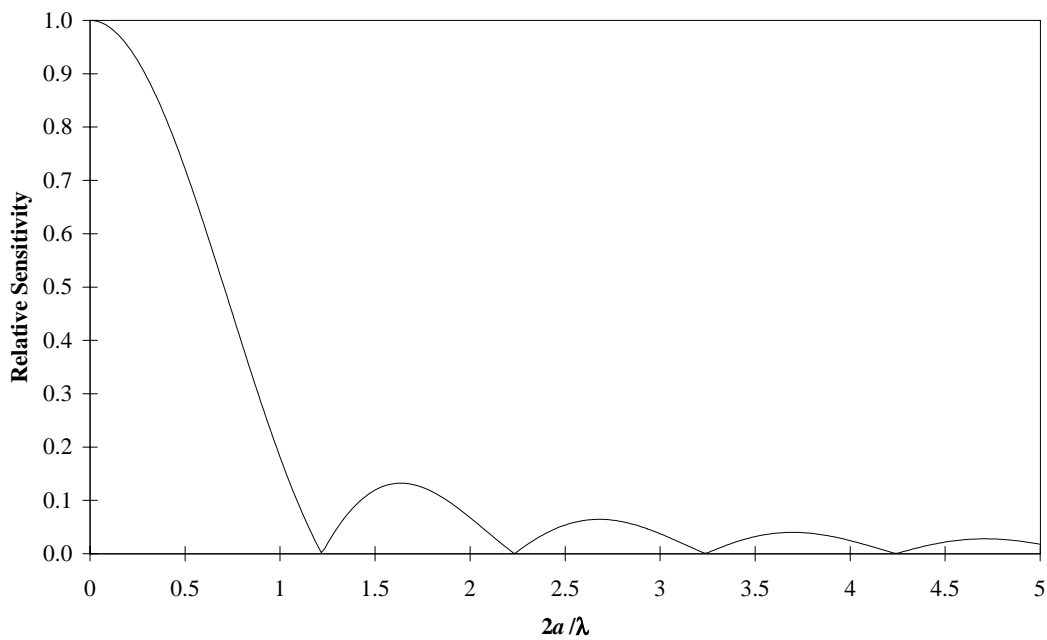


Figure 2.4 The relative sensitivity of a 10mm diameter transducer on aluminium caused by the aperture effect.

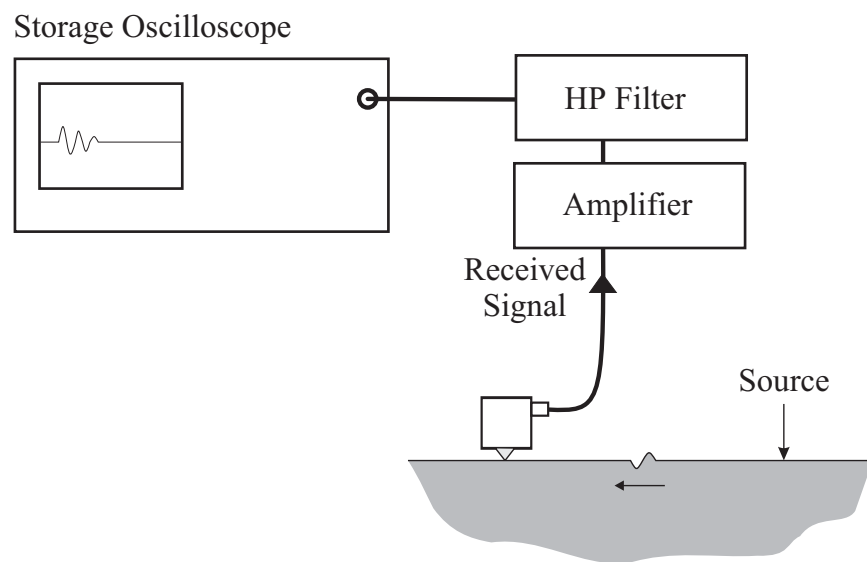


Figure 2.5 Experimental equipment used to evaluate the conical transducer response.

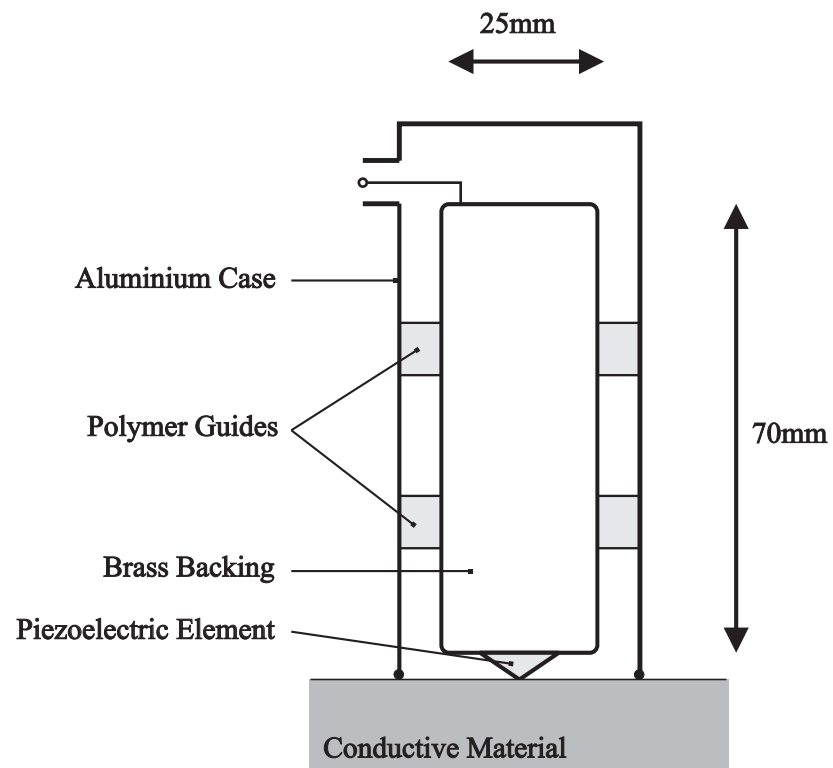


Figure 2.6 Original design of brass backed transducers.

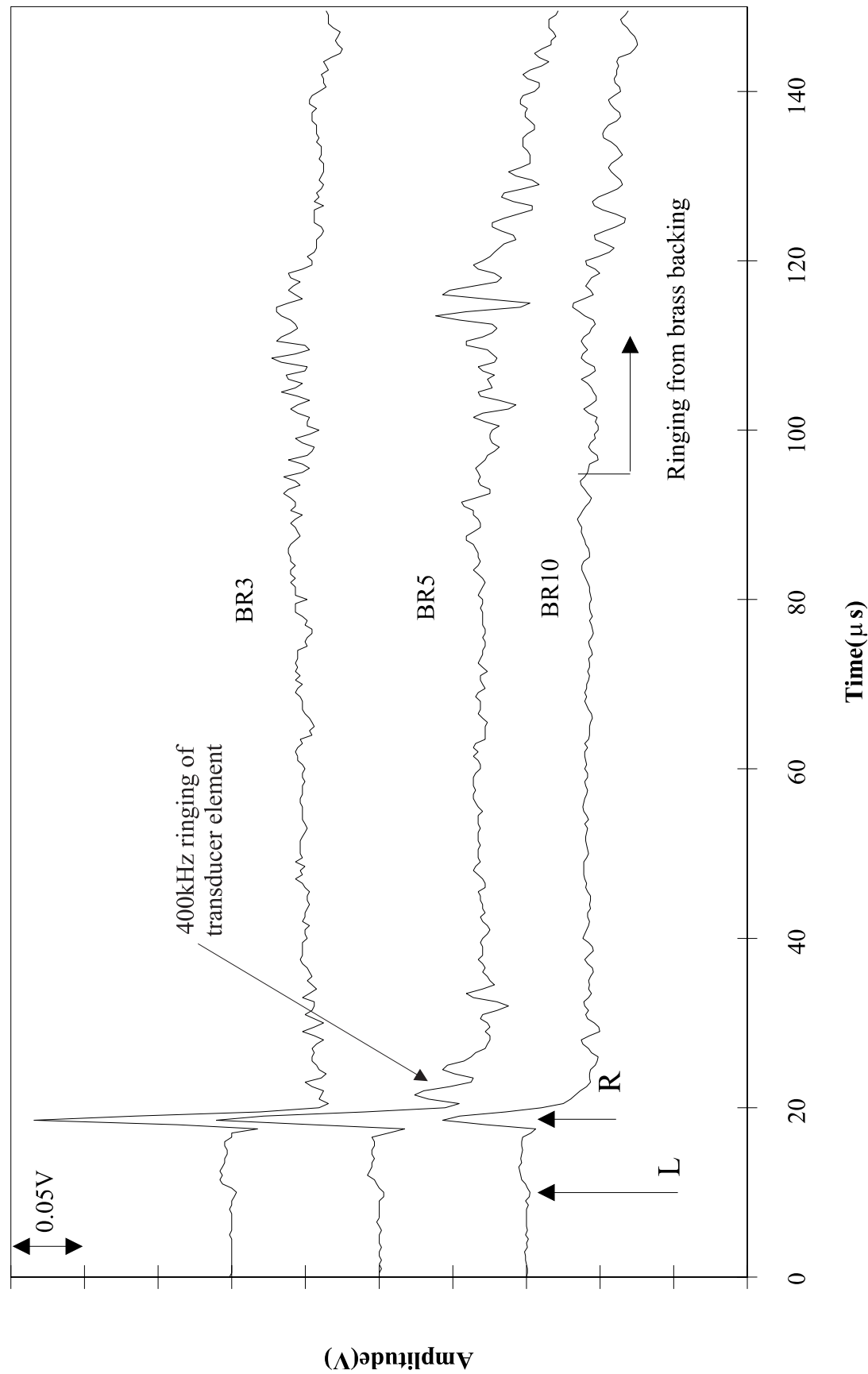


Figure 2.7 Comparison of the responses of three brass backed transducers to the same pencil break source.

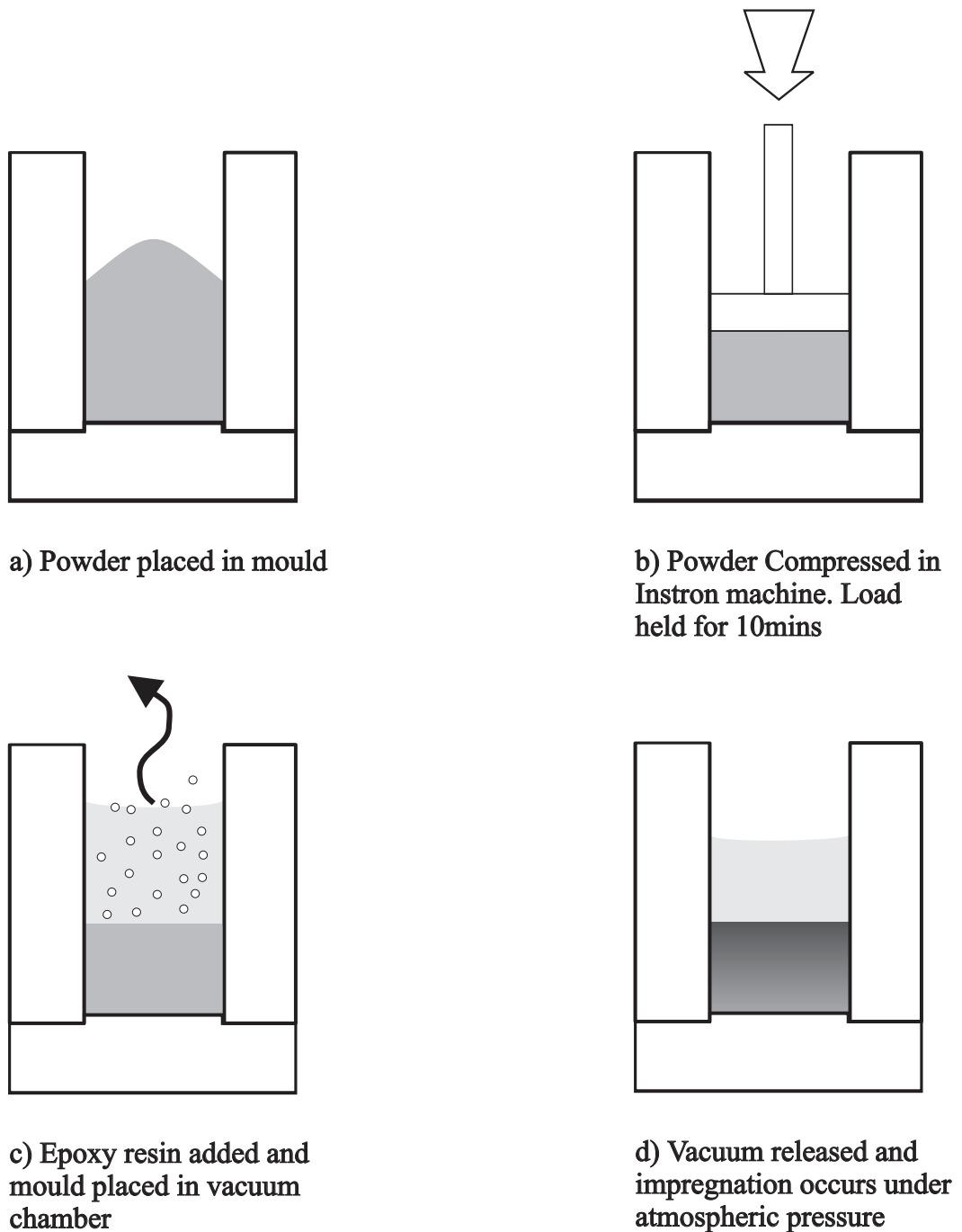


Figure 2.8 The vacuum impregnation process.

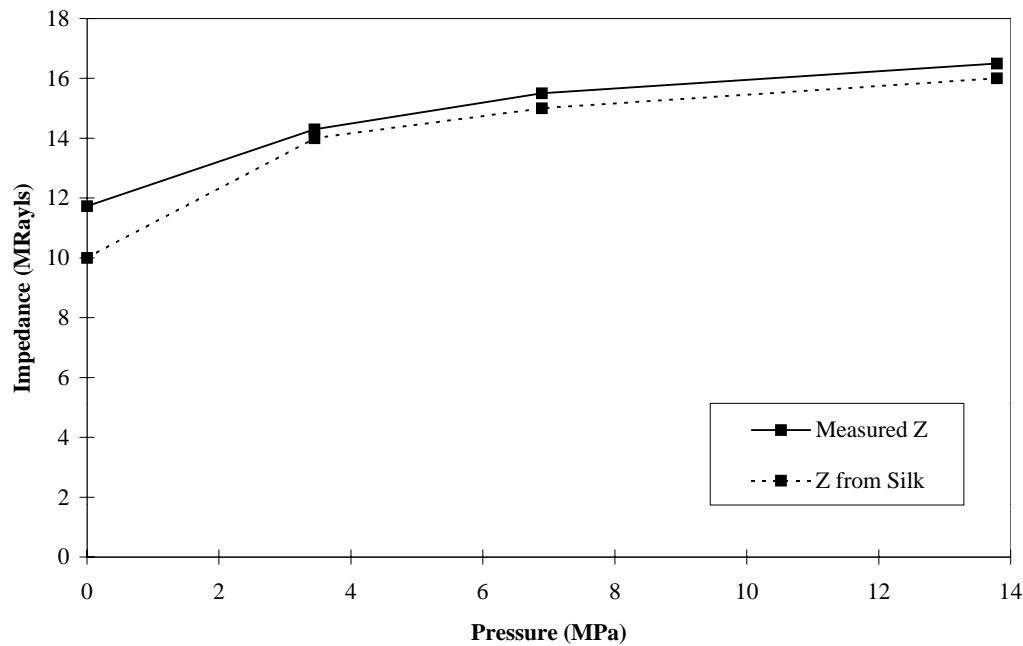


Figure 2.9 Measured impedance of the tungsten/epoxy material with respect to pressure plotted against values obtained from Silk (1984).

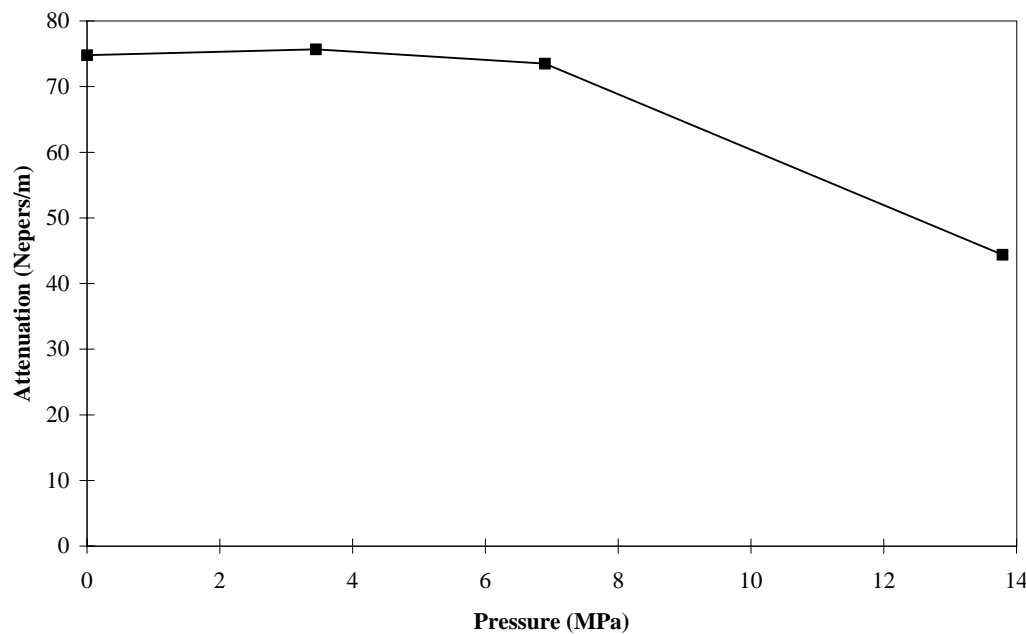


Figure 2.10 Measured attenuation of tungsten/epoxy material with respect to pressure.

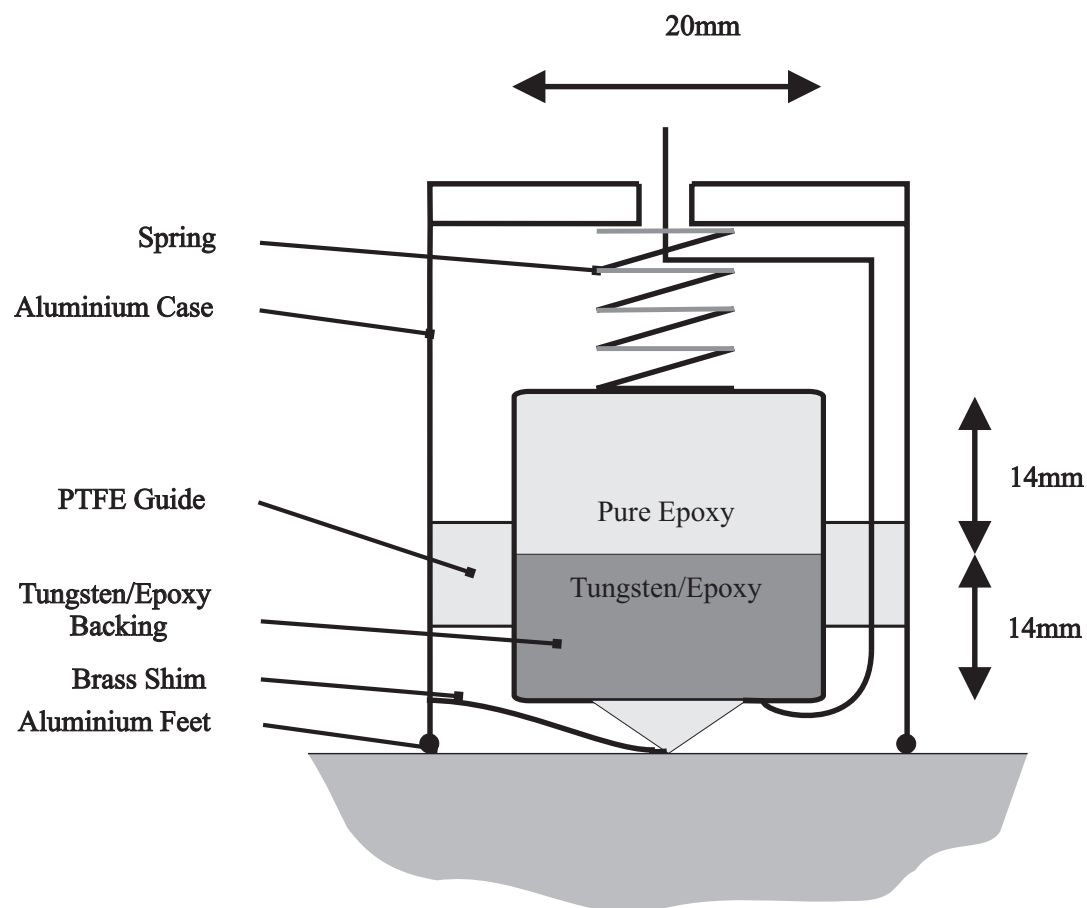
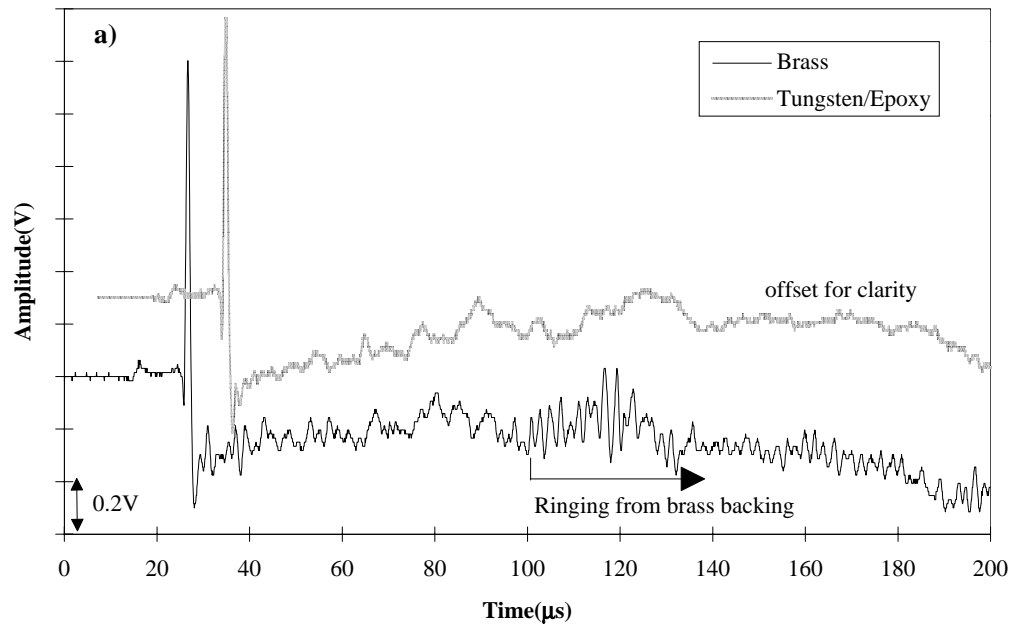


Figure 2.11 Design of new tungsten/epoxy backed transducers.



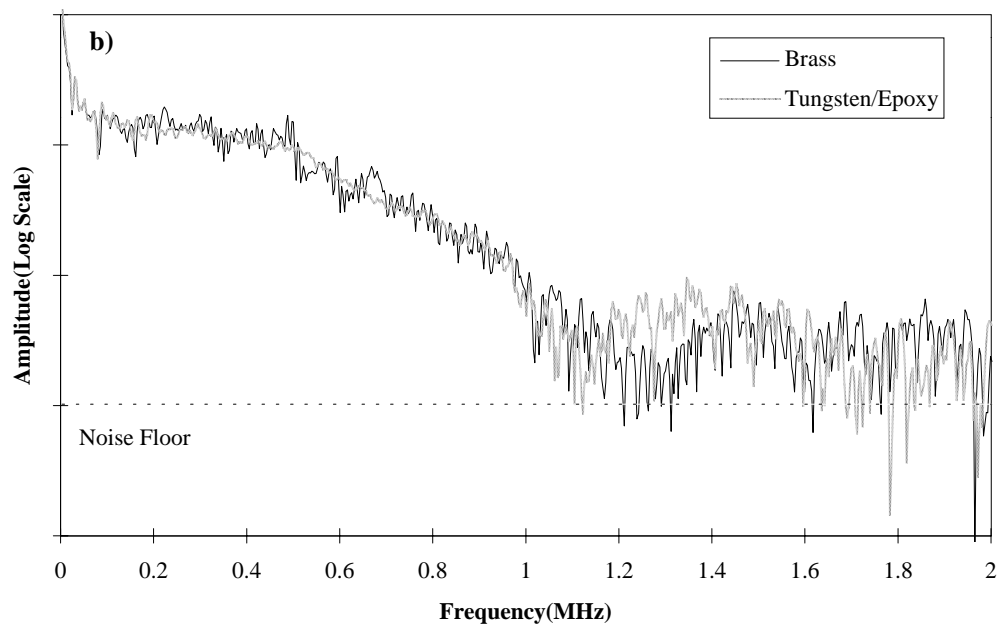
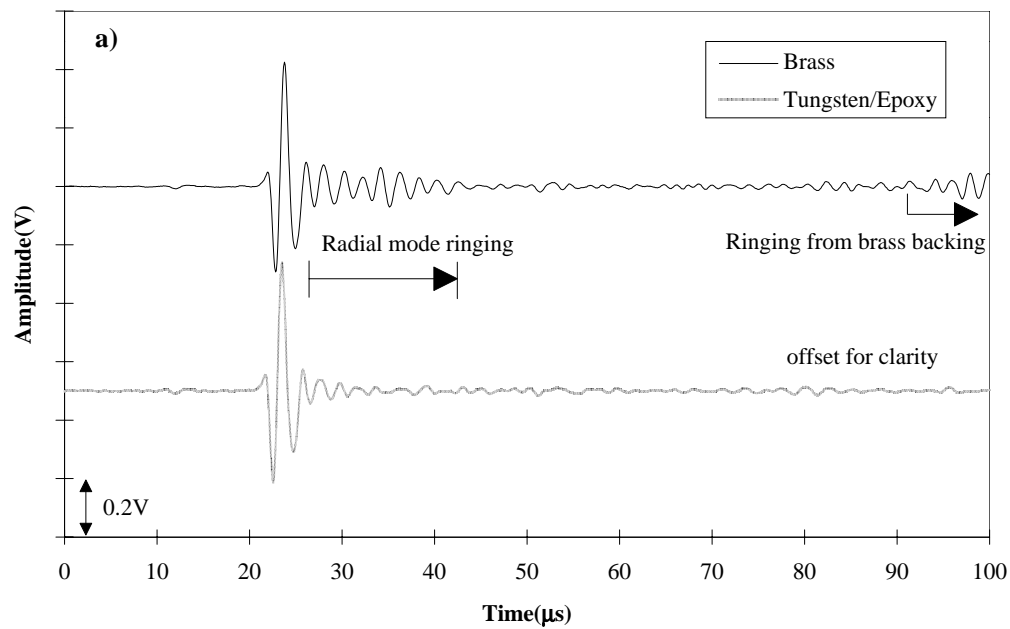


Figure 2.12 a) Comparison of time domain responses of a brass backed transducer and a tungsten/epoxy backed transducer to the same pencil source, b) Frequency content of signals shown in a).



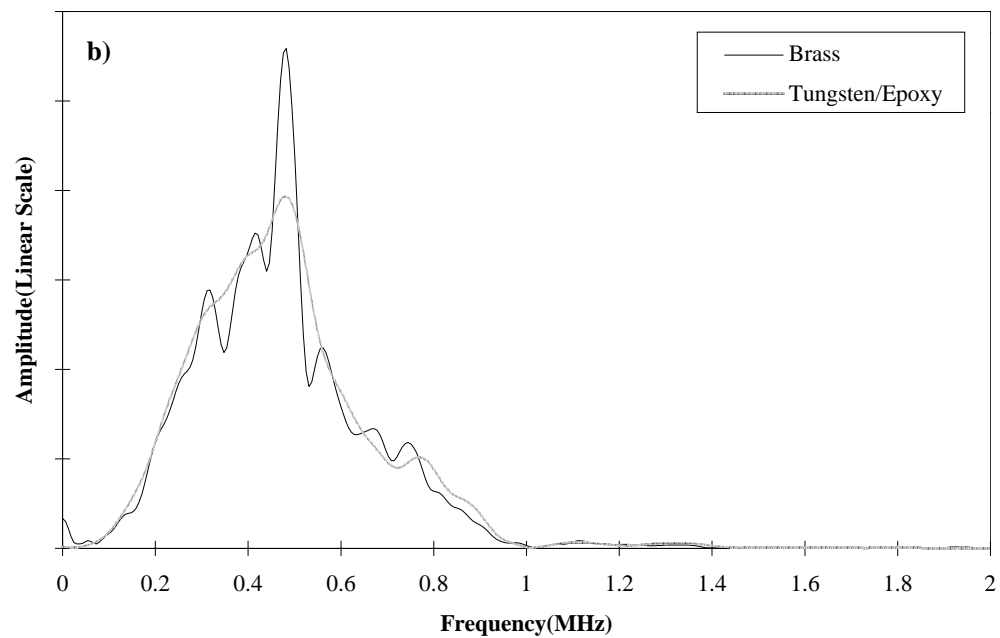


Figure 2.13 a). Comparison of the time domain responses of a brass backed transducer and a tungsten/epoxy backed transducer to the 0.5MHz input signal, b) Frequency content of signals shown in a).

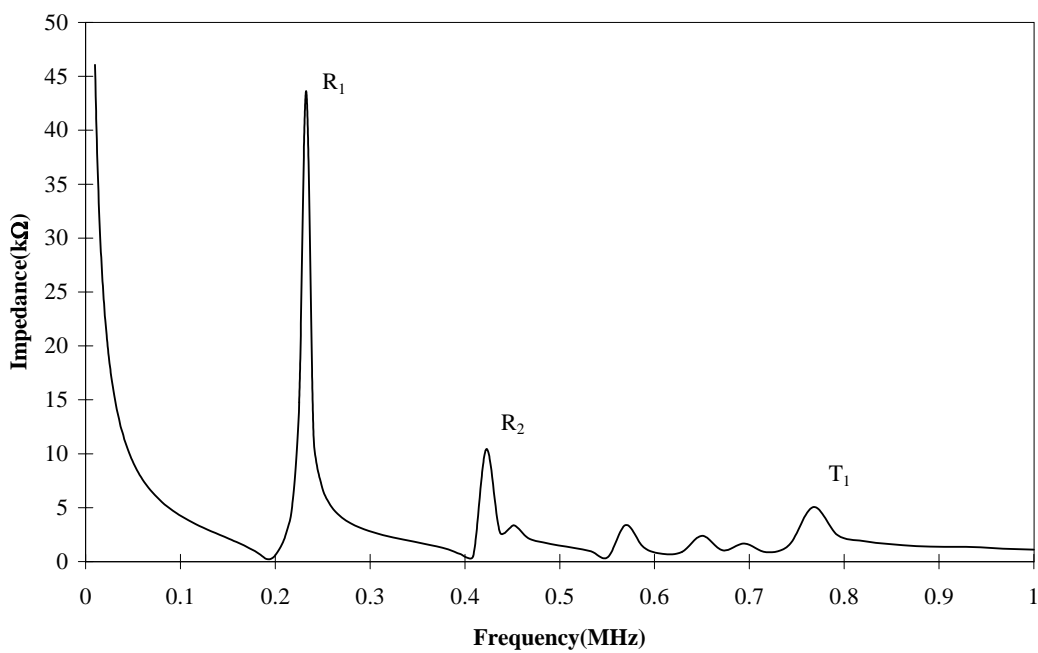


Figure 2.14 Measured electrical impedance of an unbacked 10mm diameter 3mm thick PZT disk.

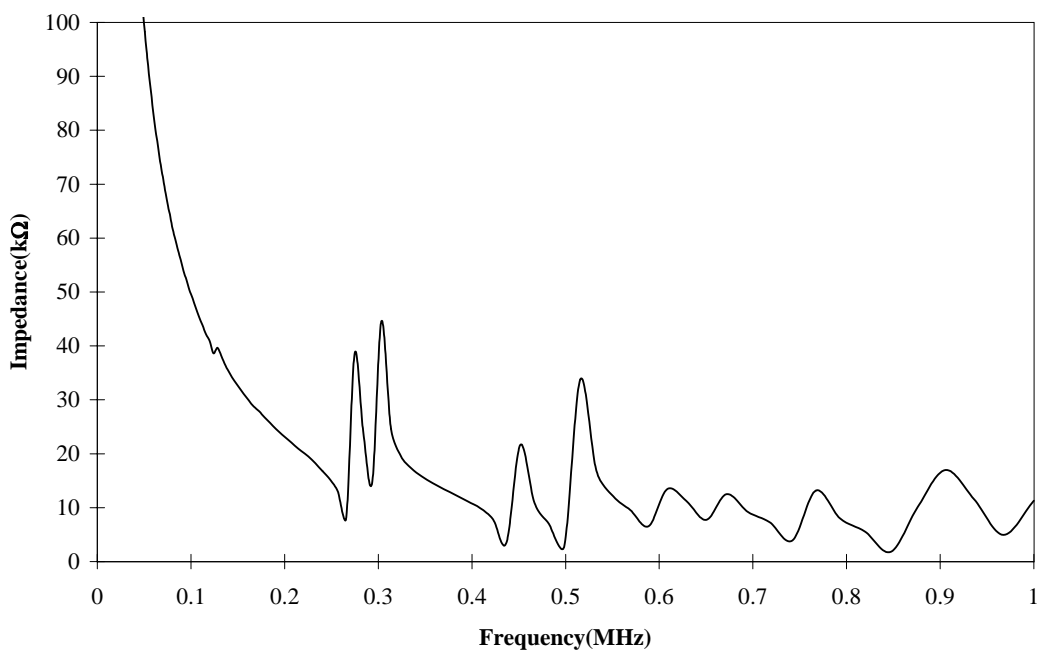


Figure 2.15 Measured electrical impedance of a 3mm thick unbacked PZT cone.

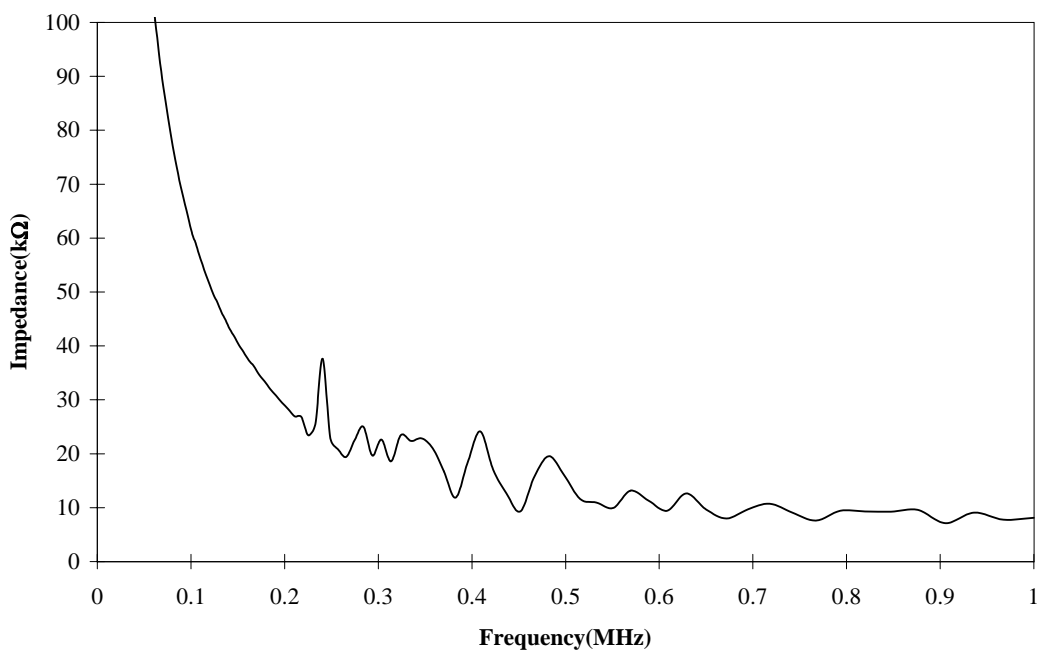


Figure 2.16 Measured electrical impedance of a 3mm thick PZT cone with brass backing.

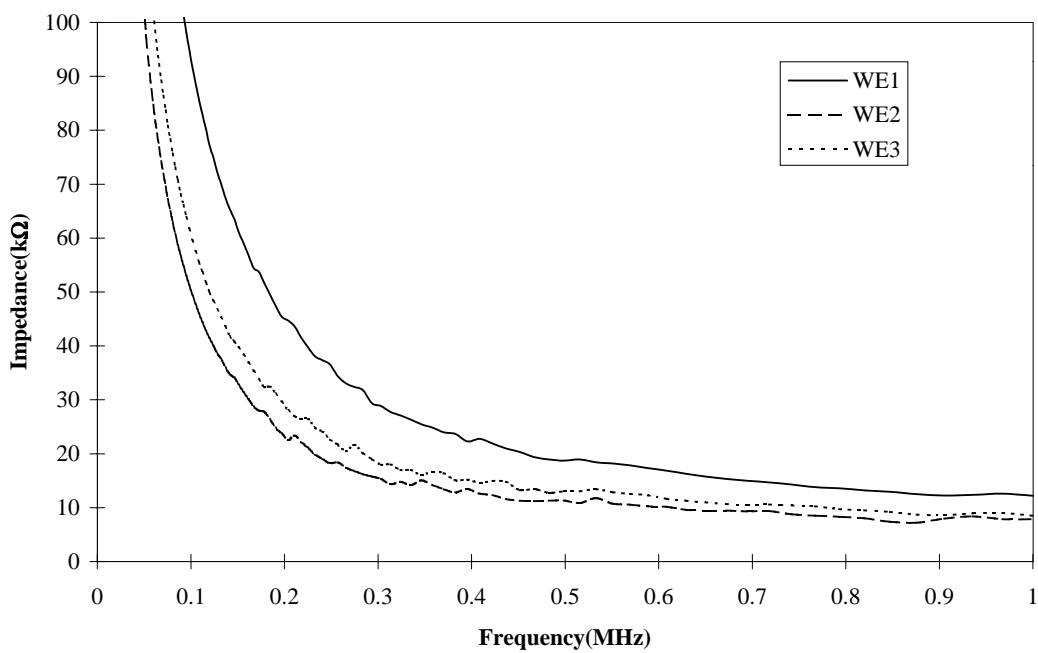


Figure 2.17 Measured electrical impedance of a 3mm thick PZT cone with tungsten/epoxy backing, comparison of three transducers.

### 3. Simulated acoustic emission sources

---

#### 3.1 Introduction

##### 3.1.1 Overview of chapter

Acoustic emission testing, unlike standard ultrasonic non-destructive testing, relies on a natural process such as crack growth to generate ultrasonic waves in the structure. The characteristics of the source such as its location and the mechanisms by which the ultrasonic energy is produced are generally not known. It is often desirable to have a repeatable and well characterised ultrasonic source in order to examine the effect of such things as the structure, transducer performance and transducer coupling. It is also desirable to be able to predict or measure the sensitivity of the measurement system as a whole. What is required is a simulated acoustic emission source; this source should have a similar bandwidth to that of the real AE sources which are of interest and should be as repeatable as possible. The frequency content should be as uniform as possible within its working range and should be well defined by theory; the variation of force with time (also known as the source function) must therefore be well defined. Coupling of the source to the structure is another area in which uncertainties may arise so point sources are favoured. The aperture effects previously discussed in Section 2.2.3 are relevant to sources and this also favours sources with small contact areas.

This chapter reviews the use of simulated sources for AE investigations appraising each method against the characteristics required for the diffuse field measurements. Many simulated sources have been suggested and a large number have been discussed in the literature, a very thorough review has been given by Breckenridge, et al. (1984). Fracture, impact and piezoelectric sources have been chosen as the most suitable source types; experimental measurements and theoretical predictions have been compared for each of these source types to ascertain their suitability and shortcomings.

##### 3.1.2 Experimental set-up

The experimental set-up used for source comparisons is shown in Figure 3.1. All experiments were carried out on an aluminium alloy cylinder with a diameter of

200mm and a height of 144mm. The receiving transducer was a tungsten/epoxy backed conical transducer as described in Section 2.3.3. The signal from the transducer was amplified and filtered with a 10kHz high-pass filter to remove mechanical and electrical background noise. A LeCroy Scope Station 140 was used for signal capture with a sampling rate of 100MHz. The oscilloscope was triggered when the signal measured by the conical transducer rose above a threshold level, this threshold was adjusted individually for each source type as each was found to produce different amplitude signals.

## 3.2 Fracture sources

When looking for a simulated AE source, a fracture is an obvious candidate since a great deal of AE work is concerned with cracking. Fracture sources have been used by many researchers as repeatable simulated AE sources, with suitable system design they can be made to have remarkable repeatability over a wide bandwidth; two methods are in common use.

### 3.2.1 Pencil break source

The breaking of a 0.5mm diameter pencil lead on the surface of a structure produces a sudden step-like release of force with an average rise time reported to be  $2.5\mu s$  (Breckenridge, et al. (1984)). The pencil break source was first proposed by Hsu and Nielsen (Nielsen (1980)). The source function can be approximated by a step release function the frequency content of which is inversely proportional to the frequency (Webster (1987)). The contact area is small, nominally less than the lead diameter and so a point source can be assumed.

A series of pencil break experiments were carried out using 0.5mm diameter 2H lead using the experimental equipment shown in Figure 3.1 to measure the first arrival waveforms at a source to receiver distance of 100mm. A typical first arrival signal is given in Figure 3.2a) where the arrivals of the longitudinal wave, shear wave and Rayleigh wave are marked, (approximate locations given by Johnson (1985)).

An understanding of this waveform shape can be gained by considering the wave modes which are excited. Spherical wavefronts of longitudinal and shear waves propagate from the source point into the material with velocities  $C_L$  and  $C_S$  respectively (where  $C_L \approx 2C_S$  for aluminium). Rayleigh waves propagate along the

surface with cylindrical wavefronts from the source point at a velocity  $C_R$  (where  $C_R \approx 0.9C_S$ ). At the measurement point the three wave types arrive at different times and have different normal displacement components. This is commonly known as Lamb's problem (Breckenridge, et al. (1975)).

Figure 3.2b) shows the frequency content of the signal shown in Figure 3.2a) plotted on a logarithmic scale. This shows that the frequency content is approximately inversely proportional to the frequency. The signal was found to be very repeatable in shape with only slight amplitude variations caused by variable fracture load of the lead. The method is simple in operation and with some practice consistent results can be obtained in the order of  $\pm 10\%$  peak amplitude.

### 3.2.2 *Glass capillary fracture source*

The second commonly used fracture source is the breaking of a glass capillary (Breckenridge (1982), Michaels, et al. (1981) and Kim and Kim (1993)). A drawn glass capillary is laid on the material surface with its axis parallel to the surface. The capillary is loaded by a force normal to the material surface until the capillary fractures. The load is applied using a loading screw and the maximum load at fracture is measured with a load cell within the loading screw itself. The source function can again be approximated by a step release function with an amplitude equal to the breaking load of the capillary and with a rise time of the order of  $0.2\mu\text{s}$  (Breckenridge (1982)). The advantages of capillary fractures over pencil fractures are the increased bandwidth caused by the shorter rise time and the improved repeatability gained by normalising the signal to the breaking load of the capillary. However, glass capillary fractures are more complicated and slow to repeat.

## 3.3 Impact sources

### 3.3.1 *Theory*

The impact of small particles on a surface produces short impulsive forces of small amplitude. Modelling of such impacts was first done by Hertz and a theoretical solution for the impact of two projectiles with a spherical contact regions formulated (Johnson (1985)).

If one of these projectiles is assumed to be stationary with very large radius and mass the model predicts the behaviour of a small particle impacting on a flat surface. The impact duration,  $t_0$ , of such an impact may be approximated by,

$$t_0 = 2.94 \frac{\alpha^{2/5}}{V} \quad (3.8)$$

where  $V$  is the impact velocity and  $\alpha$  is given by,

$$\alpha = C \frac{V^2 M}{(RE^*)^{1/2}} \quad (3.9)$$

where  $M$  is the mass of the ball,  $R$  is the radius of the ball and  $E^*$  is an averaged Young's modulus for the two materials as follows,

$$\frac{1}{E^*} = \frac{(1 - \nu_1^2)}{E_1} + \frac{(1 - \nu_2^2)}{E_2} \quad (3.10)$$

where  $E$  and  $\nu$  are the Young's Modulus and Poisson's ratio of the materials.

The frequency content of the resulting signal can be approximated by,

$$F(\omega) = \left| \frac{\alpha t_0 \cos(\pi \omega t_0)}{(1 - 4\omega^2 t_0)} \right| \quad (3.11)$$

where  $\omega$  is the frequency.

The frequency content of such an impact has a very characteristic lobed shape which contains most of its energy in the first lobe, see Figure 3.3. In order to produce a broad band signal the impact duration must be as short as possible. It can be seen from Equation (3.9) that this can be achieved by reducing the mass of the impacting particle or increasing the radius. Reducing the mass of the particle, however, drastically reduces the magnitude of the forces and displacements caused by the impact making them more difficult to detect. Also in the experiments which have been carried out the particle has always been spherical. Spheres were used because they are relatively easy to manufacture and measure. Problems arise however due to the contradictory requirements of a large radius and a small mass. These two requirements clearly cannot be met by using a sphere.

The mass is the more important of the two parameters as far as impact duration goes since impact duration is proportional to the square of the mass. Also for a sphere the mass is proportional to the cube of the radius. These two effects combined makes it necessary to use very small spheres if broad band signals are required. This problem can be reduced if non-spherical particles are used but the difficulties in accurately manufacturing and measuring such particles and ensuring repeatable impact orientation makes this option out of the scope of the current investigations.

The repeatability and practical considerations of impact sources has been examined in two parts. Firstly manual ball impact experiments were carried out to check the agreement of measured source function with the theory and then a electrically powered 'micro-hammer' was developed and tested for repeatability and suitability.

### **3.3.2 Ball impact source**

A simple method which has been used to produce repeatable impact sources is to drop a ball of known radius and mass from a fixed height onto the material surface. With knowledge of the material properties and impact velocity, the impact duration and frequency content of the source function can be estimated (Webster (1987)).

A hardened steel ball dropped from a fixed height onto the surface provided the impact source for these experiments. The ball diameter was 2mm with a mass of 30mg. The height was controlled such that the impact velocity was  $1.25\text{ms}^{-1}$ . The experimental set-up was identical to the previous experiments with the source to sensor distance 100mm, see Figure 3.1. Figure 3.4a) shows the time domain signal of the first arrival waveform measured from this impact. The frequency content of this first arrival was measured and is shown in Figure 3.4b) together with the theoretical prediction using Equation (3.4); the y-axis units are arbitrary and the theoretical results have been scaled to give a best fit to the measurements. The agreement between measurement and theory is good but the signal amplitude was insufficient to be measured above 800kHz with the current measurement system. The low frequency drop-off in signal is caused by the high-pass filter which was used for these experiments.

### 3.3.3 Micro-hammer source

For in service applications a ball impact source is not practical or controllable. A micro-hammer technique has been suggested by Chetwynd and Sachse (1991) which uses an electrically driven actuator which can produce a repeatable impact velocity. The hammer tip was a small particle which was connected to the actuator via a soft cantilever spring. In operation the actuator arm was brought to rest abruptly by a mechanical stop before the hammer tip reached the surface. The inertia of the tip carries it forward, flexing the spring, until it contacts the surface and rebounds. If the spring stiffness and stand-off distance are controlled correctly the tip will only contact the surface once and the impact velocity will be stable. Ideally the spring needs to be very compliant which makes the impact velocity relatively insensitive to the stand-off distance.

A device has been constructed using the tapping head of a Tapometer which was borrowed from Rolls Royce MatEval Ltd (Cawley and Adams (1989)). This device incorporates a rotating arm driven by an actuator, see Figure 3.5a); the actuator drives the arm down towards the surface until it impinges on a mechanical stop. The Tapometer was modified by removing the standard steel tapping head and replacing it with a micro-hammer. The spring and spherical tip of the hammer were made in one piece from Borosilicate glass (a similar method has been used at Rolls Royce for AE testing of ceramic components Webster (1996)). A glass rod was melted and drawn down to a fine fibre and a 15mm length of this fibre was used as the spring element. The spherical tip was produced by melting the end of the fibre until it formed a ball, see Figure 3.5b). It was impossible to accurately control the diameters of the fibre and ball but they were measured after fabrication using a micrometer and only the most suitable were used. The spring/ball assembly was attached to the arm with wax which allowed easy mounting and removal of these delicate components.

This device was tested using the same experimental set-up as before, see Figure 3.1. An electrical pulser was used to drive the hammer with a square pulse of peak amplitude 20V. This could be driven continuously with a frequency of 0.5Hz or manually triggered. Using this set-up the impact velocity has been estimated to be  $0.8\text{ms}^{-1}$  by measuring the time of flight of the arm and assuming constant acceleration. Two geometries were evaluated with ball diameters of 0.85mm and 0.39mm. The

spring diameter used in both cases was 0.2mm as this is the thinnest fibre that could be satisfactorily handled.

The stand-off distance between the impact ball and the surface was set such that the ball came into contact with the surface only once. This was done by first setting the stand-off to zero and then gradually increasing it. At each position the hammer was fired and a measurement was taken, any secondary strikes being easily seen. The stand-off distance was increased until these secondary strikes were no longer observed. Stand-off distances were measured for the two hammer sizes used by placing metal shims beneath the device. The required stand-off distances were 0.5mm for the 0.85mm hammer and 0.25mm for the 0.39mm hammer. Figure 3.6a) and b) show the time domain signal and frequency content of this signal measured from the 0.85mm hammer with the theoretical prediction from Equation (3.4). Agreement is generally good, with the first minimum agreeing to within 50kHz. Above 700kHz agreement is less promising due to the small signal levels. The effect of the 10kHz high-pass filter is again evident in all of the micro-hammer results.

The time domain signal and frequency content of the signal measured from the 0.39mm hammer are shown in Figure 3.7a) and b), with the theoretical prediction from Equation (3.4). Agreement is reasonable but the amplitude of the received signal was so small that measurement was very difficult. It is expected that as the mass of the ball decreases the mass of the spring will become more important thus reducing the frequency content from that which would be predicted. This effect can be seen in Figure 3.7b) where the experimental data has a minimum at 850kHz rather than 1MHz as predicted. The signal for this case was extremely small and proved very difficult to measure reliably. A hammer of this size would not be suitable for a repeatable source.

To assess the repeatability of the micro-hammer several successive impacts were recorded three of which are shown in Figure 3.8 using the 0.85mm hammer. The first signal is the first arrival of the surface wave and the second is its reflection from the right-angled edge of the block. There are amplitude variations of up to 10% which have been attributed to inconsistent impact velocity.

The micro-hammer source has many advantages over the manual ball impact source, being easier and quicker to repeat; a repeat rate of 0.5Hz was found to be the

maximum attainable using this device. The hammer itself is very delicate, however, and is easily damaged.

### 3.4 Piezoelectric sources

The problems highlighted in Chapter 2 concerning coupling, aperture effect and complex transducer response make standard AE transducers a poor choice for a simulated AE source; however, the conical transducer, due to its small contact area and relatively non-resonant behaviour makes it a promising candidate. Some work has been done in the literature in order to characterise this type of transducer as a source. Breckenridge, et al. (1984) reported good results with a repeatable flat response up to 1.5MHz on an aluminium plate where the transducer was driven with a 200V step function.

A principal advantage of using a piezoelectric transducer as a simulated AE source is the flexibility of pulse shape and amplitude which are possible. The transducer can be driven by a tailored electrical signal to alter the bandwidth of the mechanical output signal (within the limits of the frequency response of the transducer). The amplitude of the mechanical output signal can also be altered by changing the voltage of the input signal whilst keeping the pulse shape the same. The ability to accurately and easily adjust the source amplitude is an extremely useful characteristic.

Variability in the coupling of the source transducer to the material will affect its sensitivity in a similar way as was seen when calibrating the transducers as receivers, see Figure 4.8 (see next chapter). Variabilities in amplitude of up to 7.6% were measured in the frequency range from 0 to 1MHz, see Section 4.2.6. Similar variation would be expected when the same transducers are used as a source.

Experiments have been carried out to assess the usefulness of the tungsten/epoxy backed transducers as a simulated source. These have concentrated on assessing the ability to vary the bandwidth of the signal and the effect of the coupling variability on the resulting mechanical signals. The experimental set-up was identical to that used for assessing the other simulated sources, see Figure 3.1, and the source transducer was placed 100mm from the receiver. The source transducer was driven by a LeCroy 9101 arbitrary function generator (AFG) via a 50dB power amplifier. Signals of up to 200Vpkpk can be supplied to the transducer using this system.

Three measured time domain responses of the transducer to a single cycle 0.5MHz input signal are shown in Figure 3.9a). The source transducer was removed and re-coupled between each measurement. The coupling repeatability between these experiments was 9.5% and the frequency content of these signals is shown in Figure 3.9b) along with that of the electrical input signal. The time domain signal shows some ringing of the transducer immediately following the first arrival (as previously noted in Section 2.3.5); this affects the frequency content by causing a peak at 0.5MHz which can be seen in Figure 3.9b). Additionally the frequency response of the piezoelectric source to a 150kHz five cycle Hanning windowed tone burst is shown in Figure 3.10 with the frequency content of the input signal; this demonstrates the degree of bandwidth control which is possible by using a conical piezoelectric source.

### 3.5 Conclusions

Fracture sources are good simulated AE sources in the context of bandwidth and repeatability; the pencil break source has been measured to have a bandwidth of 1MHz and a shot-to-shot repeatability of 10% on amplitude (capillary fracture sources are reported to perform better on both counts). The major disadvantage encountered when using fracture sources is their awkward and time consuming nature making them poorly suited to the diffuse field measurements.

A micro-hammer has been tested as an AE source and has proved to be repeatable with peak amplitude variations of within 10% between successive impacts. The useful frequency content however was limited to well below 700kHz for the impact heads used and using smaller heads was found to produced signals which had insufficient amplitude to be detected reliably. The micro-hammer source, although easier and quicker to use than the fracture sources, was found to be slow, cumbersome and delicate making it impractical for the current application.

Conical piezoelectric transducers have been tested as ultrasonic sources and have been found to be repeatable; the coupling error associated with using the transducers have been measured to be within 9.5% over a 1MHz bandwidth. The bandwidth and amplitude of the mechanical signal produced by the source can be altered by changing the electrical excitation function, making the piezoelectric source extremely versatile.

Additionally the piezoelectric source is quick and easy to use making it the most suitable simulated source for the current application.

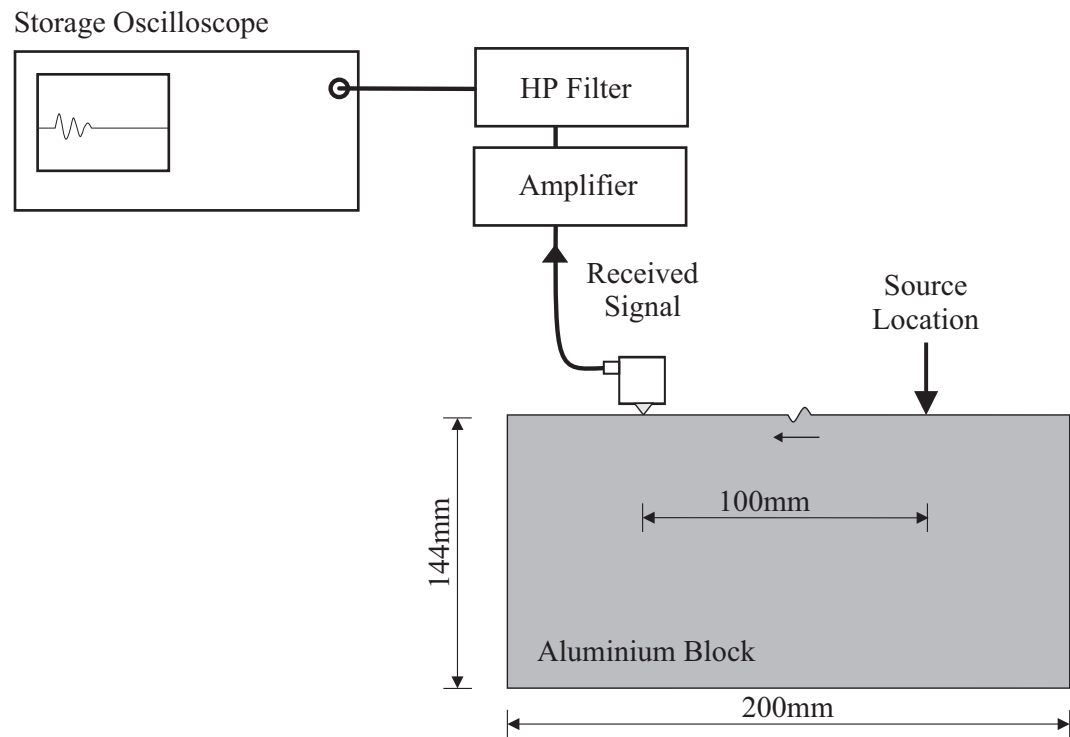
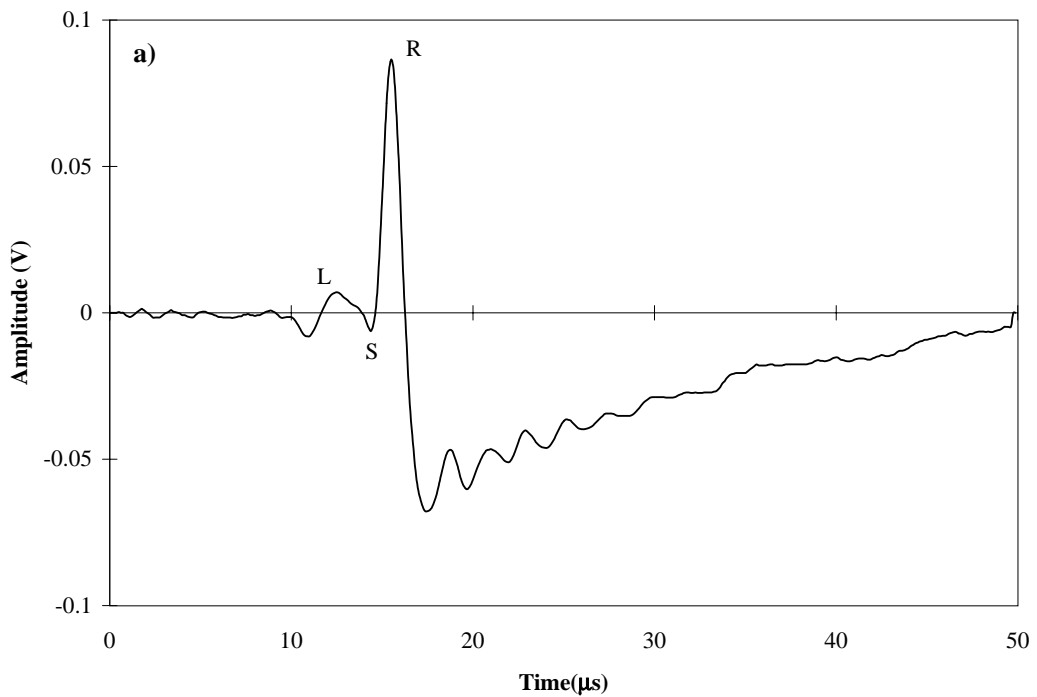


Figure 3.1 Experimental set-up used for the source comparisons.



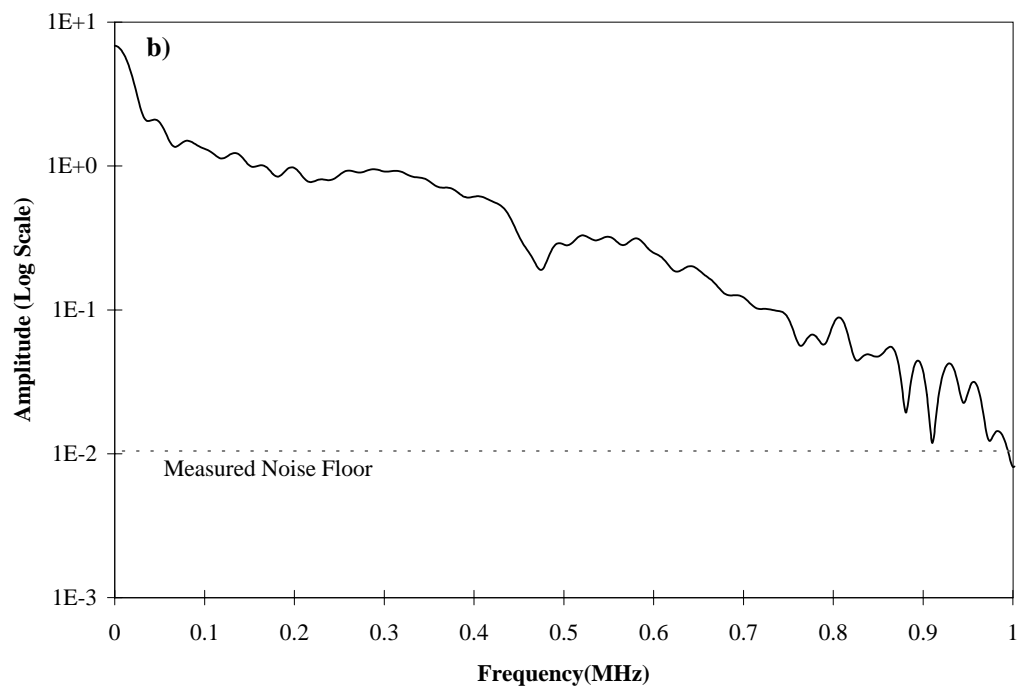


Figure 3.2    a) Time domain first arrival signal measured from a pencil break source,  
             b) Frequency content of signal shown in a).

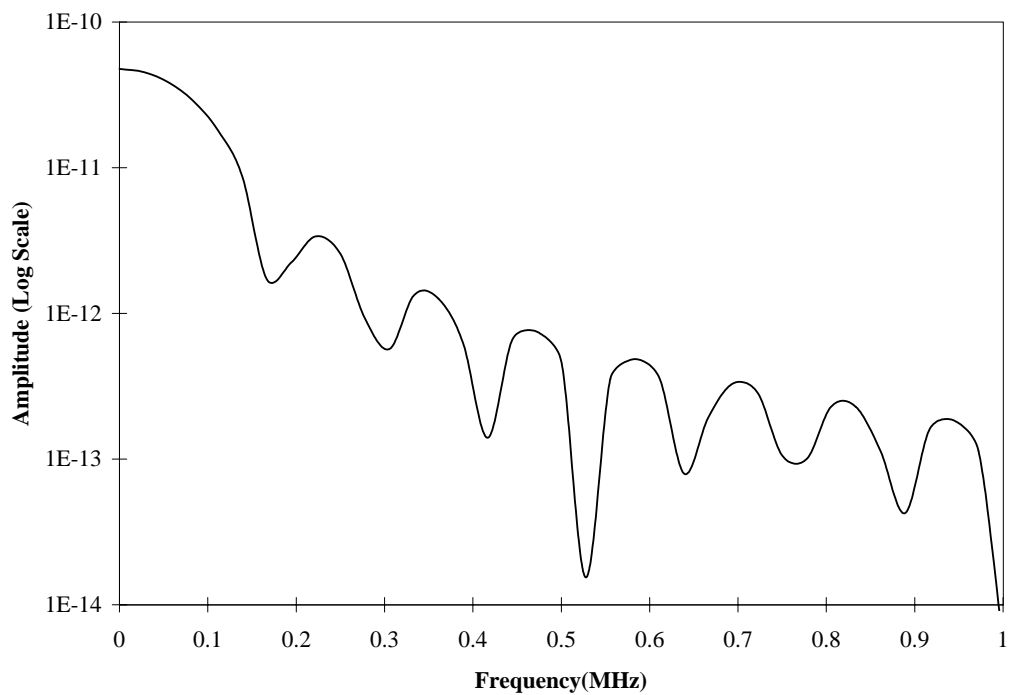
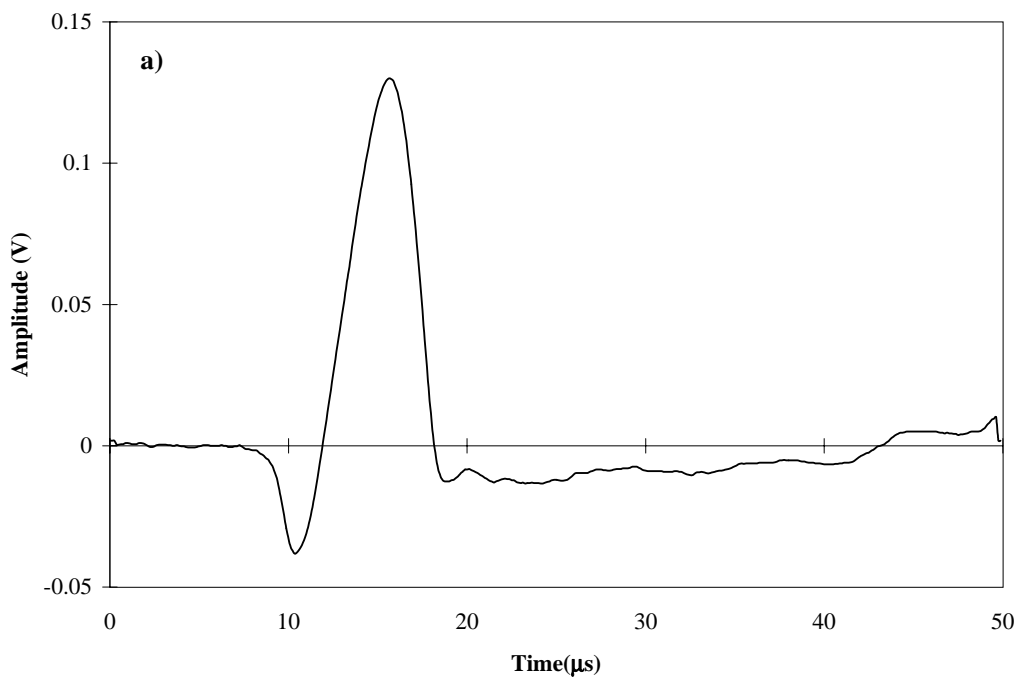


Figure 3.3 Theoretical frequency content of an impact source showing characteristic lobed shape.



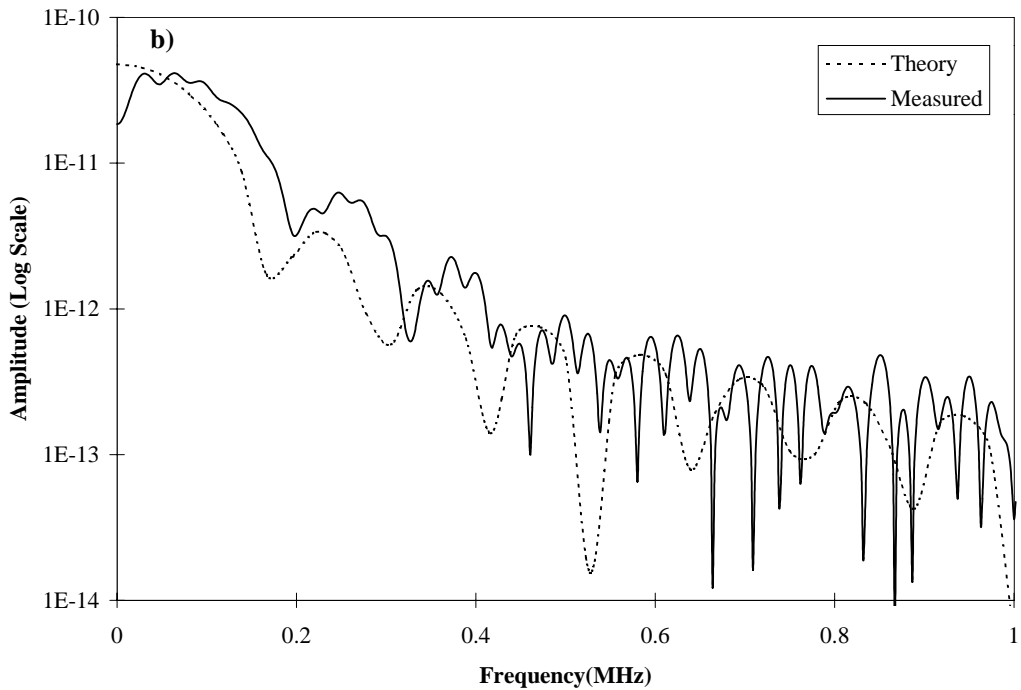


Figure 3.4 a) Time domain first arrival signal measured from the impact of a 30mg, 2mm diameter steel ball, b) Frequency content of signal shown in a) together with theoretical prediction using Equation (3.4).

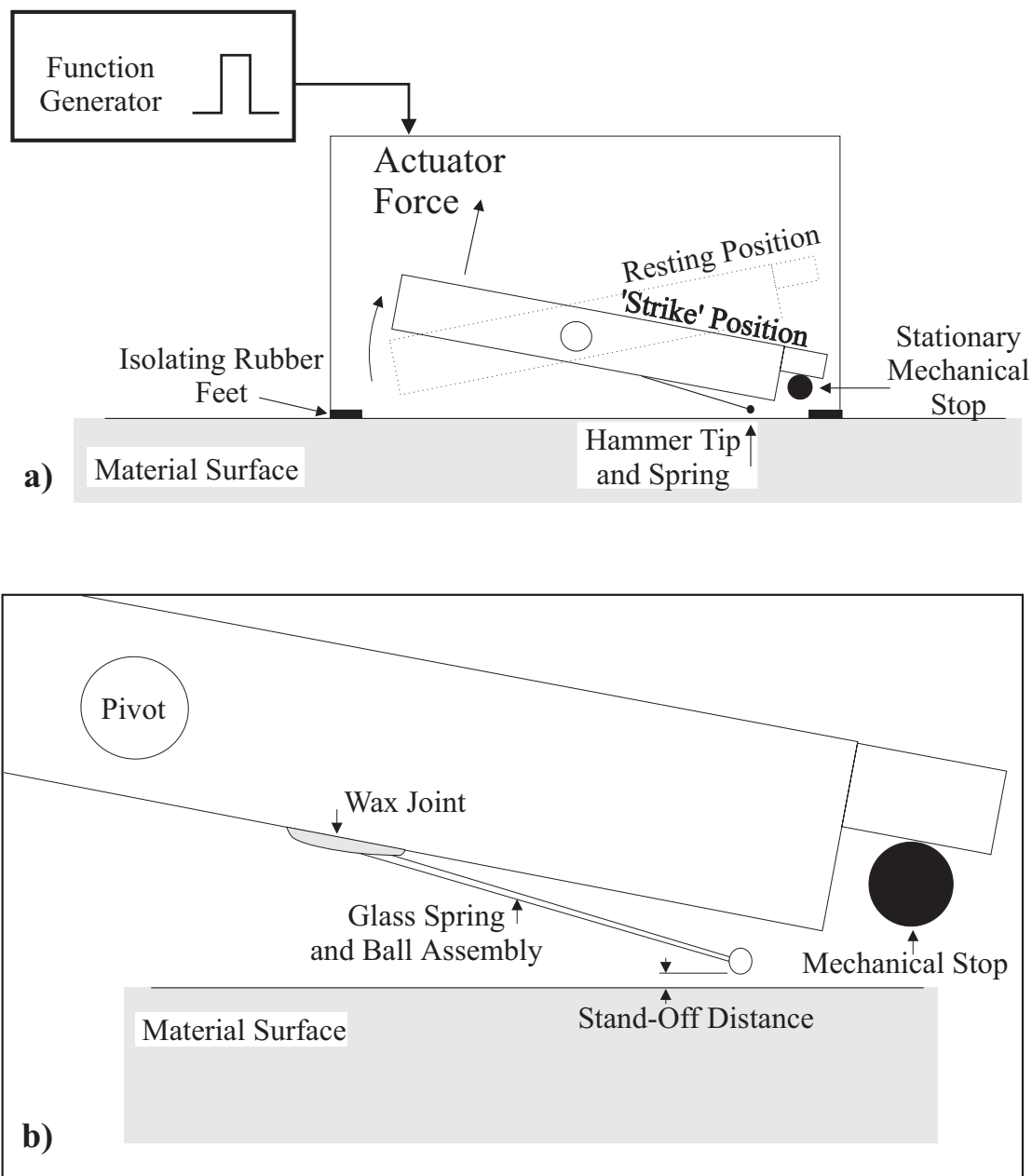
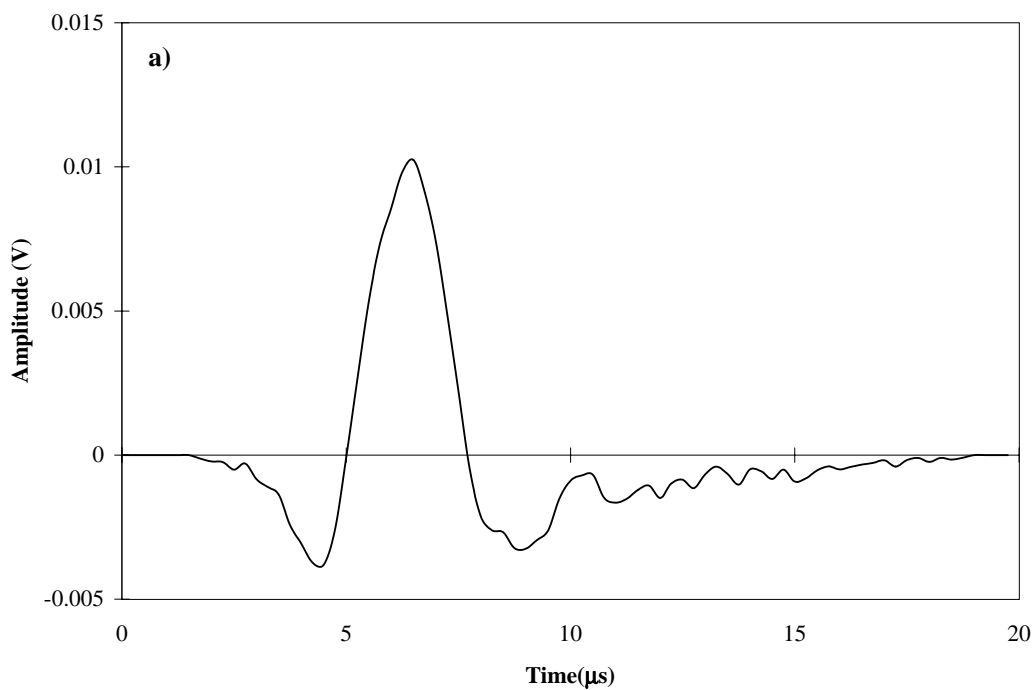


Figure 3.5 a) Schematic diagram of the micro-hammer, b) Detailed view of hammer and spring assembly.



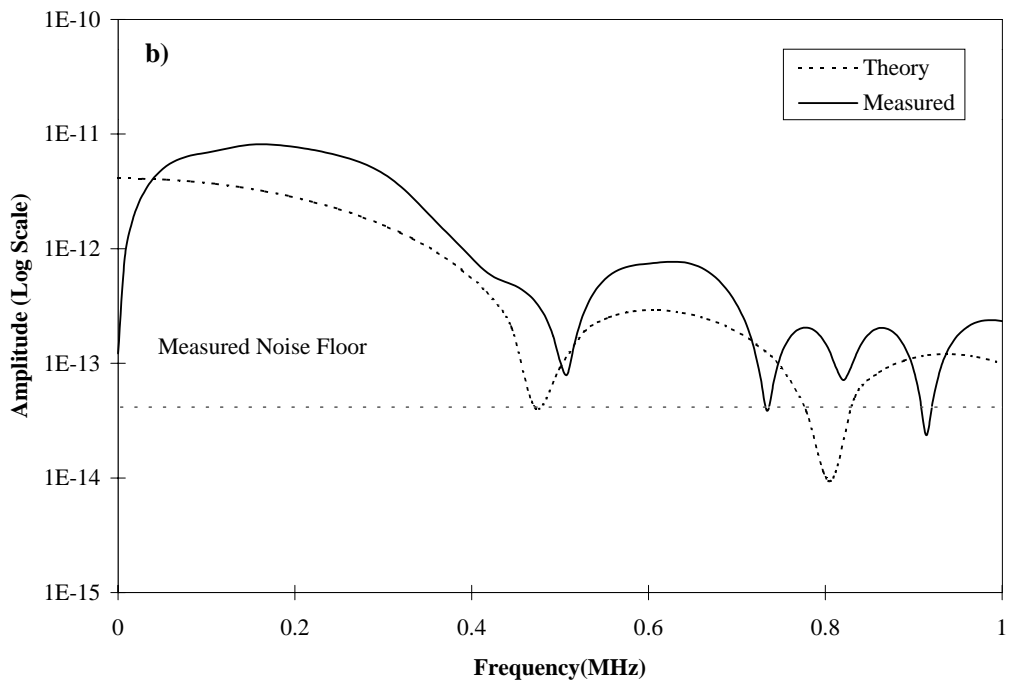
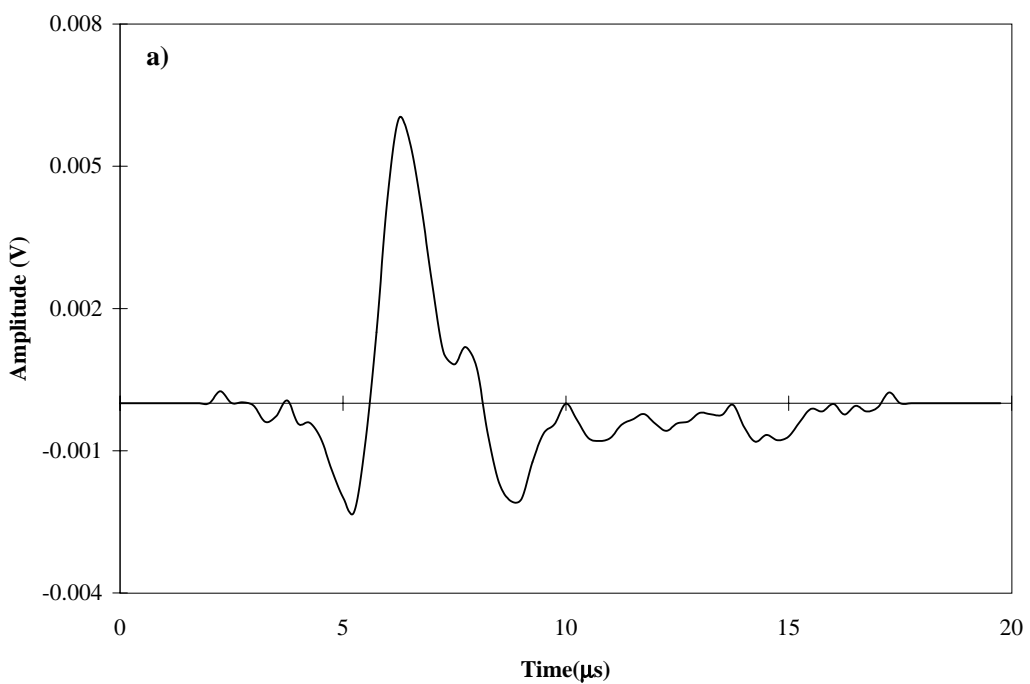


Figure 3.6 a) Time domain first arrival signal measured from the 0.85mm micro-hammer, b) Frequency content of signal shown in a).



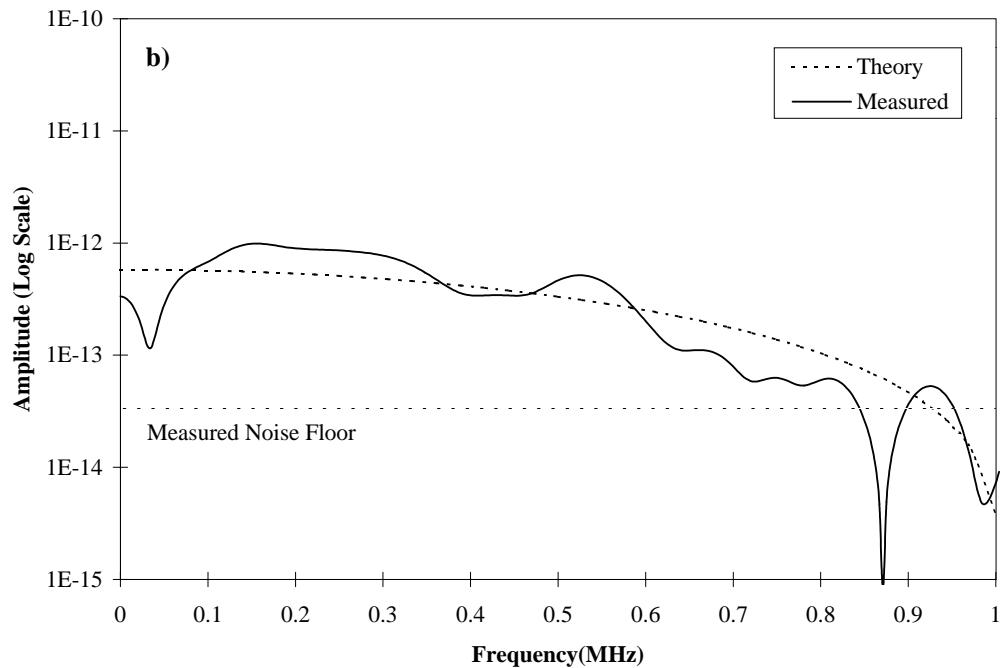


Figure 3.7 a) Time domain first arrival signal measured from the 0.39mm micro-hammer, b). Frequency content of signal shown in a).

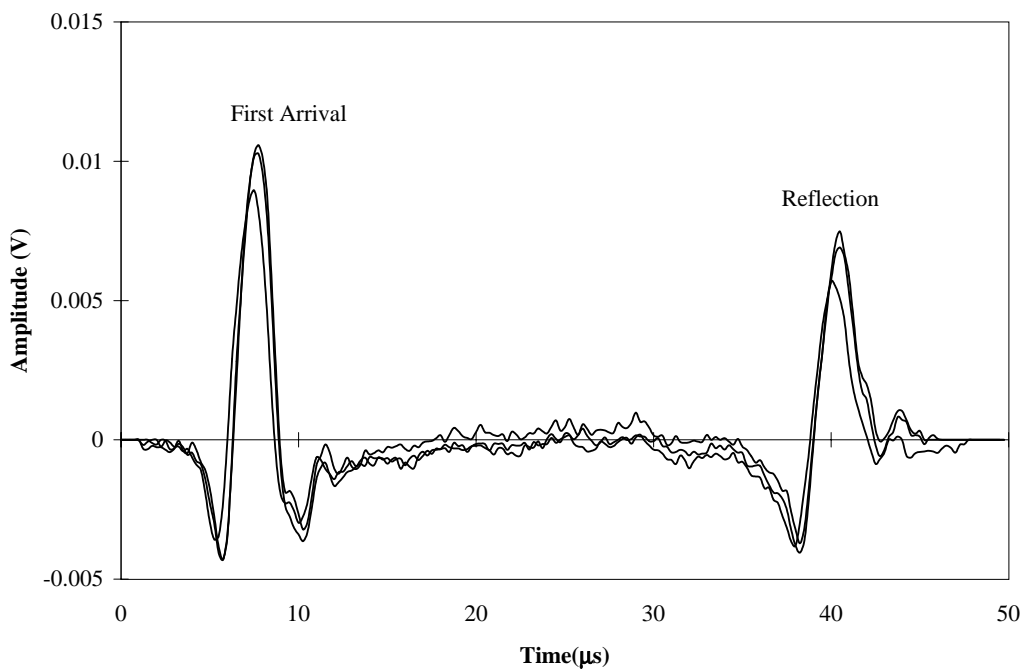
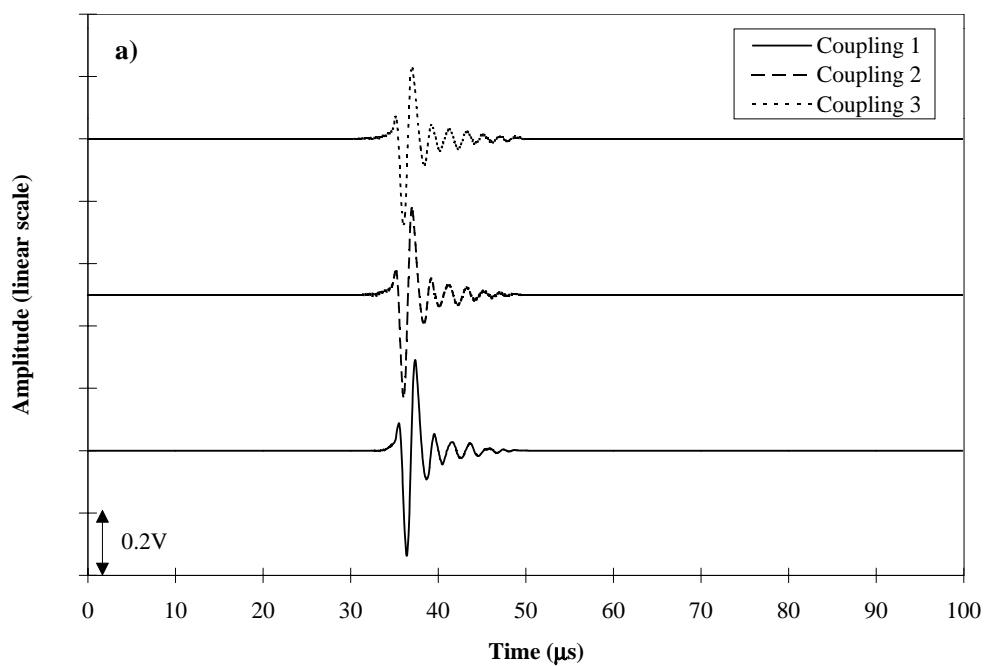


Figure 3.8 Time domain signal measured from three successive impacts of the 0.85mm micro-hammer showing the first arrival and the first edge reflection.



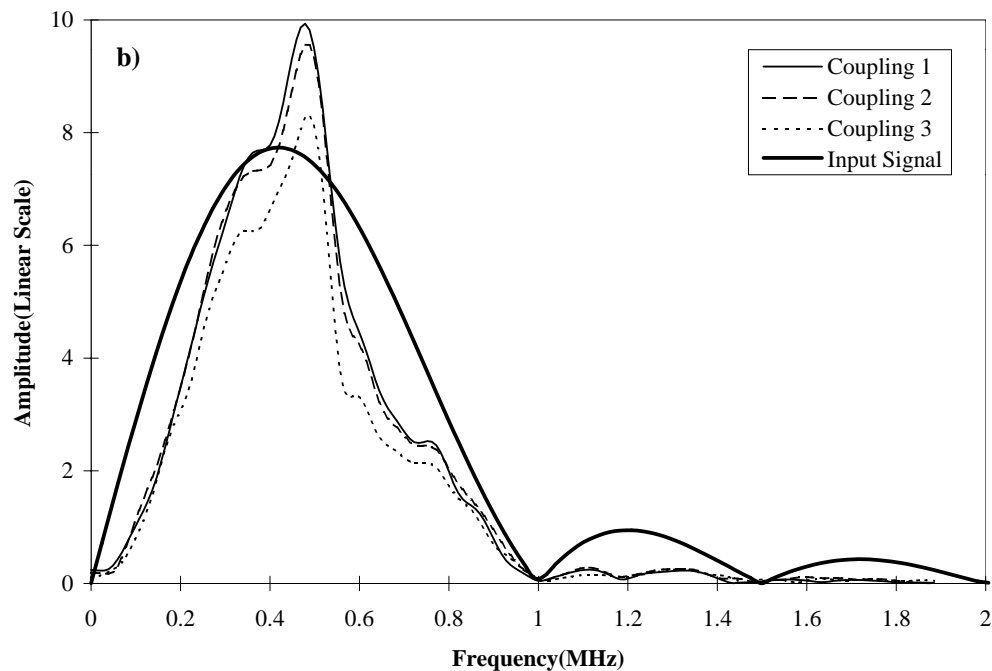


Figure 3.9 a) Time domain signal measured from three successive couplings of the piezoelectric source, b) Frequency content of signal shown in a) with spectrum of input signal sent to source transducer.

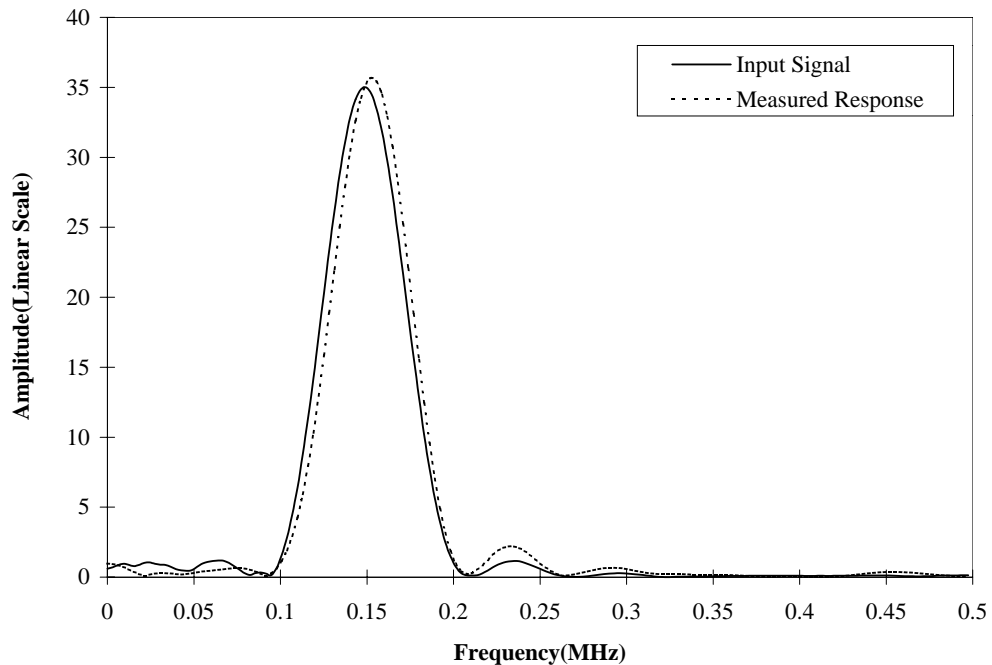


Figure 3.10 Response of the source transducer to a 5 cycle 150kHz Hanning windowed tone burst signal showing the frequency content of the input signal sent to source transducer.



## 4. Calibration and modelling of conical transducers

---

### 4.1 Introduction

#### 4.1.1 Overview of chapter

The manufacture and testing of the conical piezoelectric transducers which have been developed for this project has been discussed in Chapter 2. The transducers are nominally identical in construction, materials and design. Despite this, their acoustic responses (sensitivity and frequency response function) are unlikely to be identical due to slight inconsistencies in geometry, material properties and bond layer thicknesses. The transducers must therefore be individually calibrated, whereby the acoustic response of the transducer is measured at all frequencies within its working range (50kHz to 1MHz).

The first section of this chapter deals with the issue of transducer calibration, starting with a review of two contrasting methods which have been reported in the literature. The primary standard method, which has been selected as the most suitable calibration protocol, is then discussed in detail and the experimental equipment is described. The calibration results are presented at the end of the section along with a discussion of the main findings.

The second section introduces the equivalent circuit modelling method and how this may be adapted for the modelling of conical transducers. The formulation of the model and its main assumptions are discussed and the are compared with the calibration measurements presented in the previous chapter.

Finally a novel technique for the measurement of transducer coupling is described. A working prototype device has been manufactured, based on the conical transducer design, and results are presented which demonstrate the ability of this device to measure the coupling of the transducer to a range of materials.

### 4.2 Transducer calibration

#### 4.2.1 Literature review

In order to calibrate a transducer absolutely, the mechanical input to the transducer must be known or be calculable to a high degree of accuracy. The electrical output

from the transducer can then be compared with the known mechanical input and the absolute frequency response of the transducer/amplifier system calculated. Contact transducers, however, present an additional problem since the transducer and calibration block are directly coupled together. The presence of the transducer will affect the motion of the surface to which it is coupled; the degree to which the motion is affected depends on the material properties (specifically the mechanical impedance) of the calibration block and the transducer itself; this is commonly known as the loading effect. It is for this reason that calibrations of contact transducers are only valid on surfaces with identical material properties to those of the original calibration block. Additionally, the mechanical impedance of the surface is affected by the thickness of the structure, therefore, a transducer calibration measured on a half-space (thick specimen) may not be valid on a thin plate of the same material. There are two possible calibration methods which are reported in the literature and these will now be discussed in detail.

### **Method 1: Primary Standard**

The most intuitive and direct method for transducer calibration is to compare the response of the unknown transducer to that of a primary standard (pre-calibrated transducer) for identical mechanical inputs. The two major difficulties encountered in carrying out this form of calibration are obtaining (or manufacturing) a primary standard transducer and generating a broad band and repeatable source. The transducer calibration method recommended in standard, ASTM E1106 -86, uses a capacitive transducer to measure the surface displacement and a glass capillary fracture source to generate a broad band signal, see Sections 2.1.2 and 3.2 for a description of capacitive transducers and fracture sources respectively. Capacitive transducers are non-contacting, absolute displacement receivers so the loading effect can be ignored and the transducers output can be scaled to represent the actual surface displacement in SI units.

The primary standard transducer and the transducer under calibration are placed equidistant from the source. The first arrival waveform from the source is measured simultaneously by the two transducers and the transfer function of the unknown transducer/material combination can be calculated by taking the signal measured by the unknown transducer and dividing it, in the frequency domain, by the signal

measured by the primary standard transducer. The resulting amplitude spectrum gives the sensitivity of the transducer/amplifier/material combination in volts per metre and the phase spectrum indicates the phase information.

The layout of source and receivers recommended in ASTM E1106 -86 places both the transducers and the source on the same surface of the calibration block and the Rayleigh wave arrival is used for the calibration. In this configuration, however, the aperture of the transducers will affect their apparent frequency response, this effect being governed by the ratio of the wavelength to the transducer diameter, see Section 2.2.3. If both receivers have the same aperture size and shape this effect is cancelled but if not, some correction may need to be applied.

The Primary Standard method has been used by many authors for the calibration of transducers using various absolute displacement transducers and repeatable sources (Dusek, et al. (1990), Breckenridge (1982), Simmons, et al. (1987) and Hsu and Breckenridge (1981)).

### **Method 2: Reciprocity**

Reciprocity calibration methods have been widely used for many years for the calibration of microphones in air and have been successfully applied to AE transducers coupled to a solid (Hanato and Mori (1975), Leschenk (1975) and Hill and Adams (1979)).

In order to carry out a reciprocity calibration three uncalibrated transducers are required. One is used solely as a receiver (R), one a transmitter (T) and the third is used as a transmitter and a receiver (P). This transducer (P) and transmitting media must be reciprocal according to the following,

$$\frac{M(f)}{S(f)} = J(f) \quad (4.1)$$

where  $f$  is the frequency,  $M(f)$  is the free field voltage sensitivity and is defined as the ratio of open circuit receiver voltage to the vertical component of displacement at the receiver,  $S(f)$  is the transmission voltage response which is the ratio of the vertical component of the displacement at the receiver to the input terminal voltage at the transmitter and  $J(f)$  is known as the reciprocity parameter and is a function of the

positioning of the transducers and the material properties of the transfer medium (Hsu and Breckenridge (1981), Hill and Adams (1979)).

The formulation of the reciprocity parameter implicitly assumes that only one propagating mode is present. Expressions for the longitudinal (through transmission) and Rayleigh (same surface) configurations have been calculated by Hill and Adams (1979), these are functions of frequency, transducer spacing and material properties. In a reinterpretation of the reciprocity theorem Hill and Adams (1979) also demonstrated that the reciprocity parameter  $J(f)$  is simply the transfer admittance of the structure which can be expressed as  $J(f)=1/X(f)$  where  $X(f)$  is the transfer function of the medium between the transmission and reception locations. This function can be defined in terms of a number of physical properties (given by Hill and Adams (1979)), the most commonly used being the velocity generated at the receiver location by a given force at the transmitter location. The most significant assumption made during the formulation of the transfer function of the medium is that both source and receiver act on single points on the structure and, whilst this may be valid for small transducers at low frequency, gross errors are expected in the operating range where the wavelength of the propagating mode approaches the transducer diameter. These errors may be minimised by performing the measurements in a through transmission configuration.

Three measurements are necessary for a reciprocity calibration. Each measurement requires two transducers, one transmitter and one receiver which are coupled together through a transfer medium. In each measurement the relative positions of the transmitter and receiver must be the same so that the reciprocity parameter  $J(f)$  is identical. The measurements are as follows,

1. Transducer (T) is used as the transmitter and (R) is used as the receiver. The transmitter is driven with a current ( $I_T$ ) and the received open circuit voltage ( $E_{TR}$ ) is measured.
1. Transducer (T) is used as the transmitter and (P) is used as the receiver. The transmitter is driven with a current ( $I_T$ ) and the received open circuit voltage ( $E_{TP}$ ) is measured.
1. Transducer (P) is used as the transmitter and (R) is used as the receiver. The transmitter is driven with a current ( $I_p$ ) and the received open circuit voltage ( $E_{PR}$ ) is measured.

It can be demonstrated (Hill and Adams (1979)) that the transfer function of transducer (R) is given by,

$$M_R = \sqrt{J \left( \frac{E_{TR} E_{PR}}{E_{TP} I_P} \right)} \quad (4.2)$$

where  $J$  is the reciprocity parameter of the transmitting medium and each term in Equation (4.2) is a function of frequency.

Thus, the transfer function for the receiver may be calculated absolutely provided that the reciprocity parameter can be correctly calculated for the medium used. If simply the frequency response of the transducer is required the only information about  $J(f)$  that is needed is its variation with frequency which is given by,  $J(f) \propto f$  for bulk wave (through transmission) configuration and  $J(f) \propto f^{3/2}$  for Rayleigh (surface) configuration (Hill and Adams (1979)).

The reciprocity calibration method has the obvious attraction that all the basic measurements are electrical and can be made easily to a high degree of accuracy. However, there are several assumptions which must be made in order to make a reciprocity calibration on a solid structure which may cause gross errors in the calibration process. Firstly the calculated transfer function for the structure cannot be independently checked, without, rather ironically, the use of a calibrated receiver (Proctor and Breckenridge (1992) and (Breckenridge, et al. (1975)); additionally the transfer functions can only be calculated for an infinite structure (for example an infinite plate or half-space) and in practice these conditions can only be satisfied by large structures in which any edge reflections can be isolated and electronically gated out of the received signal. Secondly at least one transducer is assumed to behave in a reciprocal manner, meaning that the transmitting and receiving transfer functions of the transducer are identical. The validity of these assumptions will, in general, not be known and consequently a calibration of this type requires an independent verification.

Due to the uncertainties mentioned concerning reciprocity calibration, the primary standard method was selected as the preferable calibration technique for the current work. The calibration experiments were carried out using a Michelson interferometer as the primary standard receiver and a pulsed laser source. These experiments were carried out at the Department of Instrumentation and Analytical Science, University of Manchester Institute of Science and Technology.

#### 4.2.2 *Calibration set-up and specimen preparation*

Calibration was done on two separate occasions separated by a six month period. The initial calibrations were done on an aluminium calibration specimen using transducers WE1, WE2 and WE3. Subsequent calibrations were done on the original aluminium specimen using the three original transducers and four more recently manufactured transducers, WE4 to WE7. Additionally, transducer WE7 was calibrated on a stainless steel specimen and a brass specimen. Calibration of a transducer on different materials was done to assess the effect of the material properties on the sensitivity of the transducers.

The calibration specimens were manufactured for the experiments with dimensions 200mm long, 140mm wide and 38mm thick. The measurement surface of each block was polished on a diamond wheel to produce an optical finish with a flatness which was measured to be within 632.8nm (two interference fringes on a Helium Neon interferometer) over the measurement area of 4cm<sup>2</sup>. This degree of flatness is essential for the use of the Michelson interferometer which requires the reflected light to be coherent. The high reflectivity of such a surface also improves the sensitivity of the instrument. The source and receiver locations were marked on the surface of the block using a Vernier scribe to within 0.1mm; these markings were used subsequently to align the source and the receivers.

Two transducer layouts were used; in the first set of calibrations the source was located on the opposite side of the specimen to the receivers as shown in Figure 4.1a), thus the first arrivals of the through transmitted longitudinal and shear waves were measured at the receiver locations; in the second set of experiments the source and receivers were mounted on the same side of the calibration block as shown in Figure 4.1b) and the Rayleigh (surface) wave arrival was used for the calibration comparison.

The direct path between source and receiver was 55.2mm for the through transmitted waves and 40mm for the Rayleigh waves. The first longitudinal wave arrival is expected at 8.73μs ( $C_L = 6320\text{m/s}$ ), shear wave at 17.6μs ( $C_S = 3130\text{m/s}$ ) and Rayleigh wave at 13.3μs ( $C_R = 3000\text{m/s}$ ) using material properties obtained from Kaye and Laby (1995).

#### 4.2.3 Michelson interferometer as a primary standard

Interferometers are non-contacting receivers and therefore have no mechanical resonances which gives them a flat frequency response function, additionally their output can be easily scaled to SI units (with knowledge of the wavelength of the laser used). The measurement beam is focused onto the surface making the measured area small (normally less than 1mm diameter) which reduces the aperture effect and, being non-contacting, interferometers present no mechanical impedance to the surface and so exhibit no loading effect. An interferometer is therefore an ideal standard transducer for calibration purposes.

Laser interferometers use a beam of monochromatic light reflected from a surface which is vibrating ultrasonically; this beam (the measurement beam) is then recombined with a reference beam from the same light source. The fringes produced by constructive and destructive interference between the beams are used to calculate the surface motion. There are two distinct interferometer types, both of which have been used for AE measurements and transducer calibrations; these are the Heterodyne Interferometer (Jacobs and Woolsey (1993)) in which the frequency shift in the measurement beam caused by the Doppler effect is used to measure the surface velocity and the Michelson interferometer (Dewhurst, et al. (1987) and Moss and Scruby (1988)) in which the phase shift in the measurement beam caused by the change in path length between the interferometer and the surface is used to measure surface displacement.

The layout of the Michelson interferometer used for the calibration experiments is shown in Figure 4.2, after Dewhurst, et al. (1987). Monochromatic, linearly polarised laser light is split into two orthogonally polarised beams which are sent along two paths in the interferometer. One of these is a reference beam known as the reference arm. The second beam, the measurement arm, is directed onto the material surface where it is reflected and returns to the interferometer and recombined with the reference beam. At this stage no interference occurs as the beams are still orthogonally polarised. The combined beam then passes through a second polarising beam splitter with its polarising axis set at  $45^\circ$  which repolarises the beam and splits it into two beams, whose phases differ by  $180^\circ$ . These beams are directed onto the

balanced photodetectors and the resulting voltages are amplified using a differential amplifier to give the final interferometer output signal.

A Michelson interferometer measures the change in phase of the light beam travelling along the measurement arm relative to the reference arm. This phase change is caused by the change in optical path length from the interferometer to the surface of the material under test, the change in optical path length being due to the displacement of the surface. The corresponding phase shift causes interference with the reference beam and from this the absolute displacement of the surface can be calculated. The photodetectors measure the amplitude of the interference signal caused by recombining the reference and measurement beams and convert it into an electrical signal. This amplitude is given by

$$V = \bar{V} + V_0 \sin\left(\frac{4\pi x}{\lambda}\right) \quad (4.3)$$

where  $V$  is the output voltage,  $\bar{V}$  is the DC offset (if present),  $V_0$  is the amplitude of the interference signal (the fringe amplitude),  $\lambda$  is the wavelength of the laser light and  $x$  is the surface displacement. The interference signal therefore goes through one complete cycle for a path length change of  $\lambda/2$  (316.4nm for a Helium Neon laser). The range of displacements of interest for ultrasonic measurements is generally below 10nm and within this range the sinusoidal function of Equation (4.3) may be approximated by a linear function and, assuming the DC offset  $\bar{V}$  is zero, the resulting interferometer sensitivity is given by,

$$x(t) = \frac{\lambda}{4\pi V_0} V(t) \quad (4.4)$$

where  $x(t)$  is the surface displacement,  $V(t)$  is the interference signal,  $\lambda$  is the wavelength of the laser light and  $V_0$  is the fringe amplitude. The fringe amplitude (FA) is the amplitude at which saturation of the interferometer occurs; this corresponds to a path length change of  $\lambda/2$  (surface displacement of  $\lambda/4$ ). The FA can be measured easily by saturating the interferometer with a large amplitude surface displacement and capturing the signal on an oscilloscope. Once the FA is known for a particular configuration the absolute surface displacement can be calculated using Equation (4.4).

Unwanted low frequency vibration is always present in the environment and the displacements caused by these vibrations being orders of magnitude greater than the ultrasonic displacements of interest. These displacements will therefore saturate the interferometer if they are not removed. This problem can be overcome by compensation, the reflecting mirror used to return the reference beam is mounted on a moving coil, see Figure 4.2, which is driven by the differential output obtained from the balanced photodetectors (this method is known as path stabilisation). The mirror system used has a maximum response of 10kHz and so compensated for the low frequency vibrations, keeping the interferometer balanced without affecting the signals at ultrasonic frequencies.

Several studies have been undertaken using interferometers for calibration of more standard transducers (Grabec and Platte (1984), Moss and Scruby (1988), Djelouah, et al. (1989), Dewhurst, et al. (1987) and Jacobs and Woolsey (1993)) and for direct measurement of AE signals (Palmer and Green (1977)).

The major disadvantage of interferometers, as compared to more standard contact methods, is one of sensitivity. Displacements down to  $2.5 \times 10^{-11}$ m have been measured using a Michelson interferometer (Dewhurst, et al. (1987)) with a bandwidth of 50MHz, although the theoretical limit has been shown to be in the order of  $1 \times 10^{-15}$ m for a mirror surface (Boltz, et al. (1995)). Contacting piezoelectric transducers have been shown to have a theoretical sensitivity limit of around  $1 \times 10^{-17}$ m and measurements of displacements down to  $3 \times 10^{-17}$ m have been reported by Boltz, et al. (1995). The requirement for the measurement surface to be polished to a mirror finish also restricts the application of Michelson interferometers to laboratory work.

#### **4.2.4 Laser source**

The ultrasonic source used for the calibration experiments was a Q-switched Nd:YAG laser which is a high power pulsed laser. The laser has an optical wavelength of  $1.06\mu\text{m}$  with a pulse duration which was measured to be 30ns, thus the frequency content of the ultrasonic signal generated has a bandwidth of more than 20MHz (Scruby and Drain (1990)). The energy output of the laser was measured to be 215mJ and the laser beam was focused onto the surface such that the illuminated area was  $1\text{mm}^2$ . The power generated was therefore 7.2MW and the power density on the material surface was greater than  $7.2\text{MW/mm}^2$ . This laser power density is sufficient

to cause appreciable vaporisation of the material, plasma generation and permanent damage to the surface; this is known as ablation (Scruby and Drain (1990)).

#### 4.2.5 *Signal processing*

The signals from the interferometer and piezoelectric transducer were sampled simultaneously at 10MHz using a digital storage oscilloscope. The conical transducer signal was first amplified with a 60dB preamplifier and high-pass filtered at 10kHz prior to sampling. Signal to noise ratios for the interferometer measurements were found to be a factor of 100 lower than the corresponding measurements made using the piezoelectric transducer. The signal to noise ratio can be improved by averaging of the time domain signal over successive tests but this was not done as small changes in trigger stability or source amplitude can result in a loss of bandwidth and inaccurate peak amplitude measurements which would adversely affect the accuracy of the calibrations. The frequency response of the conical transducer was found by dividing the signal measured by the conical transducer by the actual displacement of the surface as measured by the interferometer. The Fourier transform of the signals was first taken and the division was done in the frequency domain.

**Through transmission configuration:** The raw time domain signals measured simultaneously by the interferometer and the conical transducer in the through transmission configuration on aluminium are shown in Figure 4.3. The longitudinal and shear arrivals are marked and their arrival times correspond well to those predicted in Section 4.2.2. In order to perform the calibration the time domain signal must contain the first arrival signal from one mode only. Multiple modes or multiple reflections of the same mode will cause interference (constructive and destructive) in the frequency domain. The resulting spectrum will have sharp discontinuities associated with these multiple arrivals and the precise shape and position of these discontinuities will be affected strongly by the position of the transducers and the block dimensions. Gating out these multiple arrivals therefore improves the repeatability of the calibration.

The shear wave amplitude in Figure 4.3 can be seen to be larger than that of the longitudinal wave; this is due to the directivity of the ablative source (Scruby and Drain (1990)). The shear wave field caused by an ablative source has a maximum at 50° to the material surface whereas the longitudinal wave field has a maximum at 90°.

In the through transmission configuration, shown in Figure 4.1a), the receivers are aligned at  $47^\circ$  to the material surface which is close to the ideal location for the reception of the shear arrival.

Consequently the shear wave arrival was used for the calibration process by windowing this portion of the signal and chopping the remainder. Windowing the signal affects its frequency content and it is important to quantify this effect to ensure that the resulting calibration is still valid. Several window functions were examined and compared to find which gave the most consistent results. The results indicated that any colouration of the frequency content of the individual interferometer and conical transducer signals was greatly reduced when the signals were divided to perform the calibration, the effect of the window function being effectively cancelled out. It is worth emphasising at this point that for this to be true the windowing must be done in a very consistent manner.

The window chosen was rectangular and was placed over the shear wave arrival from  $1\mu\text{s}$  before the maximum positive peak with a duration of  $5\mu\text{s}$ . Figure 4.4 shows the effect of the window on the signals shown in Figure 4.3. Figure 4.5 shows a comparison of the calibration curve generated by using the frequency content of the entire time domain traces shown in Figure 4.3 and the windowed traces; this demonstrates that the windowing smoothes the calibration curves without significantly changing their frequency content. A rectangular window was chosen for two reasons, firstly it is the simplest and comparisons showed that other, more complicated functions such as Hanning or Gaussian windows provided no measurable advantages for this application and secondly a rectangular window does not distort the signal amplitude.

**Rayleigh wave configuration:** Figure 4.6 shows the raw, time domain signals measured simultaneously by the interferometer and the conical transducer in the Rayleigh wave configuration on aluminium. The longitudinal and Rayleigh wave arrivals are marked and the arrival times agree well with the predicted values. In the surface wave configuration the first arrival of the Rayleigh wave was used for the calibration process. A rectangular window was used, as before, to isolate the relevant section of the trace as shown in Figure 4.7 and was placed over the Rayleigh wave arrival from  $4\mu\text{s}$  before the maximum positive peak with a duration of  $8\mu\text{s}$ . Division

of the piezoelectric transducer output by that of the interferometer, in the frequency domain, again yields the calibration curve for the transducer.

#### 4.2.6 Results

In order to ascertain the repeatability of the calibration results the calibration process was repeated several times using each transducer. As coupling has been highlighted as the main source of variability between measurements using contacting transducers the transducer was completely removed from the surface, cleaned and re-coupled at the same location before each calibration. Figure 4.8 shows three calibration curves measured for transducer WE1 after three successive couplings; the thicker line is the average of the three couplings shown. Some variability in transducer response between the couplings can be seen, between 0 and 1MHz this variability is within  $\pm 7.6\%$  and between 1 and 1.5MHz it is within  $\pm 18\%$ . The measured coupling variation of  $\pm 7.6\%$  in the sub 1MHz region is consistent with further measurements which are presented in Section 6.3.2, where coupling variations of  $\pm 6\%$  were measured over a large number of measurements. Variations in transducer response due to coupling are caused by changes in the geometry of the contact region between the transducer and the surface. These geometrical changes can be caused by contaminants between the transducer and the surface, rough surfaces, curved surfaces, or simply misalignment of the transducer. The measured increase in the effect of coupling variation with frequency (as demonstrated in Figure 4.8) is consistent with the theory of coupling variations being caused by geometrical changes at the interface. Increasing frequency causes the wavelength to reduce, thus increasing the sensitivity of the resulting waves to small geometric discontinuities.

Figure 4.9 shows a comparison of the calibration curves obtained for the conical transducers WE1, WE2 and WE3 obtained using the through transmission configuration. The transducer responses can be seen to be not identical but generally similar having slight resonances at around 0.5 and 1MHz. Additionally these three transducers were re-calibrated using the Rayleigh wave configuration which enabled the calibration curves measured using both configurations to be directly compared, for example Figure 4.10 shows the calibration curves measured for transducer WE1 using the through transmission and Rayleigh wave configurations. The calibrations curves measured using the two configurations show good agreement below 1MHz having

comparable amplitude and structure. However, as demonstrated in Figure 4.10 at frequencies above 1MHz the agreement was found to be poor (similar results were found for all three transducers), the surface wave calibrations indicating a significantly higher transducer sensitivity within this frequency range. This inconsistency is due to a change of the pre-amplifier settings between the two calibrations. The initial, through transmission, calibrations were carried out using a bandwidth which was limited to 1MHz using a low-pass filter. The effect of this filter was to reduce the conical transducer output signal above 1MHz which accounts for the apparent change in high frequency response. Further experiments on a variety of structures have shown that the effective working range of the transducers is up to 1MHz, due to aperture effects, and consequently this error is not critical.

Comparing the Rayleigh wave calibrations measured for transducers WE1 to WE7 shows a large range of sensitivities which differ in amplitude by as much as a factor of 4, see Figure 4.11. Given that the transducers were manufactured to the same design using identical materials the difference in response between transducers is, in all probability, due to slight inconsistencies in the assembly of the transducer components. The thickness of the bond layer between the piezoelectric element and the backing being the most critical parameter in terms of transducer response (Silk (1984)).

It should also be noted that the measured response of transducer WE7 has a very different shape than that of the other transducers. The sensitivity at low frequency is relatively high with an unusually high resonant peak at 0.25MHz then dropping rapidly, almost to zero, at 1.3MHz. Although the materials and assembly procedure used to manufacture transducer WE7 were identical the backing has subsequently been modified by the insertion of an additional transducer (as described in Section 4.4). Clearly this minor modification has affected the response of this transducer over the entire frequency range.

With reference to Figure 4.11, transducers WE2, WE4 and WE5 have been measured to have very similar calibration curves and are also consistently the most sensitive of the transducers within the 1MHz operating range (neglecting a peak in the WE7 calibration curve at 0.25MHz). The response demonstrated by these transducers is

likely to be the best attainable using the current design, materials and manufacturing methods.

## 4.3 Modelling of conical piezoelectric transducers

### 4.3.1 Introduction

The modelling of piezoelectric transducers is necessary in order to predict the effect of changes in geometry and materials on the transducer performance. There are two distinct sides to the problem, the mechanical response and the electrical response. The piezoelectric element couples between these two sets of properties making it necessary to model both effects simultaneously for an accurate prediction to be made. The standard modelling technique is to represent the mechanical and electrical properties as an equivalent circuit (Silk (1984) and Auld (1990)). The piezoelectric element is modelled as a three port network, shown in Figure 4.12a) and b) for a shear element. Ports one and two represent the back and front faces of the piezoelectric element respectively, the shear force and velocity of each face being represented by a voltage and a current respectively. Port three represents the electrodes of the piezoelectric element and is therefore representative of the electrical response of the system. The equivalent circuit connecting these three ports is commonly represented using the Mason model (Mason and Thurston (1972)), alternatives are the KLM model and the Redwood models (all three are discussed in detail in Kino (1987)). In this thesis, a brief discussion of the Mason model will be given as this is most relevant to the conical transducer model which will be introduced in the next section.

The Mason equivalent circuit for a shear wave transducer is shown in Figure 4.13 (using the nomenclature of Auld (1990)), where  $\bar{Z}_0$  is the stiffened mechanical impedance of the piezoelectric element and is given by,

$$\bar{Z}_0 = A\sqrt{\rho c_{44}} \quad (4.5)$$

$N$  is given by,

$$N = C_0 h_{x5} \quad (4.6)$$

where  $C_0$  is the clamped capacitance of the piezoelectric element and is calculated using,

$$C_0 = \varepsilon_{xx}^S \frac{A}{d} \quad (4.7)$$

and  $k$  is given by,

$$k = \omega \sqrt{\frac{\rho}{c_{44}}} \quad (4.8)$$

where  $A$  and  $d$  are the area and thickness of the piezoelectric layer respectively and  $\omega$  is the frequency. The remaining variables are material properties of the piezoelectric material as follows:  $\rho$  is the density,  $c_{44}$  is the stiffened Young's modulus (with piezoelectric effect included),  $h_{x5}$  is piezoelectric coefficient and  $\varepsilon_{xx}^S$  is the permittivity.

The effect of backing and fronting layers may be added to the model easily by calculating their equivalent electrical impedance and applying it to the relevant terminals of the circuit as indicated in Figure 4.13. Thus, with knowledge of the geometry and material properties of all the elements, a model of the transducer can be made.

The resulting equivalent circuit can be described in terms of an electromechanical impedance matrix  $Z_T$  which relates the electrical and mechanical variables of the system as follows,

$$\begin{bmatrix} F_1 \\ F_2 \\ V_3 \end{bmatrix} = \begin{bmatrix} Z_{11} & Z_{12} & Z_{13} \\ Z_{21} & Z_{22} & Z_{23} \\ Z_{31} & Z_{32} & Z_{33} \end{bmatrix} \begin{bmatrix} v_1 \\ v_2 \\ I_3 \end{bmatrix} \quad (4.9)$$

where  $F$  denotes force,  $V$  denotes voltage,  $v$  denotes velocity,  $I$  denotes current and the subscript indicates the port of interest (as previously defined in Figure 4.13). The individual impedance terms are calculated using simple circuit theory.

#### 4.3.2 The Greenspan model for conical transducers

Conventional transducer models, such as those described in the previous section, are only applicable to one-dimensional systems, for thin disk transducers this assumption is valid as the dominant mechanical resonances are through-thickness and the edge effects are minimal. These models are however inadequate for the modelling of conical transducers as the conical shape of the element encourages edge effects and

consequently multiple modes will always be present. The one-dimensional model has been extended by Greenspan (1987), using an asymmetric version of the standard Mason circuit in an attempt to predict the response of conical transducers. The asymmetry in the circuit components is necessary to account for the change of area (and therefore impedance) along the axis of the element. Additionally a correction has been applied to the wave velocity as the speed of sound varies along the length of the cone and the conical shape forces the wave fronts to be spherical. For simplicity the back and front media have been modelled as infinite in extent, thus only the response of the conical element is calculated. The impedances of the front and back half-spaces have been calculated for a finite spherical aperture using equations based on the work of Miller and Pursey (1954). The conical model therefore predicts the transducer receiving response (Voltage output versus displacement at the front face) as,

$$F(\omega) = \frac{z_1 \left\{ z_2 + i \left[ (1/r) \csc kl + (r-1)/rkl - \cot kl \right] \right\}}{1 + z_1 z_2 + \frac{(r-1)^2}{r(kl)^2} - \left[ \frac{(r-1)^2}{rkl} \right] \cot kl + i \left\{ z_1 \left[ \frac{(r-l)}{rkl} - \cot kl \right] - z_2 \left[ \frac{(r-l)}{kl} + \cot kl \right] \right\}} \quad (4.10)$$

where  $z_1$  and  $z_2$  are the acoustic impedances of the front and back materials normalised to the acoustic impedance of the piezoelectric material,  $r$  is the ratio of the cone back radius to the front radius,  $k$  is the wavenumber in the cone which is given by  $k = \omega/c$ ,  $c$  is the velocity of sound in the cone and  $l$  is the length of the cone (Greenspan (1987)).

Despite the many approximations and simplifications which have been made in the formulation of this model the predictions obtained have shown reasonable agreement with measured responses of conical transducers and have been used to predict the behaviour of these transducers on a variety of materials (Breckenridge, et al. (1984)).

#### 4.3.3 Results and comparisons with calibration curves

A comparison has been made between the predictions made using Equation (4.10) and the actual transducer response measured using the calibration procedure described in Section 4.2 for calibrations carried out on an aluminium half-space. The predicted response of this system is given in Figure 4.14 along with the measured response of

transducer WE4 where the predicted response has been scaled arbitrarily (the comparison has been made with the response of transducer WE4 as this transducer is one of those found to exhibit the best performance). The transducer model is seen to predict the general shape of the response, specifically the resonances at around 0.5MHz and 0.9MHz. A similar level of agreement was achieved by Greenspan (1987) using a brass backed transducer on steel, see Figure 4.15, where the geometries of the transducer elements used are shown in Table 4.1,

	a)	b)	c)	d)
Small end diameter(mm)	0.62	0.65	0.83	0.58
Large end diameter(mm)	1.74	3.91	6.85	10.05
Length(mm)	1.24	2.60	5.9	12.7

Table 4.1 Conical element dimensions used by Greenspan (1987).

The theoretical curves shown in Figure 4.15 have been arbitrarily scaled to best fit the experimental data. Whilst none of the transducer geometries shown in Table 4.1 match the transducers used for the current work, transducer b) gives the most similar response to that predicted for the current transducers shown in Figure 4.14 probably due to the similarity in cone length.

The measured transducer response given in Figure 4.14 shows a consistent loss in transducer sensitivity with frequency, this is consistent for all of the transducer responses shown in Figure 4.11. The model, however, predicts no such high frequency roll-off in sensitivity. Greenspan (1987) measured an identical high frequency roll-off, as demonstrated in Figure 4.15, and attributed this to losses in the piezoelectric material.

#### 4.3.4 The effect of fronting material properties

A comparison of the predicted response of the transducers on aluminium, brass and stainless steel is given in Figure 4.16 for a tungsten/epoxy backed transducer. The predictions show that the sensitivity of the transducer increases with the acoustic impedance of the front material ( $Z_{al}=16\text{MRayls}$ ,  $Z_{br}=37\text{MRayls}$  and  $Z_{st}=47\text{MRayls}$ ), a similar effect has previously been noted by Breckenridge, et al. (1984). The resonant frequencies of the transducer are also predicted to increase as demonstrated in Figure 4.16 for the first resonant peak. This shift is extremely small, only 15kHz (3%)

between the aluminium and steel cases, but has been found to be consistent across all the predictions made. Conceptually this can be thought of as a stiffening of the transducer assembly, the increase in acoustic impedance of the front material increasing the mechanical impedance applied to the front face of the transducer. This effectively stiffens the transducers assembly, causing an increase in the natural frequency.

Figure 4.17 shows the measured response of transducer WE7 on steel, brass and aluminium and demonstrates that, as predicted, the transducer sensitivity varies dramatically between these three cases. Steel gives the highest transducer response with aluminium at around half the amplitude; the response curve for these two cases are similar in shape and differ only in amplitude. A difference in sensitivity of a factor of two between the aluminium and steel cases agrees well with the theoretical prediction shown in Figure 4.16 and with previous work in this area (Breckenridge, et al. (1984)). Additionally, the improved low frequency response measured on steel as compared to aluminium, although not predicted by the theoretical results, is consistent with experiments reported by Breckenridge, et al. (1984) and the increase in the frequency of the resonant peak at around 0.3MHz is clear.

The transducer sensitivity measured on brass, however, is not consistent with the theoretical predictions (see again Figure 4.16 and Figure 4.17). The shape of the response curve has completely changed and the sensitivity is generally lower than that measured on aluminium. The reason for this deviation from the predicted response is not known although it may be due to the significantly lower velocity of sound in brass as compared to aluminium and steel (in brass  $c_{\text{Raleigh}}=2000\text{m/s}$  whereas in steel and aluminium  $c_{\text{Rayleigh}}=3000\text{m/s}$ ). Thus the wavelength in brass is 67% that of the wavelength in steel or aluminium; at 1MHz this corresponds to a wavelength of 2mm as compared to 3mm in steel and aluminium. The diameter of the transducer face is 1mm and consequently if any aperture effects were present in the calibration protocol, these would be more apparent for the calibration measured on brass. Additionally the calibration measurements made using the brass block were made more difficult by the lower reflectivity of the polished brass surface which reduced the reflected light used by the interferometer. The corresponding interferometer signals were lower and the signal to noise ratio was reduced by a factor of two.

In summary, the response of the conical transducers have been shown to vary dramatically with the properties of the front material (specifically acoustic impedance). This variation is consistent with the theoretical predictions for the steel and aluminium cases showing both an increase in sensitivity and resonant frequency with acoustic impedance. The measured and predicted frequency shift is extremely small but a practical use for this phenomenon has been found for the measurement of transducer coupling, as described in the next section.

## 4.4 Auto-normalising ultrasonic transducer

### 4.4.1 *Introduction*

The variability of transducer coupling is a well known shortcoming of ultrasonic inspection and acoustic emission measurements using direct coupled (contact) transducers. Absolute comparisons of measurements made on structures cannot be made without a large degree of uncertainty. With care and well mating surfaces the coupling variations can be kept to within  $\pm 10\%$  (see Section 4.2.6), however in practical situations, where rough and curved surfaces will inevitably be inspected, far higher variations in coupling efficiency can be expected.

This section describes a novel method which allows the transducer coupling efficiency to be measured independently. This method may represent a solution to the problem of variable coupling for general ultrasonic and acoustic emission measurements.

### 4.4.2 *Design and manufacture*

The auto-normalising transducer is based on the conical transducer design which has been used throughout this project with some slight modifications, the auto-normalising transducer being referred to up to now as transducer WE7. The conical element of PZT has a front face diameter of 1mm, back face diameter of 10mm and a length of 3mm, as do all the conical transducers manufactured for this project. A cylinder of tungsten loaded epoxy was again used as the backing material with a diameter of 19mm and a length of 28mm, see Figure 4.18. Additionally a commercial broad band transducer (Valpey-Fisher VP-1093 Pinducer) was permanently bonded into the tungsten/epoxy backing at a distance of 15mm from the back face of the conical element.

The pinducer itself consists of a 2mm diameter piezoelectric disk element mounted on the end of a 33mm long brass barrel. The small element dimensions give the pinducer a wide operating range which is quoted by the manufacturer to be from DC up to 10MHz (40dB down points). The brass backing, although well acoustically matched to the PZT element, has very low attenuation and the typical response of a pinducer shows some ringing within the brass backing. In the current application the first arrival waveform measured by the pinducer is of interest and therefore the ringing is of little consequence.

#### **4.4.3 Methodology and testing**

The auto-normalising transducer unit therefore has two independent piezoelectric elements, the intention being to use the conical element as an ultrasonic point source and the pinducer as a passive receiver. Driving the conical element with an electrical impulse (or function) generates ultrasonic waves in both the surface to which it is coupled and the backing, as indicated in Figure 4.18. The corresponding signal received by the pinducer shall be termed the backing signal. This signal is rather complex, consisting of several arrivals corresponding to multiple reflections within the backing and ringing within the pinducer; a representative backing signal is given in Figure 4.19.

The back face of the conical element, the backing material and the pinducer are permanently bonded together making the path length and coupling between the piezoelectric elements constant. Variation in the amplitude or frequency content of the backing signal (for a fixed excitation waveform) can only be caused by modifications in the response of the conical element due to changes in the boundary conditions present at the front face. Such modifications have been predicted and measured in the previous section due to changes of the impedance of the fronting material (refer to Figure 4.16 and Figure 4.17) and similar effects are expected due to changes in coupling between the conical element and the fronting material.

It is important to emphasise that the results and predictions presented in Figure 4.16 and Figure 4.17 are not entirely applicable to the backing signal. The predictions and calibration results give the electrical response of the transducer for a given mechanical displacement of the front face. The change in sensitivity of the transducers with fronting material impedance indicates that, according to reciprocity,

the transducer will be twice as efficient at generating ultrasonic waves in steel as in aluminium. It is not correct to assume that the backing signal will increase in the same proportions; however, the predicted and measured shift in resonant frequency of the transducer is a global transducer property and therefore should manifest itself in the waves travelling into the fronting and backing materials.

An experimental protocol was designed to test the auto-normalising transducer to ascertain whether coupling efficiency could be measured using the backing signal, Figure 4.20 shows the experimental equipment. A signal generator was used to excite the conical element with a five cycle, Hanning windowed tone-burst with an amplitude of 200Vpkpk. The backing signal, measured by the pinducer, was amplified using a 40dB preamplifier and sampled at 10MHz using a digital storage oscilloscope. An additional conical transducer was permanently bonded to the structure with cyanoacrylate adhesive, and used as a reference transducer to measure the displacement at a remote location on the surface. The signal from the reference transducer (subsequently referred to as the reference signal) was also amplified using a 40dB preamplifier and sampled simultaneously by the oscilloscope.

The amplitude of the first arrival of the reference signal was used to indicate the coupling efficiency  $\eta_c$ ; for this to be valid the distance from source to receiver must remain constant and the electrical input signal to the source be unchanged. The peak-to-peak amplitude of the reference signal will vary from zero (corresponding to no coupling) to a maximum  $V_{\max}$  (corresponding to 100% coupling). The value of  $V_{\max}$  depends on the input voltage to the source, the material properties of the surface, the mode shape of the transmitted wave, the distance between the source and the receiver and the sensitivity of the receiver/amplifier system. Nevertheless, measuring the value of  $V_{\max}$  for a given arrangement of transducers is simply a case of altering the coupling of the source systematically until an absolute maximum signal is attained. The percentage coupling efficiency is then given by,

$$\eta_c = 100 \times \frac{V_{\text{Ref}}}{V_{\text{Max}}} \quad (4.11)$$

where  $V_{\text{Ref}}$  is the measured reference signal.

#### 4.4.4 Results

Initial experiments were carried out on a variety of materials using an excitation frequency of 140kHz. The stainless steel, brass and aluminium blocks used for the calibration experiments were used to simulate half-spaces and a 5mm thick aluminium plate was used to assess the effect of material thickness. The results obtained are shown in Figure 4.21 where the amplitude of the backing signal is plotted against the measured coupling efficiency, calculated using Equation (4.11) and the solid lines are linear least squares fits to the experimental data. The backing amplitude was measured according to the definitions shown in Figure 4.19. A good fit is obtained in each case which demonstrates the linear relationship between backing voltage and coupling efficiency. This linear relationship is most evident at coupling efficiencies above 35%; below this value the backing amplitude tends rapidly towards the 0% coupled case. Coupling efficiencies of less than 35% were difficult to achieve, requiring deliberate tilting and lifting of the transducer. It is concluded that these coupling efficiencies are unlikely to occur accidentally, making this loss of correlation unimportant.

In all cases, the backing signal drops with coupling efficiency with a minimum occurring at 100% coupling which shall be termed  $V_{100\%}$ . Clearly, the backing amplitude at no coupling,  $V_{0\%}$  is the same for all cases, but the value of  $V_{100\%}$  is material dependent. The minimum  $V_{100\%}$  is measured for steel (with aluminium having the highest and brass in between); this indicates that the acoustic impedance of the material is the controlling factor, the higher impedance materials having lower  $V_{100\%}$ . Comparing the results obtained for the aluminium half-space and the 5mm thick plate shows excellent correlation, demonstrating that the mechanical impedance of a 5mm plate is very similar to that of a half-space.

An additional experiment was carried out on the steel block with an excitation frequency of 850kHz, and the results are shown in Figure 4.22. The effect of increasing the coupling efficiency of the transducer now has the opposite effect on the backing signal, although the magnitude of this change in backing amplitude is much smaller than that previously measured at 140kHz (note relative scales on Figure 4.21 and Figure 4.22). The reversal in the relationship between backing voltage and coupling efficiency has also been measured for aluminium and brass but the change in

backing amplitude was so small it was difficult to measure using the current experimental set-up.

The variation in backing signal amplitude with coupling efficiency can be explained with reference to Figure 4.23. The increase in natural frequency associated with a increase of impedance of the front face material, as predicted and measured in Section 4.3.3, is thought to be the controlling factor. The excitation signal used to drive the auto-normalising transducer was a 5 cycle tone burst having a limited bandwidth, these bandwidths are indicated in Figure 4.23 by region a) representing the below resonance case (see Figure 4.21) and b) representing the above resonance case (see Figure 4.22). The effect of a slight increase in the natural frequency is to decrease the response of the transducer within region a) and increase the response in region b). This would explain the reversal in the effect of coupling efficiency on backing voltage as the resonant frequency of the conical element moves either towards or away from the excitation band with coupling.

An additional experiment was carried out on the steel block. The excitation signal used was a single cycle tone burst at 450kHz, having energy over a broad bandwidth from 50kHz to above 1MHz. The backing signal was recorded and the first arrival pulse windowed to remove all multiple reflections in the backing or pinducer ringing. The resulting time trace was Fourier transformed and the resulting spectra are given in Figure 4.24 for coupling efficiencies of 0%, 50% and 100%. The frequency shift caused by the coupling can be clearly seen showing a decrease in response with coupling efficiency below 0.5MHz and an increase above 0.5MHz. At the extremities of the frequency spectra shown in Figure 4.24 the correlation is not totally consistent with this theory but the general trend is clear. It is interesting to note that according to Figure 4.24 the most sensitive regions for backing amplitude change with coupling efficiency should be at 400kHz and 600kHz. In practice, using the 5 cycle tone burst signals at these frequencies were not found to be sensitive; the backing amplitude change with coupling was negligible. The most sensitive frequencies were found to be 140kHz and 850kHz. This discrepancy is not fully understood and more research is necessary to further understand the phenomenon.

## 4.5 Conclusions

A primary standard calibration process has been successfully carried out on the tungsten/epoxy transducers which have been manufactured for this project. The through transmission and Rayleigh calibration configurations have been found to yield similar calibration curves aside from some inconsistencies in amplification and filtering. The through transmission configuration is recommended as it is more straightforward to align the interferometer and the signals measured in the through transmission configuration were larger than those measured in the Rayleigh configuration giving an improved signal to noise ratio.

The conical transducers generate output signals which are similar to that of the interferometer. This demonstrates that the output from the conical transducers is proportional to surface displacement (rather than velocity or acceleration). The transducers are well damped and no obvious ringing was seen.

The effect of coupling was examined and was shown to cause variability of up to  $\pm 7.6\%$  in the frequency range up to 1MHz. This variability was found to increase somewhat with frequency suggesting aperture effects caused by variable and incomplete contact of the transducer tip with the surface.

The results show that the effective bandwidth of the transducers is 1MHz. The transducers have been found to have a range of sensitivities differing by up to a factor of 4. The reasons for the difference in sensitivity are not completely understood but are thought to be caused by inconsistencies in assembly.

The conical transducer model developed by Greenspan (1987) has been found to predict the general response of the conical transducers reasonably well. The effect of front material impedance has been shown, theoretically and experimentally, to alter the response and natural frequencies of the transducers.

This change in natural frequency has successfully been used to independently measure the transducer coupling efficiency on a variety of materials. If other transducers can be shown to behave in a similar fashion this effect could be used as a standard method for measuring coupling for acoustic emission and standard ultrasonic measurements.



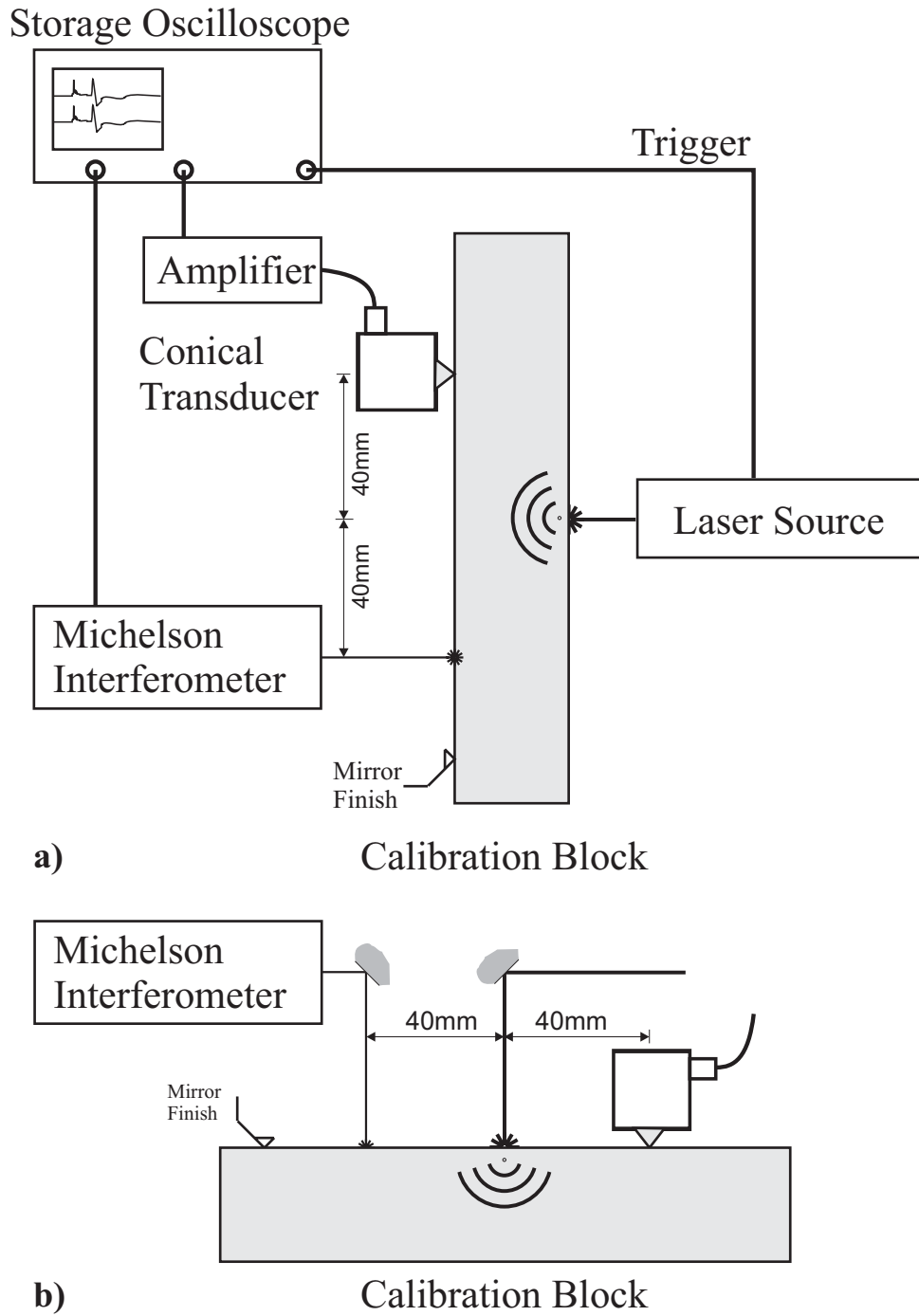


Figure 4.1 Calibration set-up showing measurement equipment including source and receiver locations for, a) The through transmission configuration and, b) The surface configuration.



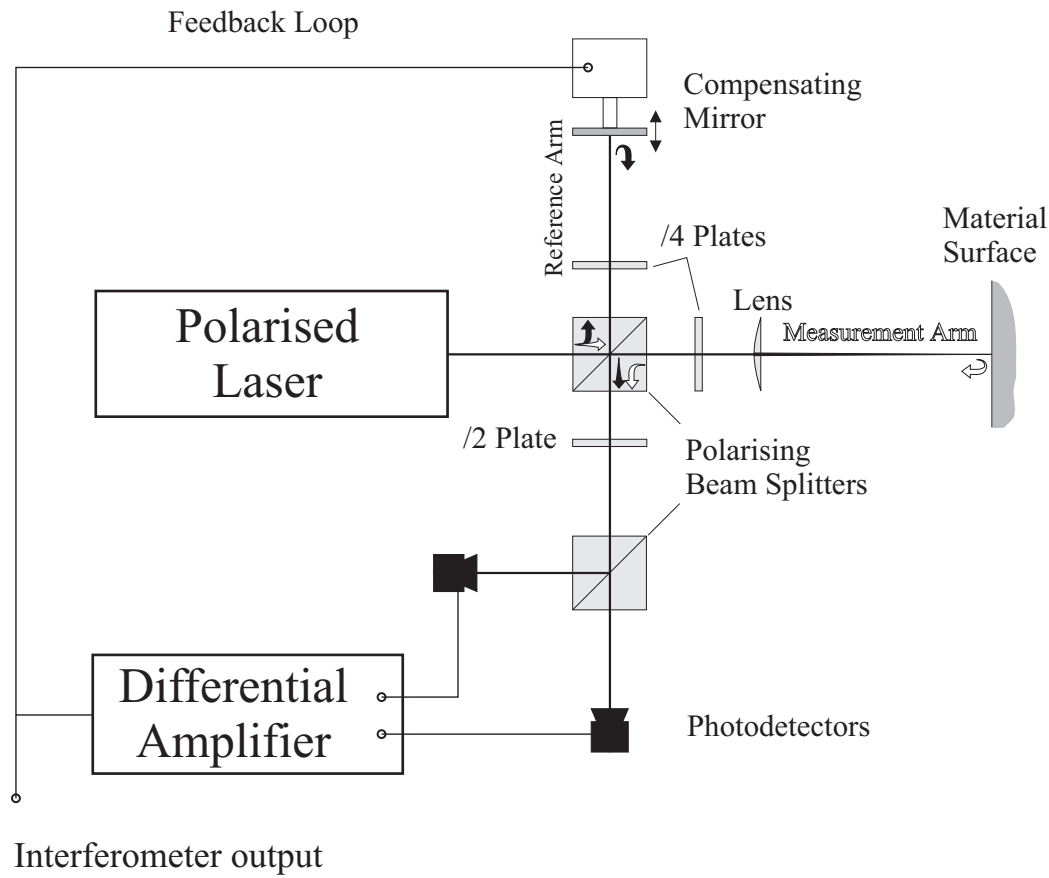


Figure 4.2 A schematic diagram of the path-stabilised Michelson interferometer used in the calibration experiments.

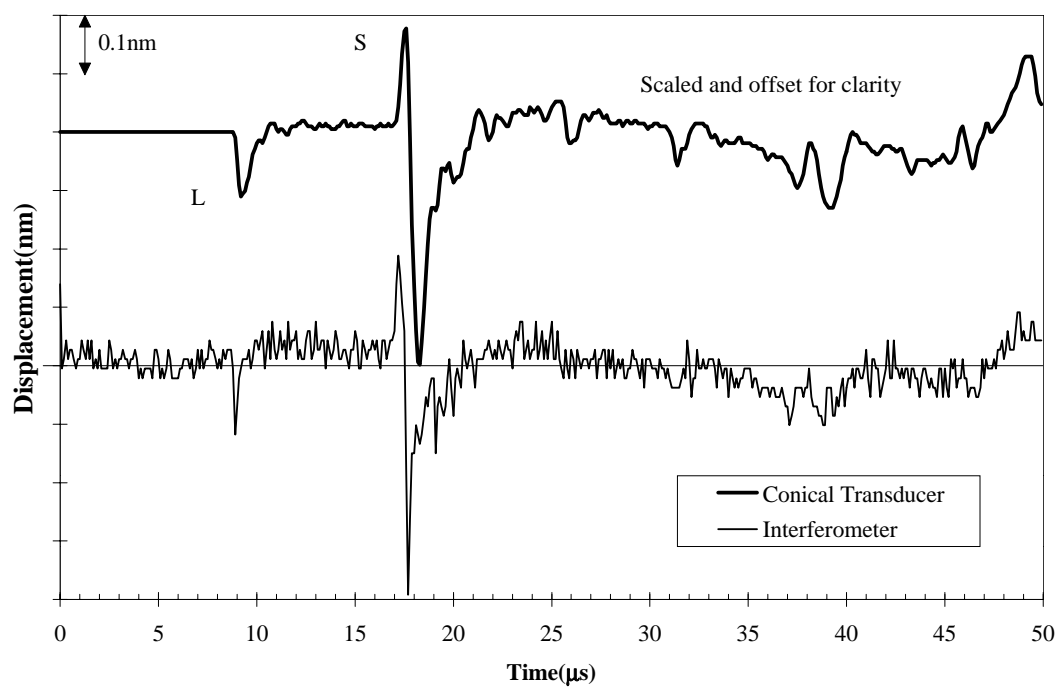


Figure 4.3 Comparison of time domain signals measured simultaneously by the interferometer and the conical transducer in the through transmission configuration showing the first arrival of the longitudinal (L) and shear (S) waves.

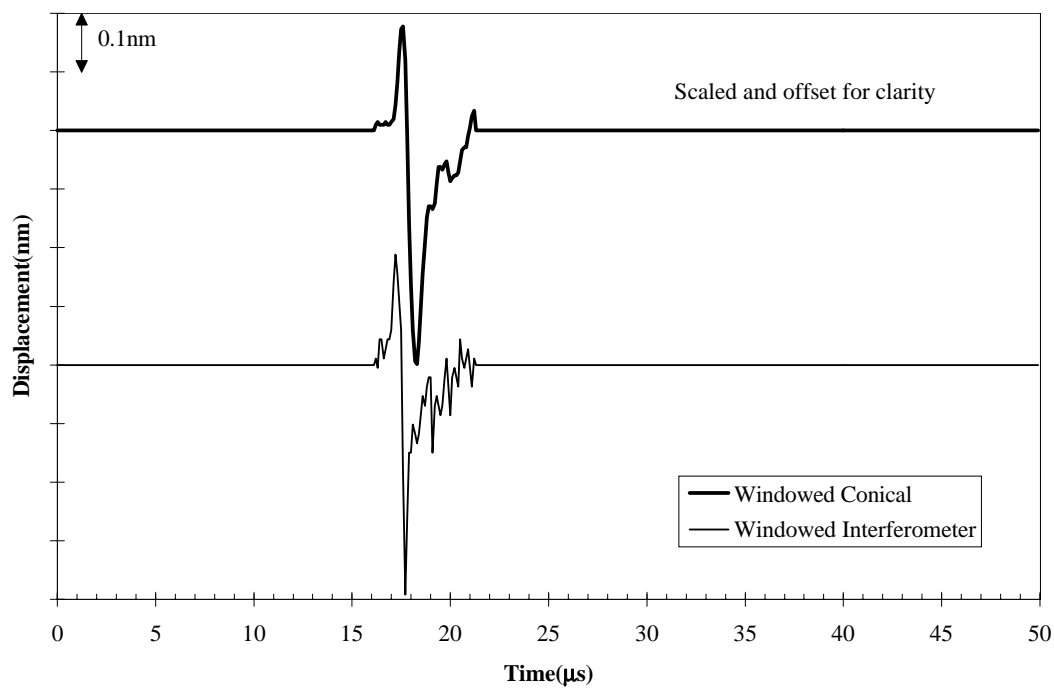


Figure 4.4 Effect of time domain windowing of the shear wave arrival shown in the previous figure.

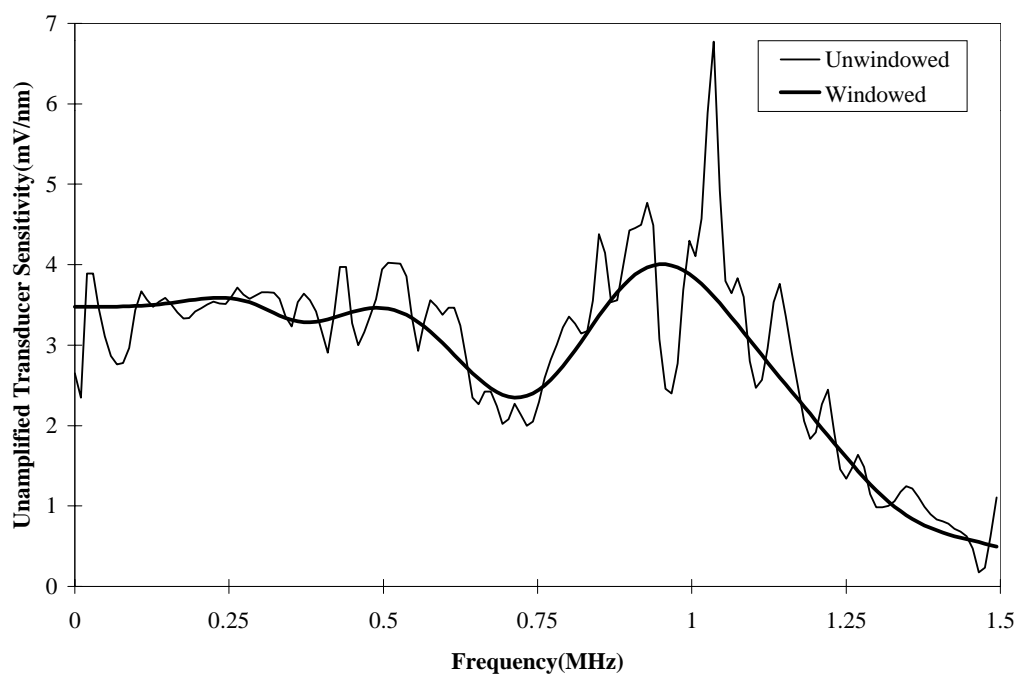


Figure 4.5 Comparison of the calibration curve generated from windowed and unwindowed signals.

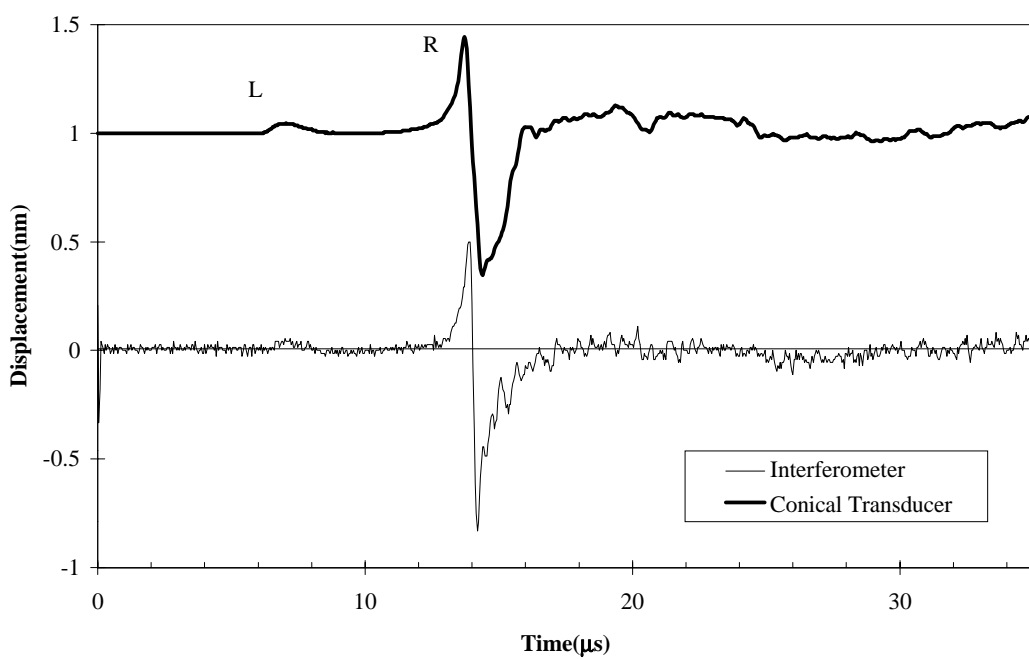


Figure 4.6 Comparison of the time domain signals measured simultaneously by the interferometer and the conical transducer in the surface configuration showing the first arrival of the longitudinal (L) and Rayleigh (R) wave.

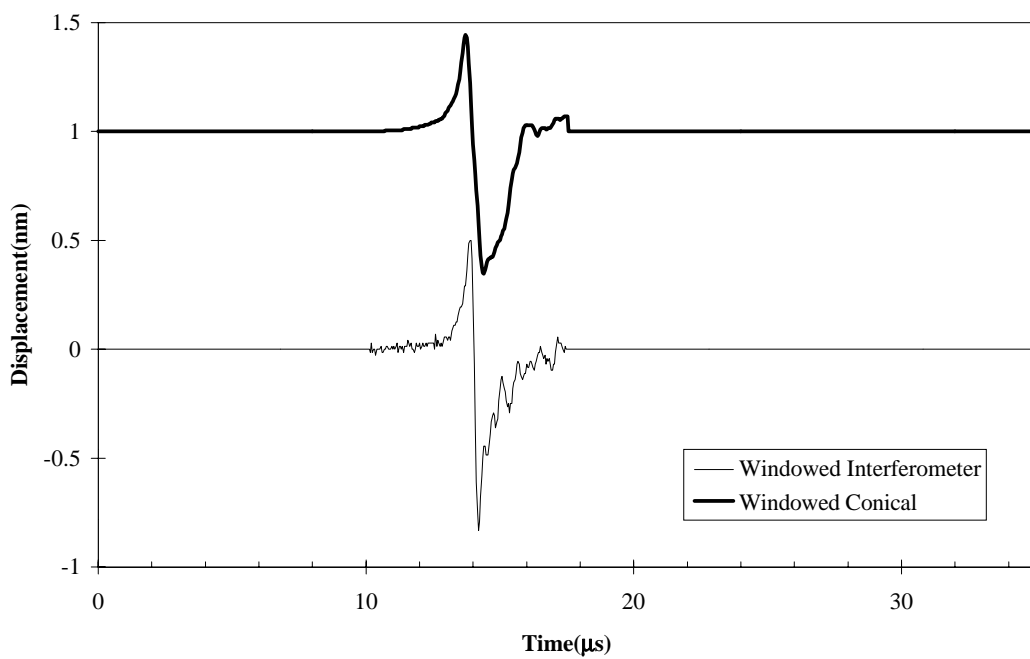


Figure 4.7 Effect of time domain windowing of the Rayleigh wave arrival shown in Figure 4.6.

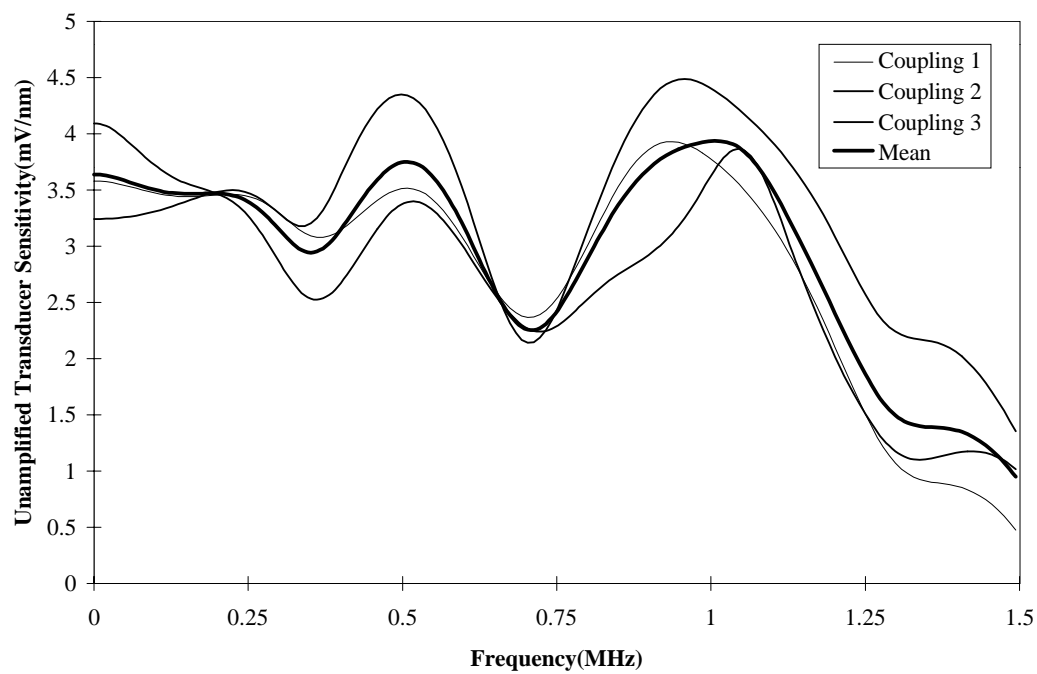


Figure 4.8 Three successive calibration curves measured for transducer WE1 after recoupling showing the change in transducer response with coupling. The thicker line is the average of the three recouplings.

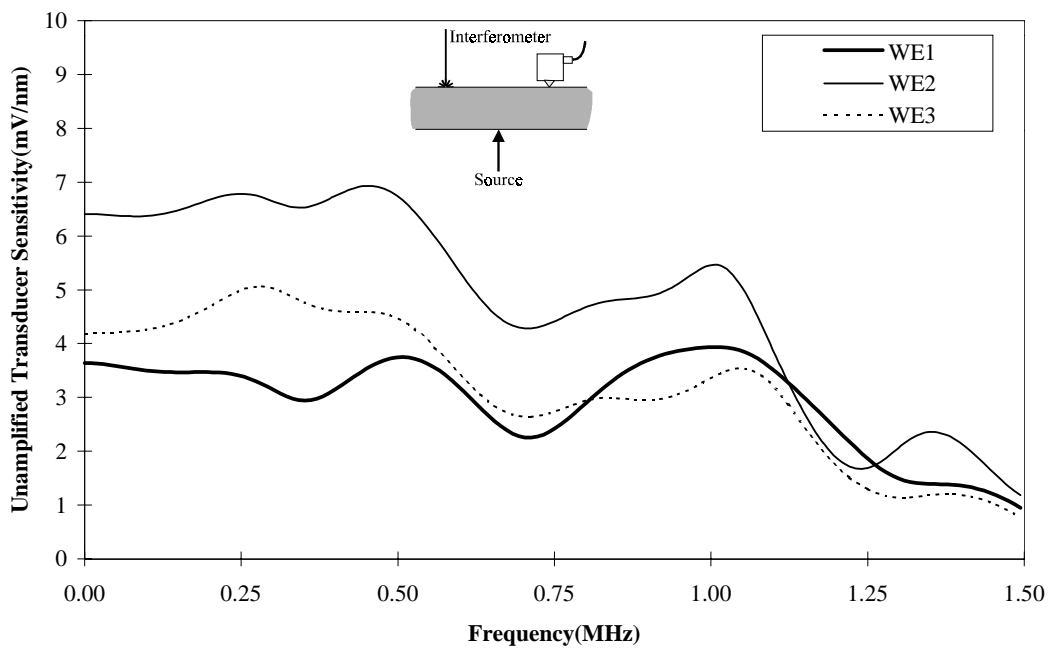


Figure 4.9 Comparison of the calibration curves generated for transducers WE1 to WE3 using the through transmission configuration.

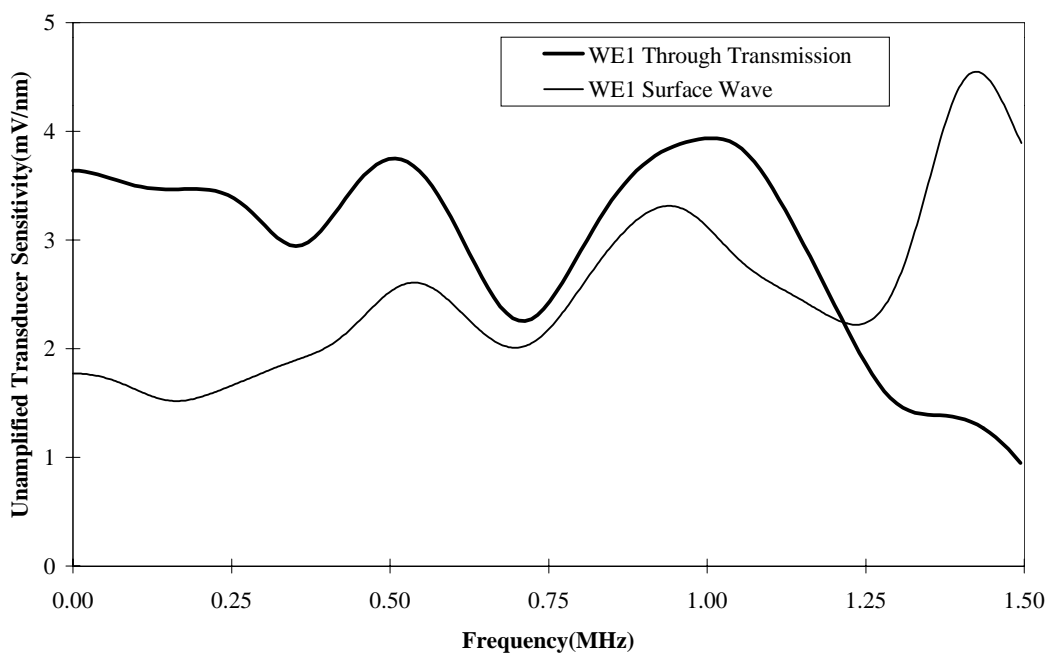


Figure 4.10 Comparison of the calibration curve measured for transducer WE1 using both the through transmission and surface wave configurations.

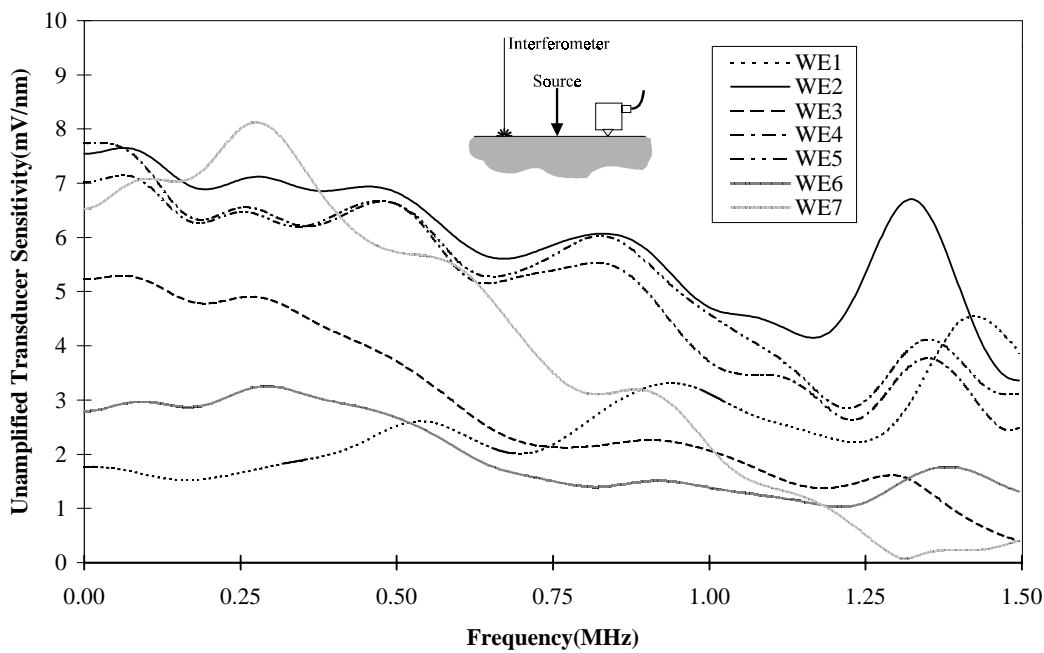


Figure 4.11 The calibration curves for all seven transducers measured using the surface wave configuration.

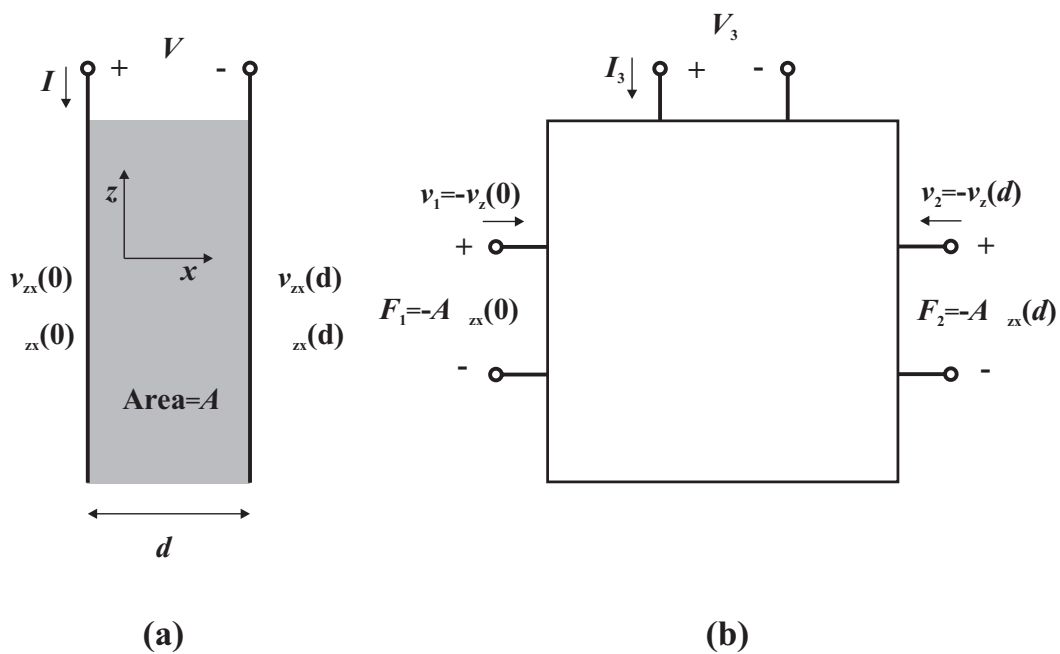


Figure 4.12 a) A schematic diagram of a piezoelectric shear element with electrodes,  
b) The equivalent three port network.

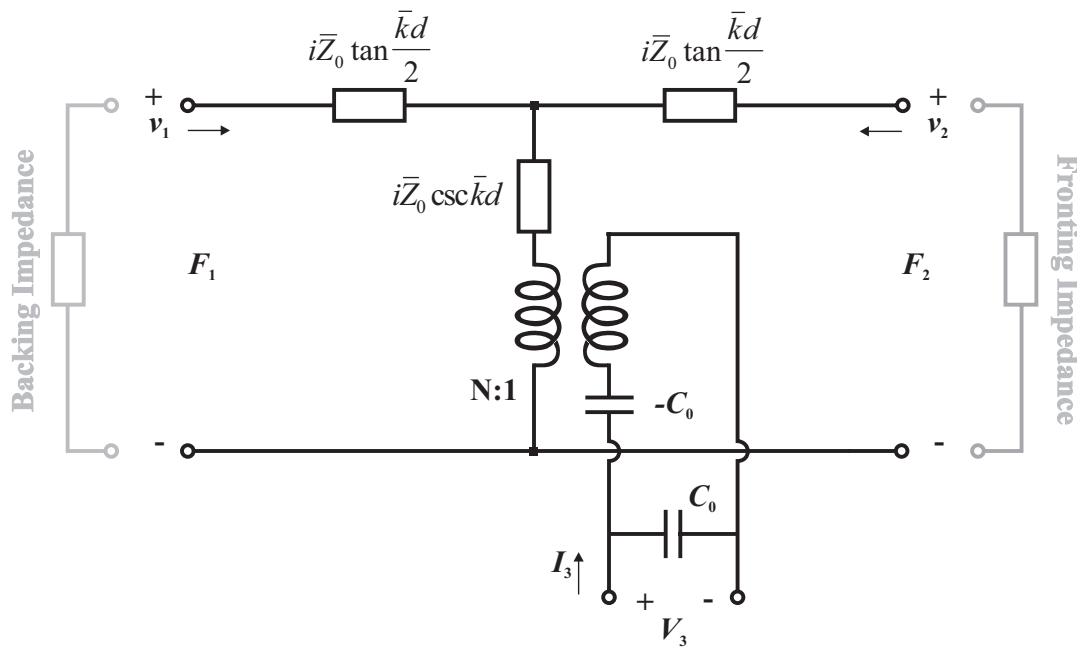


Figure 4.13 Mason equivalent circuit for a thin disk transducer showing the mechanical and electrical ports.

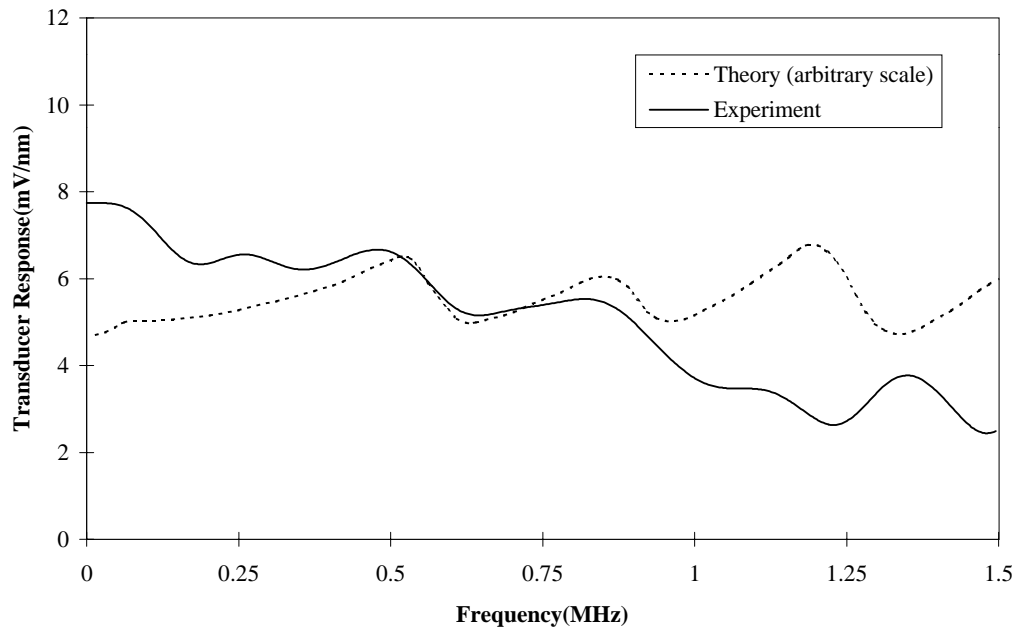


Figure 4.14 Predicted response of a tungsten/epoxy backed conical transducer on aluminium with a front face diameter of 1mm, back face diameter of 10mm and length of 3mm plotted with the actual measured response of a transducer of this geometry.

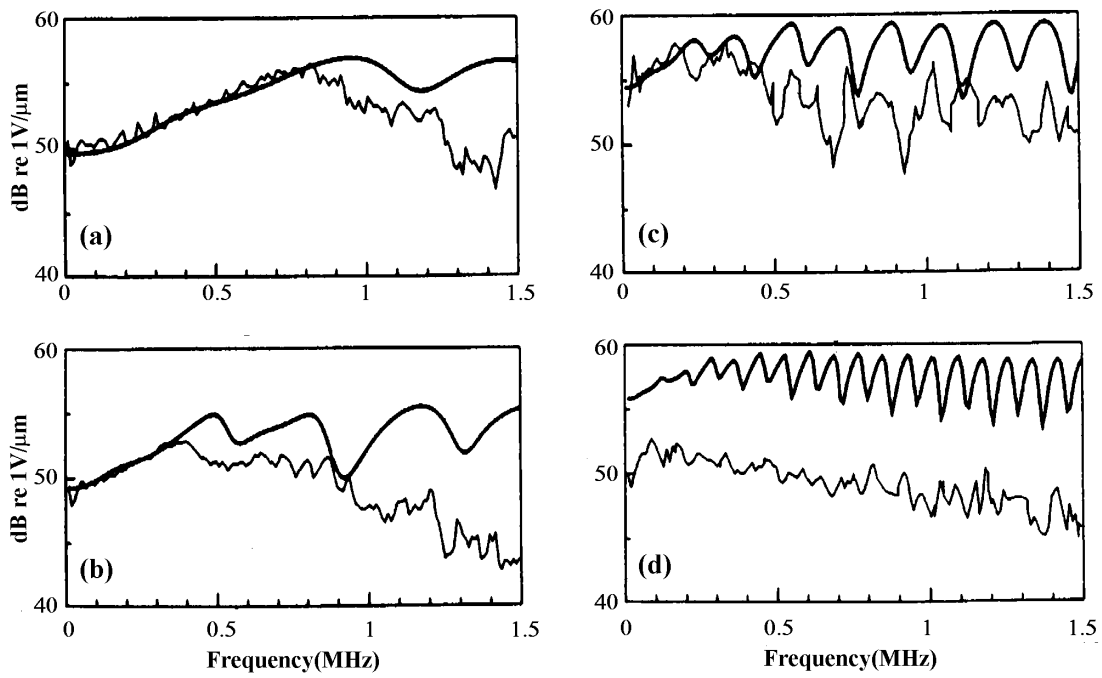


Figure 4.15 Comparison of theoretical model with calibration results for brass backed conical transducers, after Greenspan (1987) where the light lines are measurement and the heavy lines are theory. Cone dimensions are given in Table 4.1.

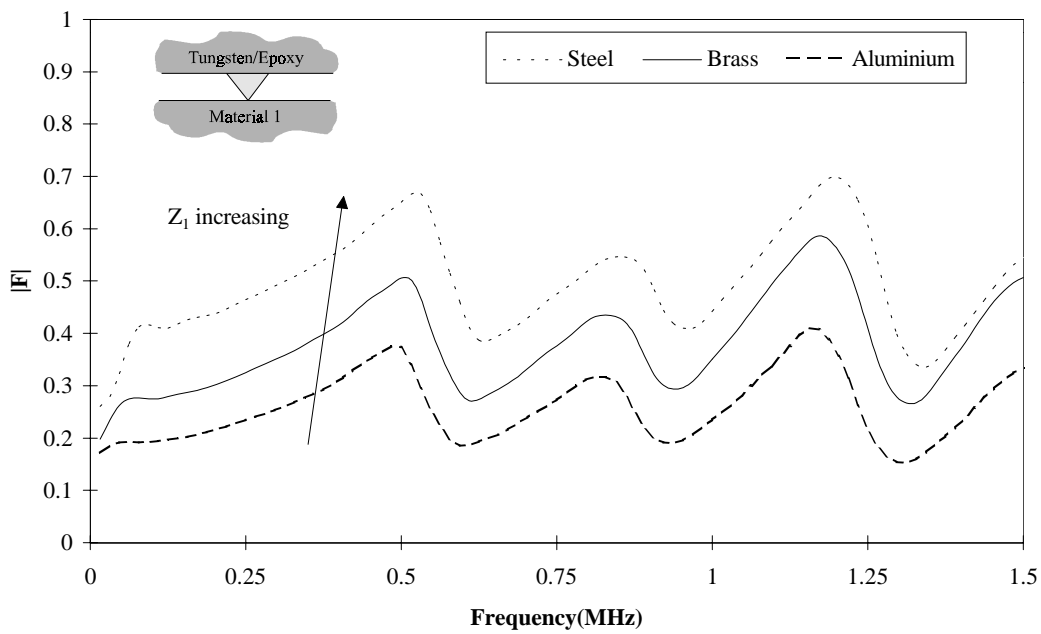


Figure 4.16 Comparison of the predicted transducer response with a variety of front materials, the backing for these predictions was tungsten/epoxy.

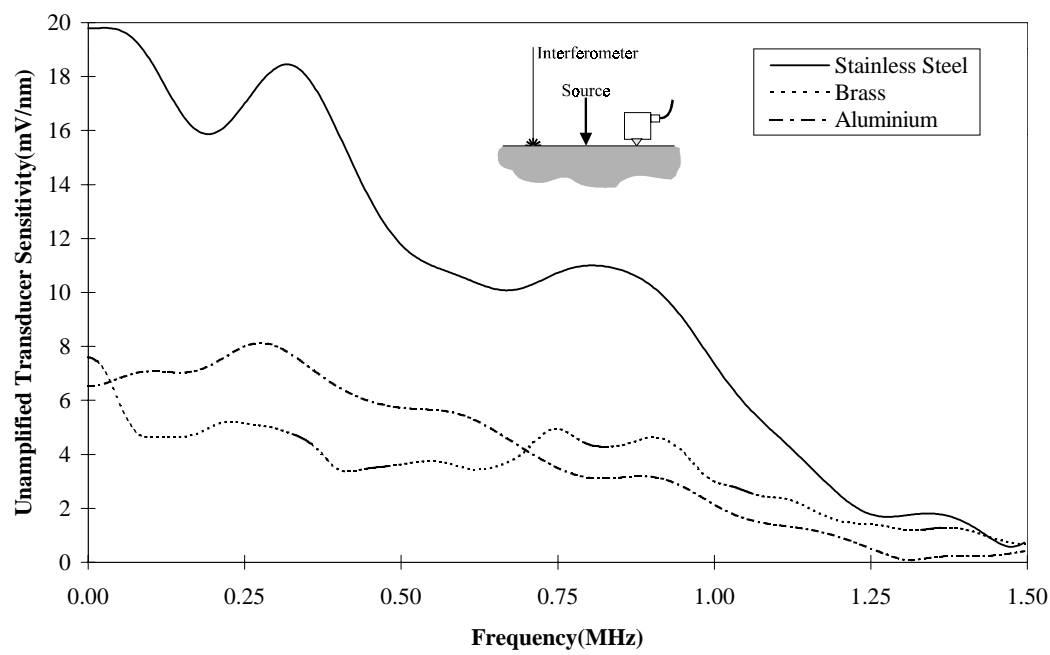


Figure 4.17 Measured response of transducer WE7 on stainless steel, brass and aluminium half-spaces (compare with predictions shown in previous figure).

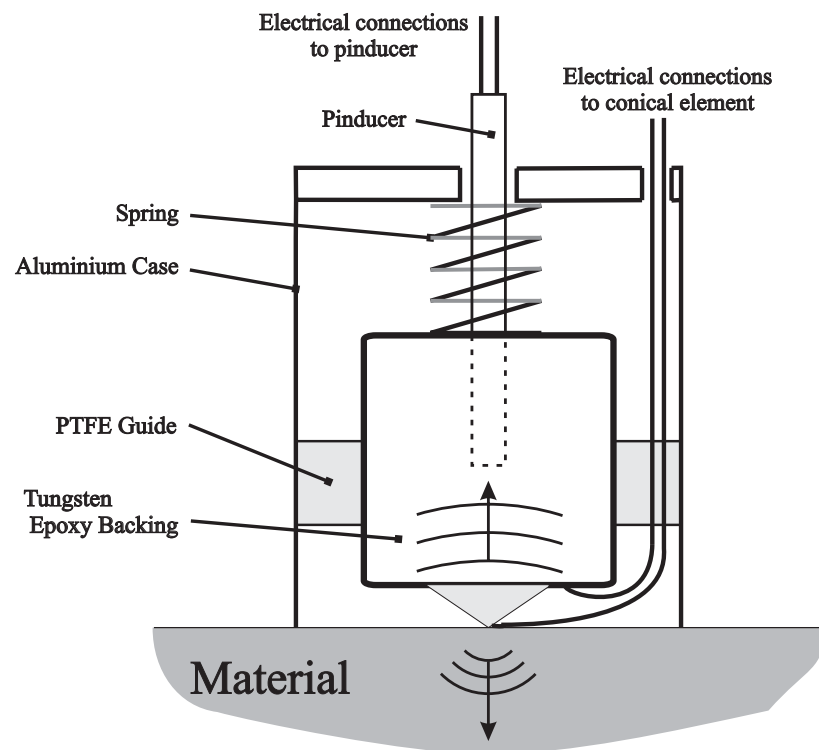


Figure 4.18 Schematic diagram of the auto-normalising transducer showing the conical element and pinducer mounted in the backing material.

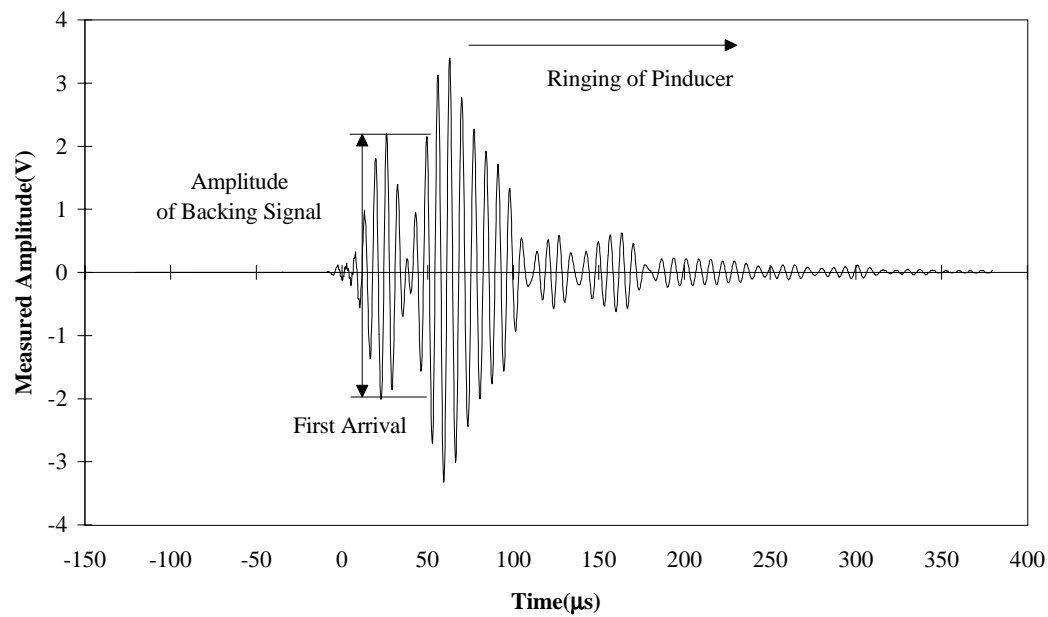


Figure 4.19 A representative backing signal measured from the auto-normalising transducer coupled to an aluminium block. The excitation signal was a five cycle, Hanning windowed toneburst at 140kHz.

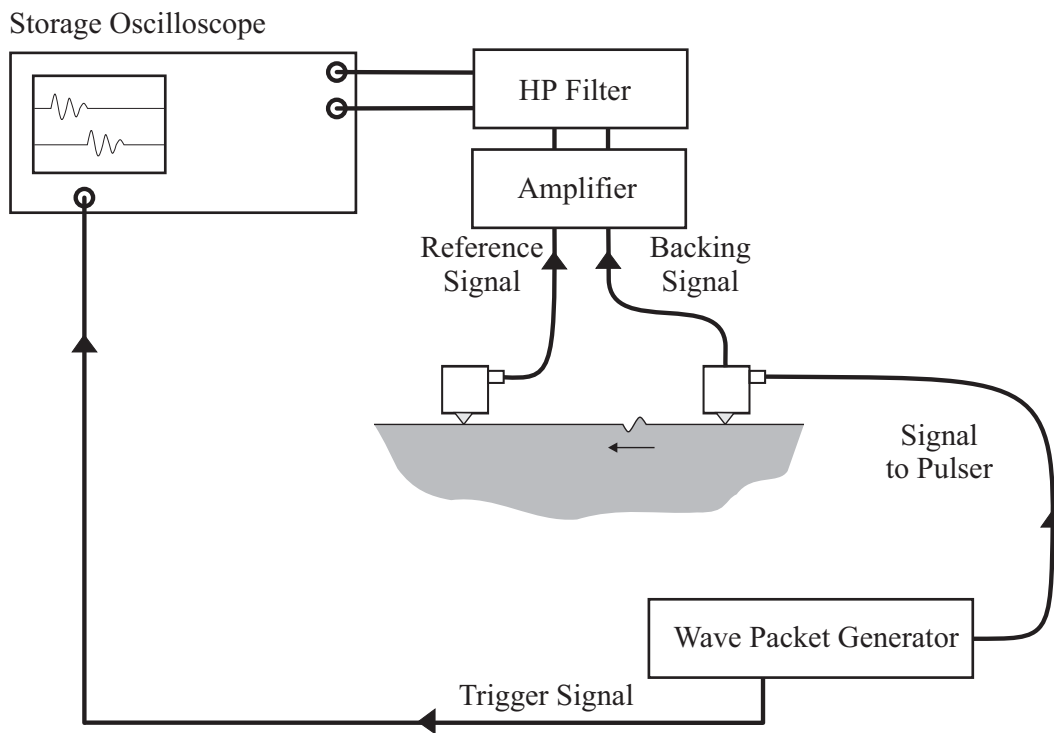


Figure 4.20 Experimental set-up used for testing the auto-normalising transducer.

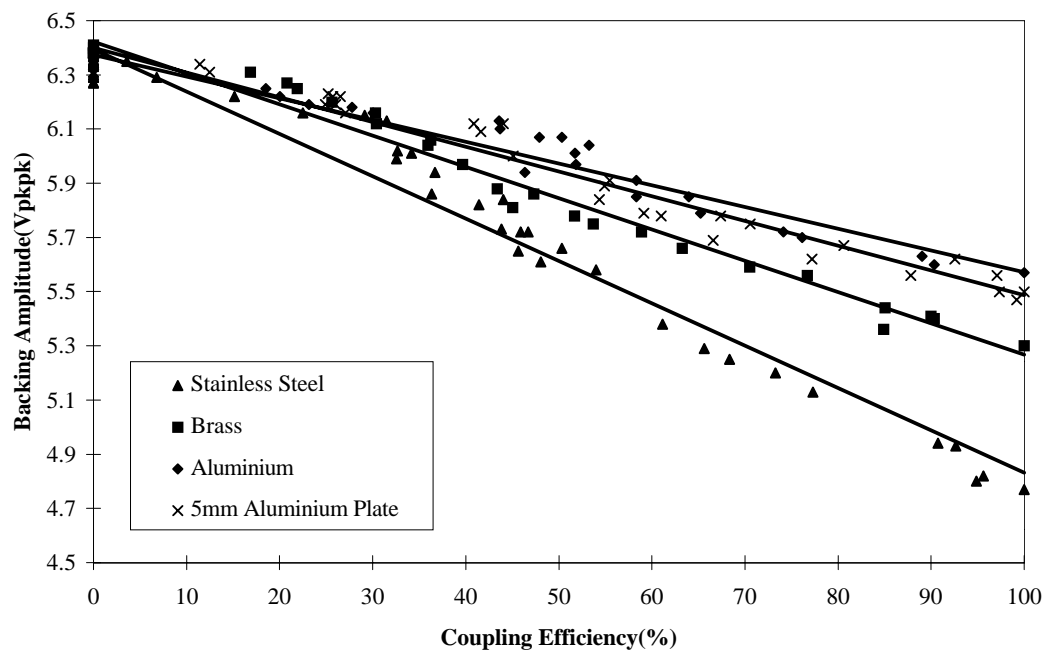


Figure 4.21 Results obtained from the auto-normalising transducer at 140kHz on stainless steel, brass and aluminium half-spaces and a 5mm thick aluminium plate, the solid lines are least squares fits.

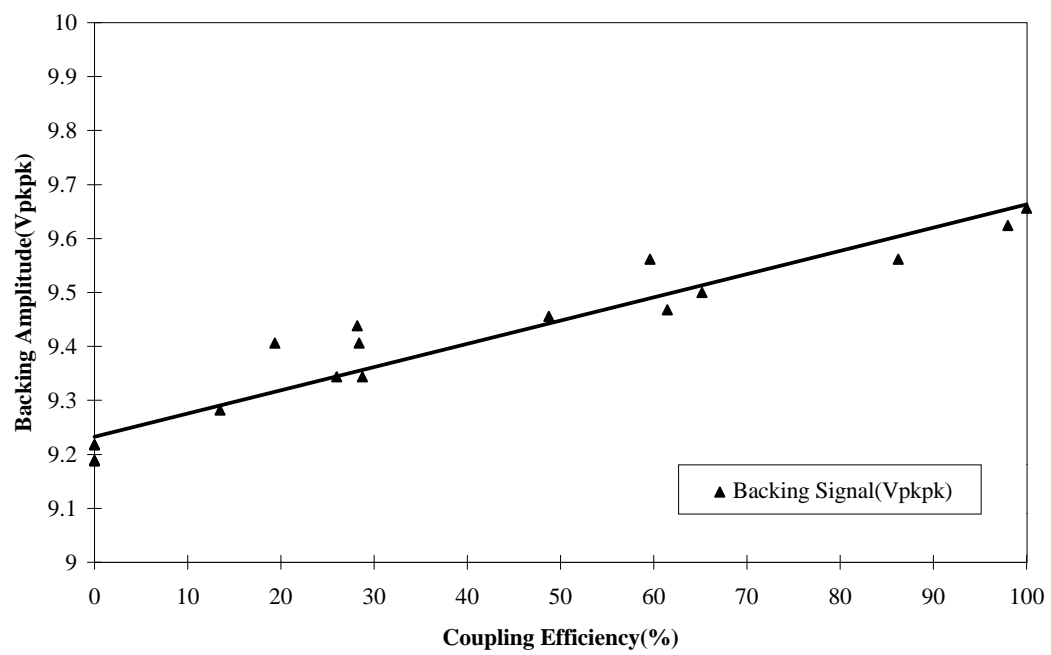


Figure 4.22 Results obtained from the auto-normalising transducer at 850kHz on the stainless steel half-space showing the opposite gradient.

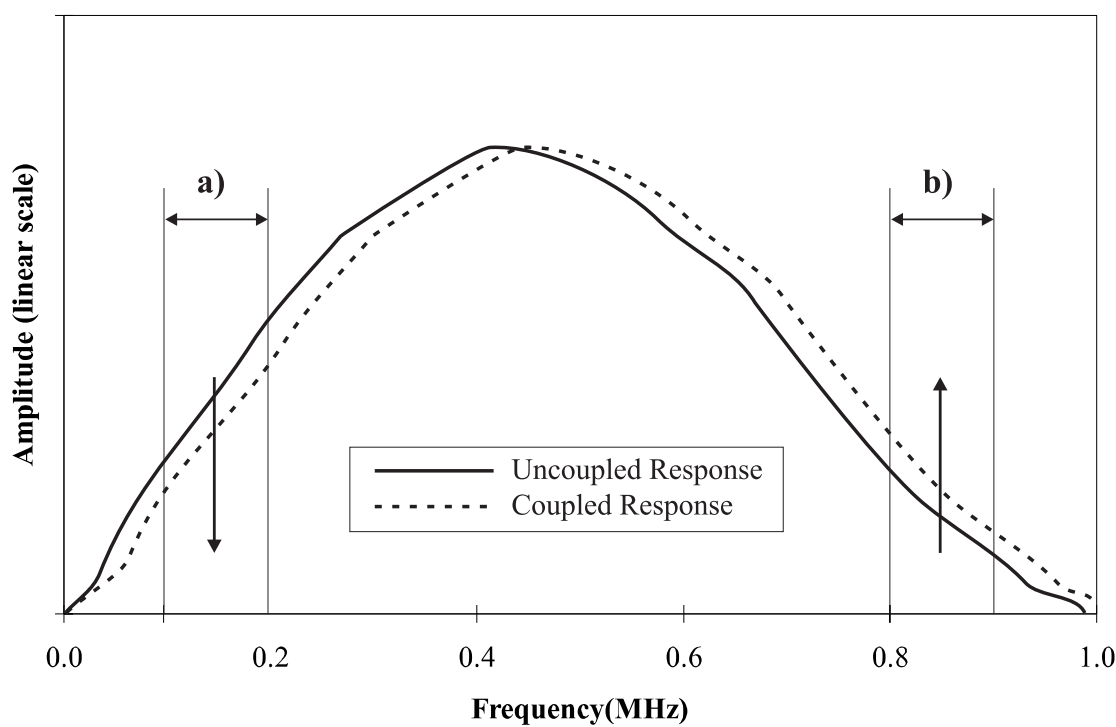


Figure 4.23 Schematic diagram of the effect of coupling on natural frequency and the corresponding change of transducer response above and below resonance.

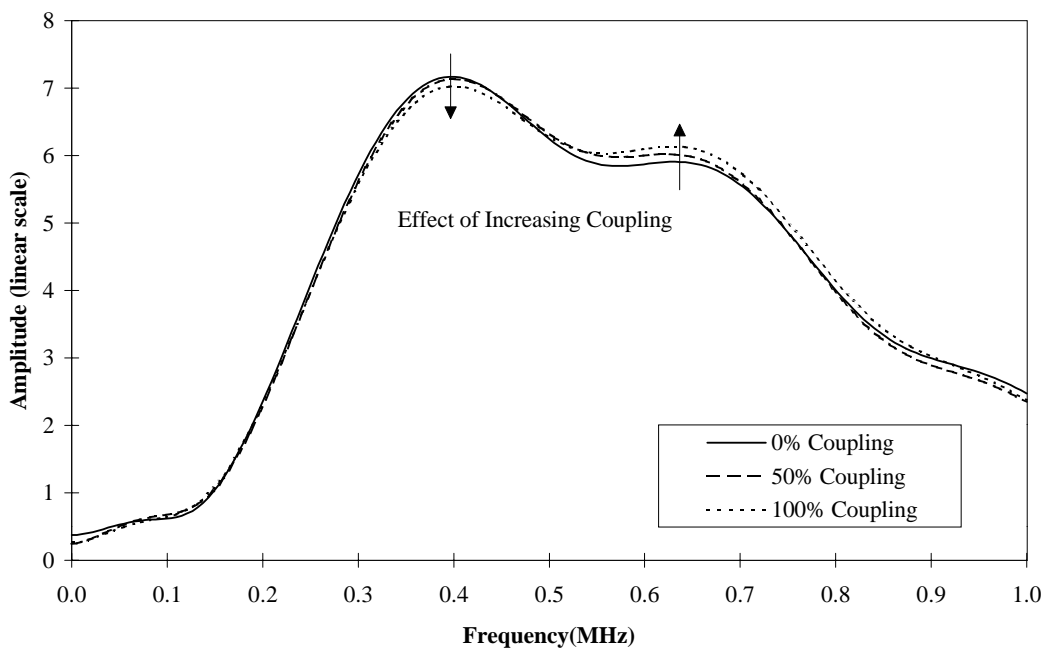


Figure 4.24 The Fourier transform of the backing signals obtained at 0%, 50% and 100% coupling to a stainless steel half-space. The excitation signal was a 1 cycle tone burst at 450kHz

## 5. Prediction of diffuse behaviour in coupled plates

---

### 5.1 Overview of chapter

It is clear from the literature that diffuse fields do exist in certain structures and complex modelling has been carried out to predict their behaviour. The complexity of this analysis and the large amounts of data required have precluded the use of these models in the field. What is required is a straightforward and easily applicable method which takes advantage of these findings and allows source strength and character to be calculated for acoustic emission testing of assembled structures.

In this chapter statistical energy analysis (SEA) is reviewed and its underlying assumptions are outlined. The formulation of a model based on SEA for predicting the energy flow between coupled structures is then given. In order to apply this model the reflection and transmission coefficients must be calculated for each connected boundary; a method for calculating these parameters for plate structures has been developed and is described.

Using these calculated parameters, structures consisting of coupled plates have been modelled and the results for several symmetric and asymmetric examples are reported. Several important conclusions concerning coupling strength, symmetry and damping can be made from these predicted results and these are presented at the end of the chapter.

### 5.2 Statistical energy analysis (SEA)

#### 5.2.1 *Introduction*

Statistical energy analysis is a method by which the acoustic response of a structure is considered as the balance of energy flow between groups of resonant modes. Energy terms are regarded as statistical averages of resonant mode response over finite frequency bands. Statistical methods are most suitable in cases where the frequency is high and many structural modes exist within the bandwidth of interest (high modal density). In these situations traditional modal analysis methods are cumbersome and often impossible to use due to the many hundreds of modes present.

SEA assumes that the detailed modal behaviour averages out as the modes become less well defined, thus allowing the structure to be analysed in a more pragmatic way. Much has been written concerning the use of SEA since its original formulation (Lyon and Eichler (1963), see also Lyon (1976)). An excellent introduction to the subject is given by Woodhouse (1981a), see also Woodhouse (1981b), in which the method, its major assumptions and limitations are introduced. These papers also give practical methods for assessing the suitability of the method for real structures.

Before continuing to describe the fundamentals of SEA it is important to define several terms which will clarify the discussion:

**Structure:** physical assemblage of components which are under analysis.

**Substructure:** individual component in the structure.

**Field:** subdivision used for the SEA model which refers to the energy in a single propagating mode type in a single substructure.

**Coupling loss factor:** coupling between connected fields (not including losses due to internal and external damping).

**Damping loss factor:** losses in an individual field due to internal and external damping (not including losses to connected fields).

Complex structures are divided into suitable fields; these need not be restricted to physical substructures but can include mode types. For example, consider a plate of uniform thickness and random shape, see Figure 5.1a). We make the initial assumption that only two Lamb wave modes can propagate, the fundamental symmetric and anti-symmetric modes ( $S_0$  and  $A_0$  respectively). An SEA model of this structure would consist of two fields, one for each mode type in the structure. Two possible models are schematically represented in Figure 5.1b) and c) representing the two possible edge conditions (symmetric and asymmetric). The coupling and damping loss factors are at this stage unknowns and will not in general be the same for each field, the damping being governed primarily by the mode shape and material properties of the plate and surrounding media and the coupling factors being governed by mode conversion between  $S_0$  and  $A_0$ .

The mode conversion phenomenon is described in more detail in Section 5.3.2; however, for clarity, a brief description of the relevant information follows. Mode conversion between symmetric and anti-symmetric branches of Lamb waves can only exist at discontinuities which exhibit some through-thickness asymmetry such as a step or an angle. Therefore for the case in question if no through-thickness asymmetry exists, the coupling terms in the SEA model will be zero and the fields will coexist without exchanging any energy, see Figure 5.1b). In a more general case where some degree of asymmetry exists, whether deliberate or accidental, mode conversion will permit the exchange of energy and the coupling terms will be nonzero (Figure 5.1c). The degree of mode conversion (and hence the strength of these coupling terms) is governed by the mode shapes and the precise geometry of the asymmetry.

The energy in each field is described by a scalar quantity, the energy density in that field. The energy densities are treated in a similar manner to heat in thermodynamic problems. Fields are assumed to have uniform energy across them (uniform temperature to use the heat transfer analogy), the power flow between fields being governed by the coupling loss factor and the ratio of energy levels in each individual field with energy flowing from high energy (hot) fields to low energy (cold) fields. A steady state partition of energy between all the fields will result, given sufficient time (Woodhouse (1981)).

The early work on SEA was concerned with steady state predictions where the source of energy was continuous. More recently, transient sources have been examined (Lai and Soom (1990), Pinnington and Lednik (1996) and Pinnington and Lednik (1996)). It is this transient analysis which will be used to predict the response of structures to simulated acoustic emission sources.

### 5.2.2 *Discussion of assumptions*

Before continuing to develop an SEA model it is first necessary to examine the assumptions which have been made. The primary assumption is that the energy in each individual substructure is evenly distributed and can be described by an average energy level. This condition is only satisfied if the field of waves within that substructure is diffuse, which has been demonstrated to be true for randomised plates

(Weaver (1986)). Further experiments have been carried out to verify that diffuse fields are generated in more general plate structures, see Section 6.3.

The coupling loss factors between connected fields are assumed to be constant for a given structure and to be independent of the actual energy level; this amounts to a simple assumption of linear material properties and no appreciable distortion of the structural geometry. The damping losses from each field are assumed to be proportional to the amount of energy present; this form of damping causes an exponential decay of energy which has been experimentally demonstrated to be a valid assumption, see Section 6.2.4.

As previously discussed, before a SEA model can be implemented the coupling loss factors must first be measured or calculated. The next section describes the method employed to facilitate this calculation.

## 5.3 Calculation of lamb wave reflection coefficients

### 5.3.1 *Introduction*

Plate structures have been used throughout this chapter, which restricts the propagating modes present to be Lamb modes. With careful choice of excitation frequency and bandwidth the number of possible modes can be restricted to the two fundamental modes  $S_0$  and  $A_0$ . Furthermore, due to the method of excitation and reception employed in the experiments the  $A_0$  mode dominates.

In order to use SEA to predict structural response the coupling loss factors must first be calculated, or measured, for a particular system. This, unfortunately is not a trivial procedure in most cases.

In this section the method of calculation of the reflection and transmission coefficients for irregular plates is described. Reflection coefficients from similar structural boundaries have previously been measured and calculated by Alleyne and Cawley (1991). However, this work has concentrated on measuring the coefficients with respect to the amplitude of the signal. What is required is the reflection, transmission and mode conversion of energy from symmetric and asymmetric changes in cross section. These coefficients will then be used as the coupling loss factors in the SEA predictions later in the chapter.

### 5.3.2 Lamb wave propagation

The solution of the wave equation for a plate of solid material surrounded by two vacuum half-spaces was first analysed by Lamb (1917) and later by Viktorov (1967) amongst others. A certain class of modal solutions give rise to a propagation of energy along the plane of the plate, with a polarisation direction out-of-plane and perpendicular to the direction of propagation. This class of propagating modes has been termed Lamb modes. This terminology may be slightly confusing as Lamb modes are in fact merely a combination of bulk shear, bulk longitudinal and (in general) inhomogeneous waves in the appropriate ratios to satisfy the boundary conditions on both interfaces (Lowe (1993)).

Lamb modes are subdivided into two classes, symmetric denoted by the letter S and anti-symmetric denoted by the letter A. The definition of a symmetric mode is one which has symmetric particle displacements about the mid-plane of the plate, and conversely for anti-symmetric modes. Examples of the mode shapes for the fundamental Lamb modes  $S_0$  and  $A_0$  are given in Figure 5.2 for a frequency-thickness of 0.75MHz-mm. The mode shape and velocity of each mode is dependent on the frequency of operation times the thickness of the plate, termed the frequency-thickness product.

The variation of velocity with frequency-thickness is termed velocity dispersion. The velocity at which each frequency component travels is known as the phase velocity ( $C_{\text{ph}}$ ), this being the velocity at which a constant phase portion of a continuous harmonic wave would travel at each frequency. The phase velocity is, however, difficult to relate to practical measurements as continuous harmonic excitation is rarely used and difficult to achieve on a finite structure. A more useful parameter is the group velocity ( $C_{\text{gr}}$ ), defined as,

$$C_{\text{gr}} = \frac{\partial \omega}{\partial k} \quad (5.12)$$

where  $k$  is the wavenumber and is given by  $k=\omega/C_{\text{ph}}$  and  $\omega$  is the circular frequency. The group velocity represents the speed at which a packet of waves will travel, centred on a certain frequency-thickness, and therefore the rate at which energy is transferred along the plate. This velocity can be plotted against frequency-thickness in what is termed a dispersion curve; an example of this is given in Figure 5.3 for the

first four modes of an aluminium plate in vacuum. The mode shapes and dispersion curves presented in this thesis have been calculated using ‘Disperse’, a program written at Imperial College (Lowe (1995) and Pavlakovic, et al. (1997)).

At low values of frequency-thickness (below 1.5MHz-mm in this case) only the fundamental modes  $S_0$  and  $A_0$  can exist, as seen from the dispersion curve of Figure 5.3. As the frequency thickness product increases, higher order modes can exist, such as the next anti-symmetric mode  $A_1$  which has a cut-off frequency just above 1.5MHz-mm and the next symmetric mode  $S_1$  at just under 3MHz-mm. There are an infinite number of these higher order modes as frequency-thickness goes to infinity. The group velocities of the fundamental modes tend asymptotically towards the Rayleigh (surface) wave velocity which is roughly 3mm/ $\mu$ s for aluminium. The group velocity of the higher order modes tend towards the bulk shear velocity of the material (Lowe (1995)).

The interaction of Lamb waves with plate discontinuities has been analysed by Alleyne (1991) and Alleyne and Cawley (1991) and further results are presented in Section 5.3.5. It is useful, however to review some of the basic characteristics at this stage. Discontinuities in the plate geometry, such as edges or changes in cross-section will cause reflection, transmission and mode conversion of the incident wave. Mode conversion exists when the incident mode cannot independently satisfy the boundary conditions enforced by the geometry of the discontinuity. An additional mode (or modes) are generated in suitable ratios such that the combined effect of all incident, reflected and transmitted waves satisfies the boundary conditions. Therefore the reflection, transmission and mode conversion coefficients are governed by this balance of modes.

Symmetric discontinuities do not cause mode conversion between the symmetric and anti-symmetric branches of Lamb modes (Alleyne (1991)). For example, consider an aluminium plate with the  $A_0$  mode propagating with a maximum frequency-thickness of below 1.5MHz-mm (below the  $A_1$  cut-off). If this wave was to reflect from a symmetric edge of the plate it would be completely reflected. If the frequency thickness was increased to above the  $A_1$  cut-off, some mode conversion will occur and both  $A_0$  and  $A_1$  will be reflected. The same is true of  $S_0$  and higher order symmetric modes. Asymmetric discontinuities cause mode conversion between

symmetric and anti-symmetric modes. Therefore, below the  $A_1$  cut-off, an  $A_0$  wave will be partially mode converted to  $S_0$  and vice versa. The degree of mode conversion is governed by the degree of asymmetry.

### 5.3.3 *The Finite Element models*

Finite element modelling was used to predict the interaction of propagating Lamb modes with discontinuities in plates. The finite element program used for the predictions was ‘Finel’ (Hitchings (1987)), a package developed at Imperial College which has been used extensively for the modelling of Lamb wave propagation (Alleyne (1991)).

A series of 5mm thick aluminium plates were modelled with a variety of symmetric and asymmetric discontinuities in order to calculate the reflection and transmission coefficients. A schematic diagram of a typical finite element mesh used is given in Figure 5.4. The elements used were two-dimensional four noded quadrilaterals and the calculations were done assuming plane strain and free boundary conditions for all cases. A uniform square mesh was used with more than 6 nodes per wavelength which proved sufficient.

Lamb waves were excited in the plate by forcing the end nodes with the exact mode shape, as calculated using Disperse (Lowe (1995)). A five cycle Hanning windowed sinusoidal input was used with a centre frequency of 150kHz, the bandwidth (40dB down points) for this signal being given by  $0.6 \times f_0 \leq f \leq 1.4 \times f_0$  where  $f_0$  is the centre frequency of the signal. Thus the highest frequency components are at 0.21MHz giving a maximum frequency thickness of 1.05MHz-mm which restricts the possible Lamb modes to  $S_0$  and  $A_0$ , see Figure 5.3.

The surface displacement was monitored over two areas, one on each side of the notch to detect the transmitted and reflected modes, as shown in Figure 5.4. Sixty nodes were monitored in each of these areas, making a total of one hundred and twenty monitoring points and both the in-plane and out-of-plane displacements were measured for each point. The results generated are in the form of a time domain signal for each monitoring node.

### 5.3.4 Method of calculation of strain energy

The results obtained from the FE model give the time domain displacement of the plate at several locations on its surface. Figure 5.5, for example, shows the predicted in-plane displacement response for an  $A_0$  signal reflecting from an asymmetric notch showing both the reflected  $A_0$  and mode converted  $S_0$  components. The example given shows an ideal case, the  $S_0$  and  $A_0$  signals are well separated and easy to distinguish. The amplitude and time of flight of each mode can be easily measured from this trace and thus the reflection coefficients calculated. Generally the situation is not so simple, modes overlap and interfere which makes amplitude measurements impossible.

The results obtained from the FE model were processed using a two-dimensional Fourier transform method (2-D FFT) (Alleyne (1991) and Alleyne and Cawley (1991)). This technique involves two Fourier transform stages. Firstly the time domain traces from each individual monitoring point are Fourier transformed into the frequency domain; this yields the frequency spectrum for each monitoring point. For each frequency component a spatial Fourier transform is carried out encompassing all consecutive monitoring points; this yields the wavenumber components present at each frequency. The resulting two-dimensional array contains the amplitudes of the corresponding frequency and wavenumber components of the signal. The Lamb modes present have different wavenumbers (owing to their different phase velocities) and therefore appear at different locations on the wavenumber axis allowing their amplitudes to be measured independently.

Applying the 2-D FFT algorithm to the FE predictions shown in Figure 5.5 for the input and reflected signals yields Figure 5.6 and Figure 5.7 respectively. These figures show the wavenumber components of the 2-D FFT at 150kHz (the excitation frequency) demonstrating the generation of  $S_0$  due to mode conversion at the asymmetric notch. The amplitudes of the input and reflected waves are easily measured from the 2-D FFT plots and these amplitudes give the ratio of maximum surface displacement between the modes. Thus the amplitude reflection and transmission coefficients can be calculated by dividing the reflected amplitudes by the amplitude of the input signal. These amplitude reflection coefficients are the ratios of the amplitudes of incident and reflected modes and are extremely useful for predicting

the detectability of defects. What is required, however, for the SEA modelling are the energy reflection coefficients and some additional processing is required in order to calculate these.

The energy stored by a Lamb mode is in the form of strain energy; the amount of energy per unit plate area (strain energy density in Joules per square metre) being governed by the mode shape and the square of the strain amplitude. The FE models were all two-dimensional making the concept of plate area undefined, if a uniform plate area of  $1\text{m}^2$  is assumed then the total energy in each mode is equal to the strain energy density. The strain energy density and mode shape for a given mode can be calculated (Lowe (1995)) and from this the ratio of strain energy density to squared surface displacement obtained. These ratios were calculated for the  $S_0$  and  $A_0$  modes at various frequency-thicknesses, see Table 5.1.

Frequency - Thickness	0.75MHz-mm		0.375MHz-mm		0.1875MHz-mm	
	U <sub>1</sub>	U <sub>2</sub>	U <sub>1</sub>	U <sub>2</sub>	U <sub>1</sub>	U <sub>2</sub>
$A_0$	1.534	0.620	1.084	0.295	0.950	0.151
$S_0$	0.729	17.516	0.345	38.020	0.170	76.647

Table 5.1 Calculated energy density ratios for  $S_0$  and  $A_0$  ( $\times 10^{11} \text{ J/m}^4$ ) where U<sub>1</sub> is in-plane displacement and U<sub>2</sub> is out-of-plane displacement.

The energy ratios were then applied to the finite element results. To calculate the energy present in each mode the surface displacement was squared and multiplied by the relevant ratio giving the strain energy density, this was then multiplied by the plate area ( $1\text{m}^2$ ) to give the total energy. Thus the reflected, transmitted and mode converted energies were calculated. The energy reflection coefficients were obtained by dividing these calculated energies by the incident energy. In order to check these results the calculation was done using both in-plane and out-of-plane displacements which should give identical results. In general these gave reflection coefficients values which differed by less than 2%. Additionally, due to the conservation of energy and the lack of any energy loss mechanism in the FE model, the sum of all transmitted and reflected energy must equal the incident energy. The results which follow all obeyed this rule to within 3%.

### 5.3.5 Results

An example of the results calculated for an  $S_0$  wave incident on a symmetric and asymmetric notch are given in Figure 5.8 and Figure 5.9 respectively. The notch width in each case was 5mm which is small in comparison to the wavelengths of interest (14mm for  $A_0$  and 35mm for  $S_0$ ). For the symmetric case, as expected, no mode conversion exists and so no  $A_0$  energy is generated. The reflection coefficient increases with notch depth reaching 1 (total reflection) when the notch depth equals the plate thickness and vice versa for the transmission coefficient. The non-linear relationship between the energy reflection and notch depth demonstrates that the strain energy is not evenly distributed through the thickness but is higher at the centre of the plate than at the edges. The asymmetric case, Figure 5.9, demonstrates the effect of mode conversion on the energy balance. The mode converted energy is zero at the 0% and 100% notch depths, as these are actually symmetric systems and the  $S_0$  reflection and transmission coefficients follow the same trend as for the symmetric case. A complete table of results for all notch geometries and incident modes is given in Appendix A.

## 5.4 Prediction of energy flow between coupled systems using SEA

### 5.4.1 Introduction

The analysis of coupled structures is essential if diffuse field methods are to be used on real structures. There are several physical types of coupling which are routinely present. Physical examples include joints, abrupt bends and changes in section. Although these coupling types may differ physically, for the purposes of SEA they may all be treated in the same manner. The energy flow between structures is governed by the coupling loss factors and the difference in energy level between them.

### 5.4.2 Exact and iterative SEA models of two-field systems

A simple example is that of a plate shown in Figure 5.10. A single plate has side notches cut in it which reduce the cross sectional area in the middle portion. The remaining ligament is acting as the coupling element between the two plane regions. An SEA model of such a system would consist of two fields pertaining to the two plane sections with a coupling loss factor between them.

The coupling factors for this system are easily approximated. The through-thickness symmetry of the system means that there is no mode conversion between the symmetric and anti-symmetric modes. Coupling between the plates is assumed to be proportional to the change in width of the plate, therefore if the remaining ligament is 10% of the width of the entire plate, the coupling will be 10% and so on.

Taking the solution for a single mode, say  $A_0$  the fundamental anti-symmetric mode. The energy balance equations for field 1 and 2 are,

$$\begin{aligned} P_1 &= \frac{dE_1}{dt} + \eta_{12}\bar{n}E_1 + \eta_1 E_1 - \eta_{21}\bar{n}E_2 \\ P_2 &= \frac{dE_2}{dt} + \eta_{21}\bar{n}E_2 + \eta_2 E_2 - \eta_{12}\bar{n}E_1 \end{aligned} \quad (5.13)$$

where  $\bar{n}$  is the mean reflection frequency (Hz);  $E$  is the mean energy in each field;  $P$  is the steady state power input to each field;  $\eta_{12}$  is the coupling loss factor from 1 to 2 per reflection and  $\eta_i$  is the damping loss in field  $i$  per second. In this case the fields are the same size and so the reflection frequency  $\bar{n}$  is identical for both systems and is given by,

$$\bar{n} = \frac{c}{\bar{l}} \quad (5.14)$$

where  $\bar{l}$  is the mean free path length which, for plates, is given by,

$$\bar{l} = \sqrt{A_p} \quad (5.15)$$

where  $A_p$  is the plan area of the plate. Equations for calculating the mean free path for other geometries can be found in Kuttruff (1973).

For impulsive excitation  $P_1$  and  $P_2 = 0$ . Introducing a differential operator  $D$  and writing Equation (5.13) in matrix format we obtain,

$$\begin{bmatrix} D + \eta_a \bar{n} & -\eta_{21} \bar{n} \\ -\eta_{12} \bar{n} & D + \eta_b \bar{n} \end{bmatrix} \begin{Bmatrix} E_1 \\ E_2 \end{Bmatrix} = 0 \quad (5.16)$$

where  $D = d/dt$ ,  $\eta_a = \eta_1 + \eta_{12}$  and  $\eta_b = \eta_2 + \eta_{21}$ .

The determinant of this equation is,

$$D^2 + (\eta_a + \eta_b)\bar{n}D + (\eta_a\eta_b - \eta_{12}\eta_{21})\bar{n}^2 = 0 \quad (5.17)$$

A transient energy,  $E_0$ , is applied to substructure 1 by setting the initial conditions,

$$\begin{aligned} E_1(0) &= E_0 \\ E_2(0) &= 0 \\ \frac{dE_1(0)}{dt} &= -\eta_a\bar{n}E_0 \\ \frac{dE_2(0)}{dt} &= \eta_{12}\bar{n}E_0 \end{aligned} \quad (5.18)$$

Solving Equation (5.17) and applying the initial conditions yields,

$$\begin{aligned} E_1(t) &= \frac{E_0}{2b} e^{-a\bar{n}t} \left[ \left( \frac{-D_2}{n} - \eta_a \right) e^{b\bar{n}t} + \left( \frac{D_1}{n} + \eta_a \right) e^{-b\bar{n}t} \right] \\ E_2(t) &= \frac{E_0}{2b} \eta_{12} e^{-a\bar{n}t} [e^{b\bar{n}t} - e^{-b\bar{n}t}] \end{aligned} \quad (5.19)$$

where  $a = -(\eta_a + \eta_b)/2$ ,  $b = \frac{1}{2}\sqrt{(\eta_a - \eta_b)^2 + 4\eta_{12}\eta_{21}}$  and  $D_1, D_2 = -\bar{n}(a \pm b)$ .

Structures having multiple subsystems become difficult to model in this way due to the complexity of the equations. A better method is to use an iterative solution (Powell and Quartararo (1987)), whereby the equilibrium equations for system 1 and 2 are as follows.

$$\begin{aligned} E_1(t + \Delta t) &= E_1(t) - \eta_{12}\bar{n}\Delta t E_1 + \eta_{21}\bar{n}\Delta t E_2 - \eta_1\Delta t E_1 \\ E_2(t + \Delta t) &= E_2(t) - \eta_{21}\bar{n}\Delta t E_2 + \eta_{12}\bar{n}\Delta t E_1 - \eta_2\Delta t E_2 \end{aligned} \quad (5.20)$$

The energy at  $t + \Delta t$  is simply equal to the energy at time  $t$  plus the sum of incoming and outgoing energy in time  $\Delta t$ . Predictions obtained using the exact solution of Equation (5.19) were compared with the iterative solution for the same boundary and initial conditions and showed excellent agreement.

Figure 5.11 shows the predicted response of the structure Figure 5.10 where the coupling loss factors were 2.5% (3.5dB/ms) and the damping loss factors were zero. This figure clearly shows a steady state partition of energy between the fields being reached after approximately 6ms. The steady state condition is defined as being when the decay rates in all fields are equal to within 5%. It is interesting to note that in this

simple case the steady state ratio of energy is 1:1 as the fields are identical. In the absence of damping the steady state partitioning of energy will always occur albeit, given very low coupling, this may take an extremely long time. We can therefore conclude that in such a system coupling can always be considered as strong.

Zero damping will never exist in practice and therefore the amount of time available for the partitioning of energy to occur is limited by the reverberation time of the structure. The strength of coupling is therefore affected by the damping loss factors.

#### 5.4.3 *Coupling strength*

Coupling strength describes the ratio of the energy exchanged by coupling between fields and the energy lost due to damping. The coupling between fields encompasses both the coupling between substructures, as demonstrated in the previous example, and the coupling between mode types, for example the  $S_0$  and  $A_0$  mode fields in a plane plate. For simplicity, consider firstly a single structure in which only two propagating modes are present giving three possible scenarios:-

**No coupling:** If no coupling exists, for example if only  $S_0$  and  $A_0$  are present and all the boundaries are perfectly symmetric, two independent wave fields exist. These fields may be individually diffuse but no energy flows between them. The ratio of energy between these wave fields is governed by the initial source partitioning and the attenuation of each mode. The decay rates of the individual fields will, in general, be different due to the difference in attenuation between the propagating modes.

**Weak coupling:** If weak coupling exists, for example if there is some slight asymmetry in the system, mode conversion exists but it is extremely slow. For the purposes of this project the coupling is defined as being weak when the damping is sufficient to attenuate the signals by 20dB before the steady state is reached. This is equivalent to having a plate with slightly asymmetric edges. The coupling loss factor afforded by the mode conversion at the edges being lower than the damping losses in the structure. Figure 5.12 gives an example of the response of a weakly coupled system with a damping loss factor of 1dB/ms and a coupling loss factor of 0.5dB/ms. The steady state partitioning of energy is reached (decay rates identical to within 5%) eventually but not before the initial signal is attenuated by more than 20dB.

Decreasing the coupling loss factor would further delay the time at which the steady state occurs.

**Strong coupling:** If mode conversion is strong, for example in a highly asymmetric system, energy transfer will occur very quickly. Thus the coupling loss factors will be larger than the damping losses in the system and a steady state will occur even in the presence of damping. Figure 5.13 demonstrates the response of a strongly coupled system with a damping loss factor of 0.5dB/ms and a coupling loss factor of 1dB/ms. This shows the steady state occurring before severe damping losses are seen (after an energy drop of 6dB). Further increase of the coupling loss factor would make this steady state occur sooner.

#### 5.4.4 Multiple fields

So far a model has been developed which can predict the energy flow and partitioning between two coupled fields. The situation is further complicated by considering models made up of more fields. A practical example of this is a plate structure consisting of two substructures which are connected by an asymmetric notch. As we have seen in Section 5.3, the asymmetry will cause mode conversion from symmetric to anti-symmetric modes (and vice versa). Therefore the corresponding SEA model will contain four fields, one symmetric and one anti-symmetric in each substructure. The coupling loss factors previously calculated can be used to predict the response of this structure. Figure 5.14 shows the predicted response of two identical 5mm thick plates coupled by an asymmetric notch of 1.25mm thickness (75% depth).

The predicted results show that the time taken for the steady state energy balance to occur is of the order of 1ms; this is very short compared to the reverberation time measured for such a structure and demonstrates strong coupling. The steady state ratio of energy predicted is predominantly  $A_0$ , the ratio of  $A_0$  to  $S_0$  energy being 2.2:1.

There are two factors which have been found to affect this ratio. Firstly the reflection frequencies of the  $A_0$  fields are lower than for  $S_0$ , due to  $A_0$  having a lower group velocity. A lower reflection frequency causes less mode conversion since mode conversion is caused by reflection from the asymmetric notch. This effectively causes energy to be stored in the fields with lower reflection frequency. The ratio of

reflection frequencies in this case is 0.59:1,  $A_0$  to  $S_0$ , from which we can predict that the ratio of energy between  $A_0$  and  $S_0$  will be 1.7:1.

Secondly, if we look closely at the reflection coefficients for this geometry, see Appendix A, we see that the mode conversion coefficients are consistently higher for conversion from  $S_0$  to  $A_0$  than from  $A_0$  to  $S_0$ , this ratio is 1.3:1. Combining these two effects the expected steady state energy ratio is 2.2:1, which equals the actual predicted value.

The prediction shown in Figure 5.14 was repeated for a different set of initial conditions to assess the effect on the final partitioning of energy, see Figure 5.15. The initial conditions were set such that all the energy originated in the  $S_0$  field in substructure 1 (rather than the  $A_0$  field as in Figure 5.14). As expected the final ratio of energies is identical and this steady state is reached in the same time ( $t^*$ ).

This result agrees well with the theories of Weaver (1982) and Egle (1981) who predicted a higher proportion of transverse waves in diffuse fields generated in bulk material with a ratio independent of initial energy partitioning.

## 5.5 Conclusions

The SEA theory is not limited to a system containing coupled substructures. It is equally applicable to a system containing groups of modes, say symmetric and anti-symmetric branches of Lamb modes. Modes are treated as individual fields (in an identical fashion to substructures) and the mode conversion at boundaries and asymmetries in the structure are treated as the coupling elements. Using the SEA model it is possible to model such coupled structures and predict their response to a transient energy source.

Strongly coupled systems are defined as those in which the coupling terms (between fields) are higher than the damping terms in any individual field. If fields are strongly coupled the energies in the individual fields will reach a steady state ratio, that is to say that their decay rates will all become equal.

The ratio of energy between fields is governed primarily by the reflection frequency of each field, high reflection frequency giving rise to high coupling losses to other fields and vice versa.

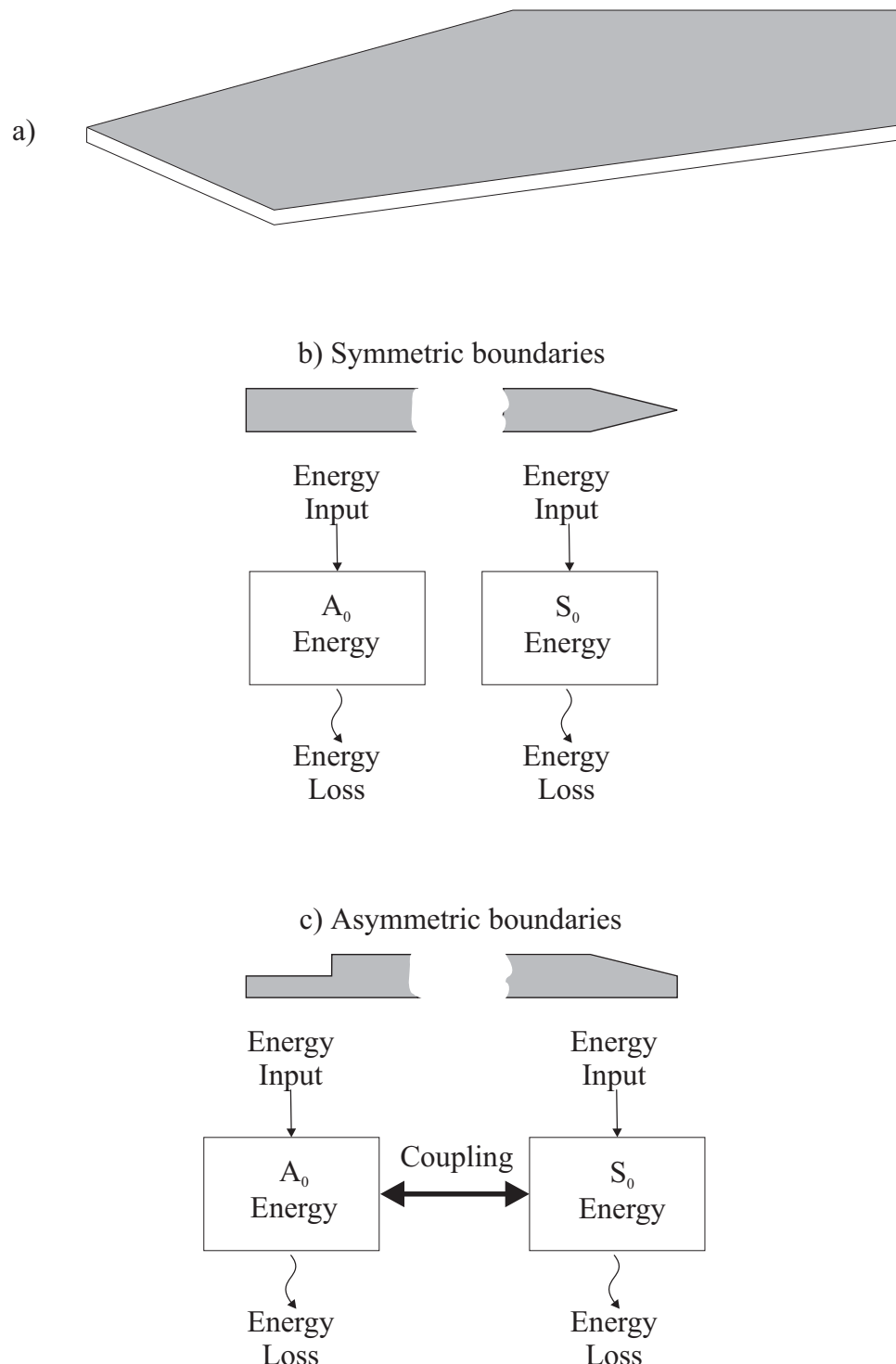


Figure 5.1 a) A simple plate structure b) Symmetric boundaries do not allow mode conversion and two separate fields of  $S_0$  and  $A_0$  exist c) Asymmetric boundaries promote mode conversion which couples the  $S_0$  and  $A_0$  fields.

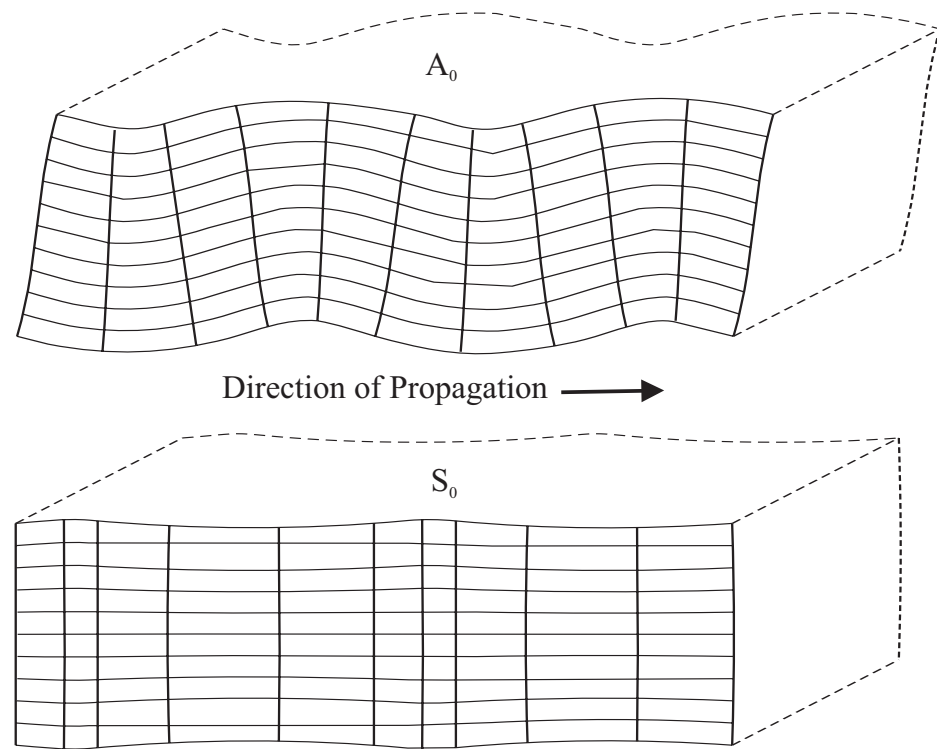


Figure 5.2 Mode shapes for the fundamental Lamb modes  $S_0$  and  $A_0$  at 0.75MHz-mm.

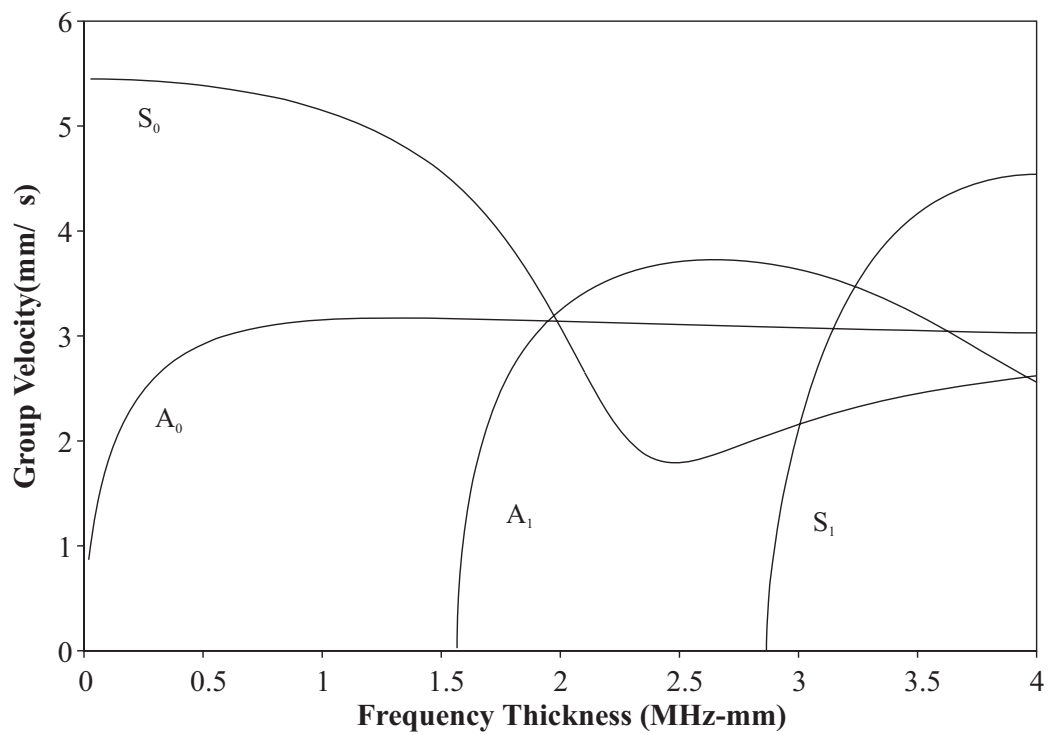


Figure 5.3 Group velocity dispersion curves for the first four Lamb modes on a 5mm thick aluminium plate in vacuum.

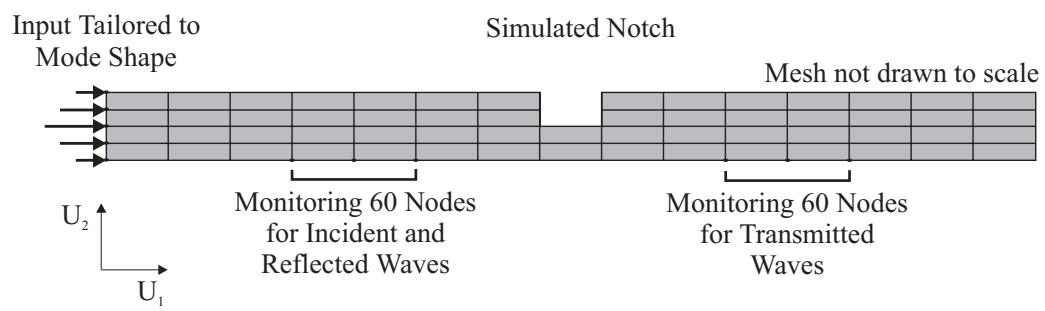


Figure 5.4 Example of the finite element mesh used for reflection, transmission and mode conversion coefficient calculations.

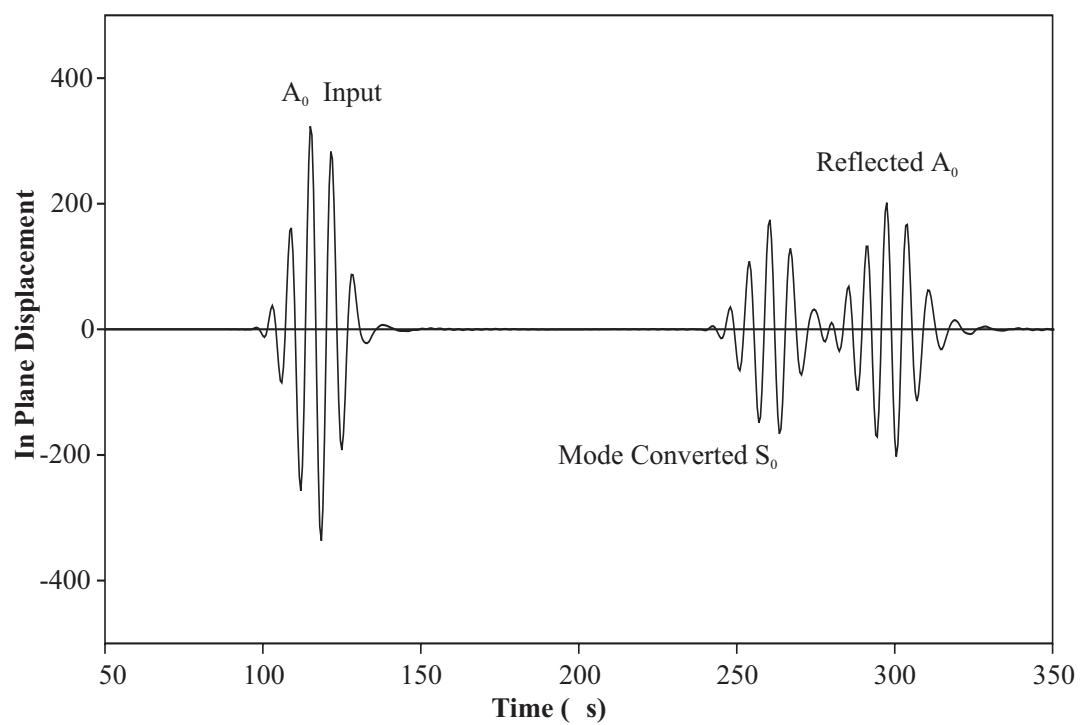


Figure 5.5 A finite element predicted time domain trace of the incident and reflected signals from an asymmetric notch.

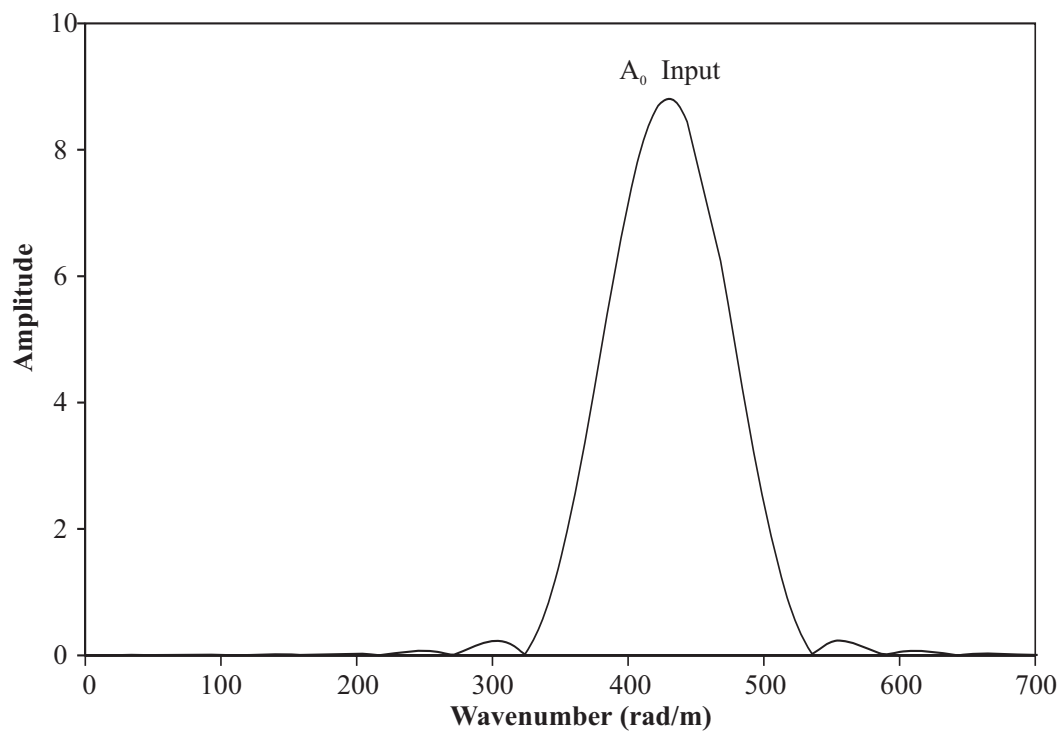


Figure 5.6 Two-dimensional Fourier transform (2-D FFT) of the incident signal at 150kHz showing a single peak corresponding to  $A_0$ .

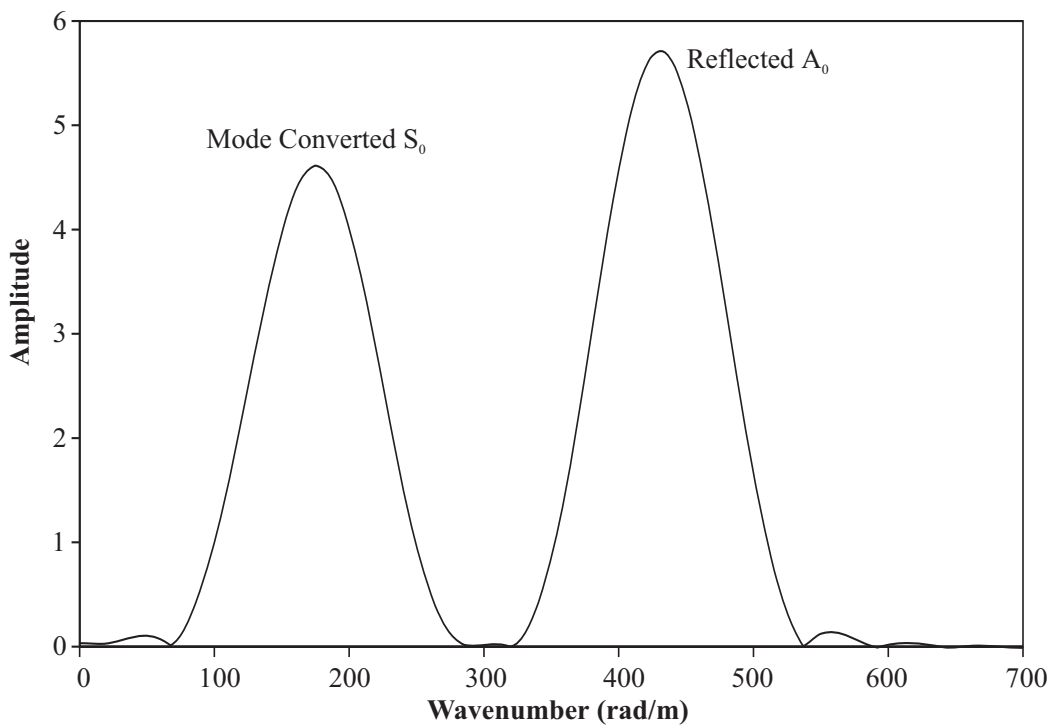


Figure 5.7 Two-dimensional Fourier transform (2-D FFT) of reflected signal at 150kHz showing peaks corresponding to the reflected  $A_0$  and mode converted  $S_0$ .

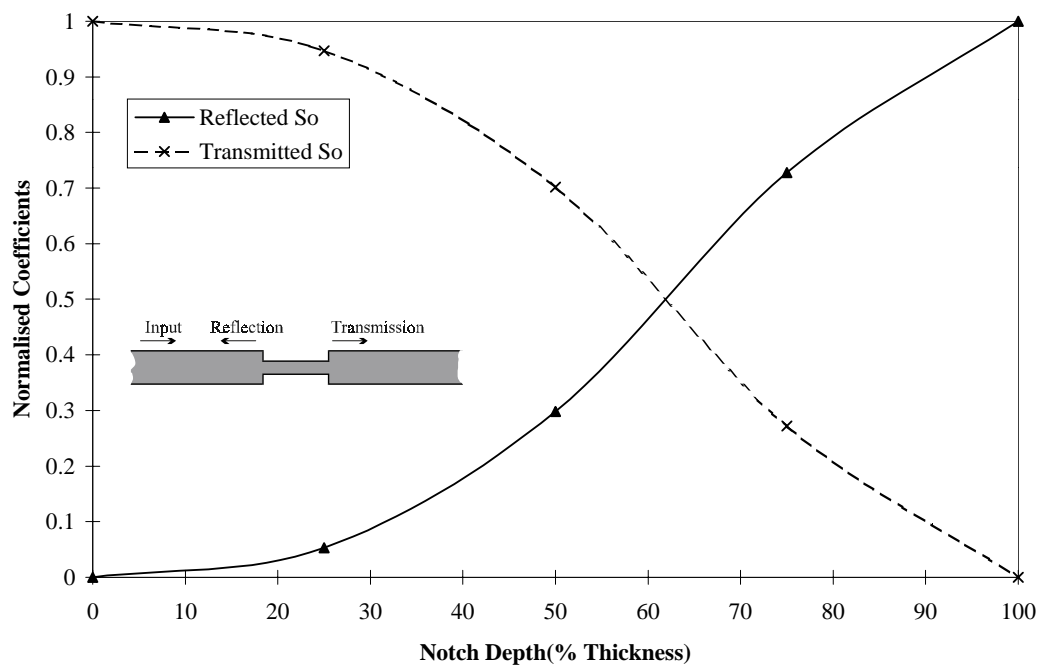


Figure 5.8 Reflection coefficients calculated for a symmetric notch at 150kHz.

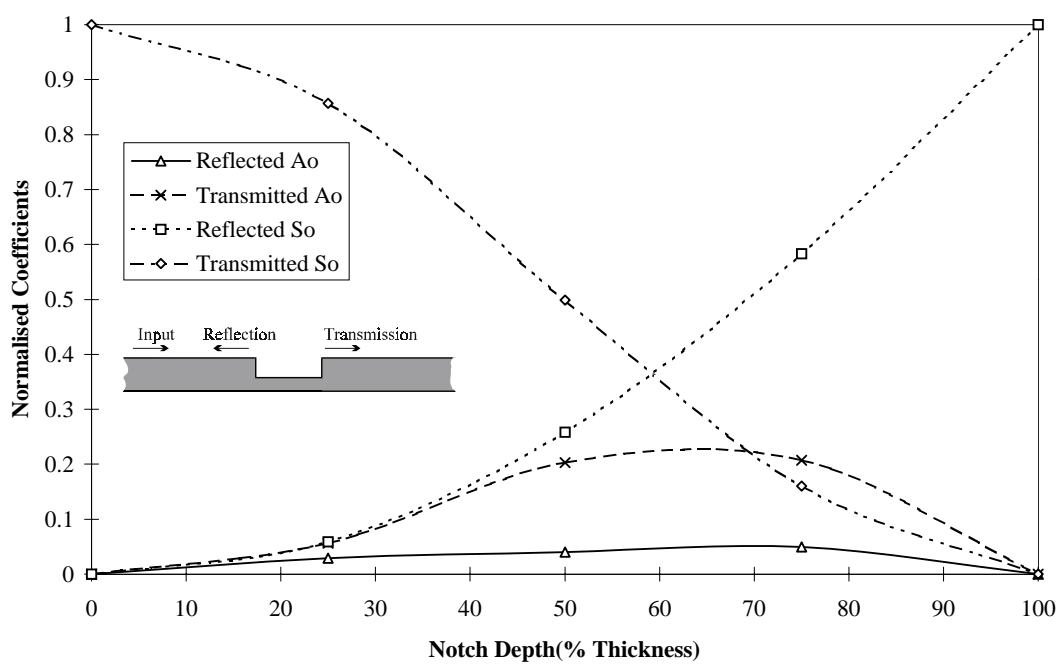


Figure 5.9 Reflection coefficients calculated for an asymmetric notch at 150kHz.

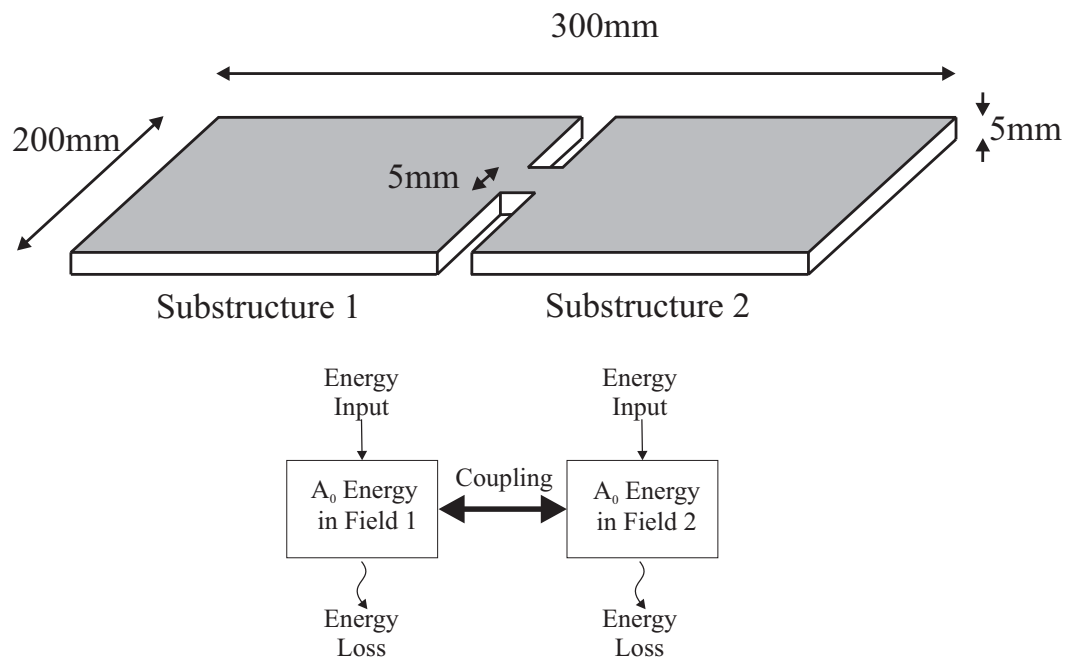


Figure 5.10 The geometry and SEA model for a simple plate system without mode conversion.

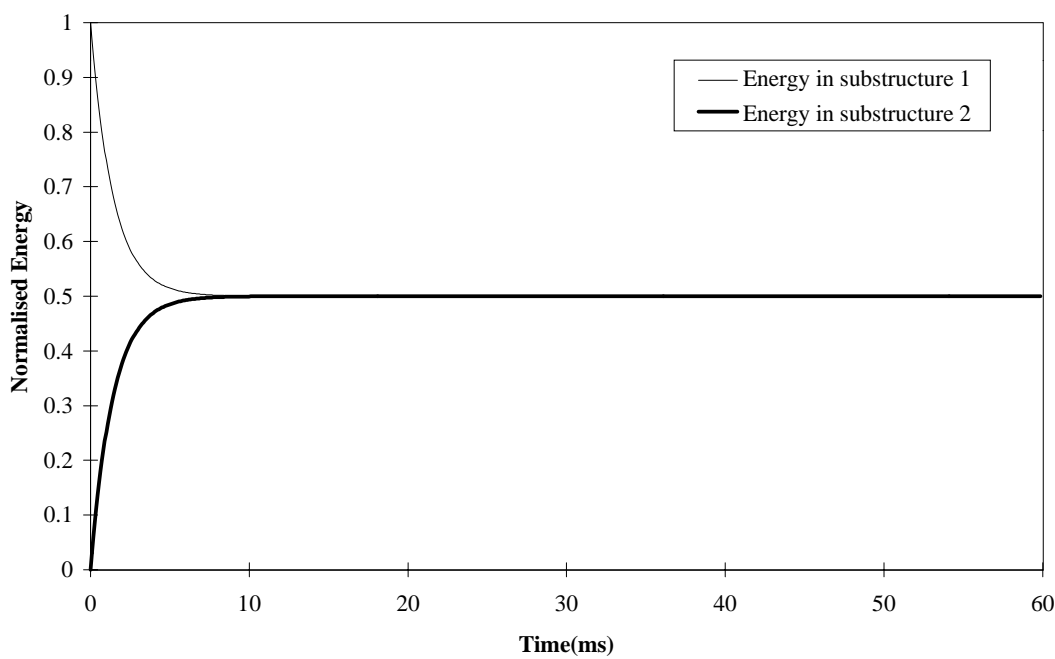


Figure 5.11 The predicted response of the SEA model shown in Figure 5.10 without damping, showing clearly the steady state partitioning of energy.

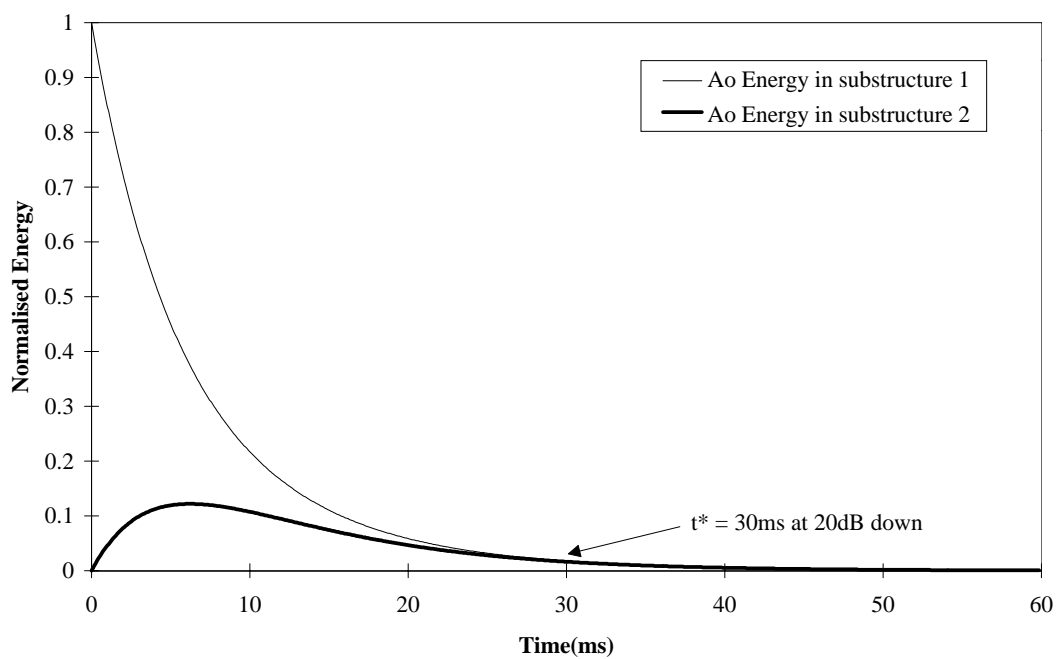


Figure 5.12 A weakly coupled system showing the predicted value of  $t^*$ .

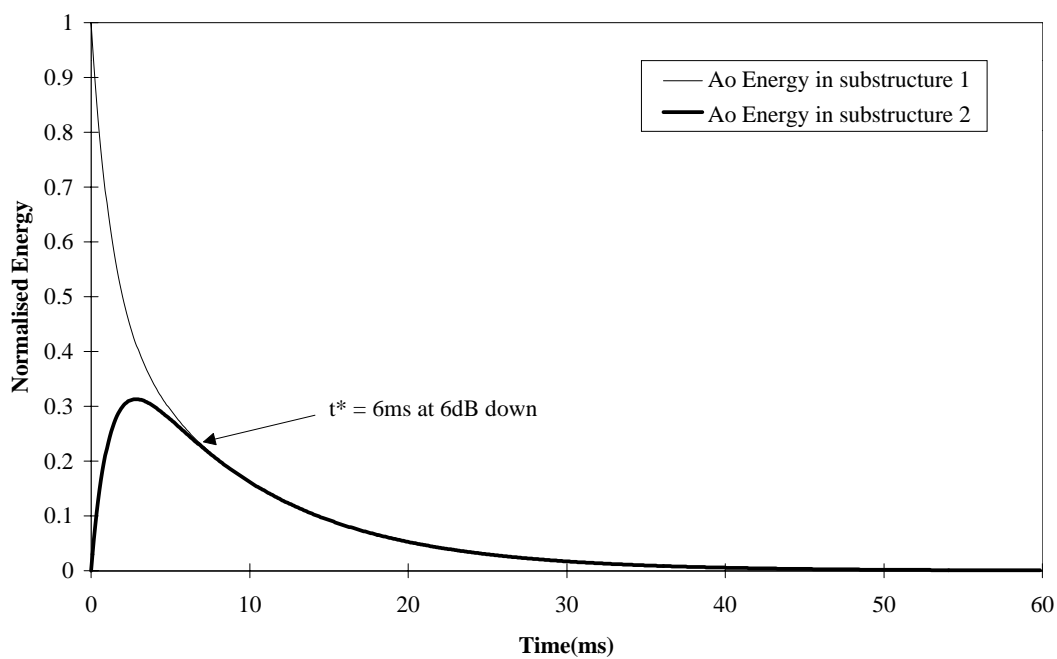


Figure 5.13 A strongly coupled system showing the predicted value of  $t^*$ .

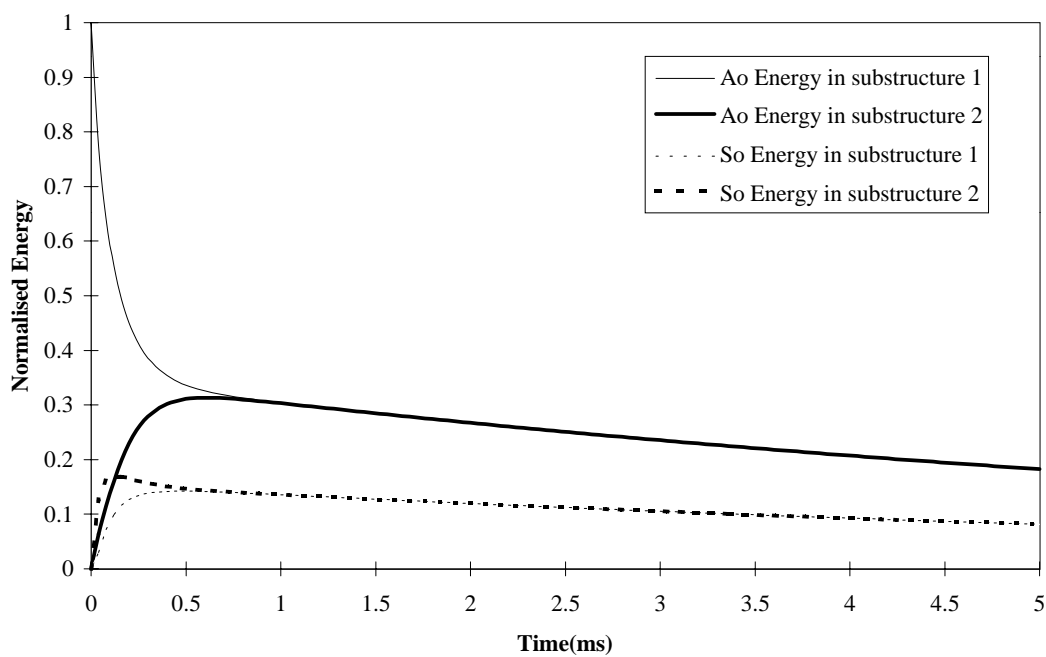


Figure 5.14 Predicted response of a plate system coupled by an asymmetric notch with  $A_0$  input in substructure 1.

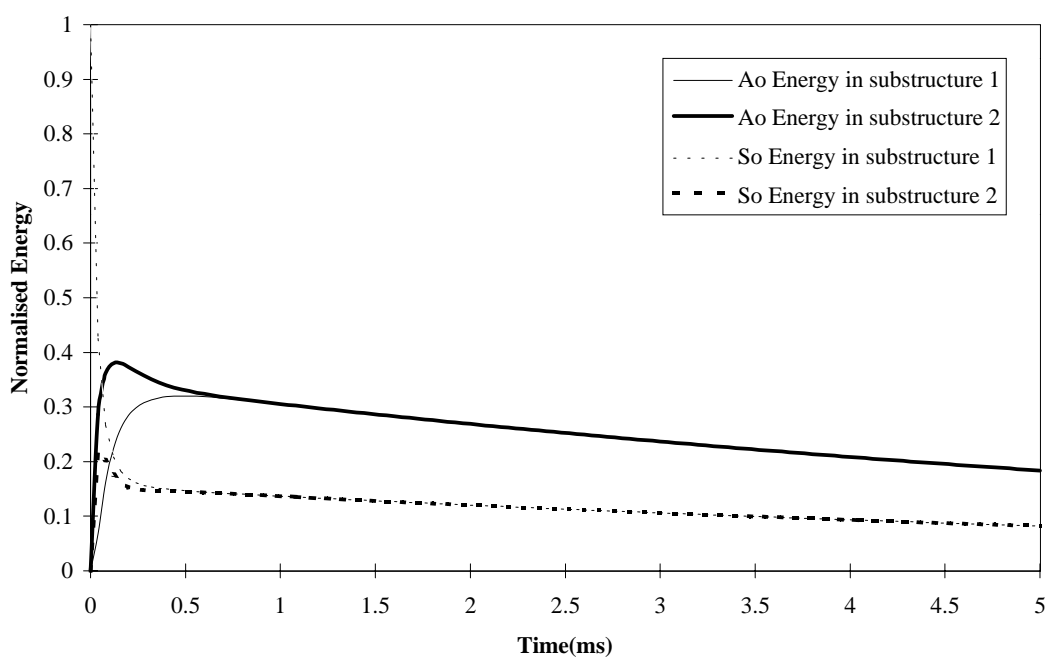


Figure 5.15 Response of the same plate system as used in the previous figure with  $S_0$  input in substructure 1 demonstrating the same  $t^*$  and final energy ratios.

# 6. Measurement of diffuse fields in structures

---

## 6.1 Introduction

### 6.1.1 Overview of chapter

This chapter describes diffuse field measurements which have been carried out on a variety of plates ranging from plane plates to assembled structures. The development manufacture and calibration of the experimental equipment required for these measurements has been discussed in previous chapters. The first section of this chapter describes how this equipment was used to both generate and measure diffuse wave fields in structures including the signal filtering and processing methods used to extract the relevant information from the measurements.

The aim of the first stage of the experimental work was to determine whether a diffuse field could be generated in a rectangular plate with plane boundaries. Experimental work carried out by Weaver (1986) has demonstrated that an aluminium plate will sustain a diffuse field when subjected to a transient point load from a pencil break source. The plate used by Weaver (1986), however, was ideally shaped to generate a diffuse field; deliberate, randomly angled notches having been cut along the edges of the structure. The rectangular plates used for the current investigation represent a more difficult case where the structure has regular boundaries and no obvious randomising influences are present. Experiments have been carried out on a number of rectangular plates of various shapes and sizes to assess the limits of the diffuse field approximation.

Following on from the encouraging results measured on the rectangular plates, a series of experiments were carried out on plate structures containing discontinuities such as joints and notches. This second stage of the experimental work was carried out to measure the extent to which discontinuities influence diffuse field generation and whether the diffuse field approximation is still valid for such structures. Several cases have been compared with the statistical energy analysis (SEA) model developed in the previous chapter showing generally good agreement. Additionally the damping effect caused by bolted and adhesively bonded joints has been measured as a function of joint overlap area (the contact area between the two structures); the importance of

this increase of structural damping is discussed, in the context of the diffuse field properties of fabricated structures.

General conclusions are made at the end of the chapter along with recommendations concerning the applicability of the technique to various types of structure.

## 6.2 Measurement equipment

### 6.2.1 Introduction

The aim of the experimental work was to study the behaviour of the wave field generated by an acoustic emission source in a structure. It is not practical, however, to use a real AE source as the generation mechanism due to the uncertainties which exist as to the amplitude, frequency content and position of real AE sources. A conical transducer was used as a simulated AE source, which enables the analysis of the structural response to a well defined, repeatable input; the repeatability of the input is an essential prerequisite if the field is to be accurately mapped. A schematic diagram of the entire experimental set-up is shown in Figure 6.1 which includes the excitation, reception, amplification and sampling stages.

### 6.2.2 Excitation

The acoustic source used throughout the experimental work was a conical piezoelectric transducer, as described in Chapter 2. Using a piezoelectric device allows the experimenter a great deal of control over the amplitude, frequency content and position of the source. The shot-to-shot repeatability of these devices is excellent which permits signal averaging and direct comparison of signals measured from different locations on the structure.

The source transducer was driven by applying a carefully controlled electrical signal in the form of a gated tone burst as shown in Figure 6.2a), with the corresponding frequency content shown in Figure 6.2b). The tone burst signals were generated using a wave-packet generator which allowed total control over amplitude, centre frequency and bandwidth of the signals. The conical transducers have been shown to be sensitive to out-of-plane motion, thus due to reciprocity, they will generate only out-of-plane force on the material surface. The contact area of the conical transducers is  $1\text{mm}^2$  which is small with respect to the smallest wavelength used (around 6mm).

Thus, the aperture effect mentioned in Section 2.2.3 is minimal and can be ignored at frequencies below 1MHz.

The structures used throughout the experiments were plates which, in the frequency range used, restricts the propagating modes present to Lamb modes, see Section 5.2.3. The bandwidth of the excitation signal is therefore extremely important as it determines the number of modes which can exist and the amount of velocity dispersion. All of the experiments were carried out within the frequency range in which only the fundamental modes  $S_0$  and  $A_0$  exist. However, as the conical transducers are only sensitive to out-of-plane motion (and only generate out-of-plane force) they are not well suited to the generation or reception of  $S_0$  within the frequency-thickness range used, the motion in the  $S_0$  mode being predominantly in-plane.

To quantify this, finite element modelling was used to predict the propagating waves generated by the source on an aluminium plate with a 5 cycle tone burst at a frequency thickness of 0.75MHz-mm. As expected only the fundamental modes  $S_0$  and  $A_0$  were generated and the ratio of  $A_0$  to  $S_0$  energy generated by the source was predicted to be 30:1. Assuming reciprocity, the transducers will be thirty times more sensitive to the reception of  $A_0$  than  $S_0$  and the combined transmit/receive response is the square of this ratio, giving a relative sensitivity of 900:1. (this ratio of  $S_0$  to  $A_0$  energy has been experimentally confirmed using the equipment shown in Figure 6.1).

### ***6.2.3 Reception, amplification and sampling***

As shown in Figure 6.1, a second conical transducer was used to detect the ultrasonic field generated in the structure. The signal from this transducer was amplified using a 40dB wide band preamplifier and filtered using a 50kHz, two pole, high-pass filter. The signal was then demodulated using an analogue demodulator with a one millisecond time constant before sampling. Demodulation reduces the bandwidth of the signal allowing it to be sampled at a lower frequency whilst preserving the signal envelope as demonstrated in Figure 6.3, showing a comparison between the demodulated and raw signals. A LeCroy digital oscilloscope was used to sample the demodulated signal, the sampling period required to capture the entire signal envelope being up to 100ms for some structures.

Given the relative sensitivity of the transducer to the  $A_0$  mode (30dB higher than the  $S_0$  sensitivity), it is reasonable to assume that the signals measured by the conical transducer are governed entirely by the behaviour of the  $A_0$  field within the structure. This decoupling of the  $S_0$  mode allows the behaviour of the  $A_0$  mode to be monitored independently which has been found to be a useful tool for measuring mode conversion, see Section 6.3.5.

#### 6.2.4 *Signal processing*

Four parameters have been measured from the demodulated signal envelopes in order to allow a quantitative comparison of the characteristics of signals measured at different locations on the structure, see Figure 6.4:

**Maximum Amplitude:** The maximum amplitude was measured directly from the signal envelopes. The shape of the envelopes, as demonstrated in Figure 6.4, means that the maximum amplitude is always near the beginning of the signal and for this reason it is reasonable to conclude that this parameter is strongly affected by the first arrival amplitude rather than any subsequent field characteristics.

**Envelope Area:** The envelope area was calculated by integrating the signal envelope between fixed starting and ending times. The beginning of the signal was taken to be time zero (the time at which the source was activated) and the end of the signal was defined as the time at which the signal decayed by 60dB from its maximum amplitude. The time interval between these two points is known as the reverberation time (Kuttruff (1973)). Initially the envelope area was measured for the entire reverberation time, however, in certain cases it has been found that it is advantageous to delay the envelope area measurement until the field has had time to become diffuse. The improvements to the diffuse field measurements gained by using a delay are demonstrated during the discussion of the large plate tests, see Section 6.3.3.

**Decay Rate:** The decay rate was measured by fitting an exponential function to the decaying envelopes; a similar technique has been used for previous diffuse field measurements (Weaver (1986)) and for the measurement of structural damping (Holroyd, et al. (1986)). As recommended in this work the beginning and end of the signal envelopes were ignored and the exponential fit was carried out using the midsection of the signal; the first few milliseconds of the signal show the randomising

of the field and consequently the decay in this region does not follow an exponential curve.

**Time Zero Amplitude:** The amplitude at time zero (as shown in Figure 6.4) was predicted by extrapolating the calculated decay curve back to the trigger time of the source, when the initial energy was transferred to the structure. The predicted amplitude of the signal at this time has been termed the ‘time zero amplitude’ (TZA). It was hoped that this value would give a consistent indication of the initial source amplitude.

### 6.2.5 Measurement of energy density

During all diffuse field measurements the important field parameter is the energy, since diffuse fields are always defined in terms of energies. It is often assumed that the energy of an AE signal is proportional to the area under the squared and demodulated signal, see Williams (1980) or Clough (1992). The envelope signals measured can be closely represented by an exponential decay function, as shown in Figure 6.4, of the form,

$$x(t) = Xe^{-\alpha t} \quad (6.1)$$

where  $X$  is the initial amplitude,  $\alpha$  is the decay rate and  $t$  is the time. Squaring and integrating with respect to time yields,

$$\int x(t)^2 dt = \frac{X^2}{2\alpha} e^{-2\alpha t} \quad (6.2)$$

which is assumed to be proportional to energy. By performing the operations in reverse order we can see a similar result, namely,

$$\left( \int x(t) dt \right)^2 = \left( \frac{X}{\alpha} \right)^2 e^{-2\alpha t} \quad (6.3)$$

This result shows that both methods yield results which are of the same form, differing only in the constant of proportionality. The energy in a signal is, therefore, simply proportional to the square of the envelope area and this value shall be termed the envelope energy. There are several advantages to be gained by squaring the signal after the envelope area measurement has been taken. The signal processing is simpler and the original amplitude and decay rate of the measured envelopes are preserved.

Before continuing it is necessary to demonstrate experimentally the proportionality between envelope energy and the actual energy in the structure. This was done by mounting the source and receiver on a 5mm thick aluminium plate of plan dimensions 0.2m×0.3m. The source amplitude was varied by known amounts by altering the peak voltage supplied by the wave packet generator; as previously discussed, the source energy is proportional to the square of the source amplitude. An envelope energy measurement was then taken at each source amplitude level and the results recorded. Figure 6.5 shows the envelope energy plotted against the energy input showing a linear relationship (the solid line is a least squares fit to the measured data). This demonstrates that the envelope energy is indeed proportional to the energy in the structure and therefore, by definition, envelope area parameter is proportional to the source amplitude.

A second experiment was carried out to measure the effect of the size of the structure on the measured envelope energy. Five rectangular aluminium plates of 5mm thickness were used; each plate had a different area and aspect ratio. The source transducer was mounted on each structure and driven with a 5 cycle tone burst at 150kHz centre frequency. The amplitude of the excitation signal remained constant for each experiment (200Vpkpk) ensuring that the source energy for all the experiments was the same.

Ten measurements were taken at random locations on each of the five structures and the envelope energies measured and averaged for each structure. The envelope energy was found to vary inversely with the plan area, the larger the plate the lower the envelope energy, see Figure 6.6. It seems likely from this result that the envelope energy is a measure of energy density in the structure (energy per square metre). If this is the case it should be possible to predict the source energy for each of the experiments on the five plates. This was done by multiplying the envelope energy by the plan area for each plate geometry which should result in the same value for each experiment. Figure 6.7 shows the predicted source energy for each plate plotted against plan area, the solid line is the mean source energy calculated from all the predictions and the error bars represent one standard deviation. The results show reasonable correlation indicating that envelope energy is reasonable indication of energy density in the structures tested.

An experimental procedure has been outlined which allows the source amplitude and energy to be calculated from measurements taken from the envelope of the received signal. Before such methods can be used to compare source energies measured on different structures it is necessary to demonstrate that the field generated within these structures is diffuse. Additionally it is important to gain an understanding of the conditions which are required for diffuse fields to be sustained.

## 6.3 Experimental confirmation of diffuse field generation in plane plates

### 6.3.1 Introduction

The diffuse field approximation, see Section 1.2, asserts that the initial source energy will become evenly distributed throughout the structure, that is to say that the energy field will become homogeneous. The measured envelope area extracted from the signal envelopes has been shown to be indicative of the signal amplitude. Determining whether a field is diffuse is then simply a case of mapping the variation of the envelope area across the surface of the structure. Additionally, as we have seen from the statistical energy analysis model, the decay rate is the same at all locations within a diffuse field, see Section 5.4.

Initial experiments were carried out on very simple structures, the intention being to excite these structures using a transient force and to measure the subsequent field across the entire surface of the structure to assess the diffuse field approximation. The excitation signal was a five cycle tone burst with a centre frequency of 150kHz having a bandwidth of 100kHz, as previously shown in Figure 6.2a) and b).

It is possible to assess whether structures are likely to sustain diffuse field by using the equations quoted in Section 1.2.1, namely,

$$\bar{l} \alpha / c \ll 1 \quad (6.4)$$

$$D_f \Delta f \gg 1 \quad (6.5)$$

where  $\bar{l}$  is the mean free path length (m) and is given by  $\bar{l} = \sqrt{A_p}$ ,  $\alpha$  is the material absorption (Nepers/s),  $c$  is the acoustic wave speed of interest (m/s),  $\Delta f$  is the

frequency bandwidth (Hz) and  $D_f$  is the modal density (Modes/Hz). For plate structures the modal density is given by,

$$D_f \approx \frac{A_p}{hc} \quad (6.6)$$

where  $A_p$  is the plan area ( $\text{m}^2$ ) and  $h$  is the thickness (m).

Equation (6.4) simply asserts that the attenuation in signal caused by one plate transit is much less than one Neper (8.7dB) and Equation (6.5) requires that the number of structural modes of vibration within the excitation bandwidth is large. These equations are guidelines only and do not stipulate any cut-off values of attenuation or bandwidth but they do provide a useful method of assessing a structure objectively for its diffuse field properties. Some recommendations are given at the end of this chapter regarding the cut-off value of attenuation for diffuse field generation to occur.

The experiments described in this chapter to determine the field generated by a source on a structure have been carried out using a single receiver. The receiver was moved to many locations on the surface of the structure and measurements were taken at each location. A major shortcoming of this technique, as opposed to using a large number of receivers sampling simultaneously, is that repositioning the receiver may affect its response and the response of the structure under test. These effects are quantified in the next section.

### 6.3.2 *Measurement of experimental errors*

Before assessing the variation of signal strengths measured at different locations on a structure it is first important to get an indication of the errors associated with each step of the measurement protocol. The major errors are expected to be due to random variations of receiver coupling and structural damping caused by the transducers themselves being removed and relocated as discussed by Dempsey and Egle (1985) and Weaver (1987).

In order to investigate the effect of each of these uncertainties on the measured parameters a series of experiments were carried out, each experiment attempting to isolate a single variable. A description of each experiment follows and the results are presented in Table 6.1.

	Max Amplitude	Envelope Area	TZA	Decay Rate
Re-coupling	6.2%	3.2%	12.4%	5.2%
Damping	1.7%	2.0%	6.6%	4.5%

Table 6.1 Experimental errors expressed as the ratio of the standard deviation to the mean value for each parameter(%).

**Re-coupling:** The first experiment was designed to measure the effect of removal and re-coupling of the transducer. It is well known that contact transducers suffer from random variations in their sensitivity which is attributed to coupling (Silk (1984) and Bainton and Silk (1980)). Coupling variations are thought to be due to changes in the contact area or angle of the transducer (if the surface is not completely flat). In order to examine this effect the receiving transducer was systematically removed and re-coupled at exactly the same location on the structure. This procedure was repeated 10 times and the received signal was measured for each coupling; the averages and standard deviations of the measured parameters were then calculated, see Table 6.1.

**Damping:** The effect of transducer relocation on the damping present in the system was then measured. This was done by placing an additional ‘dummy’ transducer onto the structure which was removed and re-coupled at ten randomly chosen locations. Each time the dummy transducer is re-coupled it is subject to the same coupling errors previously discussed and these effect the amount of damping caused by the transducer. This damping has been shown to be governed by the contact area of the transducer (Dempsey and Egle (1985)).

The results from the first experiment show that the measured parameters of area, maximum amplitude and decay rate are fairly unaffected by transducer removal and re-coupling (for the transducer set-up used). The TZA parameter is extremely sensitive to subtle variations in decay rate, not surprisingly as extrapolation of an exponential function will always lead to large uncertainties. It is interesting to note that the area measurements show better repeatability than maximum amplitude. The maximum amplitude measurement can be taken to be a direct indication of coupling efficiency (since decay rate changes will have no effect at the beginning of the signal envelope). Area measurements on the other hand will be affected by both the coupling efficiency and the decay rate; however, these effects are contradictory (poor

coupling efficiency will reduce overall amplitude and decrease the decay rate). The combination of these effects results in an improvement in repeatability.

The decay rate changes which can be seen in experiment 2 and the previous coupling experiment show that removing and re-coupling a transducer causes a change in damping of around 5%. It seems reasonable to assume that the variation in damping caused by the dummy transducer is therefore directly caused by the coupling variations mentioned and not affected by the dummy transducer location.

It can be concluded that TZA measurements are unsuitable due to large uncertainties but maximum amplitude and area measurements give consistent, repeatable results which are relatively unaffected by removal and re-coupling of the receiver. The combined effect of damping and re-coupling will be approximately the sum of the individual effects giving standard deviations of 7.9% for the maximum amplitude and 5.2% for the area measurements. The area measurement is favoured over maximum amplitude as it is an indication of the amplitude of the entire signal envelope and will be used in the experiments that follow to assess structures for their diffuse field properties.

### 6.3.3 Diffuse field verification

The experimental equipment shown in Figure 6.1 has been shown to give consistent measurements of the signal amplitude and the effect of re-coupling receiver has been quantified, see Table 6.1. In this section the experimental set-up has been used to verify the existence of a diffuse field in plate structures.

Two plane plates of aluminium 5mm thick were cut with plan dimensions of  $0.2\text{m} \times 0.3\text{m}$  and  $1\text{m} \times 1\text{m}$ , which shall be referred to as structure 1 and 2 respectively.

	E (GPa)	$\nu$	$\rho$ (kg/m <sup>3</sup> )	$\alpha_L$ (Nepers/ $\lambda$ )	$\alpha_S$ (Nepers/ $\lambda$ )	$C_L$ (m/s)	$C_S$ (m/s)
Aluminium	72.4	0.3	2710	0.00024	0.00026	5997	3206

Table 6.2 Material properties for aluminium based on Kaye and Laby (1995) and Selfridge (1985).

Table 6.2 gives the material properties which have been used, where E is Young's modulus;  $\nu$  is Poisson's ratio;  $\rho$  is the density;  $\alpha_L$  is the longitudinal attenuation;  $\alpha_S$  is the shear attenuation;  $C_L$  and  $C_S$  are the longitudinal and shear velocities respectively.

The attenuations for the material have not been measured directly as it is a difficult and fairly inaccurate measurement. The book values used are approximate as attenuation in aluminium can vary considerably with changes in alloying composition, heat treatment and cold working.

Equations (6.4) and (6.5) have been evaluated for the two plate structures of interest where the function used to excite the source was a five cycle Hanning windowed tone burst, as previously shown in Figure 6.2a) and b), having a bandwidth of 100kHz (40dB down points). The velocity of interest in these experiments is the  $A_0$  group velocity which is 3000m/s at 0.75MHz-mm for an aluminium plate in vacuum, see Figure 5.3. Measurement made on the two plate structures gave identical decay rates of 0.54dB/ms from which the attenuation of  $A_0$  has been calculated to be 62.0Nepers/s.

Structure	Modal Density (modes/kHz)	Attenuation per Transit (Nepers)	Modes in Bandwidth
1)	4	0.0051	400
2)	66	0.0206	6600

Table 6.3 Calculated parameters for plate structures with plan areas, 1) 0.2m×0.3m and 2) 1m×1m.

The results shown in Table 6.3 demonstrate that both structures satisfy the criteria stated in Equations (6.4) and (6.5). Structure 1 has an attenuation of 0.0051Nepers per transit and 400 structural modes within the excitation bandwidth while Structure 2, being larger, has a higher modal density and more attenuation per transit. The attenuation is, however, still much less than 1Neper per transit. Both structures are, according to Equations (6.4) and (6.5), predicted to sustain a diffuse field. Measurements carried out on these structures will allow the accuracy of these criteria to be judged.

Experiments were carried out on these plates where the source transducer was attached to the central region of the plate on the underside. Measurements were taken at 63 locations on the top surface of the plates in a regular grid with some locations being very close to the source, see the measurement grids indicated on Figure 6.8. Results from structure 1 were extremely consistent over the entire sample of 63 measurements. Standard deviations of the maximum amplitude and envelope area can

be seen in Table 6.4. The combined experimental errors discussed in Section 6.3.2 are given in brackets.

Structure	Maximum Amplitude	Envelope Area
1	16.6% (7.9%)	7.1% (5.2%)
2	14.8% (7.9%)	18.1% (5.2%)

Table 6.4 Standard deviations of parameters measured on plane plates expressed as a percentage of the mean value. Values in brackets show the expected standard deviations due to experimental errors.

Measurements on structure 2 were also carried out using an identical method, standard deviations are again given in Table 6.4. The standard deviation for the maximum amplitude measurements has decreased slightly, however, this change is within 2% and is not regarded as being significant. More importantly, the standard deviation for the area measurements has increased by more than a factor of 2, to 18.1%. This clearly demonstrates that the field generated in structure 2 is less uniform than structure 1 and is, by definition, less diffuse.

One possible explanation for the large standard deviation in area measurements seen on the larger plate, structure 2, is the time taken for the diffuse field to generate. Previous work has suggested that it is necessary to delay measurement of area for a short period to allow the energy to be evenly distributed (Weaver (1986)); the initial part of the signal is assumed to account for most of the variation.

This hypothesis was tested by repeating the experiment with delays of 10ms, 20ms and 30ms, to put this in perspective 10ms is equivalent to 30 wave transits across the plate and the total reverberation time for the structures was around 90ms (as shown in Figure 6.10). The variation of the envelope area measurements is shown in Table 6.5; the standard deviation of the maximum amplitude measurements was found not to vary appreciably with delay.

Delay(ms)	0	10	20	30
Area	18.1%	14.3%	14.3%	13.9%

Table 6.5 Standard deviations of the envelope area measurements, expressed as a percentage of the mean value, variation with delay.

The standard deviation of the area measurement is seen to reduce to 14.3% after 10ms and then stay fairly constant; further increases in delay time were not found to significantly affect this value. This demonstrates that the portion of the signal envelope affected by the first arrival amplitude and the gradual randomising of the field only affects the initial 10ms of the signal envelopes in this case. It can be concluded that the steady state condition is reached within the first 10ms (30 wave transits).

In conclusion, the field generated in structure 1 has been measured to have a high degree of uniformity, area measurements having a standard deviation of 7.1% and perhaps less if the experimental errors are taken into account. Area measurements taken on Structure 2 have been found to be less uniform than for structure 1 having a standard deviation of around 14.3%. The question of whether this can still be regarded as diffuse depends on what signal variation is deemed acceptable (this will ultimately be governed by the accuracy to which the source amplitude is required to be measured). A value of 15% seems reasonable at this stage, bearing in mind that the current measurement system has an inherent error of around 5%. Using this criterion both structures behave diffusely given sufficient time for the field to develop.

#### **6.3.4 Near-field effects**

During the measurements described in the previous section it was noticed that the maximum amplitude and envelope areas of signals measured at locations very close to the source were consistently higher than the averages measured over the rest of the plate. The amplitude of the cylindrical waves emanating from the source decay as the circumference of the wavefront increases, it can be shown (Kinsler (1982)) that the signal amplitude of cylindrical waves decays with  $r^{-1/2}$ , where  $r$  is the radius of the wavefront. This variation of amplitude with radius would explain the change in the maximum amplitude of signals measured close to the source (the maximum amplitude being closely related to the first arrival amplitude), however, changes in the envelope area of signals were also found.

In order to study this effect more closely measurements were taken around the source location at a range of distances. A grid of points was marked starting at zero (the source location) and extending to a distance of 20mm at 5mm intervals, see the fine

grid marked on Figure 6.8. Four locations were chosen at each distance and the corresponding signals were measured and averaged. This permitted the monitoring of the variation of signal strength with distance from the source.

The results of these measurements are shown in Figure 6.9, the error bars indicate one standard deviation. It can be seen that the maximum amplitude measurements are strongly affected by the proximity of the source within a range of 20mm (4 plate thicknesses) of the source as the maximum amplitude measurement is strongly governed by the first arrival amplitude.

The area measurement is less affected by the source proximity; the envelope area returns to a constant value at distances greater than 5mm (one plate thickness) from the source. This constant value was found to be the same as the far envelope area measured for the rest of the structure. It is difficult to explain, however, why there is any effect at all. The averaged envelopes measured at the five distances are shown in Figure 6.10. It can be seen that the four signal envelopes measured at distances of 5mm to 20mm differ significantly only in the first 3ms (where the first arrival amplitude effects the envelope). The envelope measured at the source location, however, has significantly higher amplitude throughout the entire reverberation time. This demonstrates that some energy is being trapped close to the source.

This phenomenon can be explained by considering all the waves generated by the source. Bulk longitudinal waves generated perpendicular to the transducer face will propagate through the plate and be reflected from the underside, directly back to the source location. If the plate surfaces are parallel, these waves will be trapped within the plate section directly below the source. In a practical AE measurement the source location is not usually known but it is unlikely that this near-field effect would cause significant problems as it is an extremely localised phenomenon, especially if envelope area measurements are being used.

### ***6.3.5 The effect of mode conversion on the decay rate***

The discussion so far in this chapter has assumed a single mode of propagation to be present, namely  $A_0$ . This seems reasonable given the relative efficiencies of generation and reception of  $A_0$  and  $S_0$  by the experimental equipment used, see Section 6.2.2. However, mode conversion between the  $A_0$  and  $S_0$  modes will occur

upon interaction with asymmetric features through the plate thickness (such as non-square edges), as described in the previous chapter; the rate at which this mode conversion takes place being governed primarily by the degree of asymmetry. In a general case, where some structural asymmetry exists, there will be an  $A_0$  and an  $S_0$  field present in the structure. The signals measured using the current experimental set-up can only give information regarding the  $A_0$  field, but the cross-coupling between the  $S_0$  and  $A_0$  fields may significantly alter the  $A_0$  behaviour. For example, the decay rate of the signal envelope will be governed by the attenuation of the modes present, and the steady state ratio of these modes. The attenuation of  $A_0$  due to material absorption and leakage of energy to the surroundings is far greater than that for  $S_0$  within the frequency-thickness range of interest, consequently the exact partitioning of energy between the modes present is expected to strongly affect the overall losses in the structure.

During the experiments on plane plates discussed in Section 6.3.3 it was initially assumed that the plate edges were square and no significant mode conversion was present. On closer inspection it was found that due to inaccurate machining the edges were visibly asymmetric causing rapid mode conversion from  $A_0$  to  $S_0$  and vice versa. The subsequent decay rate of the envelope must then be caused by the combined losses due to the  $S_0$  and  $A_0$  fields. To demonstrate this the plate was carefully re-machined ensuring that the edges were as symmetric as possible. The signal envelopes measured from the original and modified plates are shown in Figure 6.11, the solid line being the fitted decay rate for each envelope. The averaged decay rate measured for ten tests on the original, slightly asymmetric, plate was 0.40dB/ms with a standard deviation of 5%. The averaged decay rate measured for 10 tests on the symmetric edged plate was 0.54dB/ms with a standard deviation of 3%; this represents an increase of 26% in the overall damping of the structure. The decay rate of the symmetric plate, due to the apparent lack of mode conversion, is likely to be dominated by the attenuation of  $A_0$ . Thus the decay rate of this field should be directly indicative of the  $A_0$  attenuation in the system. Assuming only  $A_0$  propagation with a group velocity of 3000m/s this gives an attenuation of 0.021Nepers/m ( $2.89 \times 10^{-4}$ Nepers/wavelength).

Predictions of Lamb wave attenuation in aluminium have been made using Disperse, a modelling program developed at Imperial College (Lowe (1995) and Pavlakovic, et al. (1997)). Two possible mechanisms for attenuation are present, the visco-elastic properties of the aluminium and the energy leakage into the surrounding air; the attenuation values calculated for the fundamental Lamb modes due to each of these mechanisms are shown in Figure 6.12 and Figure 6.13 respectively. The attenuation caused by both mechanisms simultaneously is simply the summation of these results, therefore the calculated attenuation of  $A_0$ , at 0.75MHz-mm, due to material absorption and leakage is 0.0305Nepers/m, as compared to 0.0125Nepers/m for  $S_0$ .

As seen from Figure 6.12 and Figure 6.13 the attenuation due to both leakage and internal losses are higher for  $A_0$  than  $S_0$ . There are two reasons for this behaviour, at this stage it may help to refer back to the calculated mode shapes for the  $A_0$  and  $S_0$  modes, see Figure 5.2.

The  $A_0$  mode, at this frequency-thickness, is dominated by bending motion (i.e. a combination of out-of-plane and in-plane motion with little net volume change) and the  $S_0$  mode is dominated by longitudinal motion (i.e. in-plane motion). The internal damping of the  $A_0$  mode is therefore affected by the shear attenuation of the material (which is generally greater than the longitudinal attenuation) and the  $S_0$  mode is dominated by the longitudinal attenuation. Therefore the attenuation of  $A_0$  due to internal losses is roughly double that of  $S_0$  (for aluminium in the frequency-thickness range used) as seen in Figure 6.12 (also refer to Table 6.2 for the material properties of aluminium).

The leakage of energy into the surrounding media occurs due to the coupling of energy from the plate surface into bulk waves in the air; only longitudinal bulk waves can be generated in the air since fluids cannot support shear waves. The surface motion of the  $A_0$  mode is predominantly out-of-plane which couples well to the longitudinal waves in air; the  $S_0$  mode has mostly in-plane surface motion and consequently hardly couples into the air at all. This is reflected in the attenuations of the modes due to leakage shown in Figure 6.13.

Using the predicted attenuations for the  $S_0$  and  $A_0$  modes and the predicted steady state energy ratio between the  $S_0$  and  $A_0$  modes given in Section 5.4.4 it is possible to calculate the change in overall decay rate which would be expected due to the

presence of mode conversion. The predicted steady state energy ratio is 69%  $A_0$  and 31%  $S_0$  (a ratio of 2.2:1); as previously mentioned this ratio is governed by the ratio of the group velocities of the modes. Multiplying the calculated attenuations of the modes by this ratio yields an overall attenuation of 0.0248Nepers/m; this amounts to an overall decrease in attenuation of 19% from the pure  $A_0$  case which compares favourably with the measured reduction in attenuation of 26% going from a symmetric edged plate ( $A_0$  only) to a asymmetric edged plate ( $A_0$  and  $S_0$ ).

The difference between the predicted and measured change in attenuation is due to the inaccuracies introduced by using book values for the material (longitudinal and shear) attenuations. More specifically, the relative magnitude of the longitudinal and shear attenuations will strongly affect the  $S_0$  and  $A_0$  modal attenuations respectively.

### **6.3.6 Discussion**

The experimental set-up designed for the diffuse field measurements has been shown to give reliable and repeatable measurements. The square of the envelope area measurement has been shown to be directly proportional to the source energy and there is evidence that it is more specifically a measure of energy density at the measurement location.

The experimental results indicate that diffuse fields can be generated in plane rectangular plates without the need for deliberate randomising features. Delaying the start of the envelope area measurement was found to improve the repeatability of measurements taken on large and weakly coupled structures.

The envelope decay rate gives a repeatable measurement of the attenuation of the propagating modes present; if more than one mode is present the decay rate indicates the mean attenuation weighted by the steady state ratio of energies in the modes.

## **6.4 Experimental measurements of energy sharing in coupled structures**

### **6.4.1 Simple coupled plates**

The experiments reported so far have concentrated on plane structures without discontinuities which have exhibited broadly diffuse characteristics; however, most practical structures contain discontinuities. Any discontinuity in a structure, whether

a boundary between assembled components or a sudden change in cross section, will act as an obstruction to the propagation of energy throughout the structure.

Initial experiments have been carried out on a simple plate structure, shown in Figure 6.14. A 5mm thick aluminium plate with plan dimensions  $0.2m \times 0.3m$  was machined to simulate two plates with plan dimensions  $0.2m \times 0.145m$  connected by a 10mm long ligament. Using the SEA terminology introduced in the previous chapter the two plate sections may be regarded as substructures, the level of coupling between the two substructures being governed by the width of the coupling element. The coupling has been assumed to be proportional to the percentage of the total plate width remaining at the ligament. Therefore, in this case the coupling ligament was 2.5% of the width of the plate and so the coupling factor has been assumed to be 2.5%. The edges of the plate were machined carefully so as not to allow significant mode conversion between  $A_0$  and  $S_0$  and it is therefore assumed that  $A_0$  is the only propagating mode.

Experiments were carried out to ascertain whether this structure behaves in a diffuse manner. The source transducer was permanently attached to the central region of one substructure and measurements were taken at 10 locations on each substructure. The 10 measured envelopes on each substructure have been compared and averaged and the averaged envelopes are shown in Figure 6.15, clearly showing the diffuse field establishment time, i.e. the time at which the two envelopes coincide and decay together (the near side corresponds to the substructure in which the source is located). The initial amplitude of the envelopes shows the effect of the large first arrival signals present on the near side and the gradual leakage of this energy to the far side. The time taken for the diffuse field to generate in this case is around 3ms (50 wave transits). The standard deviation of the area measurements from all 20 locations was found to be 11% but much of this variation exists in the first 3ms where the field is not diffuse. By adding a delay of 3ms before area measurements were taken the standard deviation dropped to 7.5% which is similar to that measured on a plane plate of the same dimensions. The decay rate for both substructures was found to be 0.5dB/ms with a standard deviation of 5%; this value also agrees well with the measurements previously made on the plane structures where only  $A_0$  was present.

This simple plate case was modelled using the SEA techniques described in the previous chapter. The coupling factor between the substructures was assumed to be

2.5% and the measured damping factor of 0.5dB/ms was used. The SEA model consists of two fields, one  $A_0$  field is each substructure. The predicted response of the system using these parameters is shown in Figure 6.16 which compares favourably with the measured response shown in the previous figure. The predicted diffuse field establishment time is 6ms rather than the measured 3ms; this discrepancy could be caused by an underestimation of the coupling factor between the two substructures.

#### ***6.4.2 Plates with bolted junctions***

Bolting is a common method used for joining components in assembled structures. These joints are formed by adjacent faces of the structures being forced together by the action of one or more bolts, the intimately contacting faces providing the acoustic coupling between the structures.

Friction between the contacting surfaces of the joint also causes losses which contribute to the overall damping of the structure. It is this damping effect which is of most concern for the purposes of diffuse field measurements. As previously discussed, diffuse field generation relies on many tens or hundreds of reflections to spread the initial source energy evenly around the structure. An increase in damping will reduce the total number of reflections and may render the structure incapable of sustaining a diffuse field. Some previous work has concentrated on the damping effect caused by surfaces in contact Dempsey and Egle (1985), specifically to predict the energy loss caused by directly coupled transducers. This work has shown that the damping effect caused by transducers is directly proportional to their area of contact.

An experimental structure was made consisting of two plates of aluminium, 5mm thick, with plan dimensions 0.2m×0.14m. A row of 10 equally spaced holes was drilled along one long edge on each plate, see Figure 6.17; the substructures were then bolted together, using M5 bolts, with a range of areas of contact. The coupling between the substructures will depend on the amount of contact but, for all the possible configurations, it will be far higher than the 2.5% coupling case discussed in Section 6.4.1.

Measurements were made, using identical experimental techniques as before, at 10 locations on each substructure for 5 different structural configurations. The measured parameters of interest for each configuration are, firstly the averaged decay rate,

secondly the average standard deviation of the envelope area measurements taken across both substructures and thirdly the difference between the averaged far side and near side envelope area measurements; this difference is given in percent of the mean value with a positive sign indicating that the measurements taken on the near side were greater, see Table 6.6.

Joint Overlap Area(m <sup>2</sup> )	Decay Rate(dB/ms)	EA Std. Dev.	EA Difference
0	0.53	6.3%	-
0.0012	1.19	11.8%	+18%
0.0020	2.44	14.1%	+29%
0.0028	2.88	16.0%	+39%
0.0040	3.40	23.9%	+60%

Table 6.6 Variation of decay rate, the standard deviation of envelope area (EA) measurements and the envelope area difference between the near and far sides with the overlap area of a bolted joint.

The decay rate has been plotted against overlap area in Figure 6.18, where the error bars indicate one standard deviation and the solid line represents a least squares fit applied to the data. The results indicate a linear relationship between overlap area and damping.

The standard deviation of the area measurements taken on each individual structure shows a steadily increasing trend with joint overlap area. This indicates that the field generated in the substructures is becoming less diffuse as the damping increases, as would be expected. It is useful and informative at this stage to refer back to Equation (6.4) in order to calculate the amount of attenuation per wave transit for each overlap area as shown in Table 6.7.

Joint Overlap Area(m <sup>2</sup> )	Attenuation per Transit(Nepers)
0	0.005
0.0012	0.011
0.0020	0.023
0.0028	0.027
0.0040	0.032

Table 6.7 The equivalent attenuation per wave transit caused by increasing joint overlap area.

Previously the criterion used to determine whether a field is diffuse was that the standard deviation of envelope area measurements taken at random locations across the structure was less than 15%. This condition is only satisfied by the first three configurations, i.e. overlap areas up to 0.002m<sup>2</sup>. The equivalent attenuation per transit, see Table 6.7, for the field to be diffuse must have an upper limit of between 0.023 and 0.027Nepers/transit. This agrees well with the results obtained from the large plane plate studied in Section 6.3.3 in which the attenuation was measured to be 0.021Nepers/transit, the standard deviation of envelope area measurements being 14.3%. The individual substructures are behaving diffusely (up to an joint overlap of 0.002m<sup>2</sup>) but the question remains as to whether the structure is behaving diffusely as a whole.

The difference between the average envelope area measurements taken on either side of the joint, see Table 6.6, shows that the energy is not equally divided between the substructures; even for the smallest of the overlap areas the difference is still 18%. A delay of 3ms was used before envelope area measurements were taken, as previously described in Section 6.3.3; increasing this delay was not found to reduce the difference in envelope area measurements. The energy difference between the substructures has an increasing trend with overlap area in all cases. It can be concluded that the energy field within the bolted structure as a whole has not become truly diffuse and the two substructures are weakly coupled, see Section 5.4.3 for a description of weak coupling.

### 6.4.3 Plates with adhesively bonded joints

Adhesive joints are commonly used in aerospace structures, particularly the fuselage and wings of modern military and civil aircraft. Additionally adhesive joints are being used in the automotive industry for car body manufacture. It is important, therefore, to understand the effect of adhesive joints on the generation of diffuse fields.

An experimental structure was made consisting of two plates of aluminium, 5mm thick, with identical size and shape as the plates used for the bolted joint experiments to permit a direct comparison between the two joining methods. The joint overlap area was varied in an identical fashion as for the bolted joints and the same parameters were measured. The bonds were made using a hot curing film adhesive (REDUX 322-300GSM) which is commonly used in the aerospace industry for bonding panels and stiffeners. The adhesive was cured for one hour at 180°C and the resulting bonds were measured to be 0.1mm thick. Table 6.8 shows the results obtained.

Joint Overlap Area(m <sup>2</sup> )	Decay Rate(dB/ms)	EA Std. Dev.	EA Difference
0	0.53	5.8%	-
0.0012	0.85	7.6%	+16%
0.0020	1.24	12.3%	+18%
0.0028	1.35	6.4%	+19%
0.0040	1.28	22.8%	+59%

Table 6.8 Variation of decay rate, the standard deviation of envelope area (EA) measurements and the envelope area difference between the near and far sides of the joint with the overlap area of an adhesively bonded joint.

The measured decay rate has been plotted against overlap area in Figure 6.19, where the error bars indicate one standard deviation and the solid line represents a linear least squares fit. The decay rate exhibits a broadly increasing trend with overlap area, however, this increase is far less than that previously measured for bolted joints. Unlike bolted joints, the mating surfaces of an adhesive joint are rigidly bonded, therefore if there is no relative motion between the surfaces there can be no frictional losses. The damping increase is believed to be caused by the energy loss in the adhesive; the attenuation of the adhesive material is not known precisely but a

representative value from the literature (Selfridge (1985)) is 0.03Nepers/ $\lambda$  (longitudinal) which is more than 100 times greater than that quoted for aluminium, see Table 6.2.

The standard deviation of the area measurements taken on each individual structure shows a generally increasing trend with joint overlap area. This indicates that the field generated in the substructures is becoming less diffuse as the damping increases, as was previously found for the bolted joints. Again referring back to Equation (6.4) in order to calculate the amount of attenuation per wave transit for each overlap gives the results shown in Table 6.9. The results show that the damping is considerably less than that seen for bolted structures of the same geometry, the highest attenuation being 0.013Nepers/transit. This value is lower than the cut-off value of around 0.025Nepers/transit which was found to be the highest allowable attenuation for a diffuse field to be generated.

Joint Overlap Area( $m^2$ )	Attenuation per Transit(Nepers)
0	0.005
0.0012	0.008
0.0020	0.012
0.0028	0.013
0.0040	0.012

Table 6.9 The equivalent attenuation per wave transit caused by increasing joint overlap area for an adhesive joint.

The difference between the average envelope area measurements taken on either side of the joint is shown in Table 6.8, again a delay of 3ms was used for the envelope area measurements. The difference between these energies increases with overlap area as was seen for the bolted joints, however this increase is not proportional to overlap area. The energy difference increases slowly from a minimum of 16% (at an overlap of  $0.0012m^2$ ) to 19% (at an overlap of  $0.0012m^2$ ) then jumps suddenly to 59%. The reason for this large jump is not entirely understood although it is thought to be due to inconsistent joint properties. Again this demonstrates that the substructures are weakly coupled and it can be concluded that the energy field within the adhesively structure as a whole has not become truly diffuse.

Additional difficulties were encountered in the consistent preparation of the adhesive bonds. It was found that the cured properties of the adhesive were strongly affected by the exact curing cycle. A curing time of 45 minutes, rather than the recommended 60 minutes resulted in a doubling of the measured decay rate, the added losses being due to the visco-elastic properties of the uncured adhesive. It seems reasonable, therefore, to conclude that damping measurements could be used to continuously monitor the curing of adhesive joints during manufacture, see for example (Challis, et al. (1992)).

#### 6.4.4 Plates with step changes of thickness

The experiments carried out in the previous sections have concentrated on plates with a uniform thickness of 5mm. Many practical structures contain thickness changes due to joints, stiffening members or tapering members. It is important to understand how these thickness changes are likely to affect the diffuse field properties of the structure. Changes of thickness are expected to affect the partitioning of energy between areas of a structure, which may have important implications for diffuse field acoustic emission measurements.

The characteristics, such as mode shape and group velocity, of each mode vary with the frequency-thickness product, as shown in the dispersion curves. Thus, a change of thickness will shift the operating point to another part of the dispersion curve, assuming constant frequency.

Thickness(mm)	5	2.7	1.3
A <sub>0</sub> Group Velocity(km/s)	3.093	2.812	2.311
S <sub>0</sub> Group Velocity(km/s)	5.290	5.410	5.440

Table 6.10 Variation of A<sub>0</sub> and S<sub>0</sub> group velocities with thickness at 150kHz for an aluminium plate in vacuum.

In order to study this, two plates were machined with step changes in thickness, see Figure 6.20. Both plates had plan dimensions of 0.2m×0.3m and were machined from 5mm thick aluminium. The thickness was reduced over half the area of the plates to 2.7mm and 1.3mm respectively whilst the remaining half of each plate remained 5mm thick. Finite element predictions have been carried out to predict the reflection

coefficients of the  $S_0$  and  $A_0$  modes at these step discontinuities and the results are presented in Appendix A.

The SEA model, described in the previous chapter, was used to predict the response of these two structures which shall be referred to as Plate A (the 5mm/2.7mm plate) and Plate B (the 5mm/1.3mm plate). Figure 6.21 shows the predicted response of Plate A with the initial source input on the 5mm section. At this stage the damping is ignored in the model, the final partitioning of energy being the parameter of interest. Figure 6.21 clearly shows an uneven partitioning of energy between the  $A_0$  fields in the two substructures with a ratio of 0.87:1 (ratio of energy in substructure 1 to substructure 2); no such discrepancy exists between the energy in the  $S_0$  fields. The uneven partitioning of energy between the  $A_0$  fields can be attributed to the variation of the  $A_0$  group velocity with frequency-thickness, see Figure 5.3 (specific values of interest are given in Table 6.10). This decrease in velocity reduces the reflection frequency (number of edge reflections per second), thus providing less opportunity for mode conversion to take place in the thinner section. The  $S_0$  group velocity is relatively constant over this frequency-thickness range so the discrepancy in energy partitioning does not happen. Figure 6.22 shows the predicted response of Plate B, again a similar effect can be seen but, as the  $A_0$  group velocity has reduced further, the discrepancy has increased and the ratio of energies between the  $A_0$  fields was now found to be 0.56:1.

Measurements were carried out on the stepped plates to see if the predicted energy balance could be experimentally verified. The auto-normalising transducer, described in Section 4.4 was used as the source transducer and was mounted on the 5mm thick section of each plate and the coupling maximised. A 5 cycle tone burst at 150kHz was used as the source function, as before. Ten measurements were taken on each side of the step; the source was not disturbed between measurements.

The envelope area measurements were averaged and the standard deviations over measurements taken on each substructure were all found to be less than 8%. The envelope energy for each substructure was calculated by squaring the averaged envelope area, the energy measured is assumed to be indicative of only the  $A_0$  field due to the poor sensitivity of the receiver to  $S_0$ . These results are presented in Table 6.11.

	Envelope Energy in 5mm section	Envelope Energy in 2.7mm section	Envelope Energy in 1.3mm section
Plate A	56.0	144.1	-
Plate B	42.3	-	278.6

Table 6.11 Envelope energy in  $(\text{mVs})^2$  measured on sections of the stepped plates.

The envelope energies cannot be compared directly between the substructures of different thicknesses as the frequency-thickness change causes a change of mode shape which alters the ratio of surface displacement to energy.

The correction factors for energy, given surface displacement, were calculated in the previous chapter and are shown in Table 5.1. The relevant values are the out-of-plane displacement ( $U_2$ ) corrections for the total energy in the  $A_0$  mode at the three frequency-thickness values given (0.75MHzmm corresponds to 5mm thickness at the excitation frequency of 150kHz etc.). Applying these correction factors directly to the envelope energy values given above gives the corrected energy values shown in Table 6.12.

	Corrected energy in the 5mm section	Corrected energy reduced section	Measured ratio of energies	Predicted ratio of energies
Plate A	33.92	42.4	0.80:1	0.87:1
Plate B	26.10	41.89	0.62:1	0.56:1

Table 6.12 Corrected envelope energy(arbitrary units) measured on sections of the stepped plates and the ratio of energies in each case.

The corrected energy figures quoted in Table 6.12 should be proportional to the actual energy in each of the substructures, the quoted ratios being the ratio of energy in the thicker and thinner sections respectively. These ratios compare well with the predicted ratios calculated in Figure 6.21 and Figure 6.22 and given in Table 6.1. The predicted ratio of energies for the Plate A case was 0.87:1 and for the Plate B case 0.56:1. These experimental results demonstrate that the energy is being stored in the thinner plate section as predicted and that the energy measurements can be corrected for variations in thickness.

The total amount of energy supplied to the structure by the source is identical in each measurement, therefore, the energy contained in the 5mm thick section of plates A

and B must be different. Comparing the measurements taken on the 5mm thick section of plates A and B, gives a ratio of 1.3:1; the predicted ratio of  $A_0$  energy between these two fields is 1.22:1. Additionally, adding all of the corrected energies for structure should give the same total energy (i.e. the source energy). The agreement is fair, the total energies being 76.3 (arbitrary units) for Plate A and 68.0 (arbitrary units) for Plate B which represents a discrepancy of 11%.

#### **6.4.5 Discussion**

Measurements and predictions of the response of directly coupled plates have been carried out showing the time required for the generation of a diffuse field is in the region of 50 plate transits. Direct coupling was simulated by machining of the structures to form a thin coupling ligament between large plane sections. Theoretical predictions, based on SEA, and experimental results show good agreement as to the energy partitioning between the substructures.

Bolted joints present no problem in terms of energy transmission between substructures; the large contact areas between the connected structures provides ample energy transmission. The problem is one of damping. Bolted joints cause a dramatic increase of the damping present in structures and this damping increase was found to be directly proportional to the overlap area of the joint. None of the bolted joint specimens tested permitted the establishment of a diffuse field; although the fields in the individual substructures were found to be diffuse in some cases, the partitioning of energy between substructures was not found to be equal. This result demonstrates that the coupling between substructures for all configurations tested was weak. The strength of the coupling is given by the ratio of the coupling loss to the damping loss factor, strong coupling being when the coupling loss is larger than the damping loss. In the case of the bolted structures, as the overlap area is increased both the coupling and damping increase. It is likely, therefore that the coupling strength remains roughly constant. In conclusion, from the results presented in Section 6.4.2, it seems unlikely that structures constructed using bolted joints will behave in a truly diffuse manner as the coupling between substructures will always be weak.

Adhesive joints behave in a similar manner to bolted joints. The damping caused by an adhesive joint has been found to be considerably less than that caused by a bolted

joint but still proportional to joint overlap area. Despite the lower damping loss the adhesively bonded structures tested did not permit the establishment of a diffuse field. Additionally, changes in the material properties of the adhesive during curing were found to affect the damping strongly.

Step changes in plate thickness cause many changes in the characteristics of the modes present, such as group velocity, mode shape and attenuation. This makes it extremely difficult to make any quantitative comparisons between different locations on such a structure. Initial predictions and experiments indicate that the  $A_0$  mode energy is stored in thin sections making these ideal sites for reception of AE signals. Using the energy calibration factors calculated in the previous chapter energy measurements taken at locations with different thicknesses on a structure can be directly compared. These comparisons show good agreement with the predictions made using the SEA model developed in the previous chapter.

## 6.5 General conclusions

The experimental set-up designed for the diffuse field measurements has been shown to give reliable and repeatable measurements with experimental errors measured to be around  $\pm 5\%$ . Most of the experimental errors have been found to be due to the damping and coupling variations caused by the contact transducers. It is evident that non contact methods such as Laser, EMAT or capacitive generation and reception would produce more repeatable results. However, these methods have other disadvantages over standard contact transducers such as insensitivity, cost and robustness. The conical transducer design has therefore proved to be a good compromise.

The square of the envelope area measurement has been shown to be directly proportional to the source energy and there is some evidence that, with knowledge of the mode shape, it can be used to predict the energy density in the structure. If proven this could facilitate direct comparison of source energy on a range of structures using a simple method. The limitations and accuracy of this must be investigated further.

The field in a structure has been defined as being diffuse if the standard deviation of all envelope area measurements taken within the field is less than 15%. This value

has been arrived at arbitrarily and will depend on the final application of the technique.

Delaying the start of the envelope area measurement was found to improve the repeatability of measurements taken on several structures, this is expected to be true of large or weakly coupled structures and gives some indication of the time taken for a diffuse field to be generated. It was experimentally found that between thirty and fifty wave transits are sufficient to allow the diffusion of energy to occur.

An attenuation of 0.025Nepers per wave transit was found to be the maximum attenuation allowable for a diffuse field to be sustained in an aluminium plate at 0.75MHz-mm. This corresponds to a loss of 0.22dB per wave transit which allows 276 wave transits before the signal is attenuated by 60dB. The largest aluminium plate which was successfully measured to sustain a diffuse field had a plan area of 1m<sup>2</sup>.

Bolted and riveted structures appear to be unlikely to sustain diffuse fields in practice. This is unfortunate as these are a common form of joint found in aerospace structures. Adhesively bonded joints are also commonplace, the damping caused by adhesive joints has been shown to be less than that of bolted joints but nevertheless diffuse fields have not successfully been generated in adhesively bonded structures.

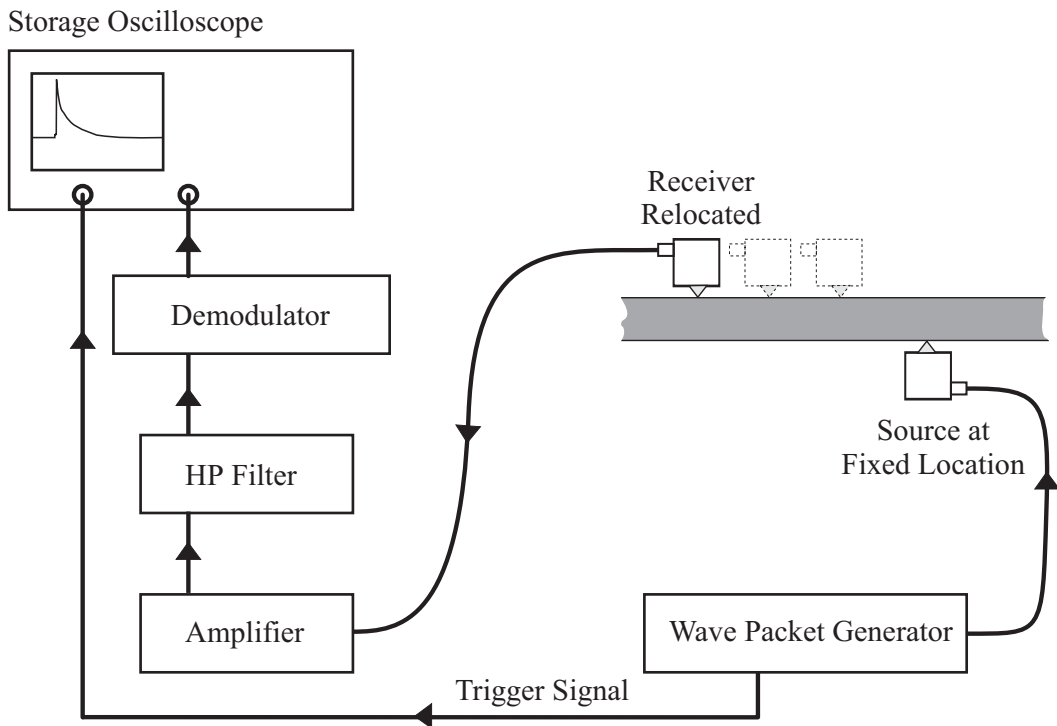
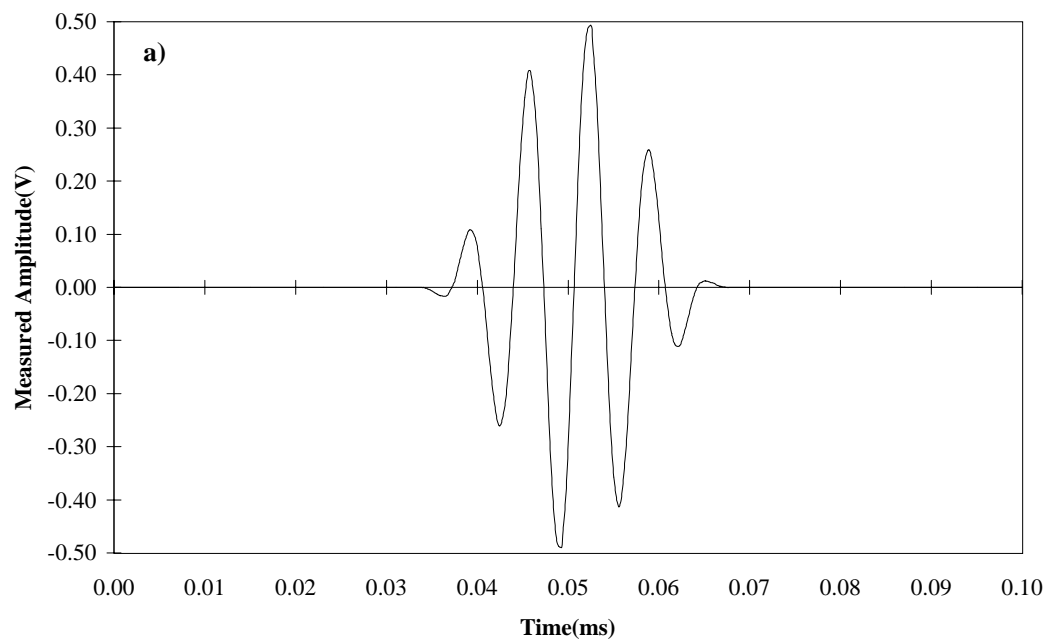


Figure 6.1. Schematic diagram of the experimental set-up showing conical piezoelectric source and receiver along with the associated signal generation, amplification, filtering and storage equipment.



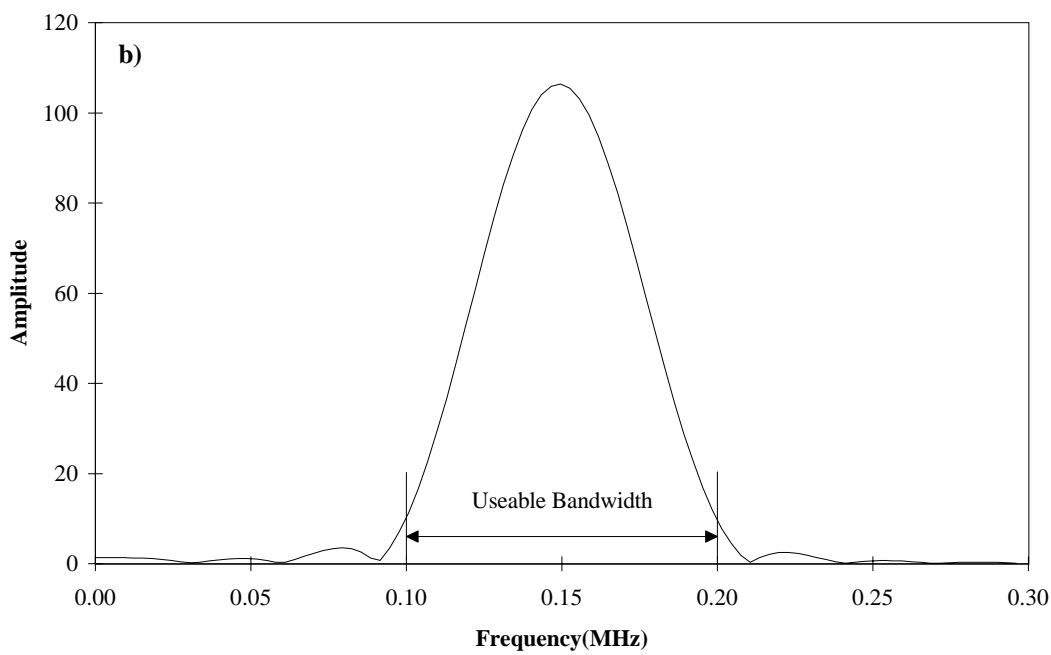


Figure 6.2 a) Five cycle tone burst signal at 150kHz, b) Corresponding frequency content.

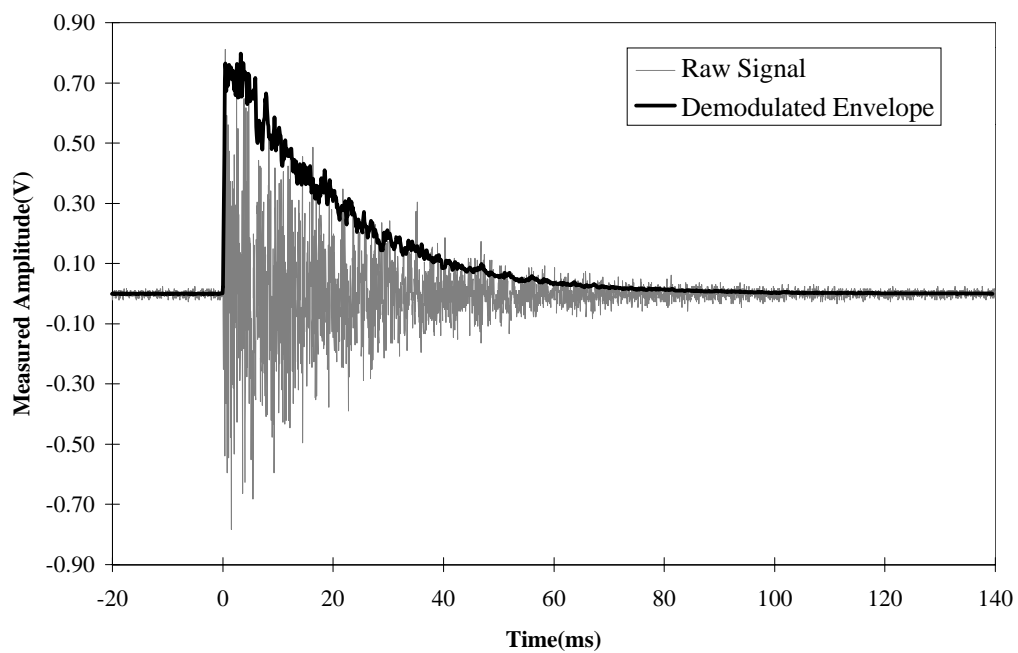


Figure 6.3 Example of raw signal before and after demodulation.

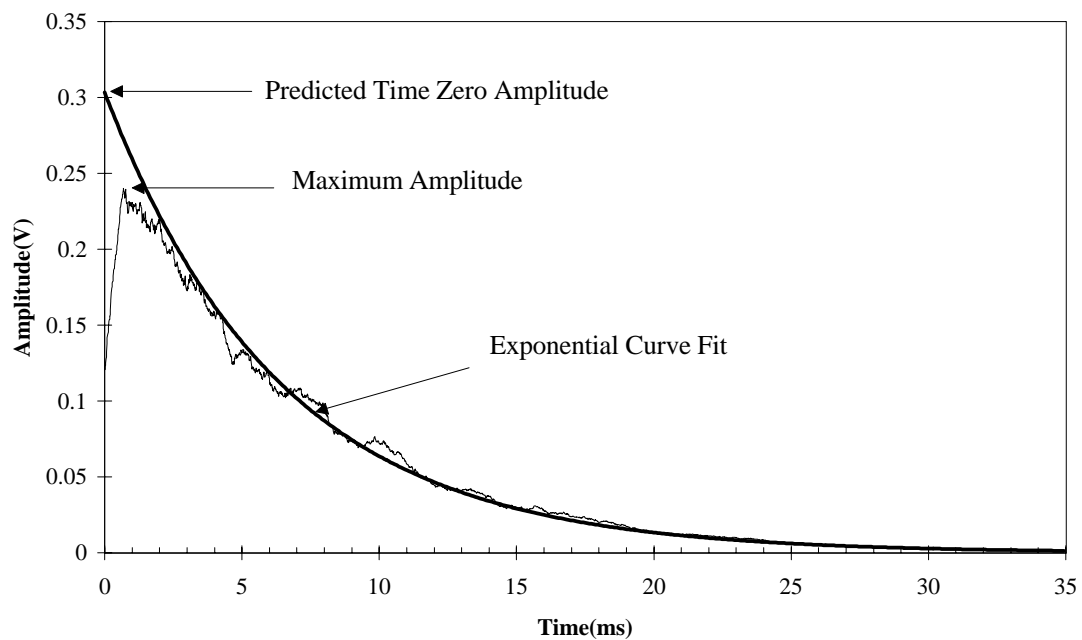


Figure 6.4 Signal processing techniques applied to the demodulated signal envelopes.

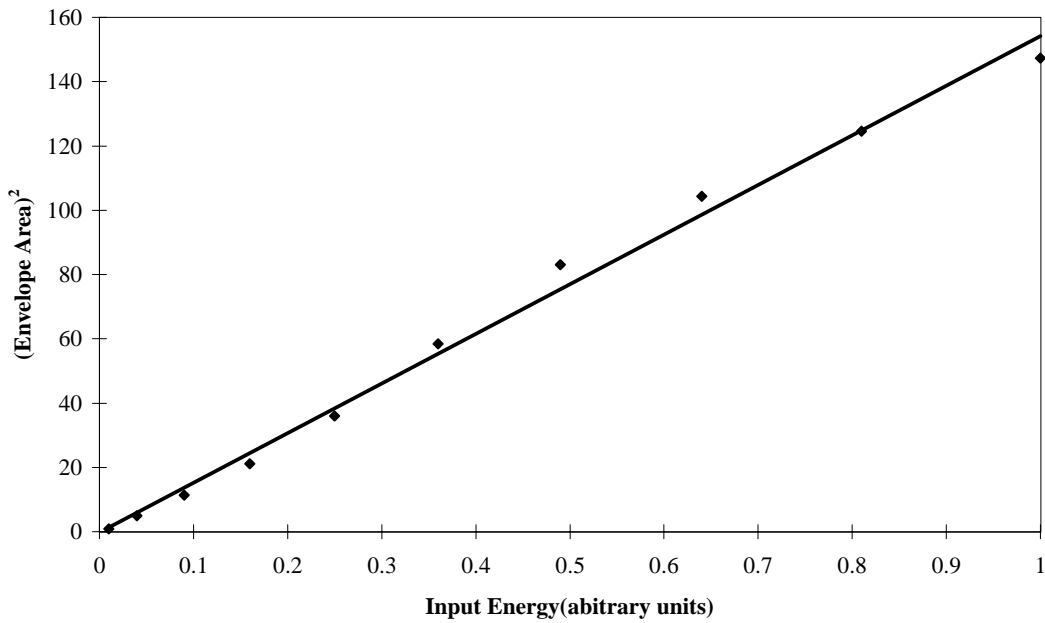


Figure 6.5 Envelope energy plotted against input energy showing a linear relationship, solid line is least squares fit.

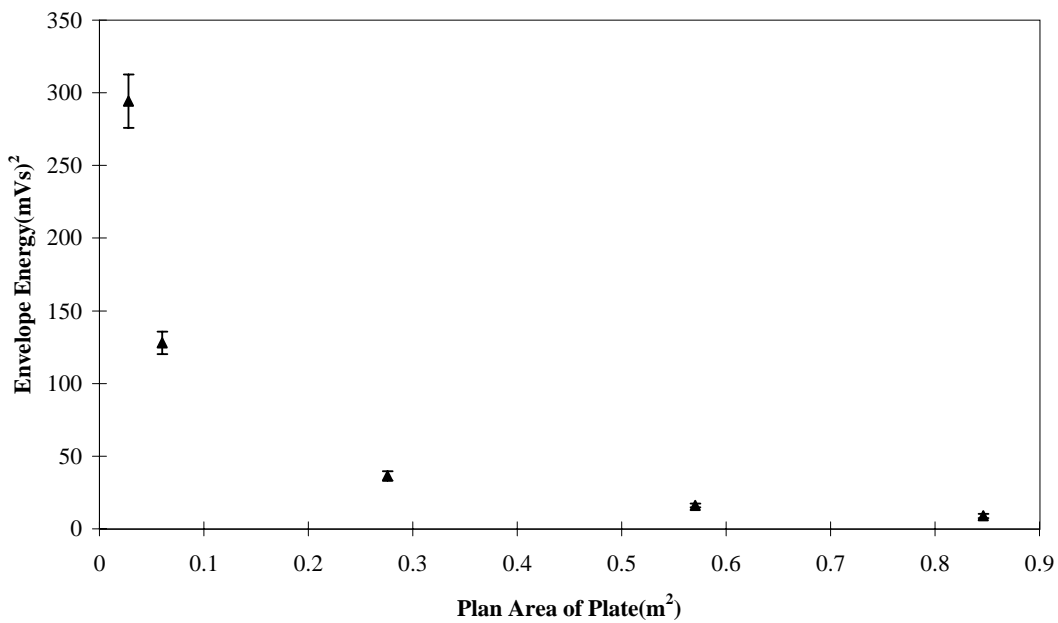


Figure 6.6 Envelope energy plotted against plan area for constant source amplitude, error bars represent 1 standard deviation.

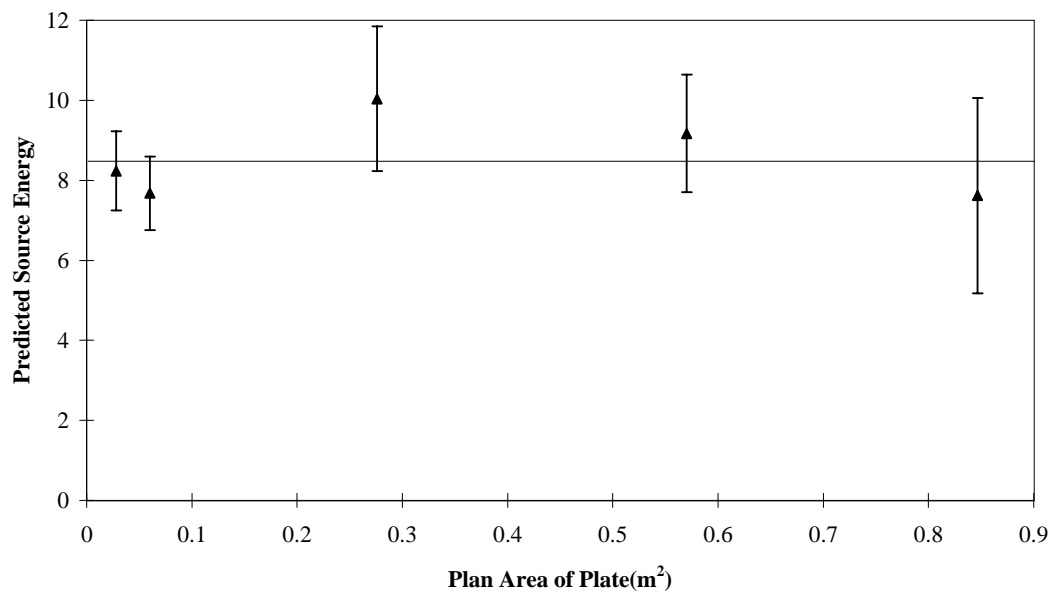


Figure 6.7 Predicted source energy plotted against plan area of structure, solid line is the mean value and error bars indicate one standard deviation.

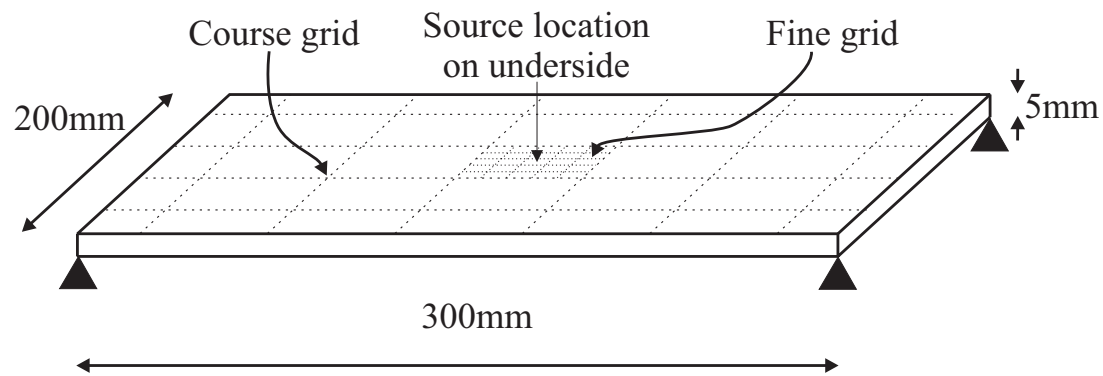


Figure 6.8 Schematic diagram of plane plate tests showing measurement grid and structural supports.

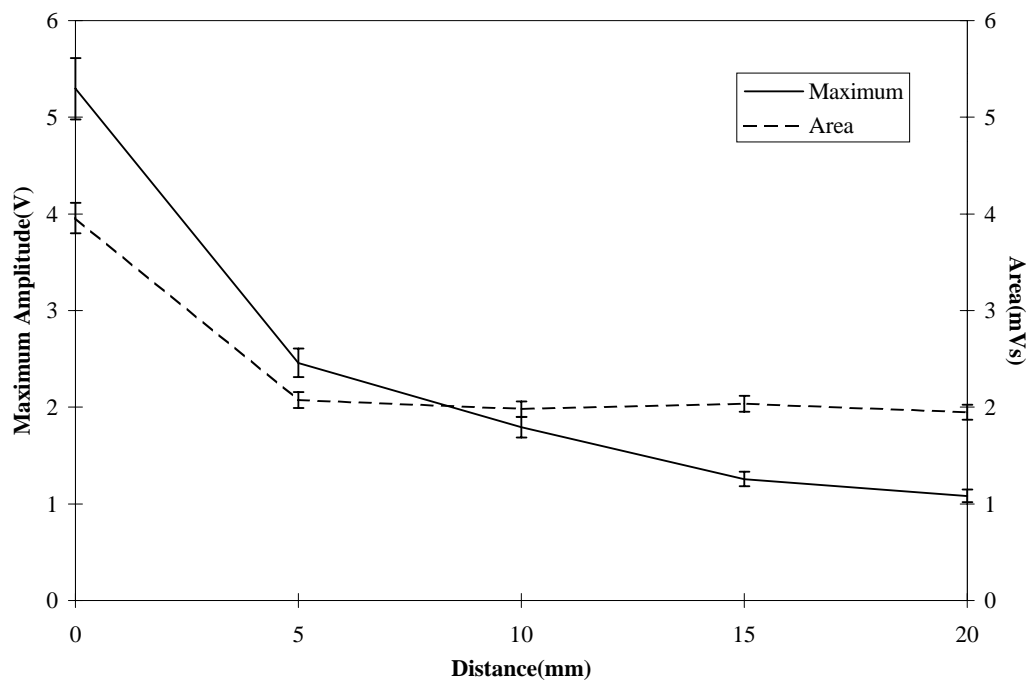


Figure 6.9 Near-field effects measured on a 5mm thick plate.

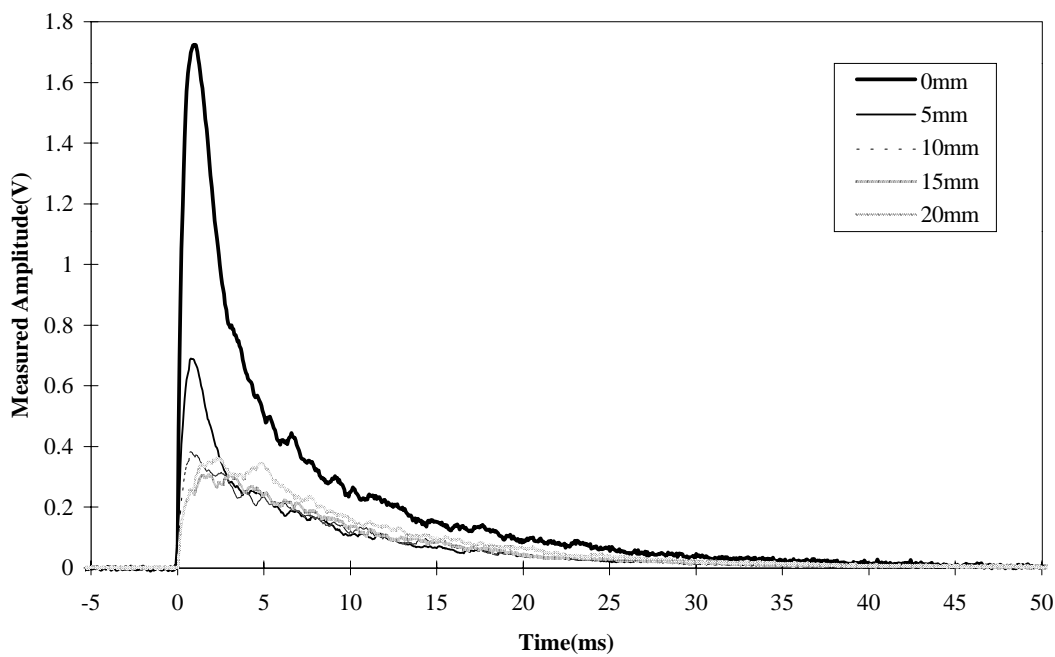


Figure 6.10 Signal envelopes measured at radial increments of 5mm from the source location.

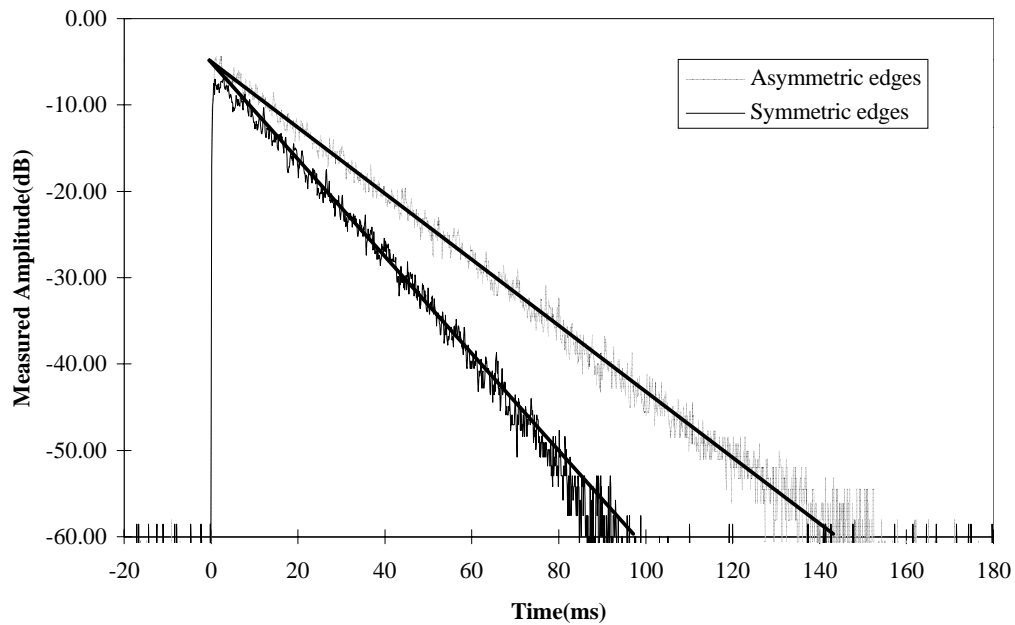


Figure 6.11 Signal envelopes measured from plane plates with symmetric and asymmetric edges showing the effect of mode conversion on the decay rate.

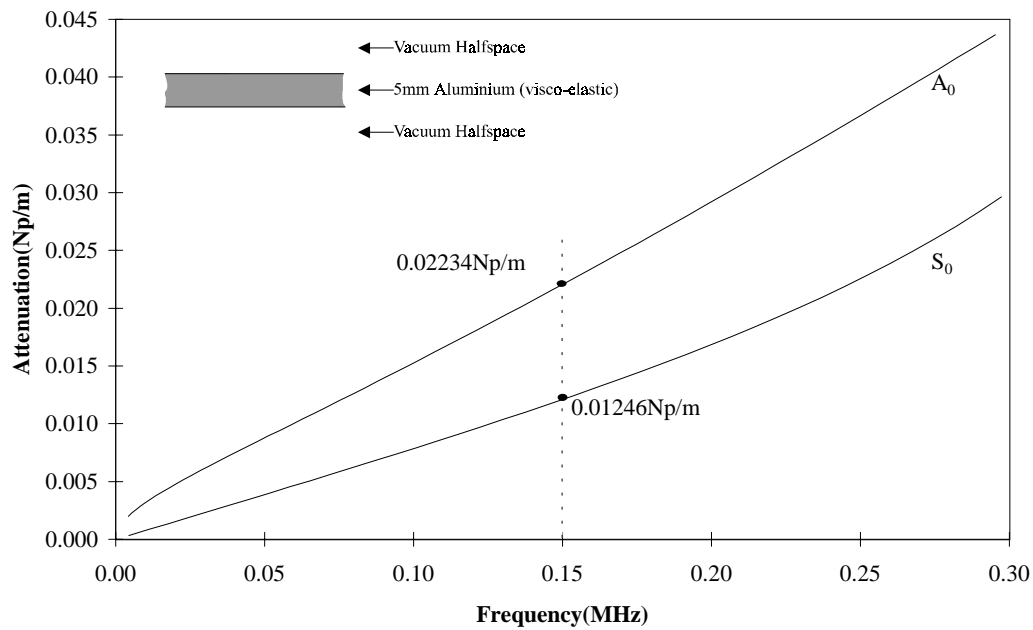


Figure 6.12 Attenuation of the fundamental Lamb modes in aluminium due to material absorption.

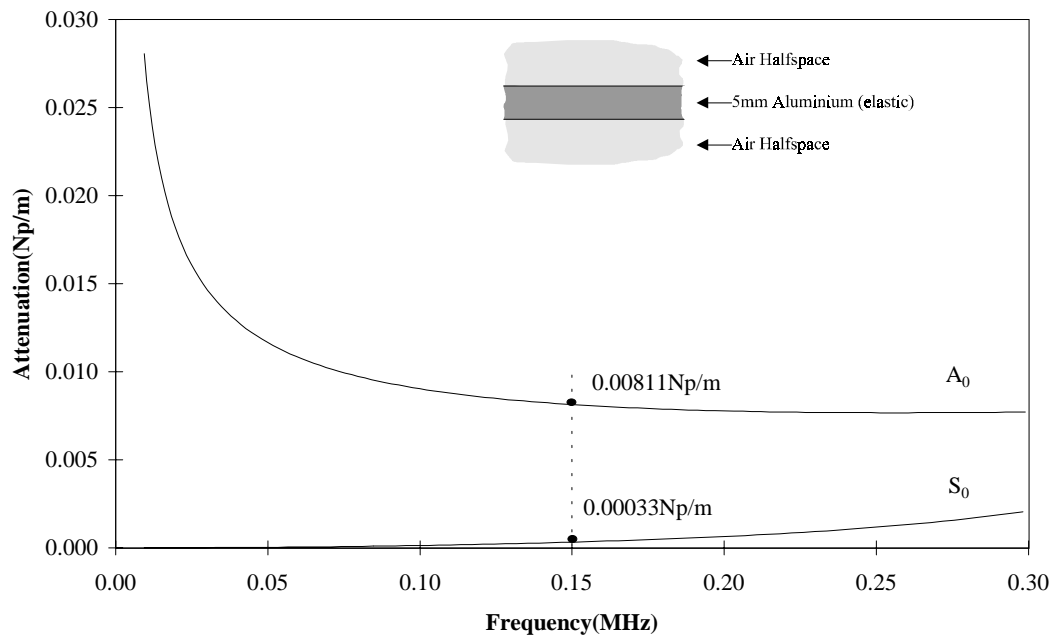


Figure 6.13 Attenuation of the fundamental Lamb modes in aluminium due to leakage into air.

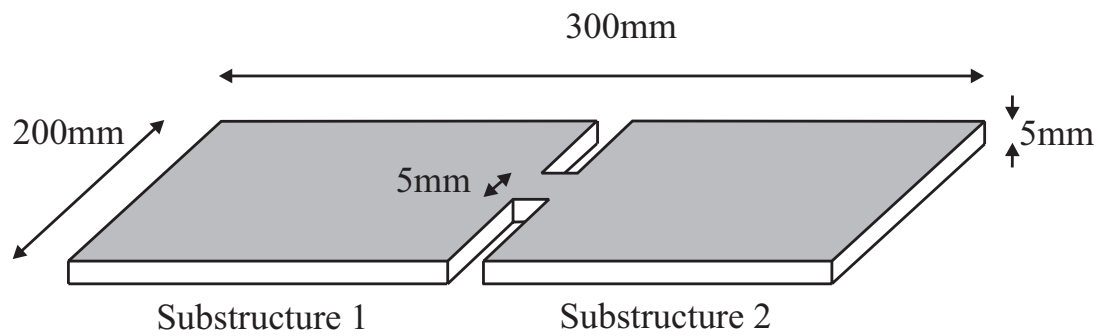


Figure 6.14 A notched plate.

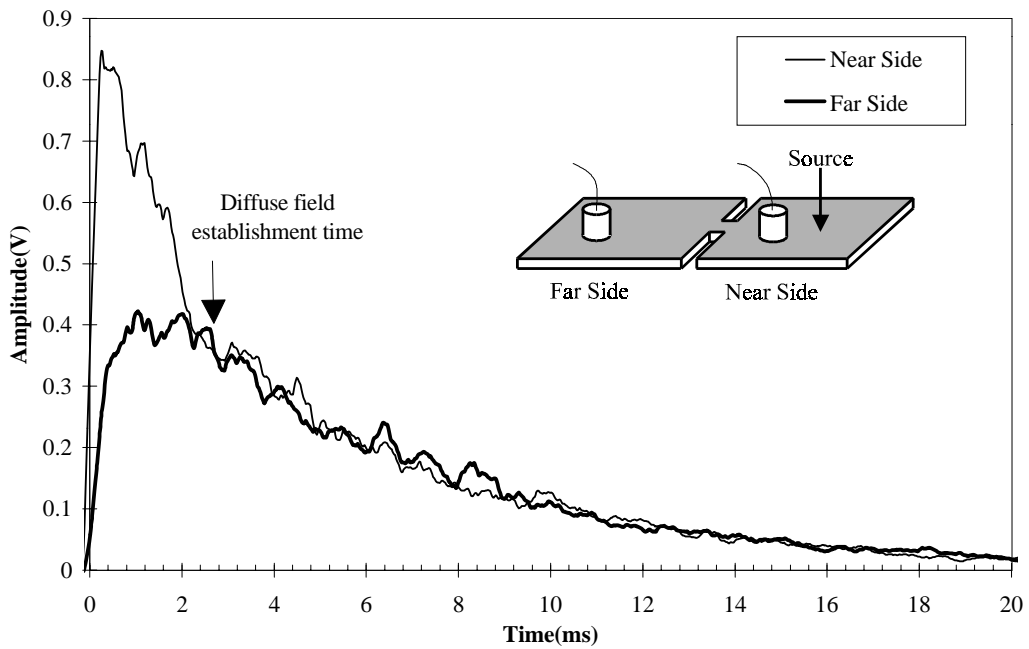


Figure 6.15 Averaged signal envelopes from notched plate substructures showing equipartition occurring.

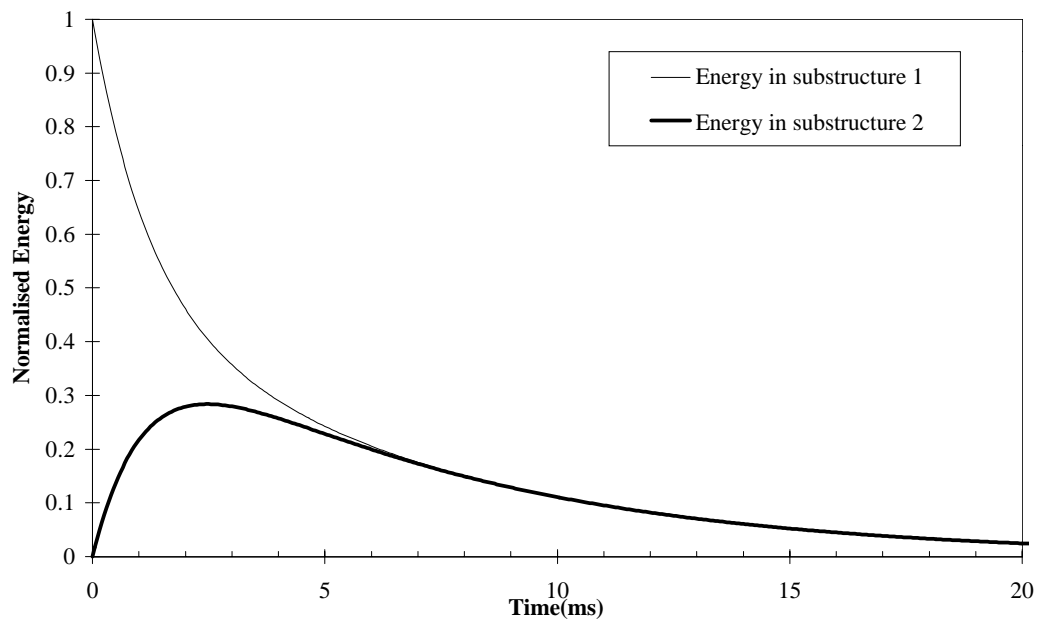


Figure 6.16 Prediction of the response of the system measured in Figure 6.15.

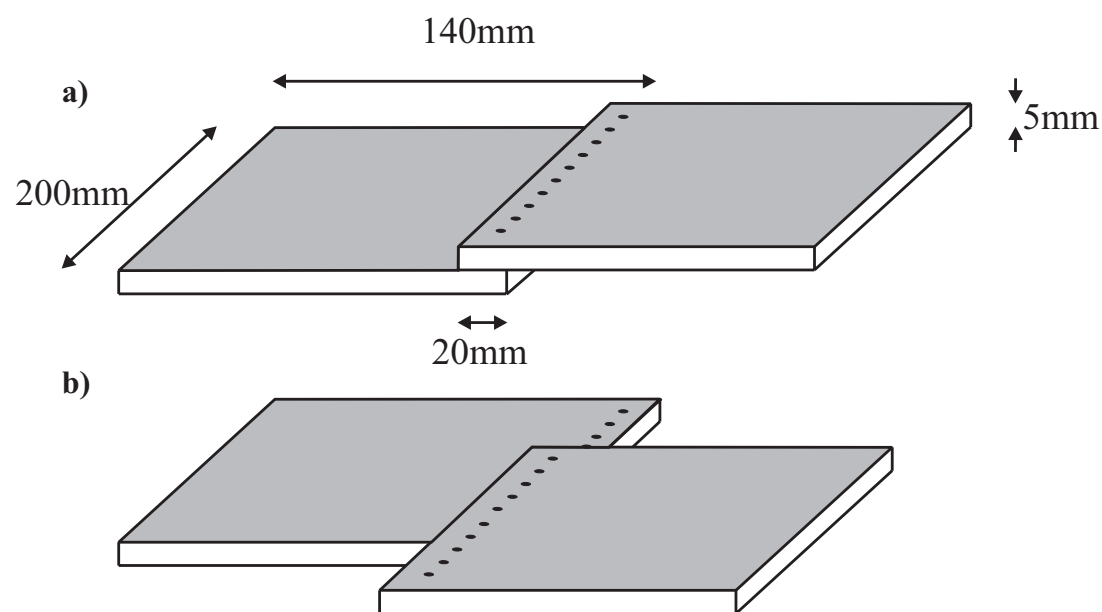


Figure 6.17 Geometry of the bolted plates used showing two possible configurations with differing overlap area.

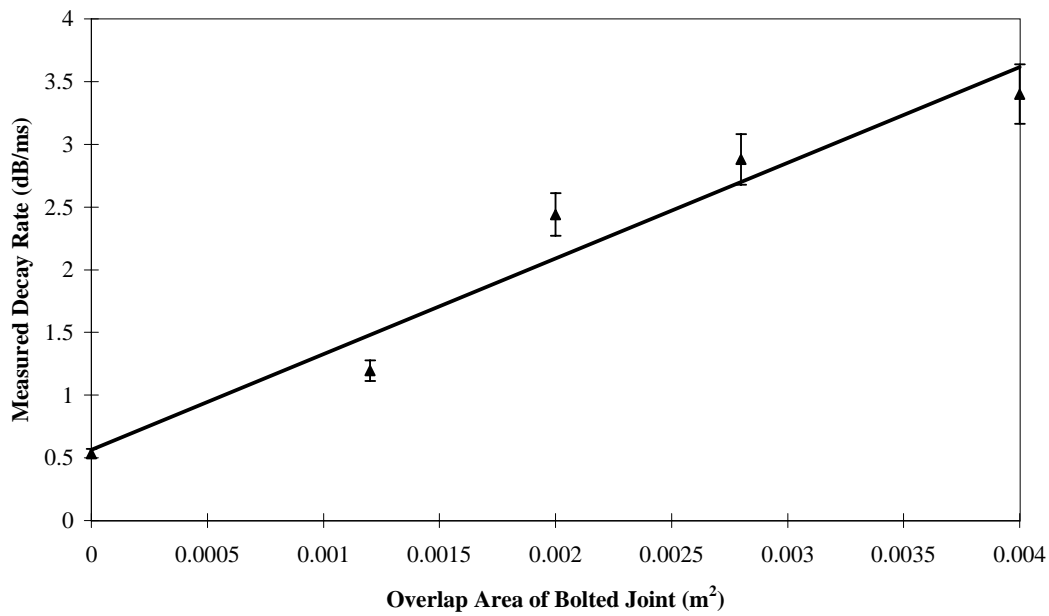


Figure 6.18 Decay rate versus joint overlap area for a bolted plate, error bars indicate 1 standard deviation and solid line is a least squares fit.

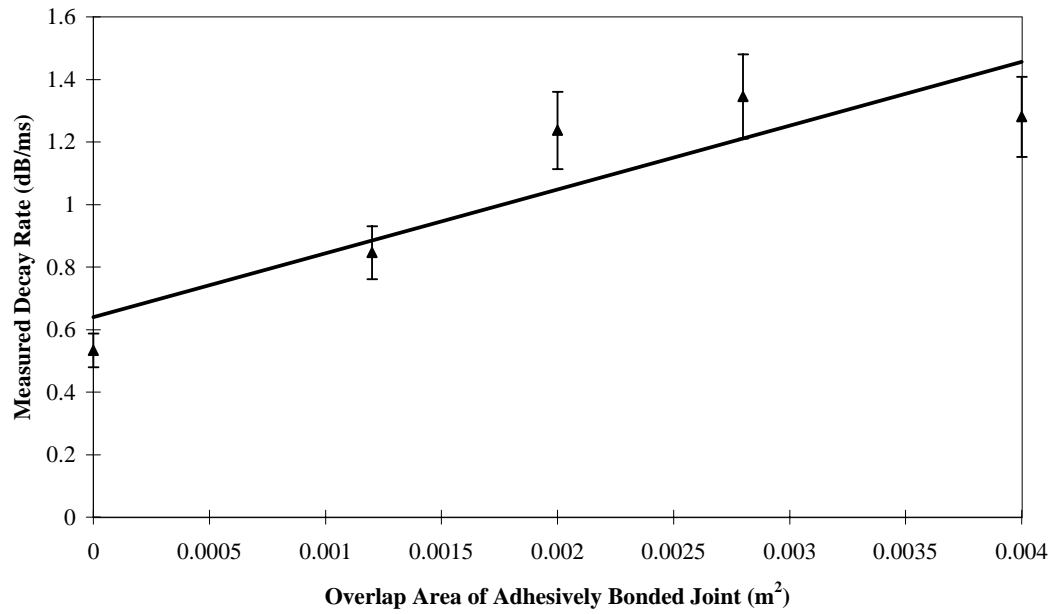


Figure 6.19 Decay rate versus joint overlap area for a adhesively bonded plate, error bars indicate 1 standard deviation and solid line is a least squares fit.

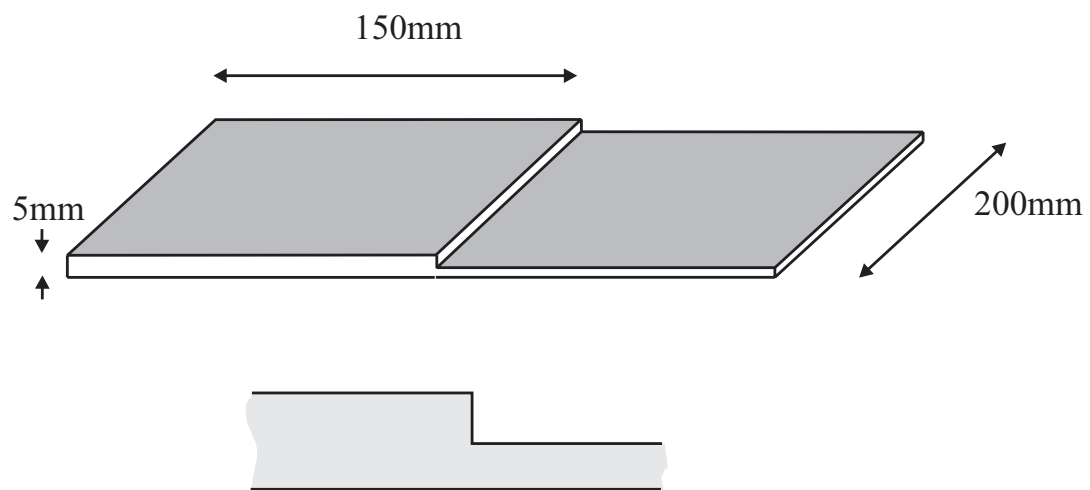


Figure 6.20 Geometry of the stepped plates used showing the cross section of the stepped region.

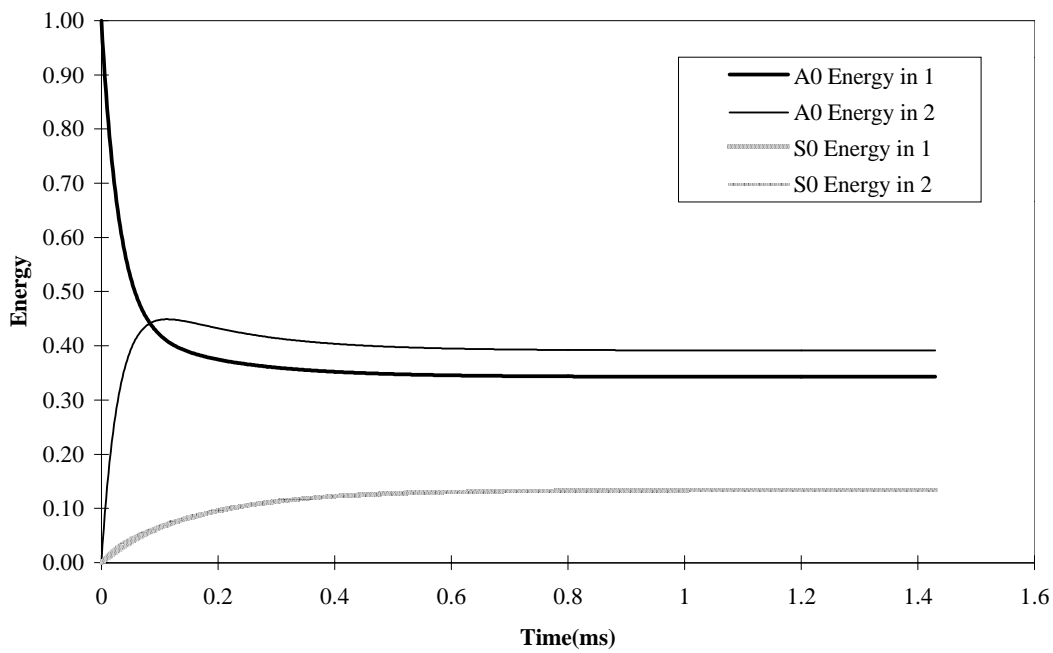


Figure 6.21 SEA prediction for the energy sharing between the  $S_0$  and  $A_0$  modes in the 5mm and 2.5mm thick plate regions.

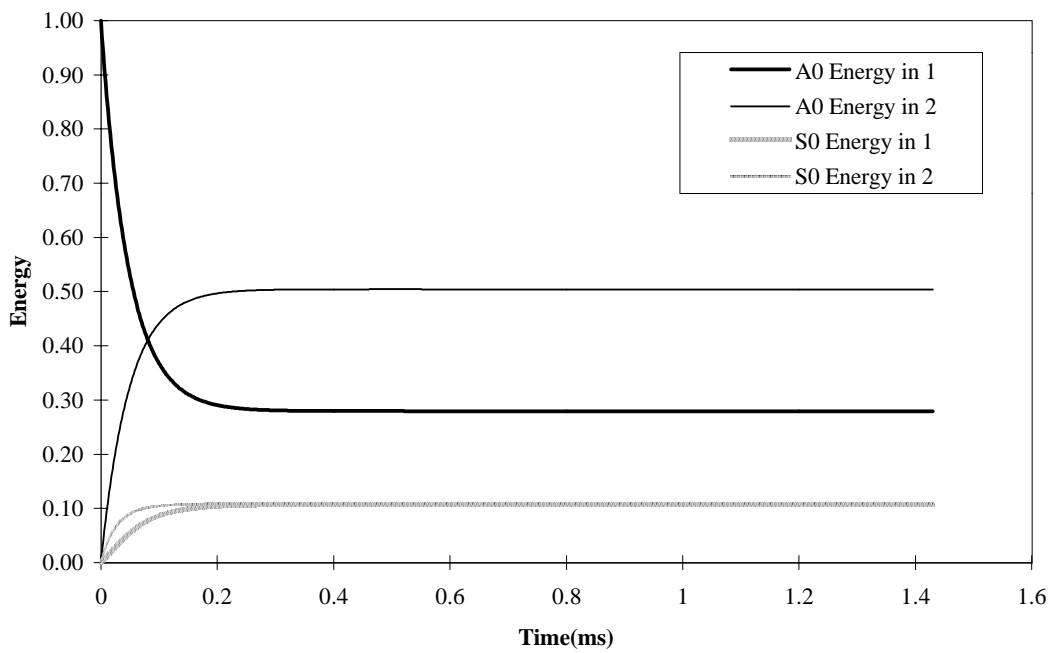


Figure 6.22 SEA prediction for the energy sharing between the S<sub>0</sub> and A<sub>0</sub> modes in the 5mm and 1.25mm thick plate regions.

## 7. Conclusions

---

### 7.1 Review of thesis

An understanding of the behaviour of diffuse fields in solid structures would greatly enhance the accuracy and applicability of Acoustic Emission (AE) measurements. The diffuse field approximation is a method whereby a complex wave field can be represented statistically in a very simple manner; however, there are certain conditions which must be satisfied before these approximations are valid. This thesis has explored the necessary conditions for diffuse wave fields to be generated by acoustic emission sources in idealised structures and developed signal processing techniques to take advantage of the diffuse field approximations.

Much of the initial work has been directed into the development and calibration of a suitable measurement system consisting of conical piezoelectric transducers as the source and receiver. In practical applications the ultrasonic source would be an AE event, such as an extending crack, but for the purposes of this project a simulated source was used instead to generate a pseudo-AE signal which was both repeatable and controllable. Repeatability and controllability are essential prerequisites if measurements are to be taken which isolate the behaviour of the structure.

An inevitable shortcoming of contact transducers is the random sensitivity variations caused by inconsistent coupling of the transducer to the material surface. Conical transducers, having a small front face diameter of around 1mm, offer improved repeatability over more standard transducers; however, random variations of around  $\pm 10\%$  in the transducers response are still commonplace. A novel method has been developed whereby the transducer coupling efficiency can be measured independently by an additional receiver mounted in the backing of the original transducer. Experiments have verified that a linear relationship exists between the amplitude of the backing signal and the coupling efficiency of the transducer.

Experiments were carried out using the equipment on aluminium plates to determine the diffuse field characteristics of these structures. The geometry, size and damping were systematically varied, thus demonstrating required conditions for a diffuse field to be sustained.

A Statistical Energy Analysis (SEA) model has been used to predict the time for a diffuse field to be generated in coupled plate structures and these results were compared with experimental data, showing promising results. Plates with step changes in thickness were also modelled and the results compared with the experimental measurements, good agreement again being shown.

## 7.2 Summary of findings

### Factors affecting receiver and source selection

The most important factors when selecting a suitable transducer for diffuse field measurements have been found to be aperture effects, damping effects and coupling variability; for contact transducers these effects can be minimised by selecting a transducer with the smallest possible front face area. The damping and coupling effects can be completely removed if a non-contacting transduction method is employed, for this reason non-contact reception methods would appear to be the most suitable for future laboratory investigations into the diffuse field properties of structures (provided that the required sensitivity can be attained). The major drawback of the non-contact methods which have been reviewed is the meticulous surface preparation which is required; EMATS (electro-magnetic acoustic transducers) or high power interferometers may achieve the necessary performance whilst not requiring optical surface finish and could constitute a viable alternative to contact piezoelectric transducers. EMATS, however, have a significant aperture and will consequently suffer from the same aperture effects as previously discussed. In conclusion, despite the coupling and damping effects, the conical transducer is an adequate receiver for diffuse field applications; of the other methods reviewed, only laser interferometry offers the possibility of major improvement.

Simulated sources must be repeatable in amplitude and frequency, controllable in amplitude and frequency and, for averaging purposes, capable of repetition rates of at least 10Hz (for standard ultrasonic measurements the repetition rate is in the kilohertz range but for diffuse field measurements a much slower repeat rate is necessary due to the long signal duration of up to 0.1 seconds). The auto-normalising piezoelectric source developed for the current work appears to satisfactorily fulfil these criteria although does suffer from the damping and aperture effects previously mentioned. Non contacting generation methods, such as lasers or EMATS, could also be

employed which would remove the inevitable damping effect caused by the source transducer. EMATS would be preferable over laser generation techniques as they allow more control over the bandwidth and amplitude of the signal although, again, the aperture effects may limit the bandwidth of the signal which can be generated. Impact sources have some attractions for this application due to the simplicity of the equipment, however, the repeatability and bandwidth of these sources has been found to be insufficient for diffuse field measurements.

### **Calibration of contact transducers**

Contact transducers load the surface of the material to which they are attached and hence alter the surface motion; this is known as the loading effect. The absolute calibration of a contact transducer is only valid when the transducer is being used on a surface with identical mechanical impedance to the original calibration surface. This, in addition to the coupling and aperture problems previously mentioned, makes absolute calibration of contact transducers of little practical use. If absolute measurement of surface motion is required, a non-contacting method is more appropriate.

### **The auto-normalising transducer**

The auto-normalising transducers shows good potential for a range of applications such as acoustic emission, condition monitoring and standard ultrasonic testing where coupling variations are problematic. At present the device only works well for a restricted band of frequencies; the reason for this is not entirely understood and more investigation is required if improvements are to be made. The method should be tested on more conventional transducer designs to see if potential exists for a device based on a more standard transducer.

### **Geometrical effects on diffuse field response**

The signal envelope energy, defined as the square of the area under the demodulated signal envelope, has been shown to be a measure of the energy density at the point of measurement and is thus inversely proportional to the volume of the structure; for plates of uniform thickness the plan area and volume are linearly proportional and so the envelope energy is also inversely proportional to the plan area. Diffuse fields have been measured in aluminium plates with plan areas of up to  $1\text{m}^2$  and there is evidence that considerably larger structures will also behave diffusely. Various

shapes of plate structure have been measured and it has been concluded that the plan geometry does not affect a structures diffuse field properties. In addition, plates consisting of simulated coupled substructures have been found to exhibit diffuse field behaviour even with coupling loss factors between substructures as low as 2.5%.

The effect of mode conversion from asymmetric boundaries can be detected using diffuse field measurements. In the case studied, only the fundamental Lamb modes ( $S_0$  and  $A_0$ ) were present; within the frequency range of the experiments these modes have very different attenuations (the attenuation of  $A_0$  being 2.4 times that of  $S_0$ ). The resulting diffuse field decay rate is therefore affected strongly by the steady state energy ratio of these two modes. The modal attenuations have been estimated from the decay rates measured from plates with symmetric and asymmetric boundaries and these compare well with the predicted attenuation of the modes present. A measurement of the diffuse field decay rate could represent an accurate and straightforward method for measuring the attenuation of propagating modes provided that single modes can be isolated or decoupled and mode conversion eliminated.

The reflection frequency (number of edge reflections per second) has been found to govern the rate at which energy is converted from one mode to another, therefore, modes with low group velocity tend to store energy. A case in point is that of  $A_0$  propagating in a stepped plate; the group velocity of  $A_0$  in the thinner section is lower than that in the thicker section and consequently the coupling loss factor is higher from the thick section into the thin section. This results in a net storage of energy in the thin section. Although this results in a non-uniform energy distribution throughout the structure, the steady state ratio of energies is the same regardless of initial conditions.

This result has extremely important consequences for AE testing of stepped structures. The optimal position for an AE transducer is clearly on the thinnest section of the structure where the displacement is highest and the majority of the energy is stored. Additionally, for the same reasons, if a structure requires additional damping, the thinnest section is the ideal location for the damping to be applied.

## Diffuse field behaviour in coupled structures

Most practical structures consist of a number of physically connected components. The most common joining methods used for the aerospace industry are bolting/riveting and adhesive bonding. The experiments carried out on coupled structures have demonstrated that the coupling required for a diffuse field to be established is less than 2.5%, these initial experiments were conducted using simulated coupled structures where a single plate was machined such that two distinct regions remained which were coupled by a narrow ligament. Bolted and adhesive joints present a rather more difficult problem due to the significant increase they cause in the damping of the structure. The damping increase is most dramatic for bolted structures due to frictional losses between the overlapping plate edges; for both bolted and adhesive joints the amount of damping has been shown to be proportional to the area of the overlap.

Bolted and adhesively bonded structures have been found not to behave diffusely as a whole, however the individual substructures do, in some cases, sustain a diffuse field. Diffuse field measurements could in theory be carried out in such cases by treating each substructure individually; this would require at least one receiver on each substructure. It can be concluded that diffuse field measurements are unlikely to be practical on most bonded structures although there are some cases where the damping introduced by the joint is low enough for some limited measurements to be made on individual substructures.

### **SEA modelling of coupled structures**

A statistical energy analysis model has been developed which successfully predicts the time required for a diffuse field to be established ( $t^*$ ) and the partitioning of energy between coupled fields within the structure. This model represents a useful tool for assessing how structures will behave and whether the diffuse field approach is valid. However, for accurate predictions to be made, the coupling and damping loss factors must be known for all modes present which can be extremely difficult to calculate or measure; it can be concluded that for most practical structures it would be simpler to assess experimentally whether a diffuse field is established and under what conditions.

### **Feasibility of diffuse field measurements for AE testing of aerospace structures**

The structures used for the diffuse field investigations are idealised in several respects

- The measurement surfaces are flat with good surface finish which reduces coupling variability.
- The structures are of uniform thickness, in the most part, which makes modes shape for each mode uniform throughout the structure.

If structures of varying thickness are to be used the ratio of surface displacement to energy must be calculated for each thickness and each mode. This makes tapered structures extremely difficult to analyse.

It seems likely that structures which can be tested individually (for example engine components which can be unbolted and removed), will sustain diffuse fields. More experimental work is required, using the equipment and techniques developed during this project, to verify this and apply the diffuse field method to real AE measurements on practical components.

## References

---

- D. N. Alleyne and P. Cawley (1991).** *The measurement and prediction of Lamb wave interaction with defects.* in Proc. IEEE Ultrasonics Symposium, pp855-857.
- D. N. Alleyne (1991).** *The Non-destructive Testing of Plates using Ultrasonic Lamb Waves.* PhD, Mechanical Engineering, Imperial College of Science Technology and Medicine, London.
- D. Alleyne and P. Cawley (1991).** *A two-dimensional Fourier transform method for the measurement of propagating multimode signals.* J. Acoust. Soc. Am., Vol 89(3), pp1159-1168.
- D. N. Alleyne and P. Cawley (1992).** *The interaction of Lamb waves with defects.* IEEE Transactions on Ultrasonics, Ferroelectrics and Frequency Control, Vol 39(3), pp381-397.
- ASTM (1982).** *Standard definition of terms relating to acoustic emission.* American Society for Testing and Materials, Philadelphia, PA.
- B. A. Auld (1990).** *Acoustic Fields and Waves in Solids.* (Krieger Publishing Company, Florida).
- B. A. Bainton and M. Silk (1980).** *Some Factors Which Affect The Performance of Ultrasonic Transducers.* British Journal of NDT, January 1983, pp15-20.
- F. M. Boler and H. A. Spetzler (1984).** *Capacitance transducer with a point-like probe for receiving acoustic emissions.* Review of Scientific Instruments, Vol 55(8), pp1293-1297.
- E. S. Boltz, C. M. Fortunko, M. A. Hamstad and M. C. Renken (1995).** *Absolute sensitivity of air, light and direct-coupled wideband acoustic emission transducers.* in Proc. Review of Progress in Quantitative NDE, eds. D. Thomson and D. Chimenti Vol 14, pp967-974.
- F. R. Breckenridge, C. E. Tschiegg and M. Greenspan (1975).** *Acoustic emission : some applications of Lamb's problem.* J. Acoust. Soc. Am., Vol 57(3), pp626-631.
- F. R. Breckenridge and M. Greenspan (1981).** *Surface-wave displacement : absolute measurements using a capacitive transducer.* J. Acoust. Soc. Am., Vol 69(4), pp1177-1185.
- F. R. Breckenridge (1982).** *Acoustic emission transducer calibration by means of the seismic surface pulse.* Journal of Acoustic Emission, Vol 1(2), pp87-94.
- F. R. Breckenridge, T. M. Proctor, N. N. Hsu and D. G. Eitzen (1984).** *Some notions concerning the behaviour of transducers.* National Bureau of Standards, Gaithersburg.
- F. R. Breckenridge, T. M. Proctor, N. N. Hsu, S. E. Fick and D. G. Eitzen (1984).** *Transient sources for acoustic emission work.* N.I.S.T, Gaithersburg.

- P. Cawley and R. D. Adams (1989).** *Defect types and non-destructive testing techniques for composites and bonded joints.* Materials Science and Technology, Vol 5, pp413-425.
- R. E. Challis, R. P. Cocker, A. K. Holmes and T. Alper (1992).** *Viscoelasticity of thin adhesive layers as a function of cure and service temperature measured by a novel technique.* Journal of Applied Polymer Science, Vol 44, pp65-81.
- D. G. Chetwynd and W. Sachse (1991).** *Design of micro-hammers for ultrasonic source applications.* Ultrasonics, Vol 29, pp68-75.
- R. B. Clough (1987).** *The energetics of acoustic emission source characterisation.* Materials Evaluation, Vol 45, pp556-563.
- B. Clough (1992).** *A scalar approach to acoustic emission.* in Proc. International Symposium on Vibroacoustic Characterisation of Materials and Structures, ASME, pp1-6.
- N. O. Cross (1982).** *Acoustic emission testing of pressure vessels for petroleum refineries and chemical plants.* ASTM, Philadelphia.
- H. A. L. Dempsey and D. M. Egle (1985).** *The effects of transducers on the decay of diffuse energy fields.* Journal of Acoustic Emission, Vol 4(1), ppS46-S49.
- S. E. Dunne (1985).** *Discussion of the application of acoustic emission methods for field monitoring of corrosion induced structural deterioration of reinforced and pre-stressed concrete structures.* Florida Atlantic University, Boca Raton.
- F. Dusek, C. Seidl, J. Siedlaczek and S. Pilecki (1990).** *The acoustic emission transducer calibration using spark method.* Archives of Acoustics, Vol 15(3-4), pp271-285.
- H. A. L. Dempsey and D. M. Egle (1985).** *The effects of transducers on the decay of diffuse energy fields.* Journal of Acoustic Emission, Vol 4(1), ppS46-S49.
- R. J. Dewhurst, C. E. Edwards, A. D. W. McKie and S. B. Palmer (1987).** *Comparative study of wide-band ultrasonic transducers.* Ultrasonics, Vol 25, pp315-321.
- H. Djelouah, J. C. Baboux and M. Pedrix (1989).** *Pulsed calibration technique of miniature ultrasonic receivers using a wideband laser interferometer.* Ultrasonics, Vol 27, pp80-85.
- D. M. Egle (1979).** *A stochastic model for transient acoustic emission signals.* J. Acoust. Soc. Am., Vol 65(5), pp1198-1203.
- D. M. Egle (1981).** *Diffuse wave fields in solid media.* J. Acoust. Soc. Am., Vol 70(2), pp476-480.
- I. Grabec and M. Platte (1984).** *A comparison of high-performance acoustic emission transducers.* Sensors and Actuators, Vol 5, pp275-284.
- M. Greenspan (1987).** *The NBS conical transducer: analysis.* J. Acoust. Soc. Am., Vol 81(1), pp173-183.

- H. Hanato (1975).** *Quantitative measurements of acoustic emission related to its microscopic mechanisms.* J. Acoust. Soc. Am., Vol 57(3), pp639-645.
- H. Hanato and E. Mori (1975).** *Acoustic-emission transducer and its absolute calibration.* J. Acoust. Soc. Am., Vol 59(2), pp344-349.
- G. Harman (1979).** *Non-destructive tests used to insure the integrity of semiconductor devices with emphasis on passive acoustic techniques.* in Non-destructive Evaluation of Semiconductor Materials and Devices (Plenum Press, New York).
- R. Hill and N. L. Adams (1979).** *Reinterpretation of the reciprocity theorem for the calibration of acoustic emission transducers operating on a solid.* Acustica, Vol 43, pp305-312.
- T. J. Holroyd, J. R. Webster, P. E. Cox and R. B. Price (1986).** *Uses of AE in Rolls-Royce plc.* in Proc. 8th International Acoustic Emission Symposium, Tokyo, pp1-7.
- N. N. Hsu and F. R. Breckenridge (1981).** *Characterisation and calibration of acoustic emission sensors.* Materials Evaluation, Vol 39, pp60-68.
- D. Hitchings (1987).** *FE77 User Manual.* Imperial College of Science Technology and Medicine, London.
- L. J. Jacobs and C. A. Woolsey (1993).** *Transfer functions for acoustic emission transducers using laser interferometry.* J. Acoust. Soc. Am., Vol 94(6), pp3506-3508.
- K. L. Johnson (1985).** *Contact Mechanics.* (Cambridge University Press, Cambridge).
- W. D. Jolly (1970).** *The application of acoustic emission to in-process inspection of welds.* Materials Evaluation, Vol 28(6), pp135-144.
- G. W. C. Kaye and T. H. Laby (1995).** *Tables of physical and chemical constants.* (Longman, Harlow).
- K. Y. Kim and W. Sachse (1986).** *Self-aligning capacitive transducer for the detection of broadband ultrasonic displacement signals.* Review of Scientific Instruments, Vol 57(2), pp264-267.
- K. Y. Kim, W. Sachse and B. Castagnede (1989).** *Miniaturised capacitive transducer for detection of broadband ultrasonic displacement signals.* Review of Scientific Instruments, Vol 60(8), pp2785-2788.
- Y. H. Kim and H. C. Kim (1993).** *Source function determination of glass capillary breaks.* Journal of Physics D; Applied Physics, Vol 26, pp253-258.
- G. S. Kino (1987).** *Acoustic waves : devices, imaging and analogue signal processing.* (Prentice-Hall Inc., New Jersey).
- L. E. Kinsler, Frey, A.R. (1982).** *Fundamentals of acoustics.* (John Wiley and Sons Inc., New York).
- B. T. Khuri-Yakub (1994).** *Private Communication.* Stanford University.
- H. Kuttruff (1973).** *Room Acoustics* (Applied Science, London).

- M. L. Lai and A. Soom (1990).** *Prediction of transient vibration envelopes using statistical energy analysis techniques.* Journal of Vibration and Acoustics, Vol 112, pp127-137.
- H. Lamb (1917).** *On waves in an elastic plate.* in Proc. The Royal Society, London, pp114-128.
- W. C. Leschenk (1975).** *Acoustic emission transducer calibrator.* Materials Evaluation, Vol 33(2), pp41-48.
- S. Lovass (1985).** *Acoustic emission of offshore structures: attenuation; noise; crack monitoring.* Journal of Acoustic Emission, Vol 26(8), ppA161-A164.
- M. J. S. Lowe (1993).** *Plate Waves for the NDT of Diffusion Bonded Titanium.* PhD, Mechanical Engineering, Imperial College of Science Technology and Medicine, London.
- M. Lowe (1995).** *Matrix techniques for modelling ultrasonic waves in multilayered media.* IEEE Transactions on Ultrasonics, Ferroelectrics and Frequency control, Vol 42(4), pp525-542.
- R. H. Lyon and E. Eichler (1963).** *Random vibration of connected structures.* J. Acoust. Soc. Am., Vol 36(7), pp1344-1354.
- R. H. Lyon (1976).** *Statistical energy analysis of dynamical systems: Theory and applications.* (Harvard University Press, Cambridge, Mass).
- W. P. Mason and R. N. Thurston (1972).** *Physical acoustics, principles and methods.* (Academic Press, London).
- R. E. McCullough (1976).** *Hermeticity and particle impact noise test techniques.* in Proc. IEEE Reliability Physics Symposium, New York, pp256-266.
- J. E. Michaels, T. E. Michaels and W. Sachse (1981).** *Applications of deconvolution to acoustic emission signal analysis.* Materials Evaluation, Vol 39(11), pp1032-1036.
- G. F. Miller and H. Pursey (1954).** *The field and radiation impedance of mechanical radiators on the free surface of a semi-infinite isotropic solid.* In Proc. The Royal Society of London, Vol 223, pp521-541.
- R. K. Miller (1987).** *Non-destructive Testing Handbook.* (American Society for Non-destructive Testing, USA).
- B. C. Moss and C. B. Scruby (1988).** *Investigation of ultrasonic transducers using optical techniques.* Ultrasonics, Vol 26, pp179-188.
- A. Nielsen (1980).** *Acoustic emission source based on pencil lead breaking.* Danish Welding Institute.
- C. H. Palmer and R. E. J. Green (1977).** *Materials evaluation by optical detection of acoustic emission signals.* Materials Evaluation, October, pp107-112.
- B. Pavlakovic, M. Lowe, D. Alleyne and P. Cawley (1997).** *Disperse: a general purpose program for creating dispersion curves.* in Proc. Review of Progress in Quantitative NDE, (Plenum Press, New York), eds. D. Thomson and D. Chimenti, Vol 16A, pp185-192.

- R. J. Pinnington and D. Lednik (1996).** *Transient statistical energy analysis of an impulsively excited two oscillator system.* Journal of Sound and Vibration, Vol 189(2), pp249-264.
- R. J. Pinnington and D. Lednik (1996).** *Transient energy flow between two coupled beams.* Journal of Sound and Vibration, Vol 189(2), pp265-287.
- D. W. Prine and T. Hopwood (1985).** *Improved structural monitoring with acoustic emission pattern recognition.* in Proc. Fourteenth Symposium on Non-destructive Evaluation, San Antonio, pp110-118.
- T. M. Proctor (1982).** *An improved piezoelectric acoustic emission transducer.* J. Acoust. Soc. Am., Vol 71(5), pp1163-1168.
- T. M. Proctor and F. R. Breckenridge (1992).** *Source waveforms : the use of a calibrated transducer in obtaining an accurate waveform of a source.* Journal of acoustic emission, Vol 10(3-4), pp43-48.
- L. Rayleigh (1885).** *On waves propagating along the plane of an elastic solid.* in Proc. London Math. Soc., Vol 17.
- C. B. Scruby and H. N. G. Wadley (1978).** *A calibrated capacitance transducer for the detection of acoustic emission.* Journal of Physics D : Applied Physics, Vol 11, pp1487-1494.
- C. B. Scruby and L. E. Drain (1990).** *Laser Ultrasonics: Techniques and Applications.* (Adam Hilger, Bristol).
- A. R. Selfridge (1985).** *Approximate Material Properties in Isotropic Materials.* IEEE Transactions on Sonics and Ultrasonics, Vol SU-32(3), pp381-394.
- G. Silk (1984).** *Ultrasonic Transducers for Non-destructive Testing.* (Adam Hilger Ltd., Bristol).
- J. A. Simmons, C. D. Turner and H. N. G. Wadley (1987).** *Vector calibration of ultrasonic and acoustic emission transducers.* J. Acoust. Soc. Am., Vol 82(4), pp1122-1130.
- R. Stonely (1924).** *Elastic waves at the surface of a separation of two solids.* in Proc. The Royal Society of London, pp106-416.
- J. Szilard (1980).** *Ultrasonic Testing.* (John Wiley & Sons, New York).
- P. Tscheliesnig and H. Theiretzbacher (1985).** *Leakage test by acoustic emission testing (AET) on flat bottomed tanks.* in Proc. Second International Conference on Acoustic Emission, Lake Tahoe, pp24-27.
- I. A. Viktorov (1967).** *Rayleigh and Lamb waves: Physical theory and applications.* (Plenum Press, New York).
- R. L. Weaver (1982).** *On diffuse waves in solid media.* J. Acoust. Soc. Am., Vol 71(6), pp1608.
- R. L. Weaver (1984).** *Diffuse waves in finite plates.* J. Acoust. Soc. Am., Vol 94(3), pp319-335.

- R. L. Weaver (1985).** *Diffuse elastic waves at a free surface.* J. Acoust. Soc. Am., Vol 78(1), pp131-136.
- R. L. Weaver (1986).** *Laboratory studies of diffuse waves in plates.* J. Acoust. Soc. Am., Vol 79(4), pp919-923.
- R. L. Weaver (1988).** *Diffuse waves for materials NDE.* in Acousto-Ultrasonics (Plenum Press, New York).
- J. R. Webster (1996).** *Private Communication.* Rolls Royce plc, Derby.
- J. R. Webster (1987).** *Vibro-acoustic emission due to Rubbing and Impact Sources in Vibrating Structures.* PhD, University of Nottingham, Nottingham.
- R. V. Williams (1980).** *Acoustic Emission.* (Adam Hilger Ltd., Bristol).
- J. Woodhouse (1981a).** *An approach to the theoretical background of statistical energy analysis applied to structural vibration.* J. Acoust. Soc. Am., Vol 69(6), pp1695-1709.
- J. Woodhouse (1981b).** *An introduction to statistical energy analysis of structural vibration.* Applied Acoustics, Vol 14, pp455-469.
- T. M. Wright and J. M. Carr (1981).** *Acoustic emission monitoring in the diagnosis of loosening in total knee arthroplasty.* in Proc. Biomechanics Symposium, New York, pp20-23.

## Appendix A: Calculated energy reflection coefficients of Lamb waves from notched and stepped plates

---

The following tables present the calculated energy reflection, transmission and mode conversion coefficients calculated for a variety of symmetric and asymmetric rectangular notches and steps. The calculations have been carried out for incident  $S_0$  and  $A_0$  with a nominal frequency-thickness of 0.75MHz-mm.

Depth	0%	25%	50%	75%	100%
Reflected $A_0$	0	0.002376	0.282694	0.789901	1
Transmitted $A_0$	1	0.997624	0.717306	0.210099	0
Reflected $S_0$	0	0	0	0	0
Transmitted $S_0$	0	0	0	0	0

Table A.1 Symmetric notch  $A_0$  input.

Depth	0%	25%	50%	75%	100%
Reflected $A_0$	0	0.030842	0.454955	0.715277	1
Transmitted $A_0$	1	0.909003	0.362711	0.078851	0
Reflected $S_0$	0	0.020751	0.030608	0.040125	0
Transmitted $S_0$	0	0.039404	0.151725	0.165748	0

Table A.2 Asymmetric notch  $A_0$  input.

Depth	0%	25%	50%	75%	100%
Reflected $A_0$	0	0	0	0	1
Transmitted $A_0$	0	0	0	0	0
Reflected $S_0$	0	0.052916	0.297856	0.727841	1
Transmitted $S_0$	1	0.947084	0.702144	0.272159	0

Table A.3 Symmetric Notch  $S_0$  input.

Depth	0%	25%	50%	75%	100%
Reflected $A_0$	0	0.028945	0.040412	0.049327	0
Transmitted $A_0$	0	0.055847	0.202866	0.207192	0
Reflected $S_0$	0	0.05846	0.25804	0.583358	1
Transmitted $S_0$	1	0.856749	0.498681	0.160124	0

Table A.4 Asymmetric notch  $S_0$  input.

Depth	0%	25%	50%	75%	100%
Reflected $A_0$	0	0.014876	0.152509	0.549657	1
Transmitted $A_0$	1	0.966552	0.787843	0.389767	0
Reflected $S_0$	0	0.009769	0.036914	0.047076	0
Transmitted $S_0$	0	0.008804	0.022734	0.013499	0

Table A.5 Asymmetric step  $A_0$  input at thin end.

Depth	0%	25%	50%	75%	100%
Reflected $A_0$	0	0.009107	0.647936	0.226643	1
Transmitted $A_0$	1	0.967955	0.200323	0.525490	0
Reflected $S_0$	0	0.009101	0.147094	0.048340	0
Transmitted $S_0$	0	0.013837	0.004647	0.199527	0

Table A.6 Asymmetric step  $A_0$  input at thick end.

Depth	0%	25%	50%	75%	100%
Reflected $A_0$	0	0.014496	0.059933	0.091784	0
Transmitted $A_0$	0	0.021011	0.114891	0.290703	0
Reflected $S_0$	0	0.015530	0.134129	0.165950	1
Transmitted $S_0$	1	0.948963	0.691047	0.0451563	0

Table A.7 Asymmetric step  $S_0$  input at thin end.

Depth	0%	25%	50%	75%	100%
Reflected $A_0$	0	0.013230	0.053432	0.073541	0
Transmitted $A_0$	0	0.013633	0.035698	0.028059	0
Reflected $S_0$	0	0.023213	0.144260	0.436593	1
Transmitted $S_0$	1	0.949924	0.766610	0.461807	0

Table A.8 Asymmetric step  $S_0$  input at thick end.

